MODELLING OF RADIONUCLIDE SEQUESTRATION BY METAL-ORGANIC FRAMEWORKS AND INTERCALATION PROCESS OF FERROCENE INTO VANADIUM PHOSPHATE BY DENSITY FUNCTIONAL THEORY

By

YUAN LIU

A DISSERTATION PRESENTED TO THE GRADUATE SCHOOL
OF THE UNIVERSITY OF FLORIDA IN PARTIAL FULFILLMENT
OF THE REQUIREMENTS FOR THE DEGREE OF
DOCTOR OF PHILOSOPHY

UNIVERSITY OF FLORIDA

2023

To my family and friends

ACKNOWLEDGMENTS

I wish to extend my heartfelt gratitude to all who have provided unwavering support and guidance throughout my Ph.D. journey. Without their encouragement, expertise, and guidance, the completion of this dissertation would have remained a distant dream.

A special note of thanks goes to my supervisor, Dr. Simon R. Phillpot. His consistent guidance, patience, and invaluable suggestions have not only provided direction to my research but have also molded my perspective as a scholar. Dr. Phillpot's dedication to academic excellence has profoundly influenced my academic and personal trajectory. Each interaction with him has been a lesson in itself, expanding my horizons and granting me the confidence to navigate through research challenges.

I am indebted to my collaborators – Prof. Natalia Shustova, Kyoungchul Park, and Dr. Shenyang Hu – and the entire EFRC-CHWM group for giving me the opportunity to delve into nuclear waste sequestration. The insights gained from our all-hands meetings have been instrumental in shaping my understanding.

I extend my appreciation to my committee members, Prof. Michael Tonks, Prof. Megan Butala, and Prof. Youping Chen. Their constructive feedback and thought-provoking insights have immensely enriched this dissertation.

I must also acknowledge the support and camaraderie of our group members, Dr. Ximeng Wang, Dr. An T. Ta, and Seaton R. Ullberg, whose invaluable suggestions have enhanced both my academic and interpersonal skills.

Beyond the academic realm, my most profound gratitude goes to my parents. Their unwavering faith in me, their sacrifices, and their ceaseless encouragement have

been my anchor. They have instilled in me the values of perseverance, humility, and diligence, guiding every step of my academic journey.

I would also like to thank my uncle, whose wisdom, stories, and unwavering support have enriched my life in countless ways. My gratitude extends to my entire family, whose collective love, belief, and encouragement have been my source of strength and motivation.

To my friends, Dr. Xinhao Liu, Nan Jiang, and Qi Zhang: Thank you for being pillars of strength and sources of laughter throughout this journey. Your companionship, wisdom, and unwavering support have been instrumental during challenging times and moments of doubt. Having you by my side made this endeavor all the more meaningful.

TABLE OF CONTENTS

page

ACKNOWLEDGMENTS 4

LIST OF TABLES 9

LIST OF FIGURES 11

LIST OF ABBREVIATIONS 15

ABSTRACT 16

CHAPTER

1 INTRODUCTION 18

1.1 Overview and Motivation 18
1.2 Metal-Organic Frameworks 21
1.3 Vanadyl Phosphate Material 23
1.4 Outline 24

2 METHODOLOGY 26

2.1 Overview 26
2.2 Density Functional Theory 26
2.2.1 Hohenberg and Kohn Theorems 28
2.2.2 Exchange-Correlation Functionals 30
2.2.3 DFT+U correction 32
2.2.4 van der Waals Correction 33
2.2.5 Spin-Orbital Coupling Effect 35
2.2.6 Solvation Effect 36
2.3 Nudged Elastic Band Method 37

3 BINDING OF URANYL CATIONS TO A ZR-BASED METAL-ORGANIC FRAMEWORK BY DENSITY FUNCTIONAL THEORY 39

3.1 Background 39
3.2 Structures 40
3.2.1 Zr-MOFs 40
3.2.2 Uranyl Cation 42
3.2.3 Uranyl Cation Binding Structures 42
3.3 Computational Method 46
3.3.1 Parameters Setting 46
3.3.2 Methods of Calculating Binding Energy Between Zr-MOF And Uranyl Ion 48
3.4 Results and Discussion 50

3.4.1 Structure, Electron Localization Function, And Density of States Of Pristine Zr-MOF....50
3.4.2 Hydrated Uranyl Ion....53
3.4.3 Evaluation of The Energy $\Delta \mathbf{E1}$....55
3.4.4 Binding Uranyl Ions To MOF....56
3.4.4.1 The choice of DFT method....56
3.4.4.2 Effects of Zr-MOF protonation on site preference....59
3.4.4.3 Charge density difference analysis....61
3.4.5 $\mathbf{OM(A)D-OE}$ is the Most Stable Configuration....64
3.4.5.1 O=U=O bond angle after uranyl ion binding....64
3.4.5.2 Zr-O_u bond formation....64
3.5 Conclusion....66

4 BINDING OF RADIONUCLIDES AND SURROGATE TO 18-CROWN-6 ETHER BY DENSITY FUNCTIONAL THEORY....68

4.1 Background....68
4.2 Computational Method....69
4.3 Structures....73
4.3.1 Crown Ether....73
4.3.2 Models of The Cerium-, Americium-, And Curium-based Salts....74
4.4 Results....76
4.4.1 18-Crown-6 Ether Complexes with Cerium, Americium, and Curium Nitrates....76
4.4.1.1 Comparison of theoretical and experimental data....76
4.4.1.2 The 18-crown-6 ether with americium and curium nitrates....78
4.4.2 Nitrogen, Sulfur, and Phosphorus-Based Crown Ethers....81
4.4.2.1 Benchmark....81
4.4.2.2 The amine and imine-based crown ethers with actinide nitrates....87
4.4.2.3 Comparison of Charge Density Maps....88
4.4.2.4 Electron localization function of nitrogen-based crown ether with actinide nitrites....90
4.4.2.5 Solvation Effect....95
4.5 Conclusions....98

5 ADDITIONAL STRATEGIES FOR THE SEQUESTRATION OF RADIONUCLIDES FROM DENSITY FUNCTIONAL THEORY....101

5.1 Background....101
5.2 Computational Methods....101
5.3 MOF Secondary Unit Buildings (SBUs) Structures....102
5.4 Results....103
5.4.1 Formation Energy of Zr- and Th-Based SBUs....103
5.4.2 Formation Energy of Transmetallation U-SBUs to Th-SBUs....105
5.4.3 Estimating Enthalpy of the Transmetallation reaction of U-SBUs to Th-SBUs....106

5.4.4 Estimation of DOS and Optical Bandgap of Transmetallation From U-SBUs to Th-SBUs 111
5.4.5 O–H bond deprotonation energy in U-8 and Th-8 nodes 115
5.5 Conclusions 120

6 FERROCENE INTERCALATION IN VANADYL PHOSPHATE: A DENSITY FUNCTIONAL THEORY STUDY OF POLARIZABLE ION DETECTION 121

6.1 Background 121
6.2 Computational Methods 122
6.3 Structures 124
6.3.1 Vanadyl Phosphate 124
6.3.2 Ferrocene 127
6.4 Results 129
6.4.1 Configurations of Ferrocene on Vanadyl Phosphate 129
6.4.2 Effect of the magnetic moment 131
6.4.3 The Total Energy Comparison 134
6.4.4 Charge Density Difference 139
6.4.5 The Electron Localized Function Plots and Hirshfeld Surface Analysis 144
6.4.6 Ferrocene Immigration Energy Preliminary Results 150
6.4.6.1 Ferrocene move along [110] direction 150
6.4.6.2 Ferrocene move along [100] direction 153
6.7 Conclusions 154

7 SUMMARY AND FUTURE WORK 156

LIST OF REFERENCES 162

BIOGRAPHICAL SKETCH 182

LIST OF TABLES

Table		page
3-1	Total energies of different proton topologies of Zr-MOF relative to the MOF-4 value	43
3-2	Comparison of experimental and computed structural parameters for the Zr-MOF.	43
3-3	The binding site configurations for the four different Zr protonation schemes.	46
3-4	Distance between neighboring Zr atoms as shown in Figure 3-7, d(Zr–Zr).	53
3-5	$UO2\{H2O\}n2+$ hydration energy per H2O	54
3-6	The O=U=O bond angle in degrees for various deprotonated Zr-MOFs as defined in Figure 3-4.	62
4-1	The six bond lengths of Ce-$O_{(crown)}$, and binding energy of cerium nitrate within 18-crown-6 ether,by applying different Hubbard U values for cerium.	70
4-2	The six bond lengths of Am-$O_{(crown)}$, and binding energy of americium nitrate within 18-crown-6 ether, by applying different Hubbard U values for americium.	70
4-3	The comparison of experimental and theoretical data of cerium nitrate in 18-crown-6 ether by using GGA+U and VDW_DF2+U method.	72
4-4	The six bond lengths of Ce/Am/Cm-$O_{(crown)}$, and binding energy of americium nitrate within 18-crown-6 ether, with and without soc correction.	73
4-5	Comparison of DFT and experimental of average bond lengths.	74
4-6	The average bond length between cerium, americium, and curium with oxygen in their corresponding nitrates complexes.	75
4-7	The dihedral angle of pure 18-crown-6 ether and 18-crown-6 ether within cerium nitrate complex.	79
4-8	The magnetic moment of Ce, Am, and Cm in pure corresponding nitrates, 18-crown-6 ether, nitrogen-based crown ether, and amine-based crown ether.	81
4-9	Comparison of binding energy and mean bond lengths of cerium with crown ether (CE), and mean diameters of corresponding pure crown ether by using the VDW_DF2+U method.	85

4-10 Bond lengths between americium/curium and nitrogen in the ether as determined by the VDW_DF2+U 88

4-11 Binding energy between americium/curium nitrates in NH-crown ether (CE) and N-crown ether by using the VDW_DF2+U method. 88

4-12 Bader charges analysis for different compounds by using the VDW_DF2+U method. 90

4-13 Binding energy between Am^{3+}/Cm^{3+} cations, $Am^{3+}(H_2O)_6$/$Cm^{3+}(H_2O)_6$ complexes, and $Am(NO_3)_3$/$Cm(NO_3)_3$ molecules in oxygen-, amine-, and imine-based crown ether by using the VASPsol method. 98

5-1 The formation energy of Zr-/Th- SBU with different coordinations. 104

5-2 The formation energy of Zr-/Th- SBU-12 with different numbers of additional phenyl functional groups 105

5-3 The formation energy of each MOF-SBU cluster. 106

5-4 Comparing the transmetallation energy based on the different reference states and experimental data. 110

5-5 The bandgap of each magnetic moment and weighted bandgap of heterometallic MOF-SBU. 114

5-6 The deprotonation energies of the U-8 and Th-8 clusters. 118

6-1 The lattice parameters of $VOPO_4$ by using GGA+U with D3 correction and compared with experimental data of $VOPO_4 \cdot 2H_2O$. 126

6-2 Optimized bond distances of eclipsed ferrocene from our calculations and other works 129

6-3 The Relative total energy of four possible charge accumulation of vanadium. The reference is the charge accumulation on the left. 142

6-4 The relative total energy of ferrocene extracted from the $VOPO_4$ layer compared to that of pure ferrocene. 146

6-5 Relative total energy comparison: with D3 (Reference: E-V-45°) versus without D3 (Reference: E-VO-0°) in eV. 147

LIST OF FIGURES

Figure page

1-1 Energy consumption from 1800-2022....18

1-2 The radioactive decay of actinide elements 20

1-3 The strategies of MOFs to capture nuclear waste 22

1-4 The specific capacity of alkali-ion batteries with $VOPO_4$ as the cathode 23

2-1 The Jacob's ladder of density functional theory 30

3-1 The crystal structure of Zr-MOFs 41

3-2 Two views of the optimized structure of pentahydrated uranyl ion, $[UO_2 \cdot (H_2O)_5]^{2+}$....42

3-3 The possible proton topologies of Zr-MOF 43

3-4 Zr-MOF structures with various equatorial Zr (Zr_1, Zr_2, Zr_3, and Zr_4) deprotonations....45

3-5 The attachment oxygen position of metal node....46

3-6 The moving path picture of uranly cation into MOFs....52

3-7 Electron localization function for various deprotonation cases 53

3-8 The density of states of MOFs. 53

3-9 The energy for removing two water molecules from the pentahydrated uranyl ion is a function of the total number of the water molecules surrounding the layer uranyl ion. 55

3-10 Binding energies (ΔE) of binding of uranyl ion to MOF-0 ion using different calculation methods....57

3-11 The binding energies (ΔE) of different protonation of Zr-MOF with different density functional theories....58

3-12 The mean bond length in Å of 19 different configuration 59

3-13 Binding energies (ΔE) of neutral system with GGA+U_D3 method to calculate the total 19 configurations binding energy. 62

3-14 The two metrics of MOF-0 space....63

3-15 Schematics of charge difference after uranyl ions attachment as determined by GGA+U_D3.....63

3-16 The energies of an isolated uranyl ion as a function of the O=U=O bond angle; the zero of energy corresponds to a bond angle of 179.6˚. 65

3-17 The density state of attaching zirconium atom and uranyl ion double bond oxygen 66

4-1 The molecular structure of 18-crown-6 crown ether. Oxygen in red, carbon in brown, and hydrogen in white. 74

4-2 The molecular structures of different actinide nitrates. 75

4-3 The density of states of different actinide nitrates within the energy window from -10 to 6 eV.....77

4-4 The molecular structure of cerium nitrate within crown ether 79

4-5 The N-Ce-N bond angle and binding energy between cerium nitrate and crown ether as a function of distance 80

4-6 The molecular structure measurements 82

4-7 The optimized structure of cerium nitrate in different crown ethers by using the VDW_DF2+U method 83

4-8 The binding energy of cerium nitrate increases as the number of oxygens substituted by the amine group in the crown ether by using the VDW_DF2+U method.....83

4-9 The charge density difference maps between cerium nitrate with different crown ether by using VDW_DF2+U method 86

4-10 The top view of optimized structure of americium nitrate in different crown ethers by using VDW_DF2+U method. 87

4-11 The charge density difference map of different Am complexes by using VDW_DF2+U method.....89

4-12 The charge density difference map of different Cm complexes by using vdw_DF2+U method.....89

4-13 The 2D plane of electron localized function of americium nitrate in amine-based crown ether.....91

4-14 The 2D plane of electron localized function of americium nitrate in nitrogen-based crown ether. 92

4-15 The 2D plane of electron localized function of curium nitrate in amine-based crown ether. 92

4-16 The 2D plane of electron localized function of curium nitrate in nitrogen-based crown ether. 92

4-17 The 1D linear profile electron localized function from americium to different nitrogen of americium nitrate in amine-based crown ether. 93

4-18 The 1D linear profile electron localized function from americium to different nitrogen of americium nitrate in nitrogen-based crown ether. 93

4-19 The 1D linear profile electron localized function from curium to different nitrogen of curium nitrate in amine-based crown ether. 94

4-20 The 1D linear profile electron localized function from curium to different nitrogen of curium nitrate in nitrogen-based crown ether. 94

5-1 Schematic representation of MOF-SBU structures. 103

5-2 The Zr-/Th-SBU-12 with one additional phenyl functional group and two additional phenyls functional groups. 105

5-3 A comparison of the transmetallation energy with theoretical and experimental data is reported in Table 5-2. 112

5-4 Transmetallation energy of substituted U-SBU by Pu-SBU 112

5-5 Possible magnetic moments of U-8 configurations adapted from Pandey *et al.*.[71] 114

5-6 The comparison bandgap of heterometallic of metal node between calculated and exprimental as a function of %Th. 115

5-7 The DOS plots of each lowest total energy configuration of each MOF composition. 116

5-8 The relative total energies of the different multiplicities of U-SBU. The reference is singlet multiplicity.The black is for the Stuggart pseudopotential while the red is for the CRENBL pseudopotential. 119

5-9 Optimized actinide SBU structure and protonation sites. 119

6-1 The crystal structure of dehydrated $VOPO_4$ 125

6-2 Illustration of the $VOPO_4$ layer displacement corresponding energies as a function of displacement relative total energy as the reference of the original structure 127

6-3 Side view depiction eclipsed, and staggered configurations of ferrocene.....129

6-4 The possible orientation of ferrocene intercalted on V side.....131

6-5 Ferrocene intercalation on the P/P site, viewed along [010] direction.....132

6-6 The different crystal configurations.....133

6-7 The relative total energy of 11 different configurations. The reference is E-V-45°.....135

6-8 The optimization of the most stable (gauche) configuration of ferrocene intercalated between phosphorus and phosphorus 137

6-9 The different relaxed crystal configurations.....138

6-10 Bader charges analysis of eight unique configurations and compared them with experimental data. 140

6-11 The charge density maps of relaxed configurations.....141

6-12 The four possible charge accumulations of vanadium. 143

6-13 The charge density difference map built by the four vanadium atoms, viewed along [001] direction. 144

6-14 The crystal structure of E-OV-0° configuration, E-OV-45° configuration, E-V-0° configuration, and E-V-45° configuration. 146

6-15 The linear profile ELF of H to O_1 and O_2, E-V-0° and E-V-45°.....148

6-16 The supercell structure of E-V-45° configuration, and the corresponding charge density difference map.....150

6-17 The Hirshfeld surface analysis of E-VO-0°, and E-V-45° configurations.....151

6-18 The schematic representation showcases ferrocene moving along the [100] direction. 151

6-19 The energy barrier of ferrocene moving along [110] direction by using NEB method, blue is eight (coarse) images and orange is seventeen(dense) images. 152

6-20 The dihedral angle of cyclopentadienyl ring. 153

6-21 The NEB calculations of ferrocene immigrated through VOPO4. 154

LIST OF ABBREVIATIONS

B3LYP	Becke, 3-parameter, Lee–Yang–Parr
CE	Crown Ether
CI-NEB	Climbing Image Nudge Elastic Band Method
DFT	Density Functional Theory
DOS	Density of State
GGA	Generalized Gradient Approximation
LDA	Local-Density Approximations
MOF	Metal-Organic Framework
PBE	Perdew-Burke-Ernzerhof
VASP	Vienna Ab-initio Simulation Package
$VOPO_4$	Vanadyl Phosphate

Abstract of Dissertation Presented to the Graduate School
of the University of Florida in Partial Fulfillment of the
Requirements for the Degree of Doctor of Philosophy

MODELLING OF RADIONUCLIDE SEQUESTRATION BY METAL-ORGANIC FRAMEWORKS AND INTERCALATION PROCESS OF FERROCENE INTO VANADIUM PHOSPHATE BY DENSITY FUNCTIONAL THEORY

By

Yuan Liu

December 2023

Chair: Simon R. Phillpot
Major: Materials Science and Engineering

Zirconium Metal-Organic Frameworks (Zr-MOFs) have been widely used as ion adsorbents for the removal or extraction of toxic and/or radionuclide species from aqueous solutions. However, the mechanisms by which uranyl ions (UO_2^{2+}) interact with Zr-MOFs have not been established. In this work, the nature of the bonding of uranyl ions with a Zr-MOF was determined using density functional theory (DFT) for nineteen structurally distinct candidate complexes. The most stable structure involved the coordination of the uranyl cation and two structurally distinct oxygens in the Zr-MOF metal node. It was also found that a higher degree of deprotonation in Zr-MOF correlated with higher binding energy between the Zr-MOF and uranyl cations. These insights can aid in the design of Zr-MOFs with optimized features for efficient capture of uranyl cations.

DFT was also used to determine the interactions of cerium, americium, and curium cations with crown ethers. Our calculations reveal that the modeled structure of cerium integrated within the crown ether is in good agreement with experimental data. Our results demonstrate that crown ethers can also bind americium and curium,

providing insights into the potential applications of crown ether in radionuclide sequestration. Finally, the impact of the modification of the skeleton of the crown ethers through substitution of nitrogen atoms for oxygen atoms is found to significantly increase the radionuclide binding energies. These findings provide insights into the potential for the use of organic linkers such as crown ethers in MOFs to address radionuclide sequestration.

A systematic investigation of 11 possible configurations of the intercalation of ferrocene into vanadyl phosphate, $VOPO_4$, revealed the existence of 8 structurally distinct configurations. Among these configurations, the most stable was determined to be that of ferrocene intercalated between a vanadium and oxygen-vanadium site, with the carbon-hydrogen apex from the cyclopentadienyl rings facing the vanadium atom, and the axis of ferrocene rotated by 45° respective to the [100] direction of the (001) plane of the $VOPO_4$. Charge density distributions indicated a charge transfer between iron and vanadium, supporting the preference for ferrocene to intercalate between a vanadium and an oxygen-vanadium site rather than on a phosphorus site. When intercalated on the vanadium site, ferrocene adopts an eclipsed arrangement, while it adopts a gauche arrangement on a phosphorus site.

CHAPTER 1
INTRODUCTION

1.1 Overview and Motivation

In the modern era, the world has seen an unprecedented rise in demand for energy due to growing populations, industrialization, and the ubiquity of technology in daily life. In Figure 1-1, this escalating hunger for power has pushed our traditional energy resources, primarily fossil fuels, to their limits. The burning of coal, oil, and gas not only depletes finite reserves but also contributes to environmental challenges like air pollution and climate change. This confluence of dwindling resources and environmental implications presents us with what is termed the "Global Energy Crisis."

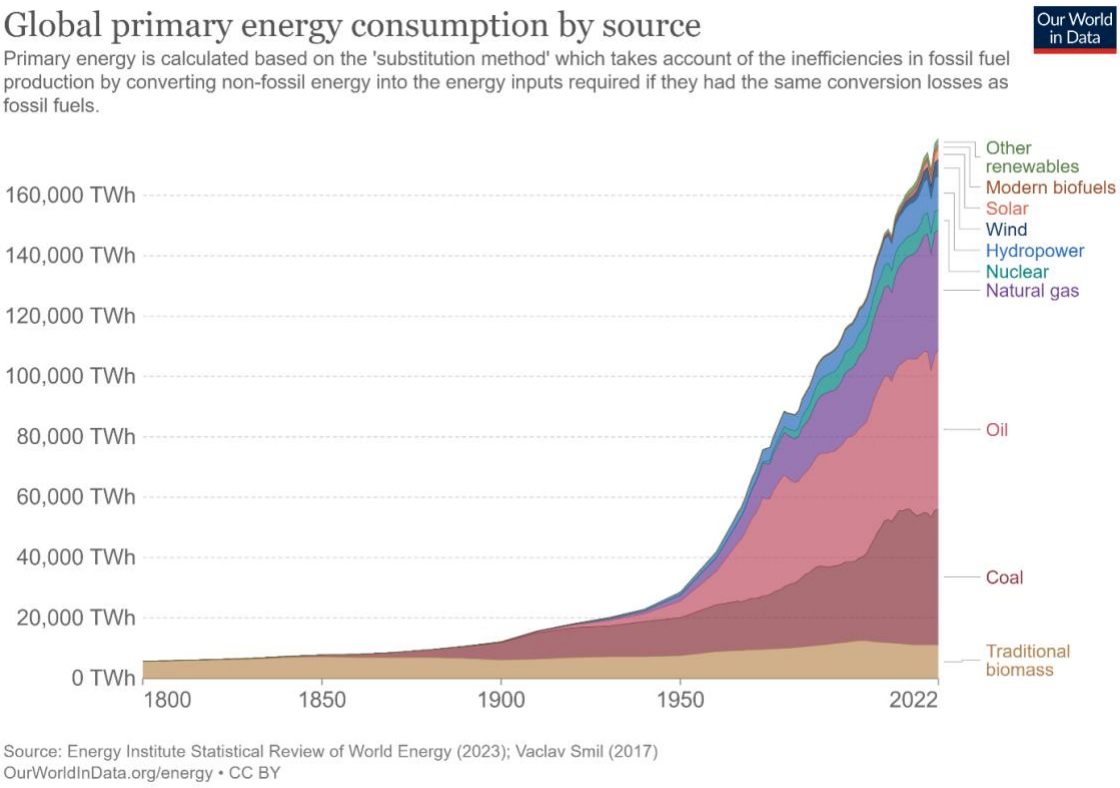

Figure 1-1. Energy consumption from 1800-2022. (Copied from weblink: https://ourworldindata.org/energy-production-consumption#global-energy-consumption)

Nuclear energy plays a pivotal role in tackling our ongoing energy challenges. Its ability to generate substantial power without emitting greenhouse gases has led to considerable progress in creating a cleaner, low-carbon energy source. Modern reactors, complemented by potential breakthroughs such as fusion technology, present a viable alternative to fossil fuels. With the rapid growth in the demand for clean energy, the use of nuclear power is expected to continue to increase.[1,2] Therefore, the management of used nuclear fuel remains as relevant as ever.

However, the sequestration and storage of radioactive waste, chiefly from nuclear reactors and other nuclear processes (e.g., nuclear weapon decommissioning), is an ongoing challenge.[3] The radioactive byproducts resulting from nuclear reactions persist for thousands of years and need meticulous containment to prevent environmental contamination in Figure 1-2. High-level radioactive waste, especially from spent fuel rods, demands highly specialized storage facilities. These facilities must ensure that no radiation leaks into the surrounding environment, posing risks to both human health and ecosystems.[4,5]

The secure storage of high-level nuclear waste is a pressing concern in today's world. Research in this realm is burgeoning, with efforts focused on identifying and engineering optimal materials for this critical task. Recent studies have illuminated the potential of hierarchical materials, tailored both at molecular and crystallographic scales, to selectively encapsulate specific radionuclides.[6] Hierarchical structures can be simply defined as materials with structural motifs spanning multiple length scales. This category embraces diverse materials, including salt inclusion compounds, metal-organic frameworks (MOFs), porous silica, and surface-functionalized nanoparticles. In this

investigation, we focus on the utility of MOFs as potential vessels for confining radionuclides.

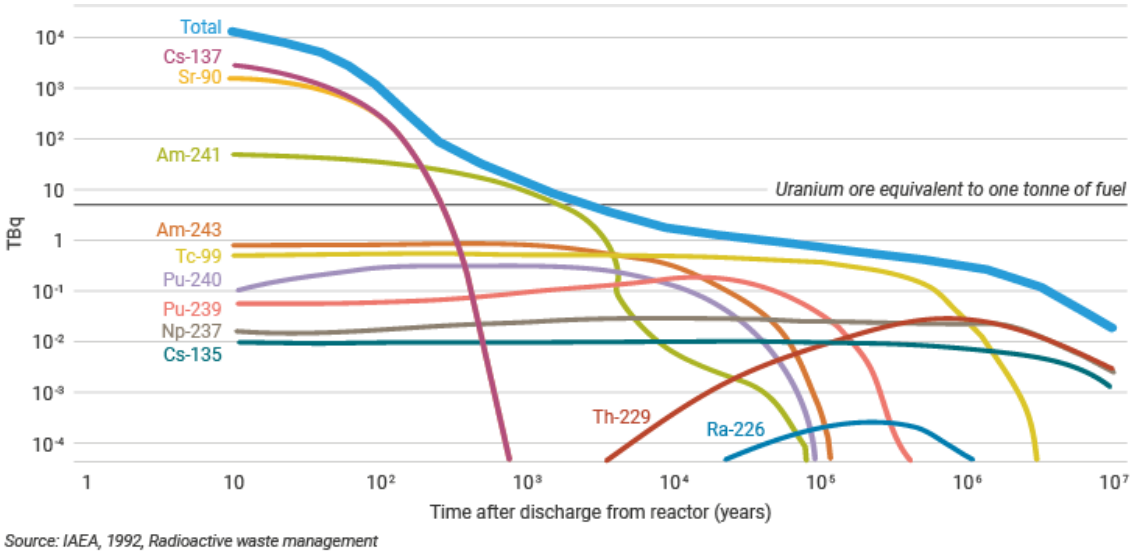

Figure 1-2. The radioactive decay of actinide elements. (Copied from weblink: https://world-nuclear.org/information-library/nuclear-fuel-cycle/introduction/physics-of-nuclear-energy.aspx)

Concurrently, efficient energy storage is crucial for resolving the energy crisis. Lithium batteries, the most prevalent form of energy storage, are integral to our daily lives, powering devices like smartphones and electric vehicles.[7] Yet, as with all technologies, they possess inherent challenges that must be tackled for a holistic solution. Their capacity and longevity still need enhancements to meet the rising global energy demands. Some of challenges lie in the battery's cathode and anode materials.[8,9] Currently, most lithium-ion batteries use a combination of materials, such as lithium cobalt oxide (for cathodes)[10] and graphite (for anodes).[11] These materials, while effective, have limitations in terms of energy density, cycle life, and safety. Overcoming these limitations necessitates the development of new materials that can store more lithium ions or allow for faster movement of these ions without degrading quickly or posing safety risks.

In the relentless pursuit of advancing battery technology, researchers are delving into alternatives beyond the conventional. Silicon anodes[12] have emerged as a promising contender, boasting a theoretical capacity to house more lithium ions than graphite. On the other side of the battery, cathodes constructed from materials like lithium iron phosphate[13] and lithium manganese oxide[14] are drawing attention for their potential merits in durability and safety. Recently, vanadyl phosphate[15] has entered the spotlight in the battery arena. Its unique properties and potential performance metrics position it as a potential game-changer in the next generation of energy storage solutions.

1.2 Metal-Organic Frameworks

Metal-Organic Frameworks (MOFs) are a class of crystalline materials comprised of metal ions or clusters coordinated to organic ligands. This arrangement forms a repeating network, giving rise to a porous structure. The metal ions act as nodes or joints, while the organic ligands serve as links or connectors. This unique arrangement creates a vast array of potential framework topologies, ranging from simple cubic or tetragonal to more complex structures.

MOFs offer a compelling solution for nuclear waste management. These structures can be tailored to selectively capture specific radionuclides like technetium (Tc) or uranium (U) due to their customizable organic linkers and metal centers. With their vast surface area and porous nature, they can hold substantial amounts of radioactive materials. Moreover, some MOFs are resilient to the heat from radioactive decay and resist radiation damage. Their modularity also enables the integration of various functional groups, making them adaptable not only for radionuclide capture but also for subsequent processing and long-term stability.

In the work of zur Loye *et al.*,[6] as depicted in Figure 1-3, the potential of MOFs in capturing nuclear waste is explored in depth. They identified four strategies. First, the metal nodes in MOFs are leveraged to interact directly with actinide cations, acting as a primary trap for radionuclides. Second, the organic ligands are modified, enhancing their capability to bind more effectively with actinides. The third strategy, transmetallation, entails strategically replacing the intrinsic metal ions within MOFs with actinide ions, thereby capturing the radionuclides. Last, by fine-tuning the MOF's pore sizes and integrating select organic ligands, the structures can be optimized to selectively trap actinide cations. Collectively, these distinct approaches illustrate the versatility and potential of MOFs as a promising solution for nuclear waste management. In this study, our primary emphasis will be on the first three methods, which correspond to Chapters 3 to 5.

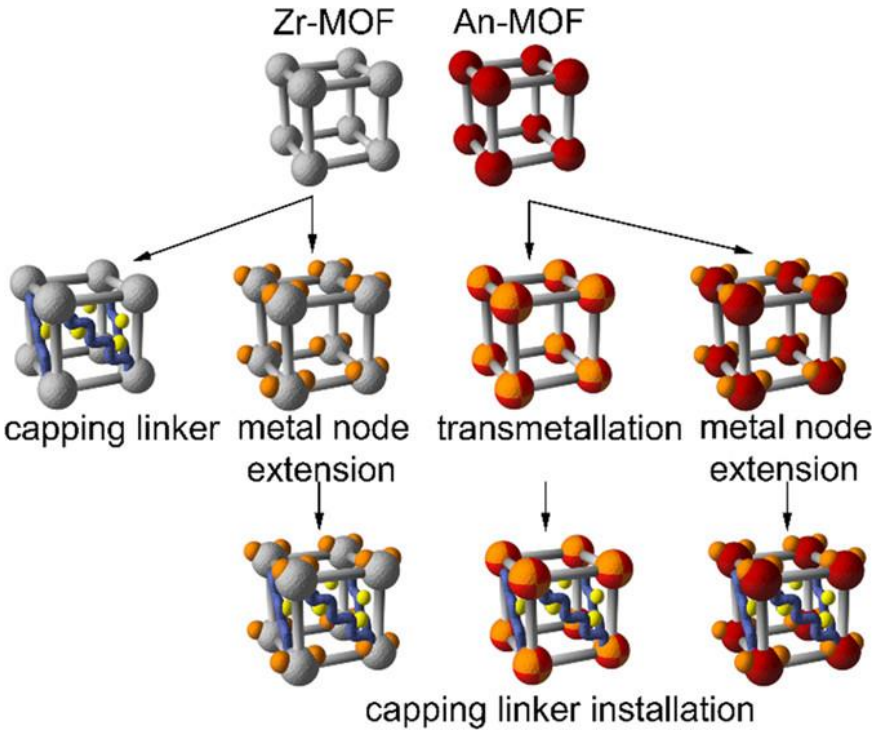

Figure 1-3. The strategies of MOFs to capture nuclear waste. (Reproduced from zur Loye, H.-C. et al., Chem. Mater. 30(14), 2018.[6])

1.3 Vanadyl Phosphate Material

In the quest to develop high-performance, durable, and sustainable energy storage solutions, researchers and scientists are constantly exploring novel materials with unique electrochemical properties. One such compound that has garnered significant attention in recent years is vanadyl phosphate ($VOPO_4$).[16,17] Rooted in its distinct chemical properties and structural features, vanadyl phosphate offers great potential in the realm of battery technology[18,19] in Figure 1-4. The specific capacity of $VOPO_4$, when used as the cathode material for alkali-ion batteries, falls within the typical range of 150-200 mAh/g.[20] Yet, even after 500 charge cycles, it retains 90% of its capacity for lithium and 73% for sodium.[21]

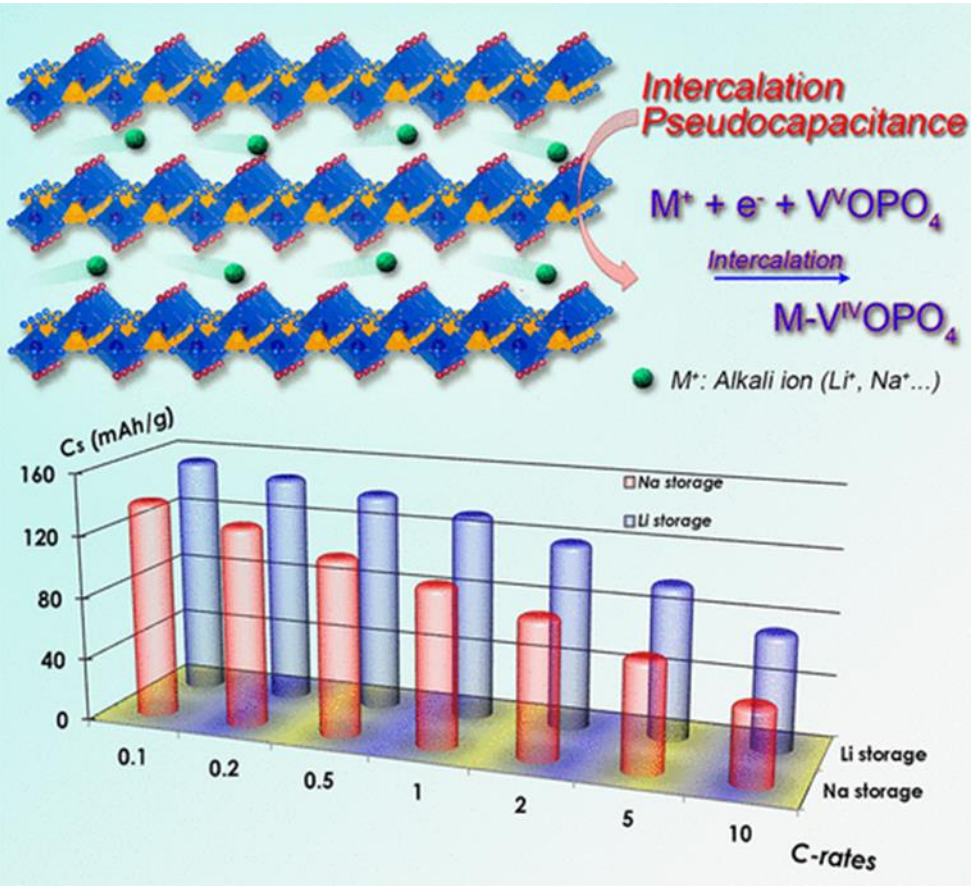

Figure 1-4. The specific capacity of alkali-ion batteries with $VOPO_4$ as the cathode. (Adapted from Zhu et al. Nano letters, 16, 2016[21])

Vanadium, known for its multivalent nature, allows for multiple electron transfer processes, making its compounds favorable candidates for energy storage. $VOPO_4$ exploits this property, exhibiting excellent reversibility and stability during charging and discharging cycles.[22]

The application of vanadyl phosphate in batteries stems from its potential to bridge the gap between the energy density of traditional lithium-ion batteries and the cycling stability of capacitive materials. Furthermore, the compound's ability to operate safely under a broad range of temperatures and its resistance to thermal runaway — a major safety concern in many battery types — sets it apart.[19]

1.4 Outline

This dissertation is structured as follows: Chapter 2 details the computational methodologies employed. In Chapter 3, we explore the interaction mechanisms between uranyl cations and zirconium-based MOFs metal nodes by using various levels of DFT methods. Our findings indicate a direct correlation between the extent of Zr-MOF deprotonation and the binding energy with uranyl cations. Simply put, solutions with higher pH values are more efficient in capturing uranyl cations. In Chapter 4, we explore the binding of cerium, americium, and curium nitrates into 18-crown-6 ether, a type of organic ligand used in MOFs. The DFT simulation results presented are in agreement with experimental data. In addition, we observe that substituting oxygen atoms in the skeleton of 18-crown-6 ether with nitrogen leads to a significant increase in the binding energy between radionuclides and the crown ether. In Chapter 5, we explore the substitution of uranium with thorium. Based on these findings, we predict the existence of uranium/plutonium transmetallation. Consequently, from a theoretical perspective, the synthesis of a plutonium-based MOF is plausible. This suggests a novel avenue for the

sequestration of plutonium ions. In Chapter 6, we explore the intercalation of ferrocene into $VOPO_4$. DFT simulations indicate the most stable configurations when ferrocene is positioned on vanadium and phosphorous sites, respectively. The simulated results of charge distribution and lattice parameters are in agreement with experimental data, thereby affirming the robustness of the simulation outcomes. Building on these insights, we also investigate the optimal diffusion pathway of ferrocene into $VOPO_4$. Chapter 7 concludes the dissertation by summarizing the key takeaways and providing a comprehensive outlook on the future prospects of our research. We underscore the importance of interdisciplinary collaborations between computational and experimental researchers to design and synthesize next-generation materials for a myriad of applications.

CHAPTER 2
METHODOLOGY

2.1 Overview

Atomic-scale simulations empower scientists and engineers to predict and comprehend the properties of materials by modeling their atomic and molecular configurations. Such simulations are pivotal in forecasting behaviors that are challenging or unfeasible to observe experimentally.

Atomic scale simulations can be broadly divided into two main categories based on their treatment of explicitly electrons: classical molecular dynamics (MD) and quantum mechanical simulations. In MD, atoms and molecules are modeled as classical particles, and their trajectories are dictated by the principles of classical physics. In contrast, quantum mechanical simulations take into account the quantum properties of atoms and electrons. And thus, these quantum mechanical methods become indispensable when examining properties influenced by electron distributions.

In this study, our primary focus lies in the utilization of density functional theory, a subset of quantum mechanical simulations. This approach is employed to probe two primary aspects: first, the binding mechanism between various MOFs and actinide cations, and second the intercalation of ferrocene within $VOPO_4$. Subsequent sections in this chapter will furnish a succinct introduction to the methods utilized in our research and elucidate their foundational concepts.

2.2 Density Functional Theory

The time-independent Schrödinger equation, see equation 2-1, is foundational to understanding quantum mechanics and describes how the quantum state of a quantum system changes over time:

$$\left[-\frac{\hbar^2}{2m}\sum_{i=1}^{N}\nabla_i^2+\sum_{\{i=1\}}^{N}V(\boldsymbol{r}_i)+\sum_{i=1}^{N}\sum_{j<i}U(\boldsymbol{r}_i,\boldsymbol{r}_j)\right]\psi=E\psi \tag{2-1}$$

In this equation, the three terms within the left brackets represent, in sequence: the kinetic energy associated with each electron, the interaction energy between an electron and a nucleus, and the interaction energy among distinct electrons. Here, the m is the electron mass, $\hbar$ is the reduced Planck constant, E is the ground state energy of electrons and ψ is the electron wavefunction. This wave function is a function dependent on the spatial coordinates of each of N electrons. As the number of electrons increases, the variables in the wave function grow correspondingly, making the Schrödinger equation for systems with more than two nuclei or two electrons a many-body problem. Therefore, treating the precise positions of electrons is impractical. Instead, interest lies in the probability distribution of a set of N electrons across various spatial coordinates. It is more practical to consider the likelihood of a set of electron coordinates than the precise location of an individual electron. Consequently, a related metric, the electron density at a specific point in space, denoted by $n(\boldsymbol{r})$, is used. This allows for a reformulation of the total number of electrons as:

$$N=\int n(\boldsymbol{r})d\boldsymbol{r} \tag{2-2}$$

The electron density can be expressed in terms of the individual electron wave functions as

$$n(\boldsymbol{r})=2\sum_{i}\psi_i^*(\boldsymbol{r})\psi_i(\boldsymbol{r}) \tag{2-3}$$

Where the $\psi_i^*(\boldsymbol{r})$ is the complex conjugate with $\psi_i(\boldsymbol{r})$.

2.2.1 Hohenberg and Kohn Theorems

In the realm of quantum mechanics, understanding the behavior of many-electron systems is a formidable challenge as the it is a function of the $3N$ variables.[23] The Hohenberg-Kohn theorem, a cornerstone of Density Functional Theory (DFT), offered a groundbreaking perspective on the problem by focusing on electron density rather than the many-body wavefunction. The Hohenberg-Kohn theorems were formulated by Pierre Hohenberg and Walter Kohn in 1965, and they lay the foundation of DFT.[24]

The theorems establish two primary ideas: The ground state energy from the equation is a unique functional of the electron density. This implies that there is a one-to-one correspondence between the ground-state wave function and the ground-state electron density. Thus, according to the first Hohenberg and Kohn theorem, the ground-state energy E can be expressed as a functional of the electron density E $[n(\boldsymbol{r})]$.

The second theorem is about the results of the functional of electron density, the electron density that minimizes the energy of the overall functional is the true electron density corresponding to the full solution of the Schrödinger equation. In other words, any trial density will yield an energy that is greater than or equal to the true ground state energy. This provides a framework for approximating the ground state energy by varying the electron density.

Building on the foundation of the two preceding theorems, Kohn and Sham introduced the Kohn–Sham equations. This formulation encapsulates the intricate relationship between electron density and the system's ground-state energy.

$$\left[-\frac{\hbar^2}{2m}\nabla^2 + V(\boldsymbol{r}) + V_H(\boldsymbol{r}) + V_{XC}(\boldsymbol{r})\right]\psi_i(\boldsymbol{r}) = \varepsilon_i\psi_i(\boldsymbol{r}) \quad (2\text{-}4)$$

The difference between Equation 2-4 and Equation 2-1 is that Equation 2-4 is missing the summations because we have treated the electrons in terms of the electron's density instead individual electrons. As a consequence, the wave function variables are reduced from $3N$ to just 3, significantly simplifying the process of solving the Schrödinger equation. In the bracket on the left-hand side of the equation the potential, $V(\boldsymbol{r})$, is the interaction between electron and atomic nuclei, as in Equation 2-1; $V_H(\boldsymbol{r})$ is called the Hartree potential and is defined as:

$$V_H(\boldsymbol{r}) = e^2\int\frac{n(\boldsymbol{r}')}{|\boldsymbol{r}-\boldsymbol{r}'|}d^3r' \quad (2\text{-}5)$$

The $V_H(\boldsymbol{r})$ the term represents the Coulomb repulsion between one of electron and total electron density defined by all electrons. $V_{XC}(\boldsymbol{r})$ denotes the contribution from exchange and correlation effects. These effects are pivotal in determining molecular structures, chemical reactivity, magnetic properties, and the electronic attributes of materials. For example, the essence of chemical bonds, especially covalent bonding, is inadequately captured without accounting for exchange effects. However, for a system comprising multiple interacting electrons, obtaining an exact solution to the Schrödinger equation is computationally daunting. The complexity grows factorially with the electron count, making the task exponentially more challenging as the number of electrons rises. Consequently, researchers have proposed several approaches to address this issue, which we'll discuss in the next section.

2.2.2 Exchange-Correlation Functionals

In DFT, the total energy of a system can be expressed as a functional of the electron density. This energy includes kinetic energy, electron-nuclear attraction, and electron-electron interaction. The last component, electron-electron interaction, is particularly tricky due to quantum correlations and exchange effects. The exchange energy arises from the Pauli exclusion principle, which states that no two electrons can occupy the same quantum state simultaneously. The correlation energy is influenced by their mutual Coulombic repulsion due to the correlated motion of electrons. Over the years, numerous approximations of the XC functional have been proposed, each with its strengths and limitations in Figure 2-1.

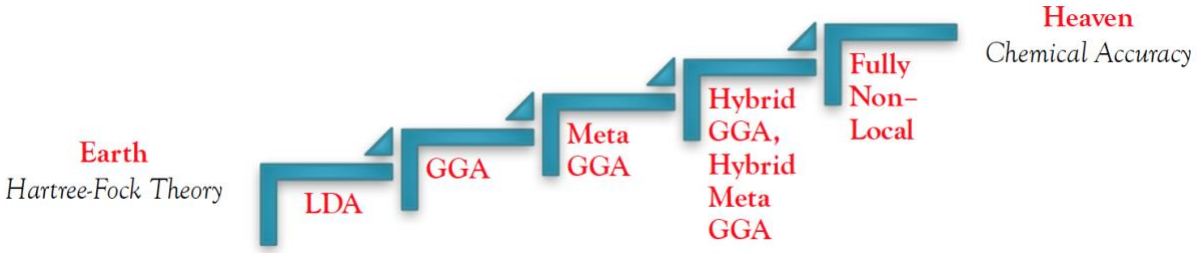

Figure 2-1. The Jacob's ladder of density functional theory (Copied from weblink: https://awoonor.github.io/DFT/)

The Jacob's ladder in Figure 2-1 shows various XC functionals, increasing in complexity and accuracy (and computational cost) from left to right. The Local Density Approximation (LDA)[23] is based on a fundamental concept: the exchange-correlation (XC) energy of a complex system is approximated as though the electron density is piece-wise uniform value. This implies that the electron density in two adjacent regions can differ, leading to a discontinuous change in value. The appeal of this approximation is twofold: its inherent simplicity and the well-developed understanding of the piece-wise uniform electron gas. Formally, the LDA for the XC energy can be articulated as:

$$V_{XC}(\boldsymbol{r}) = V_{XC}^{electron\ gas} n[\boldsymbol{r}] \quad (2\text{-}6)$$

Where $V_{XC}^{electron\ gas}$ denotes the XC energy of a homogeneous electron gas with electron density $n[\boldsymbol{r}]$.

The Generalized Gradient Approximation (GGA)[23] is an advance over the LDA. While the LDA employs solely the electron density value, the GGA broadens the scope by incorporating the gradient of the electron density, offering insights into how this density varies spatially. Mathematically, the GGA for the XC energy can be framed in the context of both the electron density, $n[\boldsymbol{r}]$, and its gradient, $\nabla n[\boldsymbol{r}]$ as:

$$V_{XC}(\boldsymbol{r}) = f(n[\boldsymbol{r}], \nabla n[\boldsymbol{r}]) \quad (2\text{-}7)$$

In this expression, f is a functional that captures the dependence of the XC energy on both the density and its spatial gradient, refining our understanding of electronic interactions beyond the LDA. Nowadays, the Perdew-Burke-Ernzerho (PBE)[25] and the Perdew–Wang (PW91)[26] functionals are the most popular GGA functionals. In this research, our emphasis is on the binding energy of various components. The PBE functional has demonstrated superior performance compared to PW91 in this regard,[27] and therefore, we have opted to use the PBE functional.

For enhanced precision in energy calculations, especially for the binding energy calculations in this work, hybrid functionals are employed. These functionals combine the conventional DFT exchange-correlation framework with a portion of the exact exchange derived from Hartree-Fock theory. Among the myriad of functionals available, B3LYP[27,28] is particularly noteworthy. This method is widely used to calculate the binding energy of molecular systems. The nomenclature "B3" corresponds to the three-parameter Becke functional delineating the exchange aspect, while "LYP" designates

the Lee-Yang-Parr functional attributed to the correlation facet. B3LYP's wide use stems from its adaptability and high precision for diverse molecular systems. Its applications range from investigating organic molecules to forecasting vibrational frequencies, reaction thresholds, and molecular configurations.

In our study, we also utilize the double-hybrid PWPB95 functional.[29] This was tailored using parameters from a detailed molecular dataset, ensuring its effectiveness in describing a diversity of molecular properties and structures. Notably, PWPB95 excels at capturing long-range electron correlations, making it invaluable for systems with charge transfers, high-energy states, and significant dispersion interactions.

2.2.3 DFT+U correction

LDA and GGA methods encounter challenges when dealing with systems that have localized or strongly correlated electron behavior. This is often the case in transition metal oxides and rare-earth compounds, where d and f orbitals play a crucial role. The electron-electron correlations in localized orbitals are strong. To address this limitation, the DFT+U method,[30] also known as the Hubbard U correction, was introduced. The "+U" refers to an additional term added to the DFT Hamiltonian to better represent the on-site Coulomb interaction of localized electrons. The mathematical equation is as follows:

$$E_U = \frac{U}{2} \sum_{i \neq j, \sigma, \sigma'} n_{i\sigma} n_{j\sigma'} \tag{2-8}$$

Where U is the Hubbard U parameter, representing the on-site Coulomb repulsion. $n_{i\sigma}$ is the electron occupation of the localized orbital i with spin σ. In this context, U is regarded as an empirical parameter. It's typically determined by matching theoretical calculations with experimental observations or employing more advanced

computational techniques, such as the linear response method. However, it's vital to note that DFT intrinsically accounts for certain electron correlation effects, see Equation 2-5. Thus, when incorporating E_U, it's crucial to ensure that these effects aren't double-counted, giving rise to the double-counting correction term $E_{double-counting}$. The precise form of this correction varies depending on the exchange-correlation approximation adopted in the DFT calculation. The standard approach to addressing the double-counting problem is as follows:

$$E_{double-counting} = U \times \frac{N(N-1)}{2} \tag{2-9}$$

Recalling that N represents the total number of electrons, and thus, the total energy for the DFT+U approach can be expressed as:

$$E[n(\boldsymbol{r})] = E_{DFT}[n(\boldsymbol{r})] + \frac{U}{2}\sum_{i\neq j,\sigma,\sigma'} n_{i\sigma}n_{j\sigma'} + U \times \frac{N(N-1)}{2} \tag{2-10}$$

The DFT+U method has been instrumental in improving the description of various materials, including transition metal oxides, actinide materials, high-temperature superconductors, and magnetic materials. It has provided insights into the electronic, magnetic, and structural properties of materials where standard DFT faced challenges.

2.2.4 van der Waals Correction

While DFT excels in modeling a wide range of phenomena, it has historically struggled with long-range correlations, most notably those arising from van der Waals (vdW) interactions. Van der Waals forces are weak, non-covalent interactions between molecules or atoms. Traditional DFT approximations, such as the LDA or the GGA, often fail to capture these interactions correctly due to their inherently local or semi-local nature. This shortcoming can result in significant errors when predicting molecular

structures, binding energies, and other properties where vdW interactions play a role. In this work, we used two methods to describe vdW interactions.

The first one involves an empirical correction, in which a term is introduced to the DFT energy, depending on the pairwise atomic distances. The DFT-D3[31] methodology stands out in this context. In this method, a dispersion term is incorporated, anchored in the potentials between atomic pairs. A common expression for the DFT-D3 method can be written as:

$$E_{disp} = -\sum_{i>j} \frac{C_{ij}}{R_{ij}^6} f(R_{ij}) \tag{2-11}$$

Where E_{disp} is the dispersion correction, C_{ij} are dispersion coefficients for atom pairs i and j, R_{ij} is the distance between atoms i and j, and $f(R_{ij})$ is a damping function to ensure that the correction does not diverge at short distances and to enable seamless integration with the DFT description.

The second approach entails the use of non-local functional methods. As the name suggests, these methods accommodate electron correlation by concurrently evaluating electron densities at two distinct spatial points. Such an approach is particularly proficient at capturing the electron system's adaptive response to alterations in the external potential. One of the most prominent non-local functional approaches is the van der Waals Density Functional (vdW-DF) method.[32] Here, the energy functional is partitioned into a local and a non-local component:

$$E_{xc}[n(\boldsymbol{r})] = E_{xc}^{LDA/GGA}[n(\boldsymbol{r})] + E_{non-local}[n(\boldsymbol{r})] \tag{2-12}$$

Where, the $E_{xc}^{LDA/GGA}[n(\boldsymbol{r})]$ is the exchange-correlation energy from LDA or GGA based on the electron density $n(\boldsymbol{r})$, and $E_{non-local}[n(\boldsymbol{r})]$ is the non-local correlation energy.

This term is typically expressed as an integral involving a kernel that represents the non-local interaction:

$$E_{non-local}[n(\boldsymbol{r})] = \frac{1}{2}\iint n(\boldsymbol{r})\emptyset(\boldsymbol{r},\boldsymbol{r}')n(\boldsymbol{r}')d\boldsymbol{r}d\boldsymbol{r}' \quad (2\text{-}13)$$

Where $\emptyset(\boldsymbol{r},\boldsymbol{r}')$ is the non-local kernel.

2.2.5 Spin-Orbital Coupling Effect

At the quantum level, electrons possess both spin ($\boldsymbol{S}$) and, in atoms, orbital angular momenta ($\boldsymbol{L}$). The spin is an intrinsic property of the electron, giving it a magnetic moment. On the other hand, the orbital angular momentum arises from the electron's motion around the atomic nucleus. As the electron moves (orbits) around the nucleus, it creates a small magnetic field. This magnetic field interacts with the electron's intrinsic magnetic property (its spin). This interaction, or coupling, between the electron's motion and its spin, is the essence of spin-orbit coupling (SOC). In atomic systems, the SOC can be compactly represented as:

$$E_{SOC} = f(R)\boldsymbol{L}\cdot\boldsymbol{S} \quad (2\text{-}14)$$

Where, the term E_{SOC} represents the energy contribution from spin-orbit coupling (SOC). The function $f(R)$ characterizes the magnitude of the SOC interaction, which is predominantly dependent on the distance R from the nucleus. This implies that the SOC strength can vary significantly across different materials. In materials with heavy elements, where spin-orbit coupling is pronounced, the contribution from E_{SOC} becomes increasingly prominent. This heightened SOC influence can lead to discernible shifts in the electronic energy states and, consequently, the dynamics of the system.

2.2.6 Solvation Effect

In the previous sections, our simulations assumed the environment is a vacuum. However, in real-world scenarios, sometimes it is crucial to consider the solvation effect. There are two primary methods to simulate an aqueous environment: the explicit solvation model and the implicit solvation model. In the explicit model, an exact number of water molecules in the system is considered. However, this method is computationally intensive. As a result, the implicit solvation model is introduced as a more efficient alternative. VASPsol[33,34] is an implicit solvation model incorporated into the Vienna Ab initio Simulation Package (VASP). Implicit solvation models, also known as continuum solvation models, treat the solvent as a continuous dielectric medium instead of explicitly modeling each solvent molecule. This significantly reduces the computational cost while maintaining a reasonable description of solvent effects. VASPsol specifically introduces the solvation effect into VASP by adding electrostatic contribution between the solute and the solvent to the total energy and the cavity energy to create the solute within the solvent. The expressions for these two terms are given by:

$$E_{elec} = -\int d\boldsymbol{r}\varepsilon(\boldsymbol{r})\frac{|\nabla\varphi(\boldsymbol{r})|^2}{8\pi} E_{cav} = \tau\int d\boldsymbol{r}|\nabla S(\boldsymbol{r})| \tag{2-15}$$

Where $\varepsilon(\boldsymbol{r})$ is the dielectric constant, $\varphi(\boldsymbol{r})$ is the total electrostatic potential, τ is the surface tension and $S(\boldsymbol{r})$ is the cavity shape function. We use the default setting parameters in our calculations, namely, bulk dielectric constant 78.4, surface tension is 0.525 meV/Å^2. All of these parameters are fitted from experimental solvation energy of neutral molecules. [35]

2.3 Nudged Elastic Band Method

The Nudged Elastic Band (NEB)[36] method is a powerful computational tool to determine reaction pathways and the associated potential energy barriers in atomic systems. Specifically tailored for probing atomic transformations on solid materials and their surfaces, NEB offers insights into the approximate minimum energy path (MEP) that bridges the initial and final states of a system. Such understanding is crucial for predicting reaction dynamics, kinetics, and mechanisms at the atomic level.

The core idea of the NEB method is to place a series of "images" (representing different system configurations or states) between the initial and terminal states. These images are connected to each other as if they were linked by an elastic band. The initial and terminal states (i.e., the two ends of the band) remain fixed, while the intermediate images are free to move on the potential energy surface.

Through iterative calculations and adjustments, these images are redistributed along the minimum energy path. Ultimately, once the images reach stable positions, this path describes the transition process from the initial to the terminal state.

To ensure that the images move only in the desired direction of the path (i.e., along the gradient of energy) and not in the direction of the band, a "nudge" correction is introduced, which is the origin of the method's name. This correction ensures that the movement of the images is mainly influenced by the potential energy surface, rather than the positions of other images.

The NEB method is widely used in computational solid-state physics and chemistry to study atomic migration processes, such as describing defect diffusion in materials or observing chemical reaction pathways on catalyst surfaces. By using the

NEB method, researchers can determine the exact structure and energy of transition states, and based on this, predict and explain phenomena observed experimentally.

CHAPTER 3
BINDING OF URANYL CATIONS TO A ZR-BASED METAL-ORGANIC FRAMEWORK BY DENSITY FUNCTIONAL THEORY*

3.1 Background

In this chapter, we explore the strategies outlined in chapter 1, the binding mechanism of uranyl cations within zirconium-based metal-organic frameworks (Zr-MOFs). Basically, uranyl cations (UO_2^{2+}) are one of the most widely found and stable radionuclides in soils, silt, and groundwater.[37] They tend to be complexed with hydroxide, carbonate, bicarbonate, nitrate, sulfate, and carboxylate ions. Because uranyl cations and its complexes are both toxic and radioactive,[38] the elimination of uranyl ions from aqueous solutions near nuclear power plants and water aquifers near uranium mines is a matter of global concern.[39,40]

Zr-MOFs, crystalline porous materials composed of inorganic zirconium nodes connected by organic carboxylate ligands,[41] have shown promise for diverse applications such as drug-delivery,[42,43] catalysis,[44] gas storage[45,46] and, more recently, heavy element adsorption and sieving.[47] Lin *et al.*[48] reported their first application as an adsorbent to extract actinides in which Zr-UIO-68-$P(O)(OEt)_2$, a Zr-MOF containing a diethoxy-phosphoryl urea group, was used. Their work indicated that owing to their tunable inorganic and organic composition, diversified structure, and multifunctional characteristics, MOFs are good candidates for the effective treatment of uranium residues. Additionally, Zr-MOFs possess high stability in aqueous solutions due to the

* This work described in this chapter has been published in Liu, Y.; Ta, A. T.; Pandey, S.; Chul Park, K.; Hu, S.; Shustova, N. B.; Phillpot, S. R. Binding of Uranyl Cations to a Zr-Based Metal-Organic Framework by Density Functional Theory. *Comput. Mater. Sci.* **2023**, *230*, 112528. https://doi.org/10.1016/J.COMMATSCI.2023.112528.

strong Zr(IV)–O bond incorporated into the framework,[49] which allows them to strongly adsorb uranyl ions in a wide range of environments.[50] Because of the low capacity for uranyl ion adsorption (217 mg/g) by pristine Zr-UIO-68, the design of MOF composite materials to improve absorption capacity has attracted considerable interest. Liu *et al.*[51] found somewhat different adsorption capacities for the Zr-UIO-66-AO MOFs, an amidoxime (AO) appended Zr-MOF with 227.8 mg/g. Using density functional theory, Lin *et al.* [48] also demonstrated that the two phosphoryl urea ligands could strongly bind with uranyl cations. Recently, Berseneva *et al.*[52] reported that each metal node of the PCN-700 Zr-MOF can bind to 1.7 uranyl cations and modeled the kinetics of uranyl cation release. Yulan *et al.*[53] further constructed a model of leaching of uranyl cations from Zr-MOF as a means to investigate the leaching mechanism, with the aim of improving the design of MOFs for capturing uranyl cations. They found that the leaching behavior is diffusion-controlled and is impacted by the initial position of the uranyl cation in Zr-MOF. Consequently, it is crucial to establish the preferred or favorable sites of uranyl cations within the MOF's structure. Therefore, to enhance the accuracy of the leaching model, in this paper we determine the specific configuration where the uranyl cation binds most strongly to the Zr-MOF. Specifically, we use DFT methods to probe the possible binding mechanisms of uranyl cations to the Zr-containing $Zr_6O_4(OH)_8(Me_2BPDC)_4$ (PCN-700) by determining the binding energies to various sites as a function of the protonation of the system.

3.2 Structures

3.2.1 Zr-MOFs

A conventional periodic 292-atom Zr-MOF (PCN-700) truncated model is used. It contains two Zr-based secondary building units (SBUs) and eight 2,2’-dimethylbiphenyl-

4,4'-dicarboxylate (Me_2BPDC^{2-}) organic linkers. This structure illustrated in Figure 3-1, is represented by a black box outlining the unit cell containing 292 atoms, with zirconium atoms in green, oxygen in red, carbon in brown, and hydrogen in white. The configuration, projected along the [001] direction, is based on structure analyses by Dolgopolova *et al.*[54] and Ejegbavwo *et al.*[55] and possesses two major components in each unit cell: the metal node with four six-coordinated equatorial Zr atoms and two eight-coordinated exterior Zr atoms (top/bottom), and the organic Me_2BPDC^{2-} ligands. The size of the Zr-MOF tetragonal unit cell is approximately 25×25×15 Å.

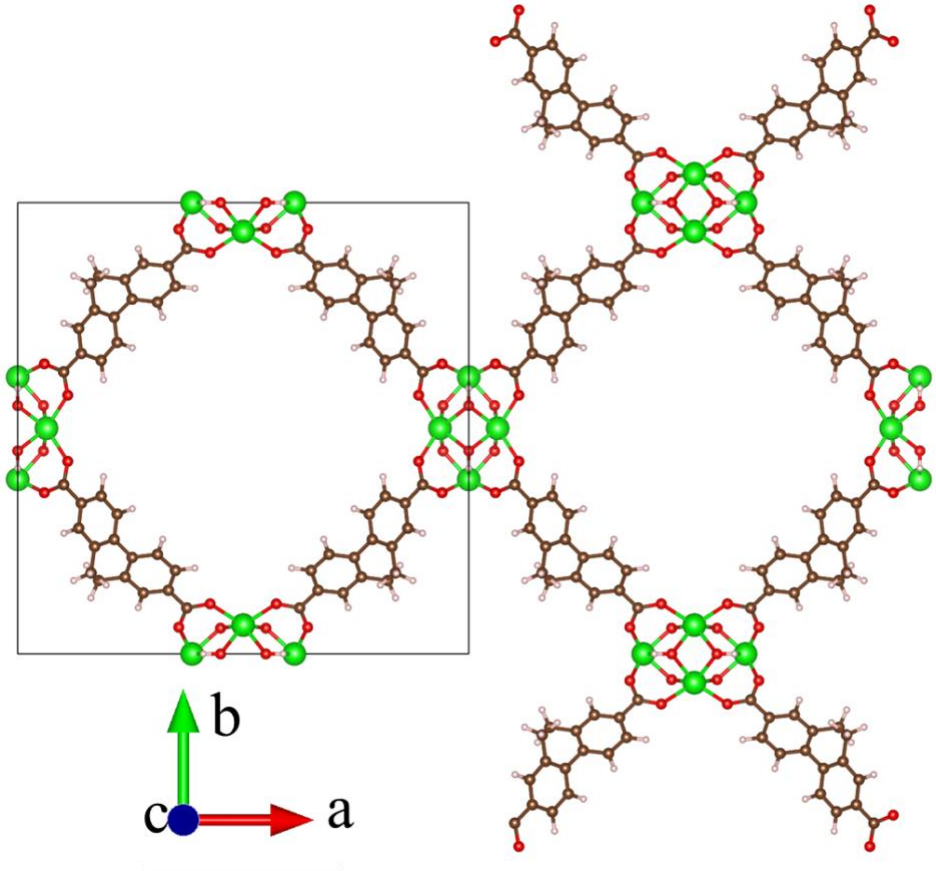

Figure 3-1. The crystal structure of Zr-MOFs. The black box denotes the edges of the unit cell which contains 292 atoms. Zirconium atoms are shown in green, oxygen in red, carbon in brown, and hydrogen in white. This configuration is projected along [0 0 1] direction.

3.2.2 Uranyl Cation

There have been a number of previous quantum mechanical calculations and molecular dynamics simulations of uranyl cations[56–60] These studies have indicated that the dominant species in the aqueous solution is a uranyl cation coordinated with five water molecules, $[UO_2 \cdot (H_2O)_5]^{2+}$. Figure 3-2 shows the geometrically optimized structure with the five H_2O molecules uniformly coordinated in the plane perpendicular to the O=U=O bond such that the O^{2-} in the H_2O is pointed towards the central U^{6+} cation. Uranium atom is shown in gray, oxygen atoms in red, and hydrogen atoms in white. Details on the DFT approach are discussed in Sec. 3.4.4.1.

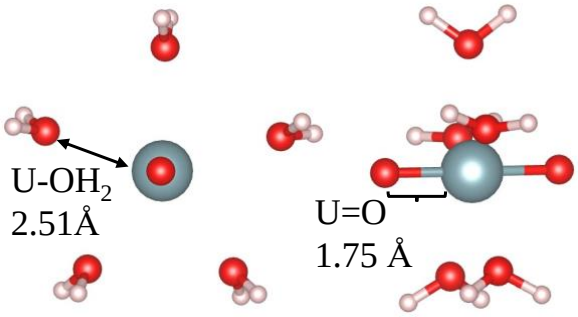

Figure 3-2. Two views of the optimized structure of pentahydrated uranyl ion, $[UO_2 \cdot (H_2O)_5]^{2+}$. Uranium in gray, oxygen in red and hydrogen in white.

3.2.3 Uranyl Cation Binding Structures

The Zr-MOF structure has been determined experimentally.[55] However, there are multiple ways in which the system could be protonated, with the three most physically plausible being shown in Figure 3-3. Here, these configurations are only for displayed, and not for relaxation. The organic ligand has been omitted for clarity. We have calculated the total energies of these three proton topologies. Table 3-1 shows that the MOF-4 has the lowest energy. As a result, the MOF-4 is the best representative parent Zr-MOF and will be used in all subsequent calculations. To validate our simulation

model, we initially conducted a comparison between the experimental and theoretical data of pristine Zr-MOF, specifically analyzing the crystal data and structure refinement. The results of this comparison are presented in Table 3-2. The a (=b) lattice parameter of the tetragonal system matches the experimental results very well. However, there is a considerable discrepancy between the two experimental values for the c lattice parameter, it is not overly surprising that the DFT value is different from both.

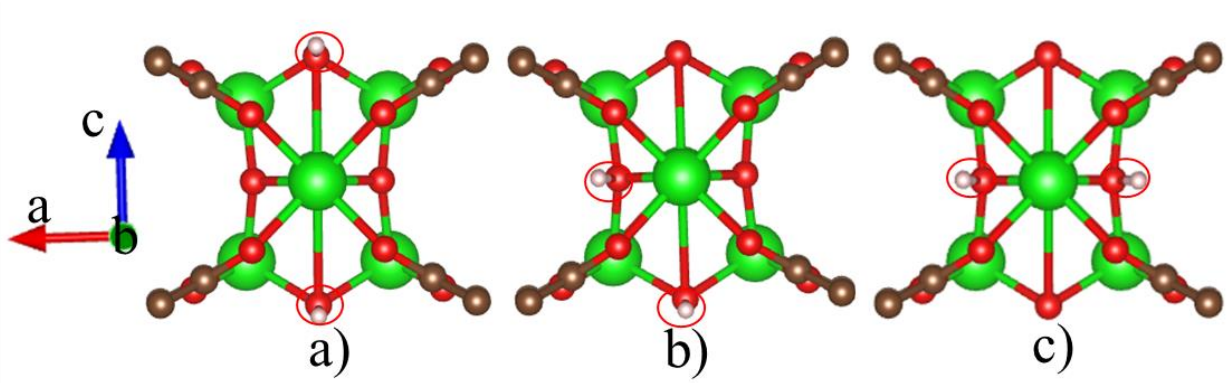

Figure 3-3. The possible proton topologies of Zr-MOF. a) MOF-4, b) MOF-B and c) MOF-C.

Table 3-1. Total energies of different proton topologies of Zr-MOF relative to the MOF-4 value. Unit in eV.

Topology	MOF-4	MOF-B	MOF-C
Relative energies	0	+0.538	+0.463

Table 3-2. Comparison of experimental and computed structural parameters for the Zr-MOF.

Compound	Experimental[52]	Experimental[61]	Theoretical (GGA+U_D3, this work)	Theoretical (VASPsol, this work)
Crystal system	Tetragonal	Tetragonal	Tetragonal	Tetragonal
a, Å	24.444	24.348	24.342	24.590
b, Å	24.444	24.348	24.342	24.590
c, Å	14.398	14.918	15.635	15.036
α,°	90	90	90	90
β, °	90	90	90	90
γ, °	90	90	90	90

Previous research has indicated that the binding energy for uranyl ions adsorption has been depends on the specific site on titanium dioxide surfaces[58,62,63] and on calcite surfaces.[64] In particular, Perron *et al.*[58] and Vandenborre *et al.*[62] found that there is a dependence of the protonation of the surface. Specifically, the less protonated the surface, the stronger the binding between the uranyl ion and the surface. It is possible to identify the protonation with the chemical conditions, with a high degree of protonation corresponding to acidic conditions and a low degree of protonation corresponding to basic conditions. They also showed the most stable configuration was a uranyl ion having two bonds to the rutile surface: one to a bridging oxygen and one to a top oxygen. To evaluate the binding modes for different deprotonation states of the equatorial Zr atoms (Zr_1 to Zr_4), four distinct configurations of the Zr-MOF were considered. The MOF-4 structure, where all oxygen are protonated, can be thought of as a representative state in an acidic chemical environment. The two configurations (MOF-2N and MOF-2O), where protonation is only present for half the oxygen, represents protonation states in more chemically neutral environments. Specifically, MOF-2N configurations possess protonation at oxygen atoms that are nearest neighbors to one another on the equatorial plane (Figure 3-4b) while MOF-2O has protonation on diagonally opposite corner oxygen (Figure 3-4c). The configuration in which none of the equatorial oxygen are protonated (Figure 3-4d) is denoted as MOF-0 and can be thought of as the protonation state in a basic environment. At last, for clarity, only the SBUs and some ligands are shown. Zirconium atoms are depicted in green, oxygen in red, carbon in brown, and hydrogen in white. Apical Zr atoms are Zr_5 (top) and Zr_6 (bottom).

Due to the symmetry of the metal node and bidentate sorption by uranyl, five structurally distinct oxygen binding sites on the MOF structure are possible and were analyzed here. As shown in Figure 3-5, the binding sites involve a combination of the following oxygen in the metal node of the MOF: (1) the top oxygen atom, which is connected to the eight-coordinated apical Zr atom, O_T, (2) edge oxygen atom, which is connected to the six-coordinated equatorial Zr atom, O_E, (3) middle oxygen atom can be either bonded to hydrogen, O_M^A, or not bonded to hydrogen, O_M^D (4) middle oxygen adjacent to at least one middle hydroxyl oxygen, O_M. In Figure 3a, to best illustrate the binding sites, the right diagram is rotated clockwise 90 degrees about the *b*-axis in the left diagram. Zirconium atoms are shown in green, oxygen in red, carbon in brown, and hydrogen in white. The organic ligands have been omitted for clarity.

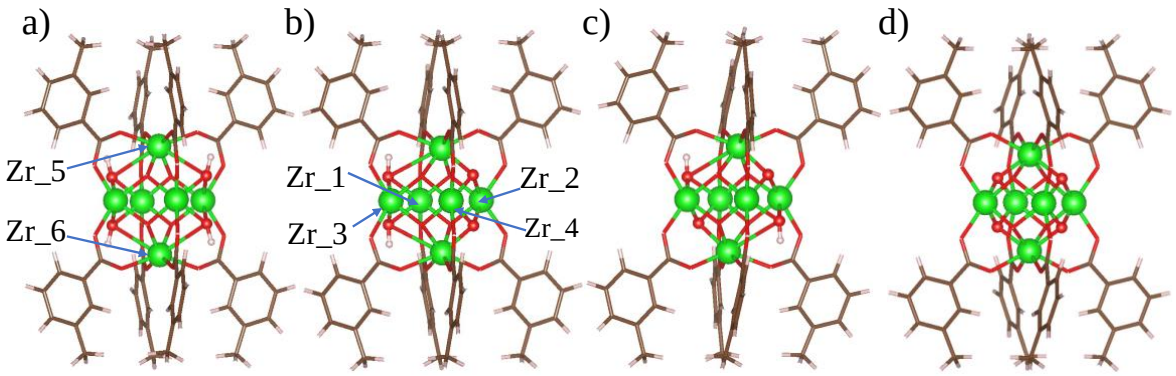

Figure 3-4. Zr-MOF structures with various equatorial Zr (Zr_1, Zr_2, Zr_3, and Zr_4) deprotonations. From left to right, (a) MOF-4 (fully protonated), (b) MOF-2N (half deprotonated, nearest neighbors: Zr_2 and Zr_4), (c) MOF-2O (half deprotonated, diagonally opposite: Zr_3 and Zr_4), and (d) MOF-4 (fully deprotonated).

Considering all possible unique protonation conditions, there are a total of nineteen different structures (Table 3-3): four for MOF-4, four for MOF-0, six for MOF-2N, and five for MOF-2O.

Table 3-3. The binding site configurations for the four different Zr protonation schemes.

Protonation	Configurations
MOF-4	$O_T - O_T$, $O_M^A - O_M^A$, $O_M - O_M$, $O_M^A - O_E$
MOF-2N	$O_T - O_T$, $O_M^A - O_M^A$, $O_M^D - O_M^D$, $O_M - O_M$, $O_M^A - O_E$, $O_M^D - O_E$
MOF-2O	$O_T - O_T$, $O_M^A - O_M^D$, $O_M - O_M$, $O_M^A - O_E$, $O_M^D - O_E$
MOF-0	$O_T - O_T$, $O_M^D - O_M^D$, $O_M - O_M$, $O_M^D - O_E$

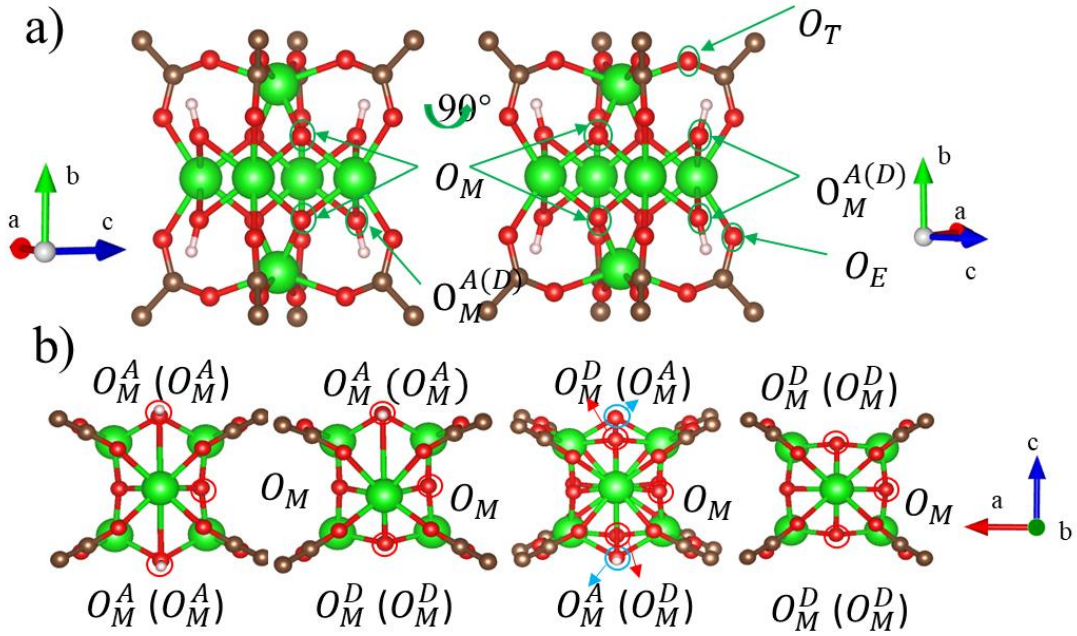

Figure 3-5. The attachment oxygen position on metal node. a) Possible Zr-O bidentate sorption sites for the uranyl ion on the MOF-4. b) the O_M^A and O_M^D positions of different protonation of Zr-MOF and O_M site, from left to right MOF-4, MOF-2N, MOF-2O and MOF-0.

3.3 Computational Method

3.3.1 Parameters Setting

All DFT calculations were carried out using the Vienna *Ab-initio* Simulation Package (VASP)[65,66] with the Generalized Gradient Approximation (GGA) with the Perdew-Burke-Ernzerhof (PBE) exchange-correlation functional.[67,68] A cut-off energy of 520 eV for the plane wave expansion of the wave functions was used to ensure the convergence of the calculations and calculations were performed only at the Γ-point. Total energies were evaluated for the MOF-0 $O_M^D - O_E$ configuration with k-points of 2 ×

2 × 3 and Γ-point only and the results differed by 0.003 eV. Furthermore, Choudhary *et al.*[69] suggested that the more atoms per unit cell, the smaller k-points are needed. Due to the small differences observed in total energy for different mesh and having systems containing ~300 atoms per unit cell, Γ-point only calculations are sufficient to evaluate the system's total energy. Thus, all subsequent calculations were performed at the Γ-point only. Spin orbital coupling (soc) effects[70] were also assessed using the MOF-0 $O_M^D - O_E$ configuration as a reference. We found that binding energy with the soc correction is 0.11 eV lower than the binding energy without. Given this small change, as well as the high computational cost and the findings of Pandey *et al.*,[71] the soc correction was not taken into consideration in our calculations. The uranium pseudopotential includes 14 valence electrons ($6s^2 6p^6 5f^3 6d^1 7s^2$), the zirconium pseudopotential includes 12 valence electrons ($4s^2 5s^2 4p^6 4d^2$), the oxygen pseudopotential includes six valence electrons ($2s^2 2p^4$) and carbon pseudopotential includes four valence electrons ($2s^2 2p^2$). The DFT+U approach[72] was used to describe electron localization on the 5f states of the uranium and 4d states of the zirconium ions[73] with an effective Hubbard U term of 4 eV, which has been found to be an appropriate value to ensure electron localization in Zr^{4+} and U^{6+}.[73]

The atomic structures were optimized using a conjugate gradient method [74,75] until the average force reached less than 0.05 eV/Å, with 1×10^{-5} eV as the energy tolerance for each electronic step. Spin-polarization was also included in all calculations. Gaussian smearing with a width of 0.05 eV was applied to all optimizations. The van der Waals (vdW) interactions were taken into account using the DFT-D3[31] dispersion correction formula with Becke−Johnson damping.[76] The electronic

density of the states was calculated using a denser 2 × 2 × 3 grid, giving approximately the same k-point density along all three axes. The four Zr-MOF structures of varying protonation were first relaxed without volume and shape constraints. Then, the shape and volume were fixed to their respective values when a hydrated uranyl ion was introduced into the supercell system. This is intended to mimic the low UO_2^{2+} concentration limit. To account for the solvation model, we used the VASPsol,[77,78] a kind of implicit solvation model. To simulate the water environment, we set the dielectric constant is 80. And the other parameters are used default value.

3.3.2 Methods of Calculating Binding Energy Between Zr-MOF And Uranyl Ion.

The physical scenario that we are simulating is that of aqueous uranyl absorbing onto a crystalline MOF. Specifically, we envisage a uranyl ion in water at some distance from a piece of the crystalline MOF large enough to be considered unlimited in extent, but still delineated by external surfaces. The uranyl ion is then coordinated to a specific site on an SBU inside the MOF far away from its external surface. Thus, the true binding energy is the decrease in energy associated with this process. It is convenient to break this process down into two distinct steps. The first step considers the energy associated with incorporating the uranyl ion into the center of the MOF pore, far from any SBU (Figure 3-6a). To estimate this, we determine the energy difference, ΔE_1, between a supercell containing a small finite fragment of MOF with a uranyl at the center of an open region and that of the same fragment with the uranyl ion far from it. The second step consists of determining the energy difference, ΔE_2, involved in moving the uranyl ion from the center of the open region to a binding site, Figure 3-6(b, c). Our best estimate of the total binding energy is then

$$\Delta E = \Delta E_1 + \Delta E_2 \quad (3\text{-}1)$$

In order to calculate the ΔE_2, we follow the method from Pan *et al.,*[79] which fixed a uranyl hydrated by three waters, $[UO_2(H_2O)_3]^{2+}$, 8 Å away from the attaching surface to minimize the interaction between the two species. However, the coordination number of uranyl ion has been reported to be five.[58] Thus, a more physical scenario likely involves a uranyl initially hydrated by five waters, $[UO_2(H_2O)_5]^{2+}$, losing two waters to bind to a Zr-MOF metal node in a bidentate fashion. The dissociation energy of these two water molecules also has to be considered as being a part of the incorporation energy. This dissociation process can be represented by the following,

$$[UO_2(H_2O)_5]^{2+} \cdot nH_2O \rightarrow [UO_2(H_2O)_3]^{2+} \cdot (n+2)H_2O$$

where the nH_2O indicates that there are *n* water molecules associated with the uranyl ion. The dissociation energy (based on the above reaction) can be defined as:

$$E_{dis} = E_{UO_2(H_2O)_3^{2+}\cdot(H_2O)_{n+2}} - E_{UO_2(H_2O)_5^{2+}\cdot(H_2O)_n} \quad (3\text{-}2)$$

where $E_{UO_2(H_2O)_3^{2+}}$ is the total energy of $[UO_2(H_2O)_5]^{2+}\cdot nH_2O$ and $E_{UO_2(H_2O)_5^{2+}}$ is the total energy of $[UO_2(H_2O)_3]^{2+}\cdot(n+2)\,H_2O$. Finally, interactions of the hydrated uranyl cation with the MOF can be written as:

$$\mathrm{UO_2(H_2O)_3^{2+}} + \mathrm{MOF} \rightarrow \mathrm{MOF \cdot UO_2(H_2O)_3^{2+}}$$

where $\mathrm{MOF \cdot UO_2(H_2O)_3^{2+}}$ denotes the MOF binding with $\mathrm{UO_2(H_2O)_3^{2+}}$. The binding energy of the uranyl ion in the MOF cavity was calculated based on three terms,

$$\Delta E_2 = E_{merge} - E_{split} + E_{dis} \quad (3\text{-}3)$$

where E_{split} denotes the total energy associated with the three-water hydrated uranyl ion initially placed at the center of the cavity of the MOF, (10 Å away from any

MOF atom, Figure 3-6b), E_{merge} is the total energy of the three-water hydrated uranyl binding to the inner surface of the MOF, and E_{dis} is Eqn. 3-2.

In the situation described above, the structure used to obtain E_{merge} possessed charge of +2. However, the treatment of charged species with VASP has been known to result in anomalous results in some cases.[79] We have therefore also looked at treating the system as charge neutral. To make the system charge-neutral, hydroxyl ions were added onto the SBU of the MOF to which the uranyl does not bind.[80] As a result, the distance between the uranium atom and the hydroxyls was greater than 8 Å and, thus, their interaction can be expected to be minimal in a charge neutral cell (Figure 3-6c). The reaction of the hydroxylated neutral system is

$$\mathrm{UO_2(H_2O)_3^{2+}} + \mathrm{MOF}(OH)_2^{2-} \longrightarrow \mathrm{MOF}(OH)_2 \cdot \mathrm{UO_2}(H_2O)_3$$

Since the addition of these charge-neutralizing ions is a computational device only, to see if there is any effect of the nature of the charge-neutralizing counter ions, we also used fluorine atoms rather than hydroxyl ions. The results are discussed in Sec. 3.4.3 Finally, because of the large cavity size, the minimal distance between uranium and its periodic image is ~15 Å, which can be expected to lead to a small interaction energy. The actual value of ΔE_2 of both charge and neutral systems are determined at two different levels of theory: (1) GGA+U and (2) GGA+U-D3, which includes dispersion forces.

3.4 Results and Discussion

3.4.1 Structure, Electron Localization Function, And Density of States Of Pristine Zr-MOF

In order to gain insights into the chemical bonding of the Zr-MOF metal node, the electron localization functions (ELFs)[81,82] of the four different Zr-MOF structures (MOF-

0, MOF-2N, MOF-2O, and MOF-4) were analyzed. As Figure 3-7 shows (The projection direction is along [010]; only SBUs of the Zr-MOFs are shown for clarity.), in the MOF-4 there is significant electron density between the Zr_1 and Zr_3 and between the Zr_2 and Zr_4. Consistent with this, when the neighboring equatorial Zr are protonated (MOF-2N, Figure 3-4b), there is significant electron density between them (Zr_1 and Zr_3) while there is no electron density between unprotonated Zr_2 and Zr_4. Similarly, there is also no electron density between the equatorial Zr atoms in either the diagonally deprotonated MOF-2O or the fully deprotonated MOF-0 structures (Figure 3-4c and 3-4d, respectively). The bond lengths between neighboring Zr atoms (e.g., Zr_1-Zr_3 and Zr_2-Zr_4) were also determined. From Table 3-4, the bonds between neighboring protonated ions were significantly shorter than those between unprotonated Zr ions (3.0 Å in MOF-4 vs. 3.3 Å in MOF-2O and MOF-0), which is also consistent with the ELF. For MOF-2N, the Zr-Zr bond distance on the pronated side is shorter than on the deprotonated side. (3.10 Å vs 3.22 Å)

To further understand the specific orbitals involved in these differences in the ELF, the electron density of states (DOS) plots was also analyzed. There is no peak near the Fermi energy in either the MOF-0 or the MOF-2O cases (DOS not shown), which is consistent with the absence of any bonding shown in the corresponding ELFs. In Figure 3-8a, the black and blue lines coincide for the MOF-4 indicating that the electron density between Zr_1 and Zr_3 is the same as for Zr_2 and Zr_4 which are nearby the Fermi energy. Figure 3-8b shows that there are no overlapping electrons between Zr_2 and Zr_4 in MOF-2N; The blue line is the sum of the density of states of Zr_1 and Zr_3 d orbitals, the black is the sum of the density of states of Zr_2 and Zr_4

3d orbitals, the red is the sum of the density of states of oxygen 2p orbitals. however, there is a peak close to the Fermi energy, corresponding to Zr_1 and Zr_3 atom d-orbital hybridization, which is also consistent with the ELF showing electron density between those Zr atoms. These results are also consistent with ELF plots of MOF-4.

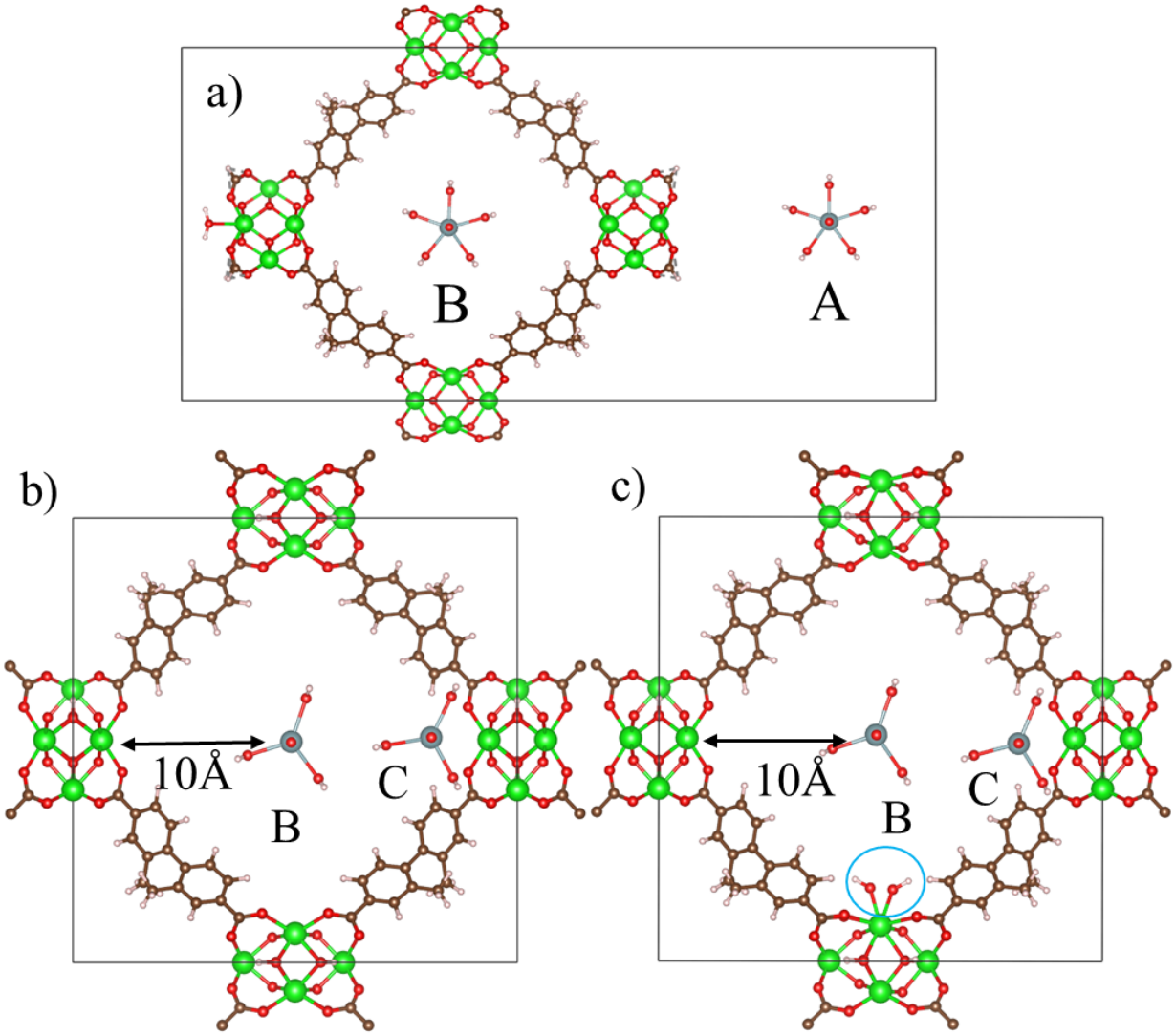

Figure 3-6. The moving path picture. a) The uranyl ions move starting from position A outside of the MOF fragment into the Zr-MOF cavity at position B; the MOF is oriented along the [100] direction. b) The uranyl in the periodic system moves from point B to a binding site C; the energy difference is ΔE_2: c) charged system; c) neutral system, showing two additional hydroxy groups (in blue circle region) attached to the metal node at the bottom of the image.

Table 3-4. Distance (Å) between neighboring Zr atoms as shown in Figure 3-7, d(Zr–Zr).

Name	MOF-4	MOF-2N	MOF-2O	MOF-0
d(Zr_1-Zr_3)	2.99	3.10	3.32	3.33
d(Zr_2-Zr_4)	3.00	3.22	3.32	3.33

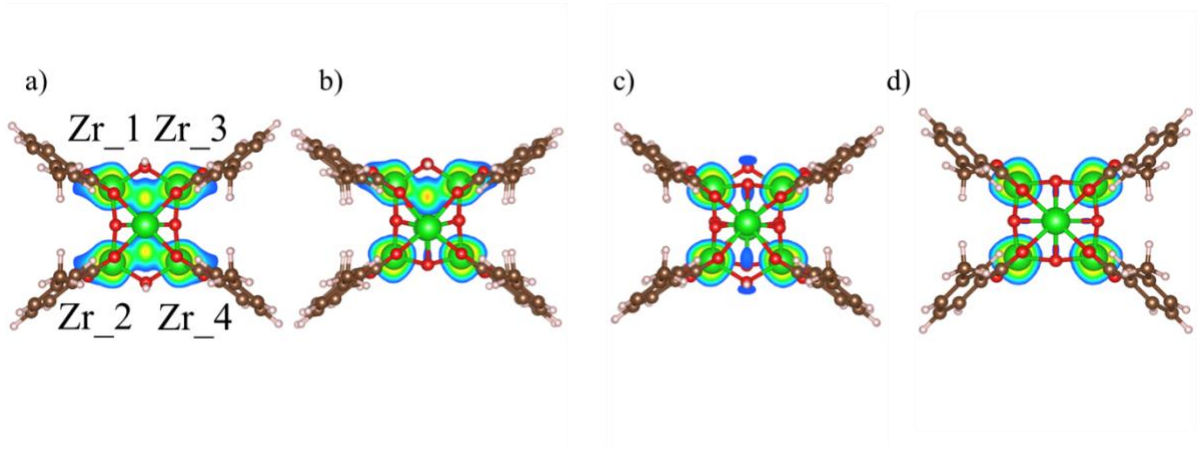

Figure 3-7. Electron localization function for various deprotonation cases: a) MOF-4, b) MOF-2N, c) MOF-2O, and d) MOF-0.

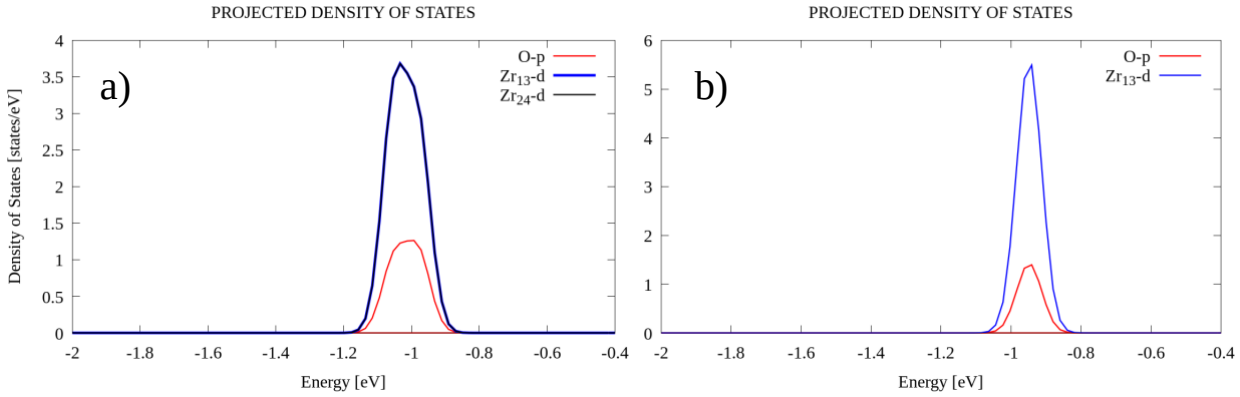

Figure 3-8. The density of states of a) MOF-4 and b) MOF-2N near the Fermi energy.

3.4.2 Hydrated Uranyl Ion

As a benchmark, the hydration energy calculations of uranyl ions determined by Perron. *et al.*[58] were reproduced. In Table 3-5, the number of water molecules coordinated to the first shell of UO_2^{2+} varied from one to six, with the 5+1 configuration corresponding to five waters in the first shell and one in the second shell. A comparison

of the first two rows of Table 3-5 shows differences of 0.02 - 0.1 eV with the results of Perron, well within expected deviations. The third row shows the effects of the inclusion of electron localization using the +U term and D3 correction, which decreases the hydration energy by 0.20 eV for one water molecule and leveling off to a decrease of 0.03–0.05 eV for four or more water molecules.

The hydration energy of the uranyl ion was observed to decrease as the number of water molecules surrounding it increased. Also, the 5+1 case had larger hydration energy than six waters in a single shell, which means the optimum coordination number of uranyl ions is five water molecules in the first shell. Therefore, the uranyl ion coordinated with 5 water molecules is used in subsequent calculations.

Table 3-5. $UO_2\{H_2O\}_n^{2+}$ hydration energy per H_2O in eV (5+1: 5 water molecules are in the first shell, one water molecule is in the second shell)

Number of water molecules	1	2	3	4	5	6	5+1
Literature (GGA)[58]	3.20	2.79	2.70	2.43	2.18	1.85	1.99
GGA	3.15	2.89	2.68	2.45	2.16	1.91	1.97
GGA + U_D3	3.01	2.79	2.65	2.40	2.17	1.88	1.95

As discussed above, the uranyl ion that bonds to the MOF is coordinated with three water molecules rather than five as it is in solution.[83] The energy associated with removing two water molecules from the first neighbor shell of the uranyl ion must be taken into account. Figure 3-9 shows this energy, given by equation 3-2, as a function of the total number of water molecules in the cluster. It can be seen that this energy converges to ~0.75 eV for the GGA method and ~1.05 eV for GGA+U_D3. Therefore, we will take 1.05 eV as the energy cost to remove the two water molecules from the uranyl ion by using GGA_U+D3.

3.4.3 Evaluation of The Energy ΔE_1

We evaluate for ΔE_1 by using GGA+U and GGA+U_D3 in the neutral system method for two slightly different SBU structures: (1) two hydroxide ions attached to Zr atoms, (2) two fluorine ions attached to Zr atoms. The values of ΔE_1 by using GGA+U were -0.051 and -0.007 eV, respectively. This indicates that incorporation into the pore of the MOF structure is energetically favored, but only by a very small amount. However, the GGA+U_D3 shows the inverse results, which are +0.25 and +0.27 eV for hydroxide and fluorine ions, respectively. To ensure consistency, we will use the GGA+U_D3 value of +0.25 eV for ΔE_1 in subsequent analysis. Black is GGA+U method, and red is the GGA+U_D3 method.

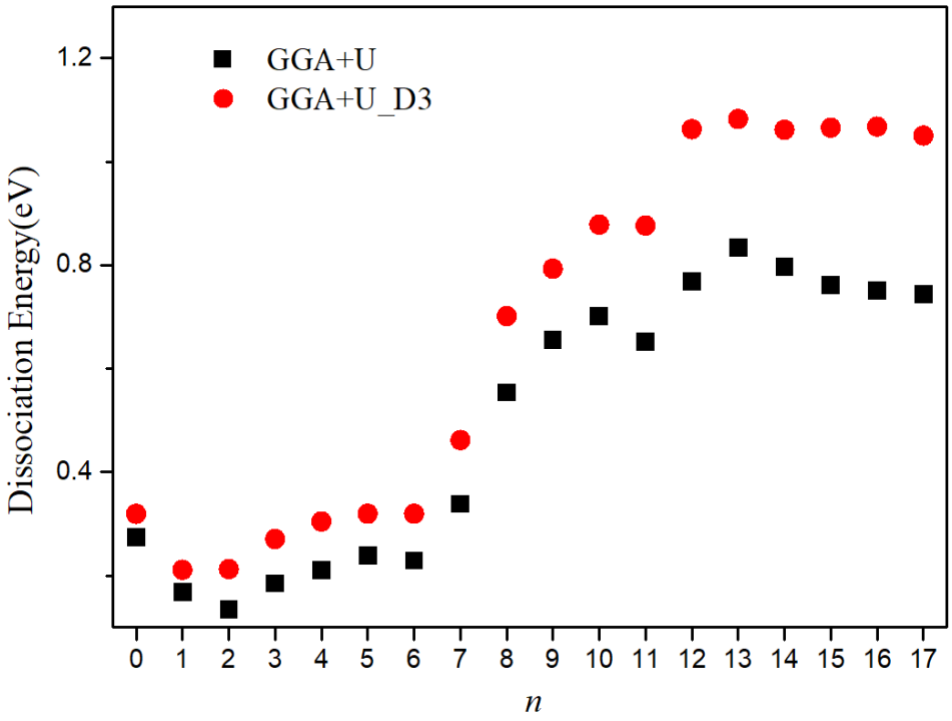

Figure 3-9. The energy for removing two water molecules from the pentahydrated uranyl ion is a function of the total number of the water molecules surrounding the layer uranyl ion.

3.4.4 Binding Uranyl Ions To MOF

3.4.4.1 The choice of DFT method

Since it is necessary to consider the effects of dispersion forces in hydrated system, we use the GGA+U_D3 method to calculate the binding energy between uranyl ions and Zr-MOF. Figure 10 shows the binding energies for the MOF-0 cases, determined from equation 3-3. Recall that the more negative binding energy, the more stable is the configuration between uranyl ion and Zr-MOF. From Figure 3-10, the order of the binding energies for the various binding sites order is the same for both DFT methods used. However, the absolute values are somewhat different. Since the handling of the charged system by DFT uses a uniform compensating counter charge, it is not expected to be the most reliable. We also calculate the GGA+U without dispersion correction, but the binding energies show only a small difference. The Figure 3-11 shows about all of configurations binding energy in detail.

The calculations to this point have considered the key coordinated water molecules explicitly in the DFT calculations. However, it is of interest to consider the effects of the total water environment. To consider these solvation effect in our calculations, we employed the implicit solvation model in VASPsol.[77,78] ,which utilizes the response of a continuum dielectric to model solvation effect. The pristine Zr-MOF crystal structure in the solvation model yielded better agreement with experimental data compared to calculations on the unsolvated system, as shown in Table 3-1. However, the VASPsol method was not able to yield a plausible physical structure for the uranyl-MOF complex. Furthermore, although VASPsol demonstrates accurate outcomes in computing solvation energies for organic main group molecules,[84] it encounters

challenges when attempting to calculate energy information for systems involving larger atom radius size, including, high-atomic number alkali[85] and alkali-earth[86] elements, as well as lanthanide[87] and actinide[88] elements. Since uranium is also an actinide element, therefore, we will not use it in our further investigations.

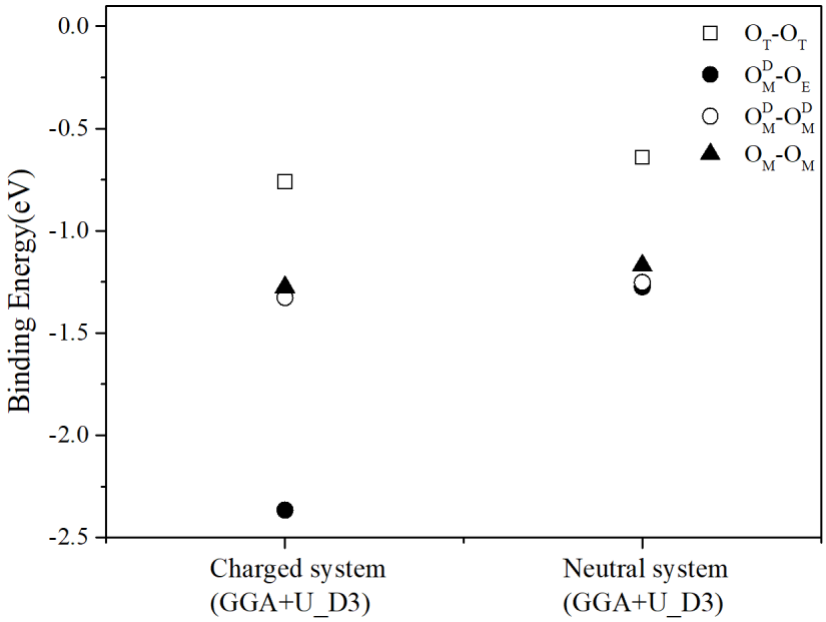

Figure 3-10. Binding energies (Δ*E*) of binding of uranyl ion to MOF-0 ion using different calculation methods.

To identify the nature of the bond to the MOF metal node, the distance between the U ion and the oxygen ions to which it binds, U-O_{ads}, was analyzed, with d(U-O_{ads}) defined as the mean bond distance instead of the separate two U-O_{ads} bond lengths. This average is useful as in all cases the bond lengths differ by less than 0.15 Å. Figure 3-12 gives the atom distances associated with all 19 configurations shown in Table 3-3. Red: charged system with GGA+U, green: charged system with GGA+U_D3, blue: neutral system with GGA+U, and cyan: neutral system with GGA+U_D3. The charged system and the neutral systems have the same trend in mean distances. For instance, the O_M-O_E configuration in MOF-0 (Figure 3-12d), the U-O_{ads} is almost same no matter

what DFT method is used, although the binding energy difference in Figure 3-10 is large. Therefore, we will use the neutral system with D3 correction in the subsequent analysis. Moreover, the bond distances can be divided into two groups: for one group the bond length is greater than 4 Å, while for the other it is roughly 2.5 Å. The long U-O_{ads} bonds at the $O_T - O_T$ is consistent with the low binding energies seen in Figure 3-11. More interestingly, the $O_M - O_M$ configuration shows short bonds in MOF-0, but much longer bonds when protonated to any degree. For a discussion of bond lengths, see section 3.4.4.2. We thus conclude that, $O_M - O_M$ and O_T-O_T should be relatively unfavorable configurations. By contrast, the $O_M^{A(D)} - O_M^{A(D)}$ and $O_M^{A(D)} - O_E$ configurations have bond lengths around 2.5 Å, consistent with strong stable bonds.

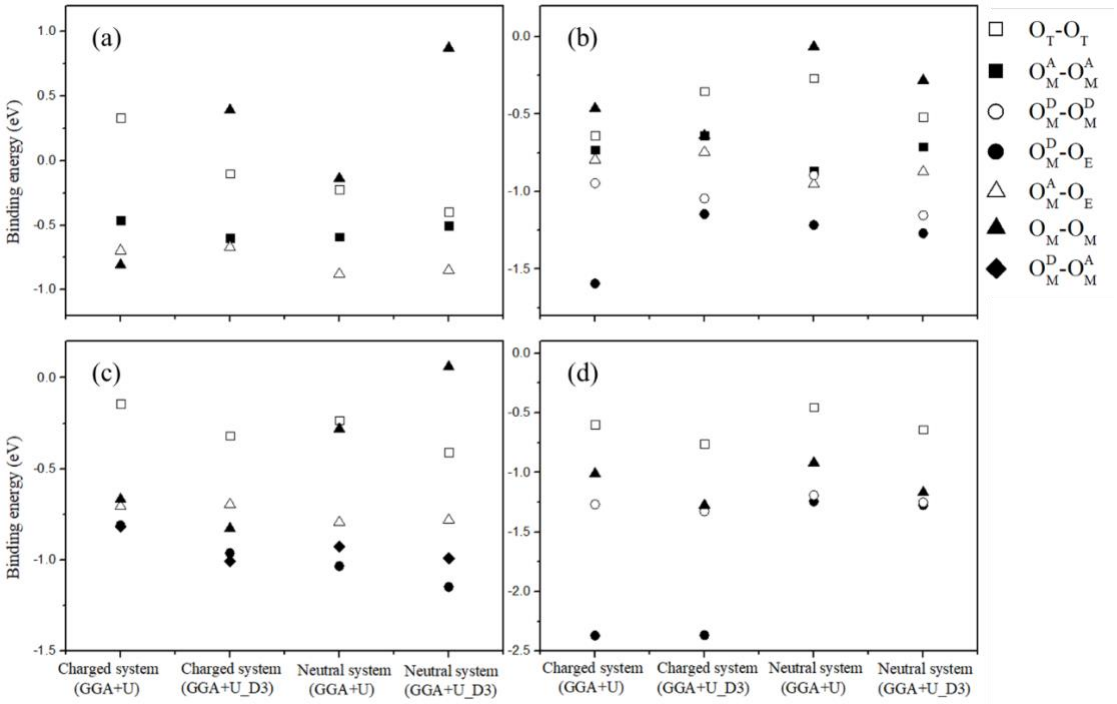

Figure 3-11. The binding energies (*ΔE*) of different protonation of Zr-MOF a) MOF-4, b) MOF-2N, c) MOF-2O, and d) MOF-0 with different density functional theories.

Figure 3-12 also shows that the mean bond length decreases slightly as the deprotonation of the MOF increases. For example, the MOF-4 O_M-O_E the mean bond

length is 2.49 Å in GGA+U_D3; however, the same configuration ion MOF-0 is 2.37 Å. This trend arises because the more the Zr-SBU is deprotonated, the less positively charged the two SBU become (charge state from +8 to 0), thereby bonding more strongly to the positive charge uranyl ion.

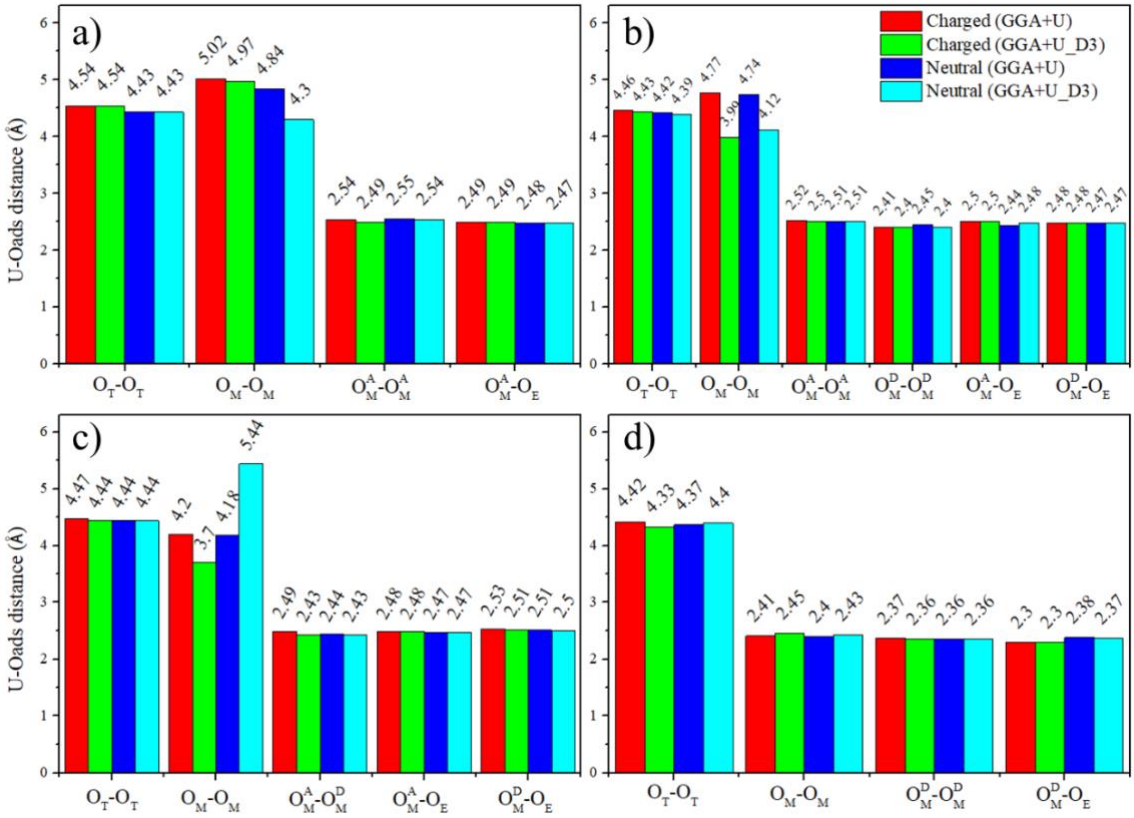

Figure 3-12. The mean bond length in Å of 19 different configuration, a) MOF-4, b) MOF-2N, c) MOF-2O and d) MOF-0.

3.4.4.2 Effects of Zr-MOF protonation on site preference

Figure 3-13 shows the binding energy of the uranyl ion to the Zr-MOF with varying protonations. The red in Figure 3-13 means the short bond length, while the blue means the long bond length. Because $O_M - O_M$ has long bonds in MOF-4, MOF-2N and MOF-2O but short bonds in MOF-0, it is two toned of $O_M - O_M$ legend. In Figure 3-12, we saw that some configurations have long bonds distance between the U and the

oxygens to which it binds, and some have short bonds. These bond distance correlate well with the binding energies in Figure 3-13, in which structures with short bonds are in red and those with long bonds are blue. We know that the energy of a hydrogen bond is usually less than 0.5 eV. Therefore, we can conclude that a relatively strong interaction is not formed between the uranyl ion and Zr-MOF metal node when the binding energy is above -0.5 eV. Thus, the all $O_T - O_T$ (square) configurations and $O_M - O_M$ except for the MOF-0 configurations show that the binding energy are above or nearly the -0.5 eV and can be considered as weak secondary bonds. By contrast, the $O_M - O_M$ in MOF-0 configuration is about -1.25 eV, and the bond distance is also only 2.4 Å; this thus appears to be a strong interaction. A possible reason for MOF-0 having a very different energy is the absence of steric hindrance in this case. The protonation of the metal node decreases the available space in which the uranyl can bond. Two metrics illustrate the differences in the size of the space in Figure 3-14. The MOF-0 have the widest O_E-O_E distance 5.12 Å and largest C-Zr-C angle, 84.5˚; it thus provides sufficient space for the uranyl ion can attach to the metal node. By contrast, for, the MOF-4, MOF-2O and MOF-2N, the bond length and angle are 4.68 Å, 80.5˚;4.77 Å, 80.2˚; and 4.77 Å, 80.8˚; respectively. Thus, the space available is so small in these structures that the uranyl ion cannot attach to the metal node.

In MOF-0, MOF-2O and MOF-2N the $O_M^D - O_E$ is the most favorable configuration. This configuration is not available to the MOF-4 structure and, rather, the $O_M^A - O_E$ is the most favorable. Notably, the $O_M^A - O_E$ configuration also shows favorable binding for other protonations (in which it is possible) with an energy that is almost independent of the degree of protonation. Because from the analysis above, the $O_M^{A(\mathrm{D})} -$

$O_M^{A(\mathrm{D})}$ and $O_M^{\mathrm{A}(D)} - O_E$ configurations are the two most energetically favorable configurations in each protonation of Zr-MOF, and the specifically configuration of the $O_M - O_M$ in MOF-0 is also stable, we focus on these configurations in further discussions.

We find that the biding energy of the most strongly bound structure increases (i.e., becomes more negative in Figure 3-13 going from MOF-4 to MOF-0; that is, the binding increases with increasing deprotonation, corresponding to decreasing pH. To support this conclusion, we performed two additional calculations. We calculated the $O_M^D - O_E$ configuration in MOF-3 (3 hydrogens) and MOF-1 (1 hydrogen). This configuration has the strongest binding energy (red circle) for all protonations, except for MOF-4 for which this configuration is not possible. This trend confirms our conclusions that increasing deprotonation leads to stronger binding energies. Therefore, the most favorable configuration is $O_M^D - O_E$ in MOF-0.

3.4.4.3 Charge density difference analysis

Charge density difference analysis [89–93] can also provide additional insight into the binding process. To characterize how the electron distribution changes on uranyl ion binding to MOF, we define the charge density difference in any small region in space to be the total charge for the complex formed by the MOF and the hydrated uranyl less the charge of the isolated MOF and three coordinated -water molecules uranyl ion separately. Figure 3-15 shows four illustrative cases. To further understand the charge transferring between those two species and illustrate the effect of charge transfer, only the MOF-4 and MOF-0 cases will be shown. It is clearly seen that the charge exchange between the uranyl and the Zr-MOF metal node in MOF-4 $O_M^A - O_M^A$ is less than MOF-0

$O_M^D - O_M^D$ in Figures 3-15a and 3-15b; that is, the Zr-SBU grabs more electrons from uranyl ions in the less protonated structures. This larger amount of charge transfer is consistent with the shorter the bond length. However, there is little difference between the charge transfers for $O_M^A - O_E$ in MOF-4 and $O_M^D - O_E$ in MOF-0 (Figure 3-15c and 3-15d).

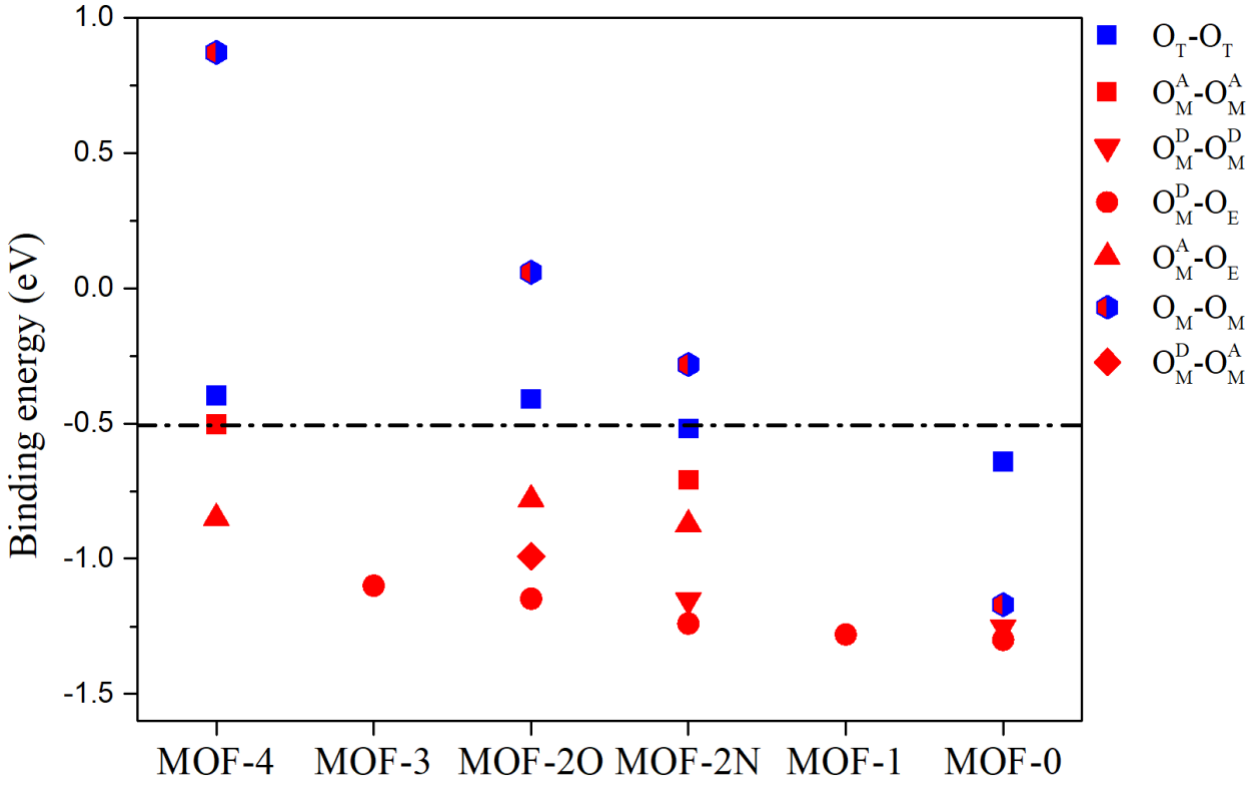

Figure 3-13. Binding energies (ΔE) of neutral system with GGA+U_D3 method to calculate the total 19 configurations binding energy.

Table 3-6. The O=U=O bond angle in degrees for various deprotonated Zr-MOFs as defined in Figure 3-4.

Name	$O_M^{A(D)} - O_E$	$O_M^{A(D)} - O_M^{A(D)}$
MOF-4	179.6	177.9
MOF-2N	$O_M^A - O_E$: 177.7 $O_M^D - O_E$: 178.1	168.1
MOF-2O	$O_M^A - O_E$: 177 $O_M^D - O_E$: 178.4	170.9
MOF-0	174.7	164.8

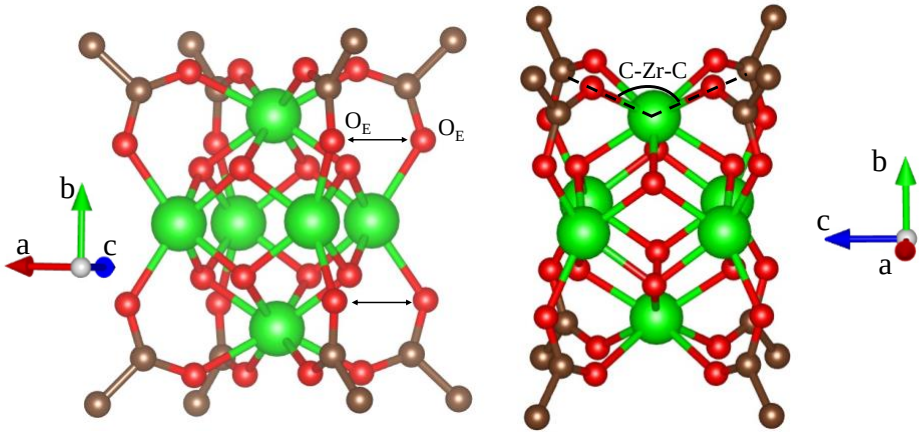

Figure 3-14. The two metrics of MOF-0 space. The left one shows the O_E–O_E distance. And the right one shows C-Zr-C angle measurement.

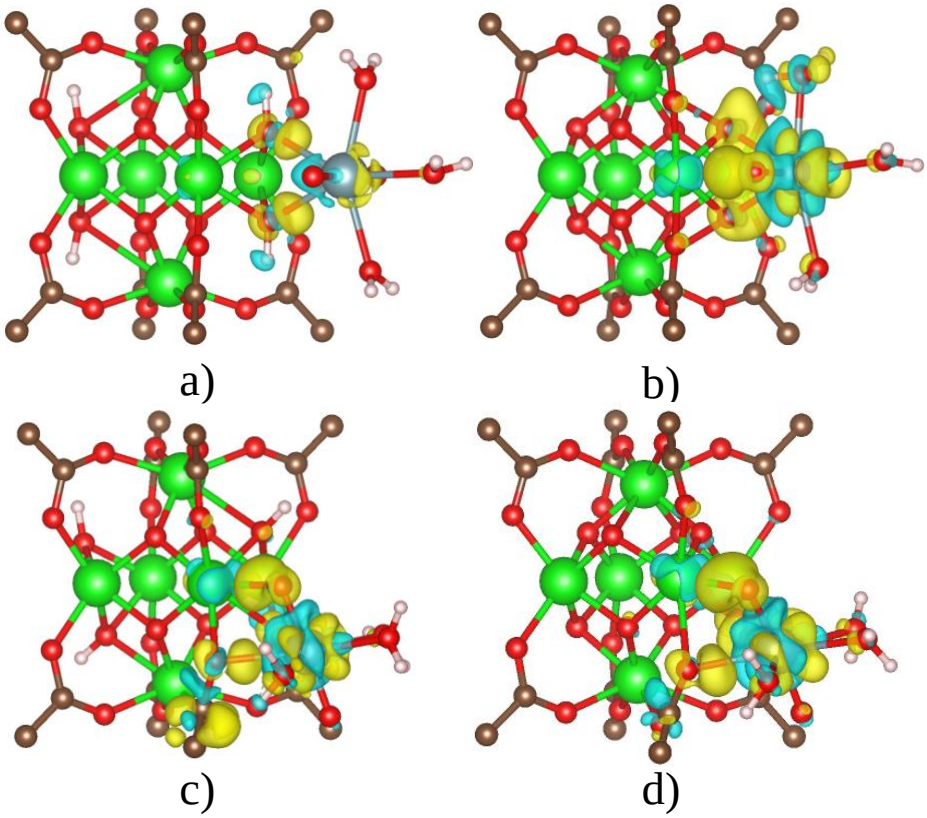

Figure 3-15. Schematics of charge difference after uranyl ions attachment as determined by GGA+U_D3 for a) MOF-4: $O_M^A - O_M^A$, b) MOF-0: $O_M^D - O_M^D$, c) MOF-4: $O_M^A - O_E$, d) MOF-0: $O_M^D - O_E$.The organic ligands have been omitted. Yellow regions correspond to an accumulation in electron density, while the cyan regions correspond to stagnation in electron density.

3.4.5 $\mathbf{O_M^{(A)D} - O_E}$ is the Most Stable Configuration

3.4.5.1 O=U=O bond angle after uranyl ion binding

We first look at the angle of the O=U=O bond after the uranyl ion attaches to the Zr-MOF metal node. The O=U=O bond angle in an isolated or hydrated uranyl ion is 180°. Table 3-6 reports the O=U=O angles and shows that the uranyl group is straighter (i.e., the bond angle closer to 180°) for the $O_M^{A(D)} - O_E$ configurations than for the $O_M^{A(D)} - O_M^{A(D)}$ configuration, except for the MOF-4 case. In order to estimate the energy cost due to this bending on the Zr-MOF metal, static energies calculations were performed on uranyl ion bent to the angles seen after attachment (Table 3-6 and Figure 3-16).

To evaluate the energy expenditure due to this bending after the uranyl ion attaches on the Zr-MOF node, we set the total energy of O=U=O bond angle of 179.6˚ as the reference state. As expected, the greater the bending of O=U=O molecule, the higher the energy cost. However, the energy cost even at a bond angle of 176˚ is only about 20 meV. As a result, the $O_M^{A(\mathrm{D})} - O_E$ and $O_M^{\mathrm{A(D)}} - O_M^{\mathrm{A(D)}}$ configurations in the MOF-4 case have almost the same energy. This means that the strain in the O=U=O bond angle does not account for the energy difference between these two configurations. In MOF-0, the $O_M^{\mathrm{D}} - O_M^{\mathrm{D}}$ configuration has a bond angle of 164.8˚ with an associated energy cost of ~ 275 meV while the $O_M - O_E$ structure has an angle of 174.7˚ and an energy cost of ~50 meV, which is consistent with the unfavourability of these configurations.

3.4.5.2 Zr-O_u bond formation

In the $O_M^A - O_E$ configuration of MOF-4, the uranyl ion not only forms U-O_{ads}

bonds but also has a Zr-O_u bond (O_u being the oxygen in the uranyl ion). This is evident from a comparison of the Zr-O_u distance lengths, which for $O_M^A - O_E$ and $O_M^A - O_M^A$ were 2.43 Å and 3.45 Å, respectively. Returning to Figure 3-15a, it shows that there is no charge transfer between the Zr atom and the uranyl ion double bond oxygen in $O_M^A - O_M^A$. In contrast, $O_M^A - O_E$ in Figure 3-15c shows considerable charge transfer. To show that this is associated with the Zr-O_u bond, in Figure 3-17, we plot the density of state of the Zr atom d orbital and O_u-p orbital for these two configurations. The $O_M^A - O_E$ shows the more orbital overlap than the $O_M^A - O_M^A$, consistent with the Zr atom has a stronger bond with uranyl ion double bond oxygen in $O_M^A - O_E$.

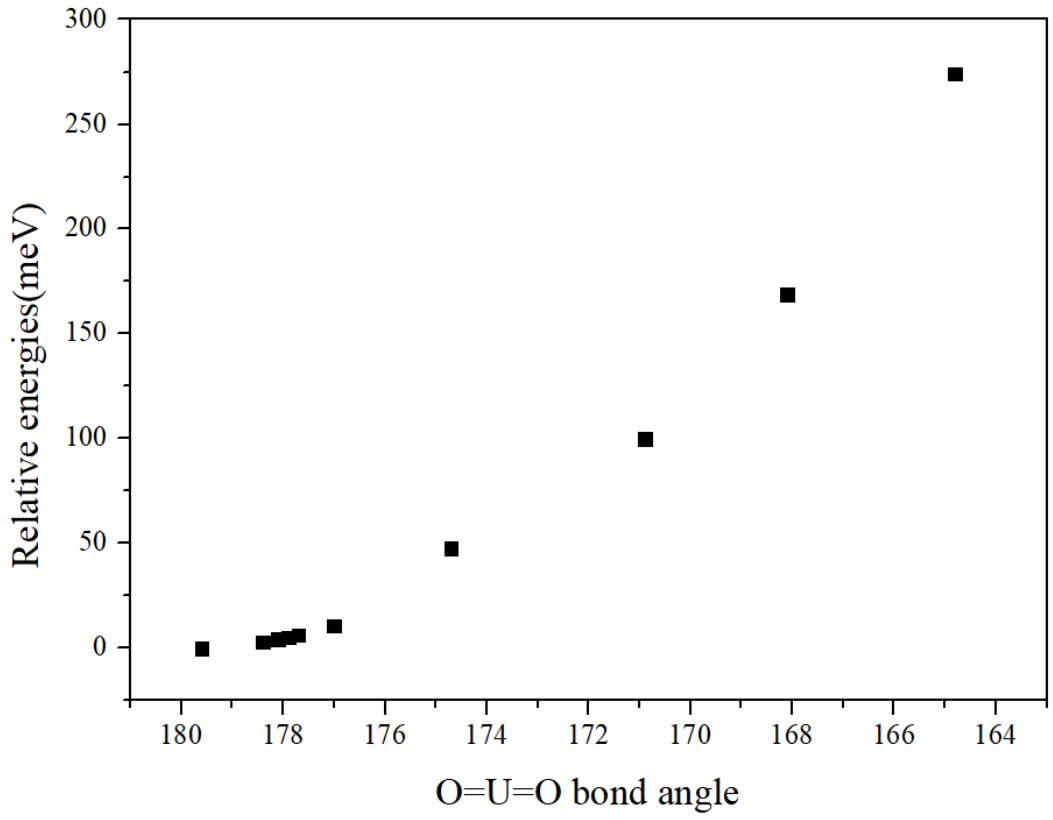

Figure 3-16. The energies of an isolated uranyl ion as a function of the O=U=O bond angle; the zero of energy corresponds to a bond angle of 179.6˚.

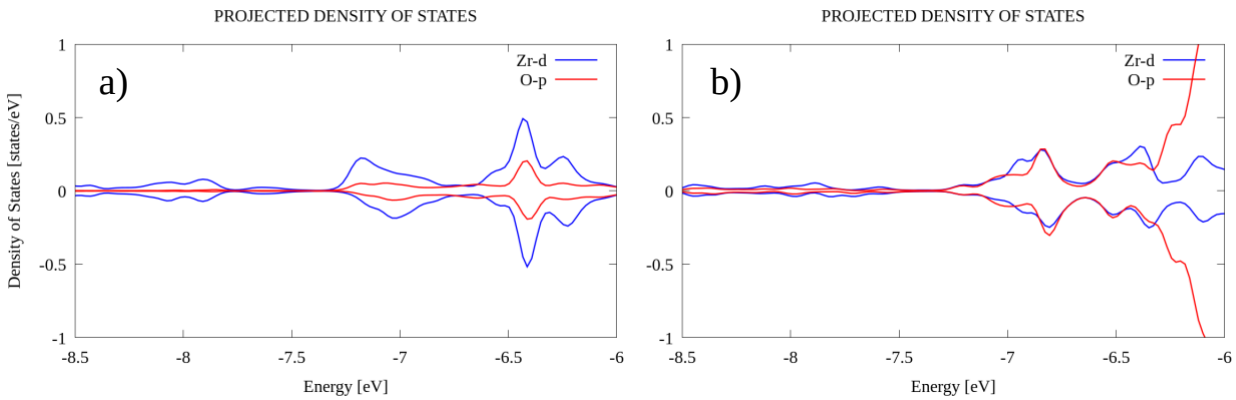

Figure 3-17. The density state of attaching zirconium atom and uranyl ion double bond oxygen. a) MOF-4 $O_M^A - O_M^A$, b) MOF-4 $O_M^A - O_E$. The blue line is the d orbital of the zirconium atom, and the red line is the p orbital of oxygen.

3.5 Conclusion

In this work we have identified the preferred binding sites of the uranyl ion to the Zr MOF structure. Our results are also in good agreement with the earlier studies of the bonding of the uranyl ion to titanium dioxide[58] and calcite surfaces[64], in which the binding energy was determined by the protonation of the surface and the specific binding site, with binding being stronger under more basic (more deprotonated) conditions.

Based on that, this work explored the dissociation energy of uranyl cation and binding mechanism of uranyl cation with Zr-MOF metal node. To achieve this, we thoroughly investigated the 19 different configurations of uranyl cation coordinating to Zr-MOFs for charged and neutralized systems using GGA+U and GGA+U with D3. The results clearly show that the binding of the uranyl ion is stronger in deprotonated conditions than in protonated conditions due to the larger amount of charge transfer. The most stable configuration is always the uranyl ion attached to the deprotonated middle oxygen and the edge oxygen of the Zr metal node, since this configuration not

only has U–O bonds but also forms a Zr-O_u bond between the Zr-MOF and axial oxygen of the uranyl ion. The identification of the preferred configuration for uranyl cation binding with Zr-MOF metal node represents significant mechanistic information that will be valuable for the development of more sophisticated leaching models. In addition, the strength of the binding of the uranyl to the MOF must be strong enough to offset the energy for any bending in the O=U=O bond, which was found to be straighter for the $O_M^{A(D)} - O_E$ configuration than for the $O_M^{A(D)} - O_M^{A(D)}$ configuration. The identification of this configuration may have implications for the design of MOFs with improved uranyl capture efficiency.

We conclude that the considered Zr-MOF possesses the ability to strongly bind uranyl ions. Moreover, while the strength of the binding does depend on the degree of protonation, which will change depending on the pH of the system, the binding to some sites is relatively strong for a wide pH range. Thus, these results strongly suggest that the Zr-MOFs could be utilized as valuable materials for the sequestration of uranyl ions.

CHAPTER 4
BINDING OF RADIONUCLIDES AND SURROGATE TO 18-CROWN-6 ETHER BY DENSITY FUNCTIONAL THEORY†

4.1 Background

In chapter 3, we discussed the interaction between metal node and uranyl ions. In this chapter, we shift our focus to another strategy mentioned in chapter 1, namely, the interaction of organic ligands of MOFs with actinide ions. Nowadays, the growing use of nuclear energy results in the enhanced generation of hazardous radioactive waste. This not only includes uranyl ions but also other ions such as americium and curium cations, which are highly radioactive.[94] As a result, the importance of effectively sequestering and confining radionuclides has significantly risen. Therefore, it is crucial to prioritize the development of robust and sustainable management strategies for the storage and sequestration of these radioactive cations.[95,96] Currently, hierarchical materials[6] including salt-inclusion extended structures,[97] zeolites,[98,99] metal-organic frameworks (MOFs),[100,101,102] and materials containing macrocyclic ligands[103,104] are being explored for their potential in the field of nuclear waste extraction. Recent work by Li *et al.*[105] has demonstrated the efficacy of 18-crown-6 ether in trapping plutonium. Additionally, numerous theoretical[106,107,108,109] and experimental[110,111,112] studies have shown that crown ether can capture actinide cations. Interestingly, Park *et al.*[113] synthesized a novel zirconium-based MOF whose linkers, containing 18-crown-6 ether, efficiently captured Ce^{3+}, a surrogate for transuranic elements. However, the loading capacity of this MOF was found to be limited, at only 0.2 cerium cations per metal node.

†This work described in this chapter has been published in Liu, Y.; Ta, A. T.; Park, K. C.; Hu, S.; Shustova, N. B.; Phillpot, S. R. Binding of Radionuclides and Surrogate to 18-Crown-6 Ether by Density Functional Theory. *Microporous Mesoporous Mater.* **2023**, 112882. https://doi.org/10.1016/j.micromeso.2023.112882

Any increase in the material loading capacity will be beneficial to sequestration efforts. Due to the radiotoxicity of transuranic elements and the small amounts available for studies, experimental efforts are limited and very challenging. Therefore, by computationally evaluating the radionuclide-substrate interactions, specifically the binding ability of the crown ether toward specific radionuclides, we can shed light on specific mechanisms and use the acquired fundamental knowledge for material selection. we will also examine cerium salt as a reference since it is commonly used as surrogate in experiments of actinide binding. The insights gained from these studies will serve as a valuable guide in the development of organic-based systems that can effectively capture radionuclides to address challenging questions in the nuclear waste.

4.2 Computational Method

All DFT calculations were carried out using the Vienna *Ab-initio* Simulation Package (VASP)[65,66] with the Perdew-Burke-Ernzerhof (PBE) exchange-correlation functional.[67,68] To ensure calculation convergence, the cut-off energy of the wave-function plane was 520 eV, and all calculations were only performed at the Γ point. The complexes of crown ether and nitrates were treated as isolated and were relaxed in a 20 Å cubic box, which provides a vacuum space that is large enough to completely remove interactions from the periodic boundary. The cerium pseudopotential included 12 valence electrons ($5s^2 5p^6 6s^2 6d^1 4f^1$); the americium pseudopotential included 17 valence electrons ($6s^2 6p^6 7s^2 6d^2 5f^5$); the curium pseudopotential included 18 valence electrons ($6s^2 6p^6 7s^2 6d^2 5f^6$). The oxygen pseudopotential included 6 valence electrons ($2s^2 2p^4$); the carbon pseudopotential included 4 valence electrons ($2s^2 2p^2$), and the nitrogen pseudopotential included 5 valence electrons ($2s^2 2p^3$). The present study employed the DFT+U[114] method to describe electron localization in the 5f states of the

actinide and 4f states of cerium. To establish an appropriate value of U for the heavy elements, Tables 4-1 and 4-2 report the structural parameters determined using various U values. Through the integration of our computational results and literature values, after checking the binding energy and structure parameters, the optimal U values of 4.5 eV[115,116,117,118] 4.8 eV[119,120], and 4 eV[121] were identified for cerium, americium, and curium, respectively.

Table 4-1. The six bond lengths of Ce-$O_{(crown)}$ unit in (Å), and binding energy of cerium nitrate within 18-crown-6 ether, unit in eV by applying different Hubbard U values for cerium.

Hubbard U	0	0.5	1	1.5	2	2.5
Ce-O_6	2.697	2.693	2.693	2.693	2.693	2.693
Ce-O_5	2.740	2.740	2.741	2.741	2.741	2.742
Ce-O_4	2.790	2.787	2.787	2.787	2.787	2.786
Ce-O_3	2.812	2.800	2.800	2.801	2.802	2.802
Ce-O_2	2.849	2.844	2.844	2.844	2.844	2.844
Ce-O_1	2.877	2.871	2.871	2.871	2.872	2.870
Binding Energy	-1.694	-1.710	-1.723	-1.734	-1.746	-1.756

Hubbard U	3	3.5	4	4.5	5	5.5	6
Ce-O_6	2.693	2.697	2.698	2.699	2.699	2.699	2.700
Ce-O_5	2.743	2.741	2.743	2.742	2.742	2.743	2.744
Ce-O_4	2.787	2.785	2.785	2.787	2.784	2.785	2.787
Ce-O_3	2.803	2.804	2.804	2.803	2.805	2.805	2.805
Ce-O_2	2.843	2.847	2.847	2.848	2.846	2.846	2.845
Ce-O_1	2.872	2.869	2.869	2.869	2.870	2.870	2.870
Binding Energy	-1.766	1.773	-1.781	-1.782	-1.797	-1.803	-1.800

Table 4-2. The six bond lengths of Am-$O_{(crown)}$ unit in (Å), and binding energy of americium nitrate within 18-crown-6 ether, unit in eV, by applying different Hubbard U values for americium.

Hubbard U	4.0	4.1	4.2	4.3	4.4	4.5
Am-O_6	2.669	2.669	2.671	2.671	2.671	2.671
Am-O_5	2.738	2.737	2.737	2.737	2.737	2.737
Am-O_4	2.775	2.775	2.778	2.778	2.778	2.778
Am-O_3	2.812	2.812	2.812	2.812	2.812	2.812
Am-O_2	2.868	2.868	2.869	2.869	2.869	2.869
Am-O_1	2.890	2.890	2.892	2.892	2.892	2.892
Binding Energy	-1.592	-1.594	-1.596	-1.598	-1.600	-1.602

Table 4-2. Continued.

Hubbard U	4.6	4.7	4.8	4.9	5.0
Am-O_6	2.671	2.671	2.671	2.671	2.671
Am-O_5	2.737	2.737	2.737	2.737	2.737
Am-O_4	2.778	2.778	2.778	2.778	2.778
Am-O_3	2.812	2.812	2.812	2.812	2.812
Am-O_2	2.869	2.869	2.869	2.869	2.869
Am-O_1	2.892	2.892	2.892	2.892	2.892
Binding Energy	-1.605	-1.607	-1.609	-1.611	-1.613

In our study, we employed two different DFT functionals, namely the Generalized Gradient Approximation (GGA)+U[25] and van der Waals (VDW)_DF2+U[32,122] to calculate the binding energy of cerium nitrate with 18-crown-6 ether. There is a notable difference in the binding energy between calculations using GGA+U (-1.782 eV) and VDW-DF2+U (-3.144 eV), despite the similarities in the structural parameters (shown in Table 4-3). These results showed that the van der Waals forces are an important factor in the interaction of the crown ether with cerium nitrate. Therefore, the calculations in the rest of this used the VDW_DF2+U method.

The atomic structures were optimized using a conjugate gradient method[74,75] until the average force reached less than 0.025 eV/Å, with 1×10^{-5} eV as the energy tolerance for each electronic step. Spin-polarization was also included in all calculations. Gaussian smearing with a width of 0.05 eV was applied to all optimizations. Preliminary GGA+U calculations showed that the incorporation spin orbital coupling (soc) effects[70] had little impact on binding energies and bond lengths, see Table 4-4. Given this small difference, the high computational cost and the fact that soc effects are not available for the VDW_D2+U function, the soc correction was not taken into consideration in our calculations.

To account for solvent effects, the solvation behavior of crown ether with the actinide complex was implicitly modeled with VASPsol.[33,34] The default parameters for VASPsol in a water environment were set as follows: bulk dielectric constant was 80, the width of the dielectric cavity was 0.6,[33,34] the cutoff charge density was 0.0025 $Å^{-3}$,[33,34] and a surface tension parameter was 0.525 meV/$Å^2$. [33,34] The equation of solvation energy was defined below:

$$E_{sol} = E_{vaspsol} - E_{vacuum} \quad (4\text{-}1)$$

where, $E_{vaspsol}$ was the total energy in implicit aqueous solvent and E_{vacuum} was the total energy in a vacuum.

The binding energy was defined below:

$$E_b = E_{complex} - E_{nitrate} - E_{crown} \quad (4\text{-}2)$$

where $E_{complex}$ was the total energy of the crown ether complex, $E_{nitrate}$ was the total energy of cerium/actinide nitrates, and E_{crown} was the total energy of the crown ether alone.

The charge density difference was analyzed with VASPKIT.[123] The visulizations of structures, charge density differences and electron localization functions (ELF) were performed in VESTA.[124]

Table 4-3. The comparison of experimental and theoretical data of cerium nitrate in 18-crown-6 ether by using GGA+U and VDW_DF2+U method. Bond length unit in (Å), binding energy unit in eV.

Name	GGA+U	VDW_DF2+U	Experimental[125]
Ce-O_6	2.699	2.720	2.618
Ce-O_5	2.742	2.757	2.667
Ce-O_4	2.787	2.795	2.716
Ce-O_3	2.803	2.818	2.737
Ce-O_2	2.848	2.848	2.773
Ce-O_1	2.869	2.876	2.795
Average Ce-$O_{(crown)}$	2.791	2.802	2.716

Table 4-3. Continued

Average Ce-$O_{(nitrate)}$	2.617	2.663	2.642
Average $O_{(nitrate)}$-Ce-$O_{(nitrate)}$ bond angle	49.3	49.1	47.8
Average $O_{(crown)}$-Ce-$O_{(crown)}$ bond angle	60.5	60.6	60.7
Binding Energy	-1.782	-3.144	/

Table 4-4. The six bond lengths of Ce/Am/Cm-$O_{(crown)}$ unit in (Å), and binding energy of americium nitrate within 18-crown-6 ether, unit in eV with and without soc correction.

Name	GGA+U	GGA+U+soc	Name	GGA+U	GGA+U+soc
Ce-O_6	2.699	2.699	Am-O_6	2.671	2.670
Ce-O_5	2.742	2.742	Am-O_5	2.738	2.736
Ce-O_4	2.787	2.786	Am-O_4	2.778	2.772
Ce-O_3	2.803	2.803	Am-O_3	2.812	2.813
Ce-O_2	2.848	2.846	Am-O_2	2.870	2.870
Ce-O_1	2.869	2.868	Am-O_1	2.892	2.891
Binding Energy	-1.782	-1.840	Binding Energy	-1.609	-1.571

Name	GGA+U	GGA+U+soc
Cm-O_6	2.667	2.666
Cm-O_5	2.722	2.724
Cm-O_4	2.774	2.773
Cm-O_3	2.804	2.803
Cm-O_2	2.863	2.864
Cm-O_1	2.886	2.888
Binding Energy	-1.561	-1.541

4.3 Structures

4.3.1 Crown Ether

Park *et al.*[113] used a 18-crown-6 ether-based ligand following to connect the metallic secondary building units (SBUs) in a Zr-based MOF to sequester cerium cations. We mimicked this process in our simulation study, as depicted in Figure 4-1. In the presented paper, we focused only on the core of 4,4′-(2,3,5,6,8,9,11,12,14,15-decahydrobenzo[*b*][1,4,7,10,13,16]hexaoxacycloocta-decine-17,20-diyl)dibenzoic acid

(H_2TPDC-18C6)[113] and omitted the rest of the skeleton of reported organic linker from consideration (Figure 4-1). Table 4-5 summarizes the average bond length of C–C and C–O, obtained from both density functional theory and experimental data; the bond lengths were similar, with those determined from DFT being longer by roughly 2%. The observed difference were consistent with the findings of Callsen *et al.*,[126] who noted that the VDW_DF2 method calculated bond lengths within 1.34 % deviation for diatomic molecules.

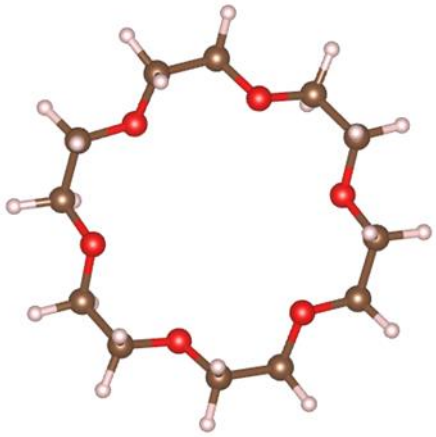

Figure 4-1. The molecular structure of 18-crown-6 crown ether. Oxygen in red, carbon in brown, and hydrogen in white.

Table 4-5. Comparison of DFT and experimental of average bond lengths. Unit in Å.

Bond length	C–C	C–O
DFT (this work)	1.513	1.432
Experimental[127]	1.507	1.411

4.3.2 Models of The Cerium-, Americium-, And Curium-based Salts

To maintain consistency with the work of Park *et al*.,[113] who utilized cerium nitrate as the source of the cerium cation, we conducted calculations using cerium, americium and curium nitrates. The three nitrate anions, which were symmetrically coordinated to the central atom, are illustrated in Figure 4-2. The N-Ce/Am/Cm–N angle was equal to 120° . Experimental bond length data for these three complexes were not available,

however, our structural parameters for the Ce–O bond length (2.494 Å) are similar, albeit slightly shorter, to report on the average Ce–O bond lengths for similar structures like tris(nitrate-O, O')bis(l,10-phenanthroline-N, N')-cerium[128] and cerium nitrates-18-crown-6 complex,[129] which were 2.566 Å and 2.642 Å, respectively. The calculated Ce/Am/Cm-O bond lengths are shown in Table 4-6. The decreasing ionic radii of 6-coordinated of Ce^{3+} (115 pm), Am^{3+} (111.5pm), and Cm^{3+} (111 pm) was expected to result in a corresponding decrease in bond length with oxygen, as Table 4-6 indeed shows.

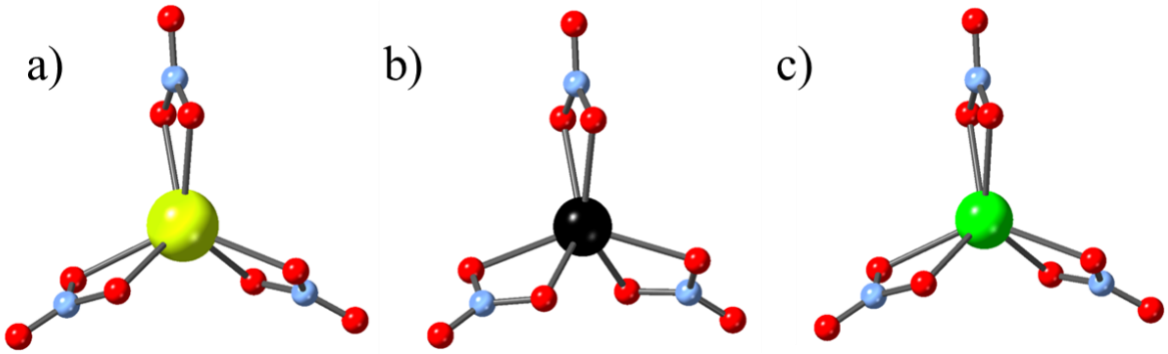

Figure 4-2. The molecular structures of a) cerium nitrate, b) americium nitrate, and c) curium nitrate. Cerium in yellow, americium in black, curium in green, oxygen in red, and nitrogen in blue.

Table 4-6. The average bond length between cerium, americium, and curium with oxygen in their corresponding nitrates complexes. Unit in Å.

Name	Ce-O	Am-O	Cm-O
Bond length	2.494	2.452	2.440

After the relaxation, the magnetic moments on cerium, americium, and curium were 0.98, 6.12, and 6.77 μ B, respectively. To understand the presence of magnetic moments, we plot the densities of state (DOS) in Figure 4-3. From these figures, it can be seen that the DOS of cerium nitrate is almost symmetrical except for one peak around -1 eV, originating from the cerium 4f orbital. However, the DOS of americium

and curium nitrates display significant asymmetry, indicating the presence of a higher number of unpaired electrons, primarily originating from the 5f orbital electrons within the energy window range from -4 to -2 eV (indicated by the cyan line in americium and the purple line in curium). This accounts for the larger magnetic moments exhibited by americium and curium.

4.4 Results

4.4.1 18-Crown-6 Ether Complexes with Cerium, Americium, and Curium Nitrates

4.4.1.1 Comparison of theoretical and experimental data

To validate our calculations of the crown ether/actinide complex, we compared our DFT results to the experimental molecular structure,[129] in Figure 4-4 and Table 4-3. Specifically, we compared six Ce-$O_{(crown)}$ bond lengths by ranking the bond lengths from shortest to longest. DFT calculations were able to reproduce bond lengths in the same order as the experiment and were able to capture the most important structural features. The DFT calculations gave longer bond lengths than experimentally reported, with all differences less than 5%, a difference that is consistent with the larger DFT values for bond lengths in the pure crown ether, discussed above. The average bond lengths of Ce–$O_{(nitrate)}$ bonds, $O_{(nitrate)}$-Ce-$O_{(nitrate)}$ bond angles, and $O_{(crown)}$-Ce-$O_{(crown)}$ bond angles are also shown in Table 4-3. The average bond length of Ce–$O_{(crown)}$ was found to be longer than the average Ce–$O_{(nitrate)}$ bond length, which is consistent with experimental observations. Additionally, we observed the similarity in bond angles between our calculations and experimental data, further supporting the validity of our simulation model.

Figure 4-4 shows the distortion of the cerium nitrates after its capture by crown ether. There is one nitrate above the crown ether ring and two nitrates below the ring.

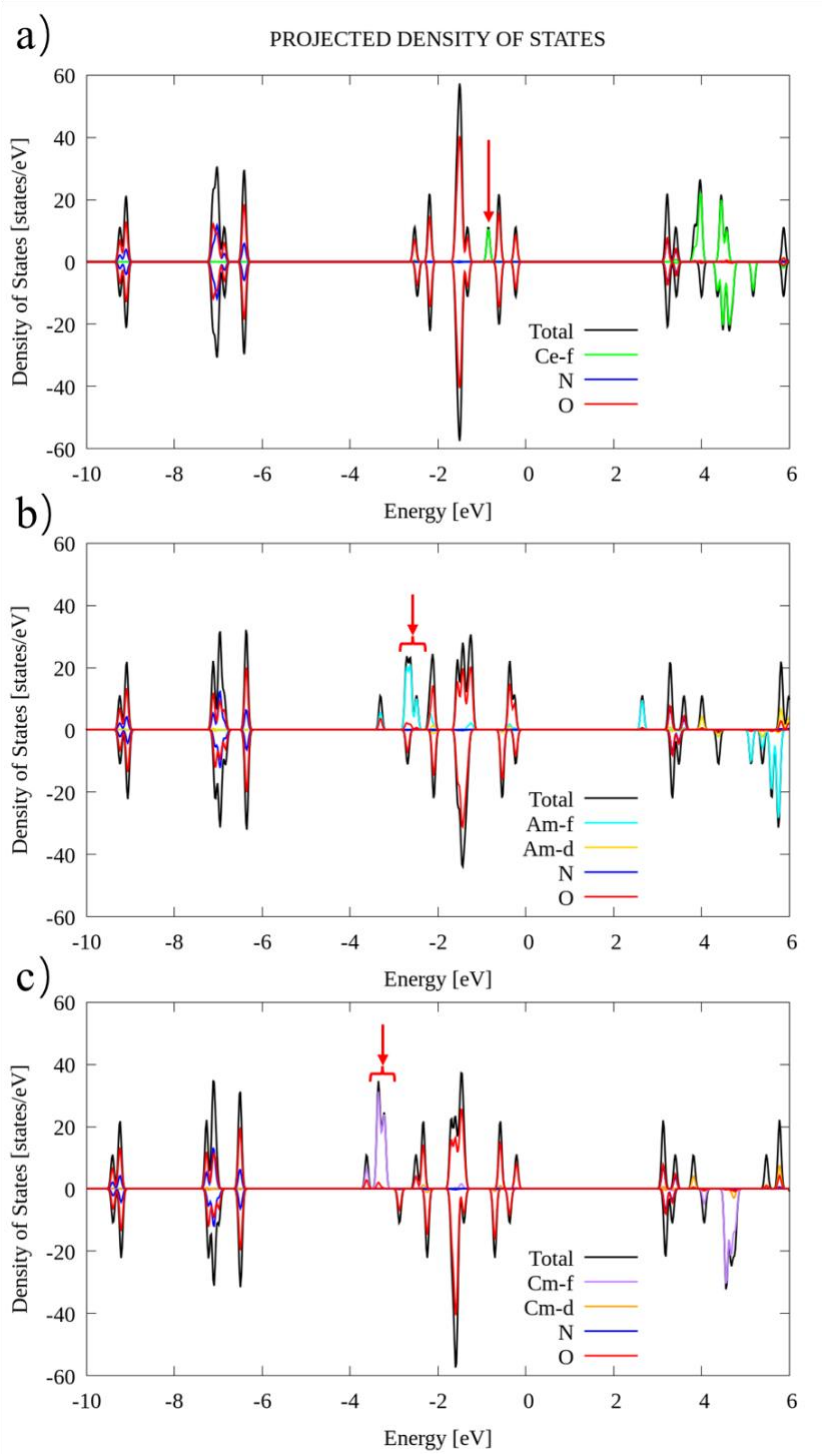

Figure 4-3. The density of states of a) cerium, b) americium, and c) curium nitrates within the energy window from -10 to 6 eV. The black line is the total density of state, and the others are nitrogen in blue line, oxygen in the red line, cerium 4f orbital in green line, americium 5f orbital in cyan line, americium 6d orbital in gold line, curium 5f orbital in purple line, and curium 6d orbital in orange line.

The binding of cerium nitrate with crown ether induced structural changes that lead to the loss of its original three-fold symmetry. In particular, the bottom two nitrates have squeezed to fit with the N-Ce-N angle undergoing a reduction from 120° to 75°, concomitant with a tilting of both nitrate moieties. Also, the Ce-$O_{(nitrate)}$ bond length has increased. Additionally, the symmetry of the crown ether was broken via a distortion to accommodate the cerium nitrates. Specifically, the dihedral angles increased, see Table 4-7. For example, consider the O_3-O_6-O_2-O_4 dihedral angle: the first plane was built by O_3, O_6, and O_2 atoms, while the other plane consisted of O_6, O_2, and O_4 atoms (Figure 4-4). The dihedral angle in the pure crown ether was 3.5°. However, in the merged complex, the dihedral angle significantly increased to 32.6°. This notable change in the dihedral angle indicates a substantial distortion of the crown ether upon complex formation, which breaks its six-fold symmetry in Figure 4-4a. These broken symmetries of the cerium nitrate and crown ether are consistent with the slightly different Ce-$O_{(crown)}$ bond lengths. We are also interested in the distortion of cerium nitrate. Therefore, we simulated a stepwise approach of the cerium nitrate into the ether ring. As Figure 4-5 shows, the distortion in the bond angles takes place when the cerium atom is about 2.5 Å from the crown ether, which corresponds to the position at which the end oxygen of the nitrate group reaches the ether ring, in Figures 4-4a and 4-4b.

4.4.1.2 The 18-crown-6 ether with americium and curium nitrates

The primary aim of this work was to assess the efficacy of 18-crown-6 ether in capturing radionuclide waste, specifically americium and curium nitrate. Figure 4-6(a) presents the bond lengths of americium and curium obtained using the VDW_DF2+U method. The bond lengths of Am-$O_{(crown)}$ and Cm-$O_{(crown)}$ are similar to each other, typically differing by less than 0.01 Å. The average bond lengths of Ce/Am/Cm-$O_{(crown)}$

are similar, presumably largely governed by the bond lengths in the pure crown ether. However, the variation in bond lengths for Am-$O_{(crown)}$ and Cm-$O_{(crown)}$ is larger compared to Ce-$O_{(crown)}$, with values ranging 0.199 Å and 0.200 Å for Am and Cm, respectively, while Ce has a range of 0.156 Å, Figure 4-6(a). Figure 4-6(b) shows that the bond angles in all three cases are also very similar, although the $O_{(nitrate)}$-Am/Cm-$O_{(nitrate)}$ angles are slightly larger than the $O_{(nitrate)}$-Ce-$O_{(nitrate)}$ angle. Moreover, the dihedral angle with Am and Cm cases is slightly larger than Ce case, which means the 18-crown-6 ether exhibits more distortion in the cases of Am and Cm compared to Ce.

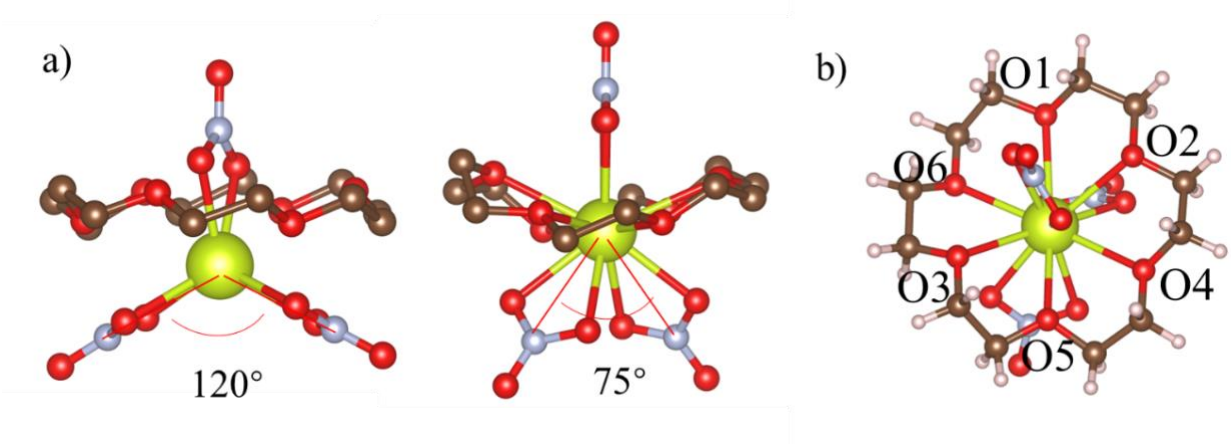

Figure 4-4. The molecular structure of cerium within crown ether, a) comparison of cerium nitrate structure before and after insertion crown ether; the hydrogen has been omitted for clarity, b) Top view of the optimized structure of cerium nitrates inside of crown ether. Cerium atoms are shown in yellow, oxygen in red, nitrogen in blue, carbon in brown, and hydrogen in white.

Table 4-7. The dihedral angle of pure 18-crown-6 ether and 18-crown-6 ether within cerium nitrate complex.

Atom build planes	Pure 18-crown-6 ether	cerium nitrate complex
O_3-O_6-O_2-O_4	3.45°	32.60°
O_6-O_1-O_4-O_5	4.74°	45.98°
O_1-O_2-O_5-O_3	1.24°	13.71°
O_2-O_4-O_3-O_6	3.48°	32.69°
O_4-O_5-O_6-O_1	4.72°	45.04°
O_5-O_3-O_1-O_2	1.23°	12.99°

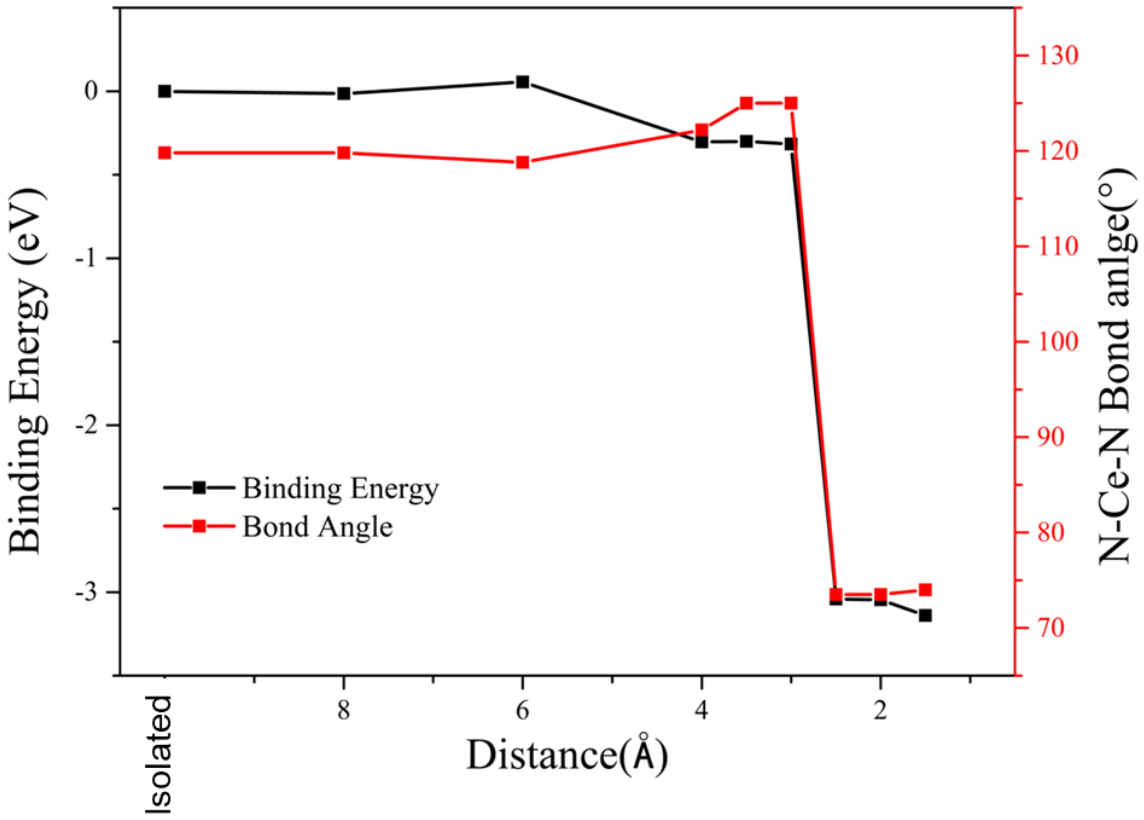

Figure 4-5. The N-Ce-N bond angle and binding energy between cerium nitrate and crown ether as a function of distance. In the "isolated" tag, the bond angle and binding energy were calculated with the two entities separated from each other.

The binding energies of americium and curium nitrate in the crown ether were calculated to be -2.99 eV and -2.94 eV, respectively. These values were similar to the binding energy of -3.14 eV observed for cerium nitrate. It appears that the higher distortion of the crown ether in Am and Cm cases is the reason for their less negative binding energy compared to Ce. The increased distortion of the crown ether requires more energy, resulting in a weaker binding in Am and Cm systems. Finally, the close similarity in binding energy suggested that cerium could serve as a suitable surrogate for americium and curium. There are also small differences in the magnetic moment of Ce, Am, and Cm, as shown in Table 4-8.

Table 4-8. The magnetic moment of Ce, Am, and Cm in pure corresponding nitrates, 18-crown-6 ether, nitrogen-based crown ether, and amine-based crown ether. Unit in (μB).

Magnetic moment	Ce	Am	Cm
Corresponding nitrates	0.98	6.12	6.77
18-crown-6 ether	0.98	6.10	6.74
Nitrogen-based crown ether	0.98	6.09	6.75
Amine-based crown ether	0.98	6.10	6.75

4.4.2 Nitrogen, Sulfur, and Phosphorus-Based Crown Ethers

4.4.2.1 Benchmark

Recent computational analyses indicate that the affinity between the uranyl cation and crown ether amplifies with an incremental substitution of oxygen atoms by the amine (-NH) functional group.[130] We, therefore, considered amine-based crown ethers with cerium nitrates, Figure 4-7(a). To systematically show the effects of the amine group, the binding energy of cerium nitrate with different numbers of amine groups in the crown ether ring was calculated. As depicted in Figure 4-8, the substitution of oxygen by amine leads to an enhancement in the binding energy. In studying the chemical compositions, we found that there are three distinct variations when it comes to the amine group substitution. These variations correspond to the unique configurations of 4O2N, 3O3N, and 2O4N. The differences arise from the diverse arrangements of oxygen and amine molecules in each case. What's intriguing about this observation is its similarity to patterns we previously identified with the uranyl cation. [130]

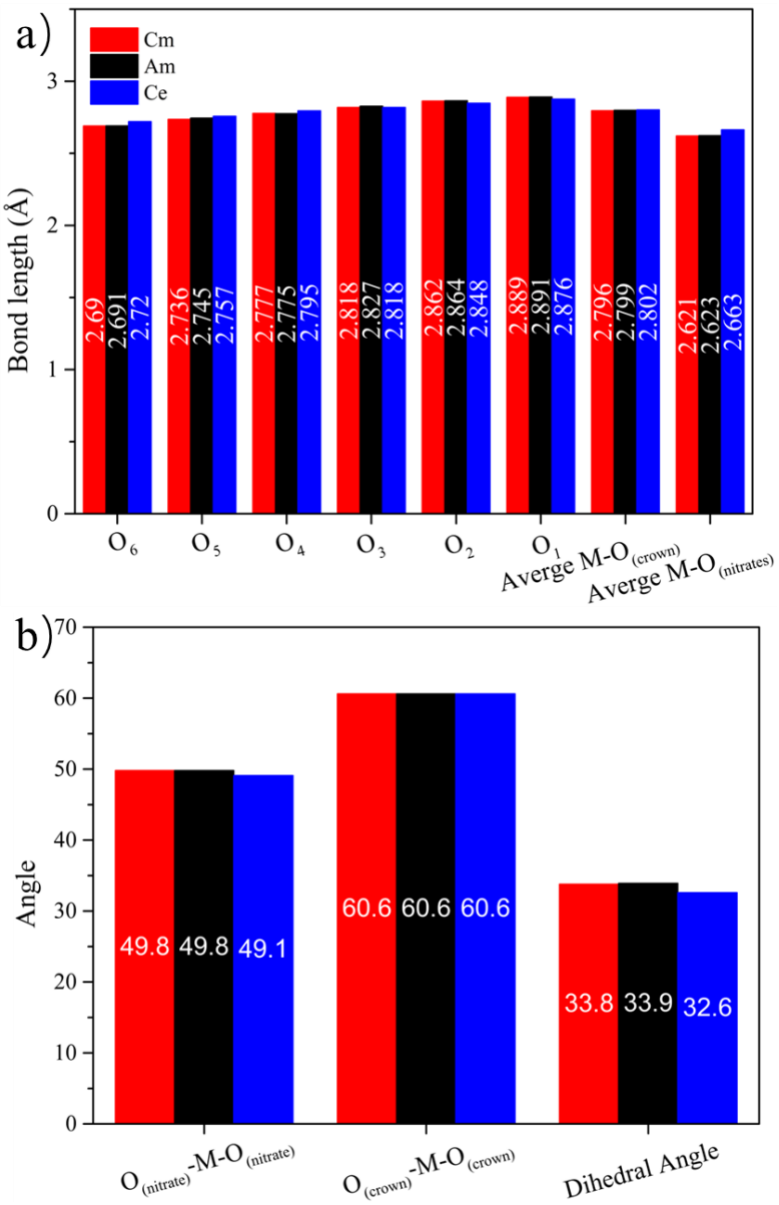

Figure 4-6. The molecular structure measurements, (a) bond length and (b) bond angles of americium/curium/cerium with oxygen in 18-crown-6 ether by using the VDW_DF2+U method. The dihedral angle is measured by the two planes: one is built by O_1, O_2, and O_5 atoms, while the other plane is O_2, O_3, and O_5 atoms. The M represents Ce, Am, and Cm.

To gain further insight into the binding behavior of cerium nitrates and crown ether, our investigation focused on exploring alternative substitutions for oxygen in the crown ether molecule; for the purpose of this analysis, it is not important whether these systems have been synthesized or not. To explore the effects of electronegativity, we

evaluated the impact of oxygen substitution by three other species: nitrogen, phosphorus, and sulfur, also shown in Figure 4-7.

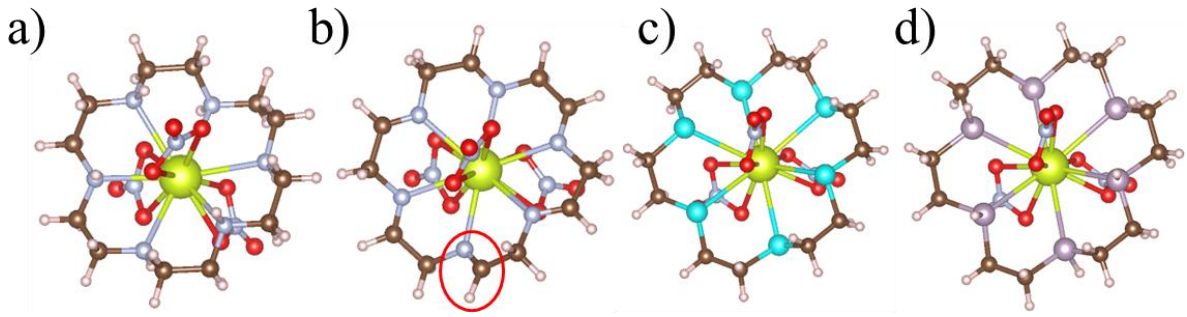

Figure 4-7. The optimized structure of cerium nitrate in a) amine-based, b) imine-based, c) sulfur-based, and d) phosphorus-based crown ether by using the VDW_DF2+U method. The cerium atom is in yellow, nitrogen in blue, carbon in brown, oxygen in red, phosphorus in purple, sulfur in cyan, and hydrogen in white.

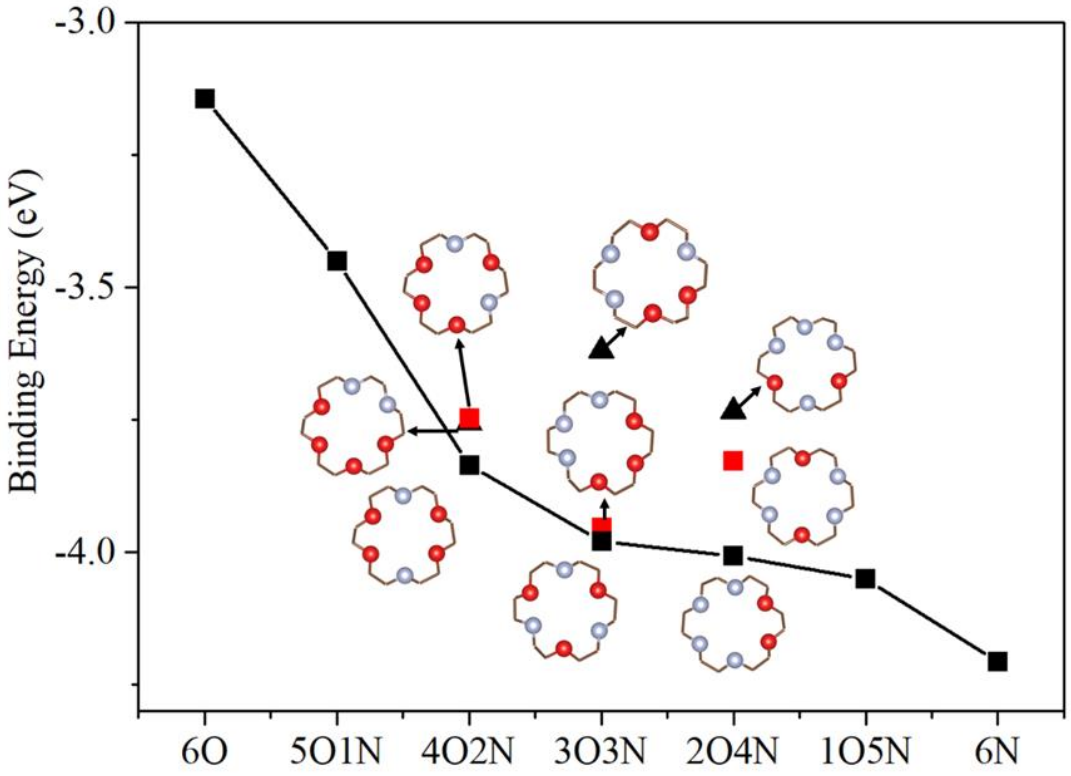

Figure 4-8. The binding energy of cerium nitrate increases as the number of oxygens substituted by the amine group in the crown ether by using the VDW_DF2+U method. The x-axis identifies the number of oxygens and amines in the crown ether ring.

To distinguish the difference substitution, the -O, -NH, -N, -S and -PH in the crown ether ring are dubbed oxygen-, amine-, imine-, sulfur-, and phosphorus-based crown ether. The imine-substituted crown ether exhibits a distinct characteristic compared to the amine-substituted case. This difference arises from the need to fulfill the coordination requirements of nitrogen and carbon atoms. To achieve this coordination, the -N(H)-C$(H)_2$- bond undergoes hydrogen removal, resulting in the formation of an -N=CH- bond. To ensure a physically reasonable structure of the crown ether, one hydrogen atom on the nitrogen of adjacent carbon is consequently removed. see the red circle in Fig. 4-7(b). Although the imine- and phosphorus- based crown ether have not yet been experimentally synthesized, we still consider their potential application to assess their energetic properties in binding cerium nitrates. It is important to note that the label imine-based crown ether may not be entirely chemically correct due to the presence of -N=C- double bonds; nevertheless, we use this nomenclature for the sake of simplicity. Our findings, as determined through the binding energy calculations in Table 4-9, indicate that amine/imine-substituted crown ethers exhibit higher binding energies than phosphorus and sulfur-based crown ethers. We find that the amine-substituted ether has the highest binding energy of all. Table 4-9 also shows the mean bond lengths, averaging over all six Ce-(NH/N/O/S/PH) $_{(crown)}$ bonds. The average bond lengths for phosphorus and sulfur are significantly longer than for the other three, consistent with the much lower binding energies. To understand the longer bond distance between these two crown ethers and cerium atom, we measure the mean diameters of the corresponding oxygen, nitrogen, sulfur, and phosphorus atoms along the diagonals in the pure crown ether, as shown in the third row of Table 4-9.

These calculations show that sulfur and phosphorus-based crown ethers have significantly larger diameters, indicating that the size of the crown ether rings is larger than that of amine-, imine-, and oxygen-based crown ethers. Indeed, this difference in crown ether ring size accounts for the longer distances observed between cerium and these two crown ethers.

Table 4-9. Comparison of binding energy and mean bond lengths of cerium with crown ether (CE), and mean diameters of corresponding pure crown ether by using the VDW_DF2+U method.

	Ce-NH_CE	Ce-N_CE	Ce-O_CE	Ce-S_CE	Ce-PH_CE
Binding Energy (eV)	-4.207	-3.681	-3.144	-2.620	-2.400
Mean bond length (Å)	2.878	2.782	2.803	3.300	3.253
Mean diameter (Å)	5.712	5.401	5.868	6.382	7.058

To understand the binding behavior in Table 4-9, charge density difference maps are shown in Figure 4-9. The charge density difference was determined by subtracting the charge density of the merged complex from that of the isolated cerium nitrate and crown ether at the same positions; if there were no interactions between the two, then the charge difference would be zero everywhere. The charge density difference maps clearly demonstrated the accumulation of charge between the cerium and crown ether atoms in all five systems. This indicated that, upon the encapsulation of cerium nitrates within the crown ether, electron sharing occurred between them. However, there were notable differences in the charge distribution patterns among the amine, imine, oxygen, sulfur, and phosphorus atoms. In the amine, imine, and oxygen-based crown ether cases (Figures 4-9(a)-4-9(c)), a similar and complex charge distribution was observed. On the NH/N/O atoms facing of the cerium side (see red

circle in Figures 4-9(a)-4-9(c)) there was a reduction in charge density, while on the opposite side, there was a back-donation of charge density. By contrast, in the sulfur case (Figure 4-9d) there was no evident charge density reduction on sulfur atoms facing the cerium side, but there was a reduction on the other side. Moreover, the amount of charge transfer in the sulfur case was lower than that observed in the amine-based crown ether. The charge transfer for the phosphorus case (Figure 4-9e) was even less than the sulfur case. Additionally, there was no back-donation observed on the other side. These differences in charge transfer are consistent with differences in binding energy, with the latter two cases exhibiting less negative binding energies.

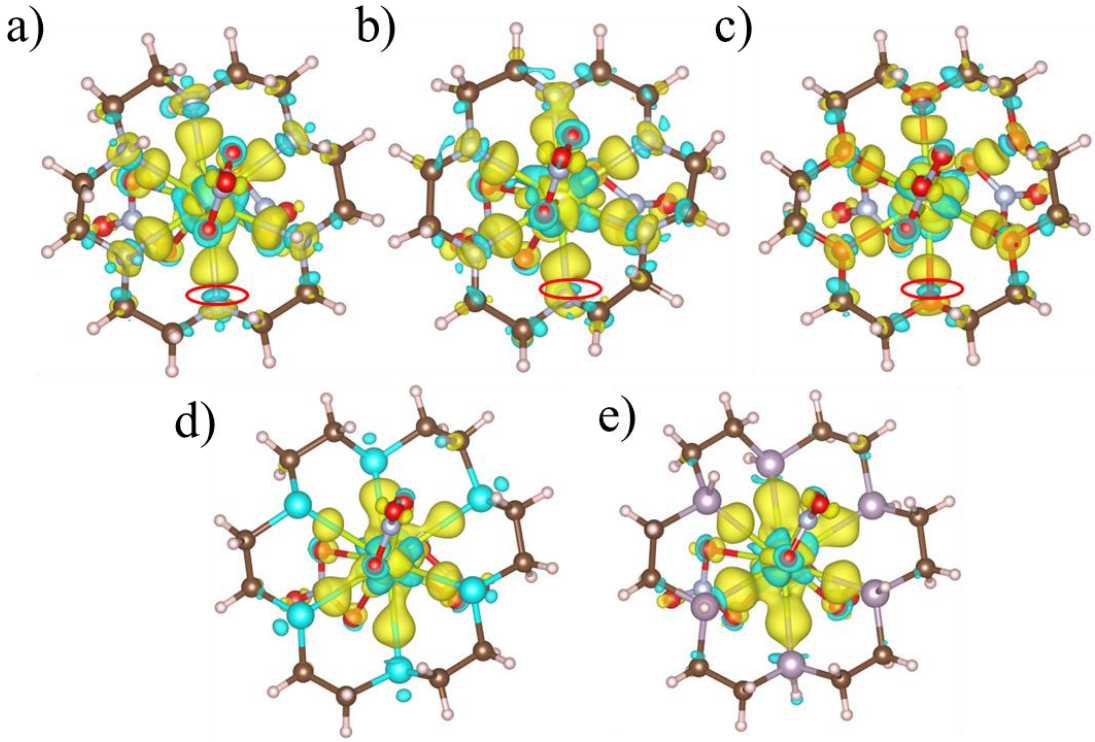

Figure 4-9. The charge density difference maps between cerium nitrate with a) amine-based, b) imine-based, c) oxygen-based, d) sulfur-based, and e) phosphorus-based crown ether by using VDW_DF2+U method. The yellow region means the charge density accumulation, and the cyan region means the charge density reduction. The surfaces shown correspond to electron isovalues of 0.004 e/Å^3.

4.4.2.2 The amine and imine-based crown ethers with actinide nitrates

Based on the results above, the N and NH-based crown ether have the strongest binding energies with cerium nitrate, and thus we focus on these two crown ethers with americium and curium nitrates. The optimized structures for the americium/curium nitrate are shown in Figure 4-10.

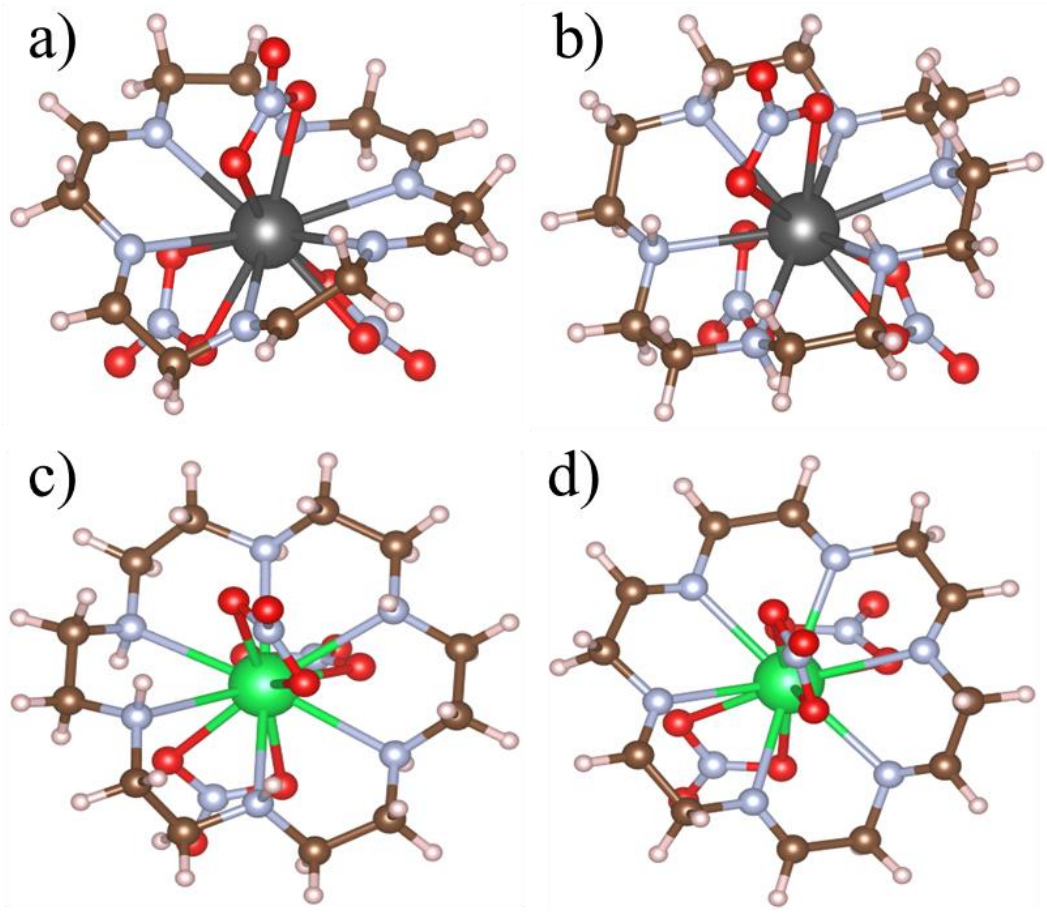

Figure 4-10. The top view of optimized structure of americium nitrate in a) amine-based crown ether and b) nitrogen-based crown ether, curium nitrate in c) amine-based crown ether and d) imine-based crown ether by using VDW_DF2+U method. The americium in black, curium in green, nitrogen in blue, carbon in brown, oxygen in red and hydrogen in white.

To quantify the clear differences in the structures, Table 4-10 presents the bond distances of Am-NH, Cm-NH, Am-N, and Cm-N, which were slightly longer than the Am-

O and Cm-O bond distances. However, despite the longer bond distances, as Table 4-11 shows, the binding of Am-NH and Cm-NH were -4.082 eV and -4.045 eV, which were about 0.5 eV more negative than those of Am-N and Cm-N. These values represented a substantial increase in binding compared to the pure oxygen-based crown ether: -2.99 eV and -2.94 eV, respectively. The magnetic moment is shown in Table 4-8.

Table 4-10. Bond lengths between americium/curium and nitrogen in the ether as determined by the VDW_DF2+U. Unit in Å.

Compounds		Bond lengths					
Am-N_6	2.777	Am-NH_6	2.839	Cm-N_6	2.771	Cm-NH_6	2.819
Am-N_5	2.698	Am-NH_5	2.815	Cm-N_5	2.699	Cm-NH_5	2.826
Am-N_4	2.769	Am-NH_4	2.877	Cm-N_4	2.760	Cm-NH_4	2.877
Am-N_3	2.795	Am-NH_3	2.875	Cm-N_3	2.786	Cm-NH_3	2.854
Am-N_2	2.728	Am-NH_2	2.799	Cm-N_2	2.732	Cm-NH_2	2.805
Am-N_1	2.802	Am-NH_1	2.998	Cm-N_1	2.791	Cm-NH_1	2.981

Table 4-11. Binding energy (in eV) between americium/curium nitrates in NH-crown ether (CE) and N-crown ether by using the VDW_DF2+U method.

Name	$Am(NO_3)_3$-NH_CE	$Cm(NO_3)_3$-NH_CE	$Am(NO_3)_3$-N_CE	$Cm(NO_3)_3$-N_CE
Binding Energy	-4.082	-4.045	-3.582	-3.557

4.4.2.3 Comparison of Charge Density Maps

To characterize the bonding of americium and curium nitrate in crown ether, we analyzed the charge density differences[123], in Figures 4-11 and 4-12. In the trajectory of the Am (Cm)-O/NH/N bond, a diminution in charge density was observed on both the oxygen/nitrogen and the americium (curium) atoms. Concurrently, an augmentation in charge density was noted interstitially between these atoms, signaling a charge transfer event between the two entities.

Furthermore, the charge accumulation associated with americium (curium) in conjunction with the imine/amine functional group in the imine/amine-modified crown

ether surpassed that observed between americium (curium) and oxygen atoms in the traditional oxygen-containing crown ether. The augmented electron observation in the amine/imine-functionalized ether aligns with the observation that the amine/imine-modified crown ether manifests an elevated binding energy. To quantify the charge transfer after the inclusion of americium (curium) nitrates in the crown ether, we employed Bader charge analysis[131, 132, 133, 134]. Table 4-12 shows that the NH-crown ether exhibits the highest amount of charge transfer, which is consistent with the highest binding energy.

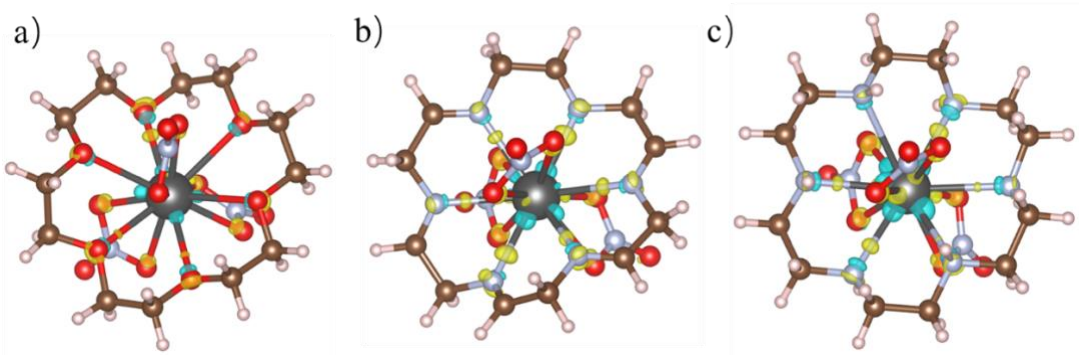

Figure 4-11. The charge density difference map of a) Am $(NO_3)_3$-O_CE, b) Am $(NO_3)_3$-N_CE and c) Am $(NO_3)_3$-NH_CE by using VDW_DF2+U method. The cyan area represents the charge density reduction, while the yellow represents the charge density accumulation. The electron isovalue is 0.01 e/Å^3.

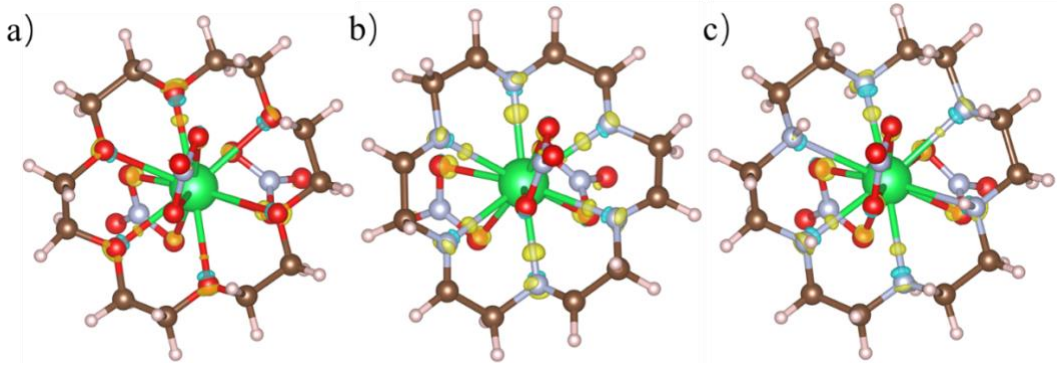

Figure 4-12. The charge density difference map of a) Cm $(NO_3)_3$-O_CE, b) Cm $(NO_3)_3$-N_CE and c) Cm $(NO_3)_3$-N(H)_CE by using vdw_DF2+U method. The cyan area represents the charge density reduction, while the yellow represents the charge density accumulation. The isovalue is 0.01 e/Å^3.

Table 4-12. Bader charges analysis for different compounds by using the VDW_DF2+U method.

Compounds	charge on actinide nitrates	charge on crown ether
$Am(NO_3)_3$-O_CE	-0.23	+0.23
$Am(NO_3)_3$-N_CE	-0.35	+0.35
$Am(NO_3)_3$-NH_CE	-0.40	+0.40
Cm $(NO_3)_3$-O_CE	-0.23	+0.23
Cm $(NO_3)_3$-N_CE	-0.36	+0.36
Cm $(NO_3)_3$-N(H)_CE	-0.40	+0.40

4.4.2.4 Electron localization function of nitrogen-based crown ether with actinide nitrites

To gain a deeper understanding of the bonding behavior between the actinide element and crown ether, we analyzed the electron localization function (ELF).[135] The ELF is a measure of the probability density of finding a pair of electrons with the same spin near a reference electron pair. It is related to the electron density and reflects the extent of electron localization in a system. In other words, it measures the tendency of electrons to localize in pairs, rather than spreading uniformly throughout the molecule. Thus, the ELF is a useful tool to characterize the bond behavior as a primary bonding (metallic, ionic, and covalent) or secondary bonding (van der Waal bonding). Specifically, Koumpouras[136] *et al.* reported the electron localization function (ELF) as a scalar function with values ranging from 0 to 1; when ELF is greater than 0.7, electrons are considered to be localized and can be found in the core, covalent bonding, or lone pair regions. When ELF is between 0.7 and 0.2, electrons can be electron-gas or typically found in metallic bonds. When ELF is less than 0.2, the electrons are considered to be delocalized and involved in non-covalent bonds.

As shown in Figures 4-13 to 4-16 below, a plane was constructed through two nitrogen atoms denoted by red circles and the americium (curium) atom. The resulting visualization indicates the presence of an indigo-hued region of low electron localization

between the nitrogen and americium atoms; the ELF value in these regions was less than 0.2, which is suggestive of a non-covalent bond between them. To make interpretation of the ELF easier, this was converted into a linear profile (as shown in Figures 4-17 and 4-20). Only the ELF values of americium (curium) with different nitrogen atoms in the crown ether are presented, as they indicated the interaction between these atoms.; the curves were shown very similar. The analysis revealed notable differences in the ELF between the nitrogen and americium (curium) regions. The high ELF values observed on the nitrogen side indicate strong electron localization. In contrast, the ELF values around 0.5 on the americium (curium) side indicated a tendency towards electron gas-like behavior. Moreover, the non-zero ELF value (0.05) at the minimum point of two curves[136] suggested the presence of van der Waals (vdW) bonding between americium (curium) and crown ether, as the minimum ELF value for ionic bonding is typically even close to zero (less than 0.01).[136] In short, this observation suggested that the interaction between the actinide and crown ether is primarily driven by the long-range dispersion force.

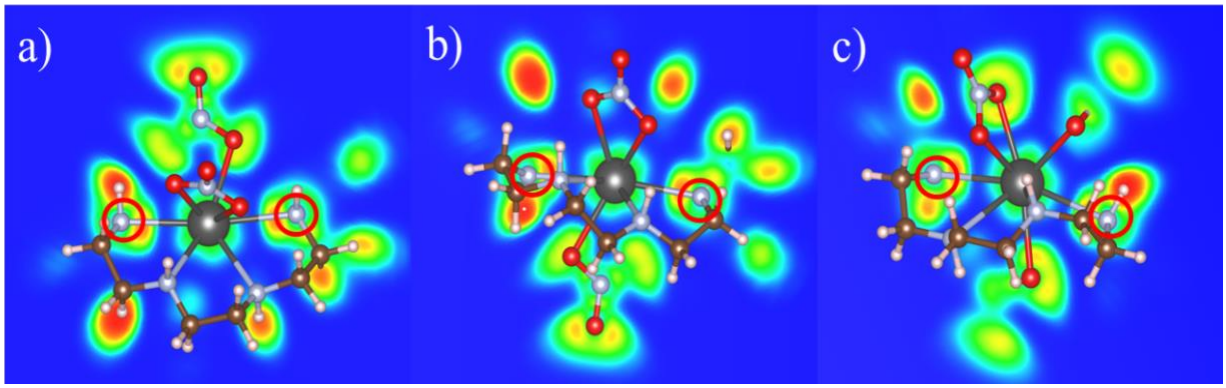

Figure 4-13. The 2D plane of electron localized function is built by a) N1-Am-N6, b) N2-Am-N5 and c) N3-Am-N4 of americium nitrate in amine-based crown ether. The red circle denotes the two nitrogen that is used for building the plane.

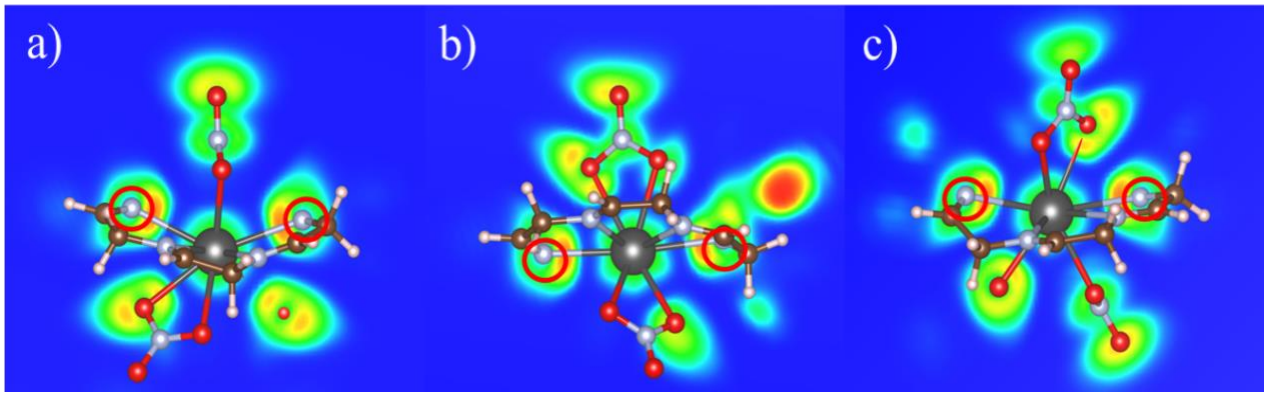

Figure 4-14. The 2D plane of electron localized function is built by a) N1-Am-N6, b) N2-Am-N5 and c) N3-Am-N4 of americium nitrate in nitrogen-based crown ether.

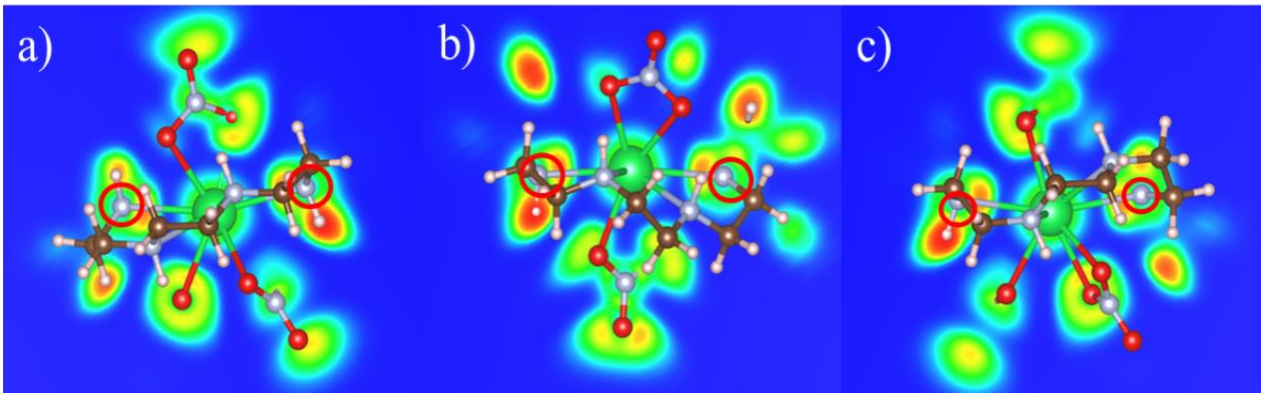

Figure 4-15. The 2D plane of electron localized function is built by a) N1-Cm-N6, b) N2-Cm-N5 and c) N3-Cm-N4 of curium nitrate in amine-based crown ether.

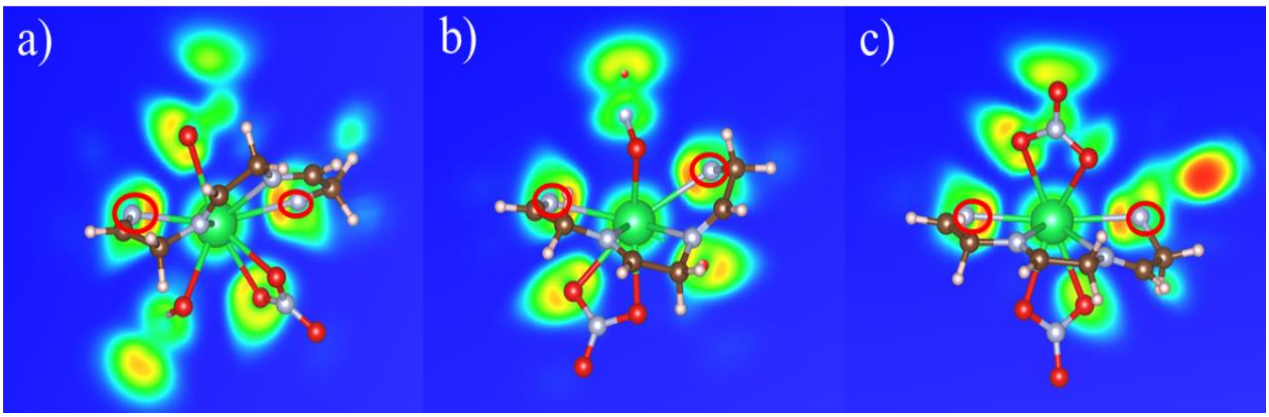

Figure 4-16. The 2D plane of electron localized function is built by a) N1-Cm-N6, b) N2-Cm-N5 and c) N3-Cm-N4 of curium nitrate in nitrogen-based crown ether.

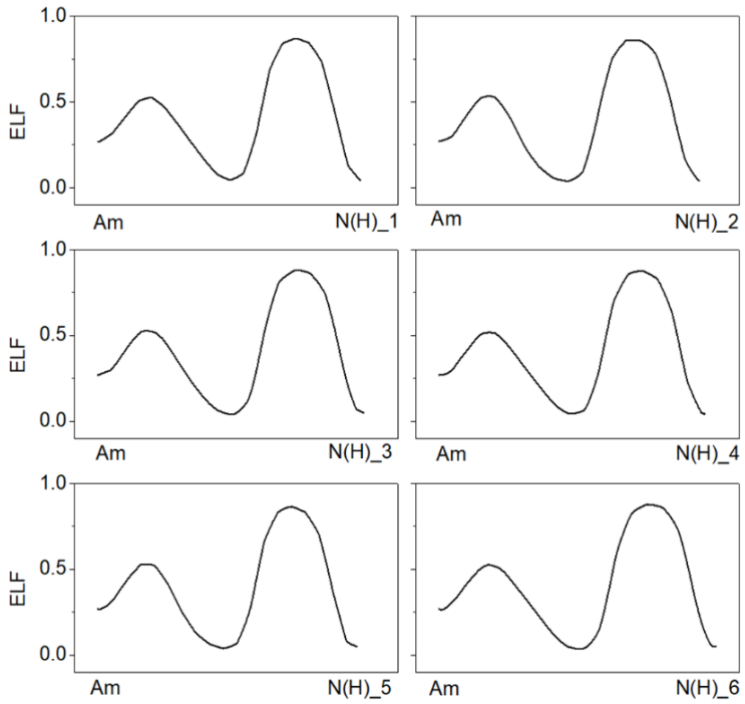

Figure 4-17. The 1D linear profile electron localized function from americium to different nitrogen of americium nitrate in amine-based crown ether.

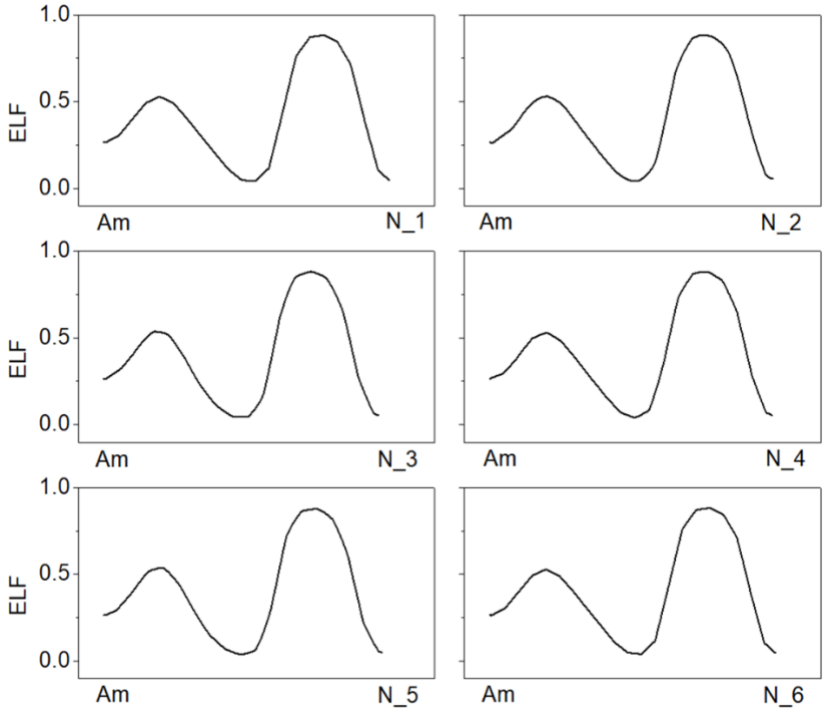

Figure 4-18. The 1D linear profile electron localized function from americium to different nitrogen of americium nitrate in nitrogen-based crown ether.

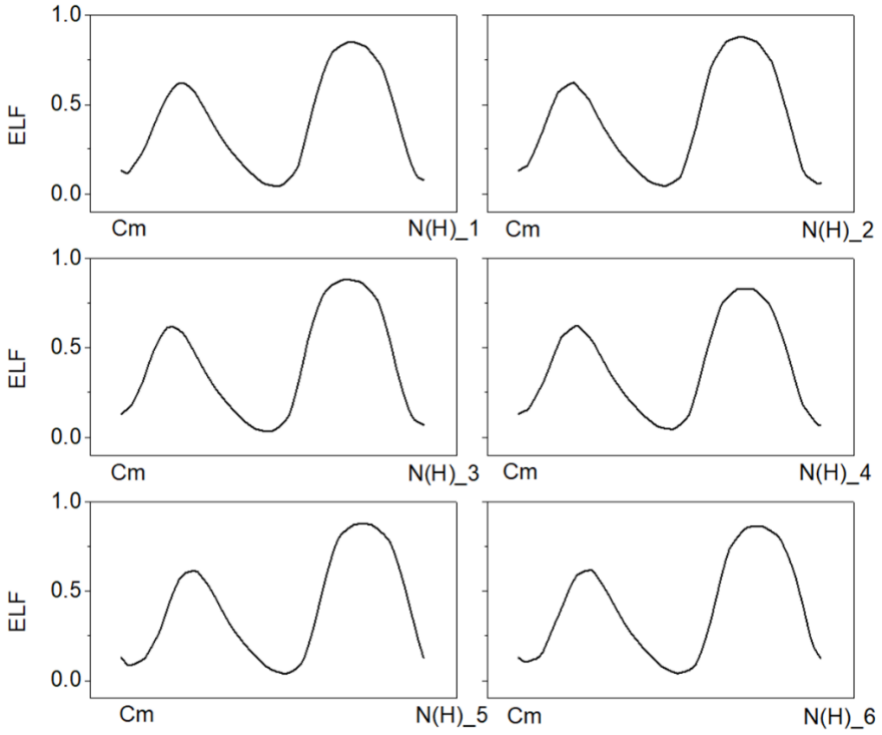

Figure 4-19. The 1D linear profile electron localized function from curium to different nitrogen of curium nitrate in amine-based crown ether.

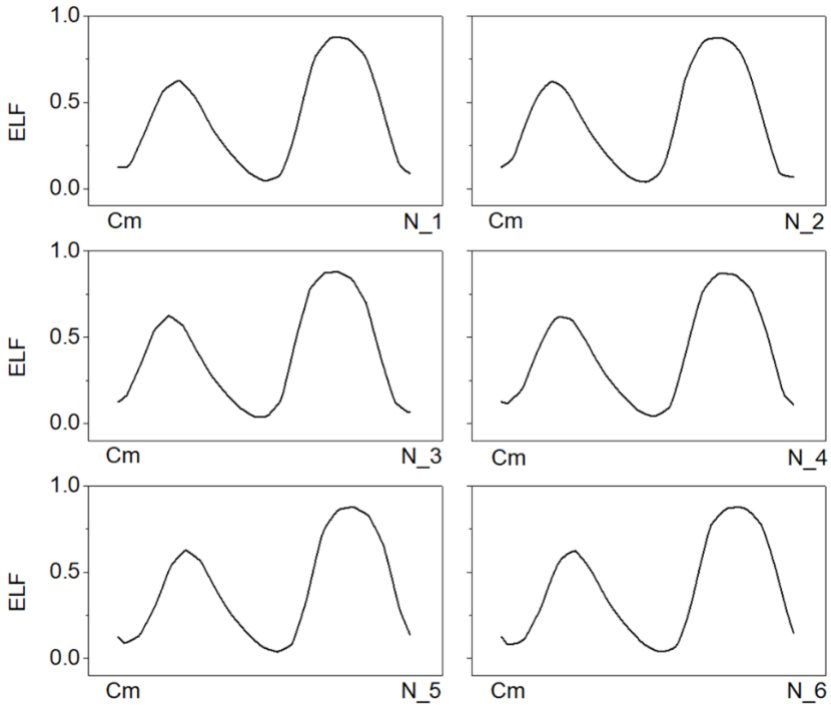

Figure 4-20. The 1D linear profile electron localized function from curium to different nitrogen of curium nitrate in nitrogen-based crown ether.

4.4.2.5 Solvation Effect

In Table 4-3, we benchmarked our simulation of the intact molecule, cerium nitrate, within the oxygen-based crown ether against the experimental crystal molecular structure. However, it is also essential to consider the effect of dissolution of the molecules to calculate the binding energy because the extraction of cations usually occurs in an aqueous environment. [113] Since cerium/americium/curium nitrates are also water-soluble, the coordination of actinide cations are dynamic in an aqueous environment. They can exist as bare cations, coordinate with water molecules, associate with nitrates, or even form a mixture of both water and nitrates. Consequently, we considered three reference conditions: bare actinide cations, actinide cation-water clusters, and intact actinide nitrates. It is known that the coordination number of Am^{3+} with water is nine[137],[138] and Cm^{3+} varies between eight and nine water molecules;[139] we consistently used nine for uniformity. When these actinide-water complexes were positioned within the crown ether's cavity, the six-fold crown ether occupied six of the actinide cation's coordination sites. The three remaining coordination sites of the actinide cation were occupied by three water molecules: one situated above the crown ether plane and the other two positioned below it. In addition to this explicit treatment of the water in the first solvation cell, the more distant effects of the water medium were accounted for using an implicit solvation model.

Table 4-13 showed the effects of solvation of americium (III) and curium (III) cations as determined using VASPsol.[33,34] There are several points to highlight. First, for the oxygen-based crown ethers, both actinide cations hydrated implicitly only and actinide ions with the first neighbor shell treated explicitly in addition, yield binding energies within ~0.04eV of each other for both Am (-0.496 and -0.460 eV) and Cm (-

0.433 and -0.396 V). This is an important consistency between the methods and gives confidence in these results. Indeed, they are consistent with experimental data, which lie in the range of is -0.2 to -0.5 eV,[140,141] The level of agreement between the methods is also very good for the imines: -1.651 and -1.607 eV for Am and -1.598 and -1.544 for Cm.

However, there are larger differences in binding energy emerged with amine-crown ethers. -2.030 eV vs -1.763 eV for Am and -1.954 and -1.683 eV for Cm. Despite being larger than for the imine and oxygen cases, these still point to the robustness of these calculations. Since the model with explicit as well as implicit hydration embeds more of the physics of the real system,[142] we can consider these to be the most reliable.

Table 4-13. Binding energy (in eV) of Am^{3+}/Cm^{3+} cations and $Am^{3+}(H_2O)_9$/$Cm^{3+}(H_2O)_9$ complexes in oxygen-, imine-, and amine-based crown ether using the VASPsol method.

	X^{3+}-O_CE		**X^{3+}-N_CE**		**X^{3+}-NH_CE**	
	X=Am	X=Cm	X=Am	X=Cm	X=Am	X=Cm
Implicit	-0.496	-0.433	-1.651	-1.598	-2.030	-1.954
Expilcit+Implicit	-0.460	-0.396	-1.607	-1.544	-1.763	-1.683

When we assessed the binding energies using the actinide nitrates reference, they were more negative compared to those of the bare cations and the actinide-water clusters, as shown in Table 4-14 below. Considering the dynamic coordination of actinide cations mentioned above and the presence of a water solvent, it is improbable that three nitrates would anchor to the actinide cations simultaneously. As such, we considered the results from actinide nitrates as an upper limit of magnitude of the binding energy.

Moreover, considering solvation effects, the binding energy difference between NH- and N-based crown ether decreased, dropping from approximately 0.5 eV in a vacuum in Table 4-11 to 0.3 eV in an aqueous environment. This variation was due to

the N-based crown ether's more negative solvation energy of -0.769 eV than the NH-based crown ether's -0.298 eV. This indicated that the N-based crown ether is more hydrophilic than the NH-based variant.

Table 4-14. Binding energy (in eV) of $Am(NO_3)_3$/$Cm(NO_3)_3$ complexes in oxygen-, imine-, and amine-based crown ether using the VASPsol method.

	X^{3+}-O_CE		**X^{3+}-N_CE**		**X^{3+}-NH_CE**	
	X=Am	X=Cm	X=Am	X=Cm	X=Am	X=Cm
Actinide-nitrates+Implicit	-1.561	-1.534	-2.534	-2.518	-2.818	-2.790

In Section 3.1.2, our calculations showed that the binding energies of cerium/americium/curium nitrates within oxygen-based crown ether were approximately -3 eV in vacuum. Additionally, we further calculated the bare Am^{3+} and Cm^{3+} cations in the oxygen-based crown ether in vacuum, the binding energy were -19.910 eV and -19.841 eV, respectively. Based on the above results these vacuum results are clearly a very large overestimate of the binding strength in aqueous conditions. For instance, in the case of Am, the binding energies in implicit solvation model for bare cations, americium-water clusters, and americium nitrates were -0.496 eV, -0.460 eV, and -1.561 eV, respectively as compared to the vacuum value of -2.990 eV. Thus, consideration of the solvation effect was crucial when calculating the binding energy of an actinide cation inside the crown ether cavity.

Finally, even though the binding energies were different for the different levels of analysis, the trends remain consistent: NH-crown ether had the highest binding energy, followed by N-crown ether, with O-crown ether exhibiting the lowest binding energy. These trends aligned with the energy trends observed in vacuum cases and do not change our primary conclusions.

4.5 Conclusions

Our results indicated that GGA+U[25] and VDW_DF2+U[32,122] methods yielded good agreement with experimental data for the structure of the cerium nitrate/crown ether system. However, the use of the VDW_DF2 method revealed a more negative binding energy, indicating the significant contribution of van der Waals interactions in the interaction between cerium nitrate and crown ether. The analysis of the electron localization function (ELF)[135] further supported this finding, as it demonstrated non-sharing bond behavior because of the presence of non-zero ELF,[136] characteristics of van der Waals interactions. As such, the VDW_DF2 method was deemed the most suitable for calculating the binding energy, especially given the unavailability of DFT_D3[31,76] for transuranic elements. After verifying the accuracy of our calculations for cerium nitrate binding, we extended our calculations to include americium and curium nitrates within the crown ether, thereby gaining a deeper understanding of the interactions involving actinide species within crown ether. Furthermore, when considering the solvation effect using VASPsol,[33,34] an implicit solvation model, the binding energy of the crown ether with actinide nitrates was less negative than in the vacuum calculation. However, the binding energy remained negative, indicating that the process of the crown ether capturing actinide nitrates was thermodynamically favorable.

Additionally, the comparable binding energies observed for cerium, americium, and curium nitrate complexes with the 18-crown-6 ether, along with the similarity in their corresponding charge density difference maps, provided strong evidence supporting the notion that cerium nitrates could serve as suitable surrogates for americium and curium nitrates. These findings suggested that the behavior and properties of cerium in complexation with the crown ether closely resembled those of americium and curium.

Furthermore, we explored the impact of amine substitution for oxygen in the crown ether ring and observed a correlation between the number of amine groups in the ring and the resulting binding energy. We also explored the substitution of oxygen with imine, sulfur, and phosphorus. Our calculations revealed that the substitution of amine and imine resulted in the highest binding energy. This can be attributed to the significant charge transfer observed between the nitrogen atoms and the actinide atoms, as revealed by the charge density difference map. In contrast, the substitution of oxygen, sulfur, and phosphorus showed comparatively less charge transfer with the actinide atoms. Consequently, we suggested that imine/amine-based crown ether could efficiently trap actinide nitrates and thus provide a new ligand option for the MOF to capture radionuclide species.

We began with the scenario in which the nitrate groups remain attached to the metallic ions, aligning our findings with experimental studies on crown ether molecular structures.[129] However, to describe aqueous conditions,[113] it was also essential to account for solvation effects. We examined this influence using three references: bare cations, actinide-water clusters, and actinide nitrates, utilizing VASPsol[33],[34] as our implicit solvation model. In each case, the binding energies between the crown ether and actinide cations were less negative compared to the values from vacuum calculations. This suggested that the vacuum calculations of the molecular systems overestimate the binding energy, indicating the importance of considering solvation effects in such assessments.

In the future, we propose further investigations into modifying other crown ethers, which was reported by the work of George et al.,[143] by substituting oxygen atoms with

nitrogen. This exploration, coupled with the design of novel metal-organic frameworks via experimental work to incorporate these modified crown ethers, holds promise for increasing the capacity of MOFs in capturing and sequestering radionuclide waste. By combining computational insights with experimental efforts, we can contribute to the development of more efficient and sustainable approaches for the remediation of actinide-contaminated environments.

CHAPTER 5
ADDITIONAL STRATEGIES FOR THE SEQUESTRATION OF RADIONUCLIDES FROM DENSITY FUNCTIONAL THEORY‡

5.1 Background

In this chapter, we present results of our collaborative approach, blending experiments with computational simulations. Here, the primary focus here will be on the computational aspects, with relevant experimental findings will be introduced as needed.

In earlier chapters, we delved into the intricacies of using metal nodes and organic ligands within MOFs as a strategy for nuclear waste containment. Both demonstrated significant promise in achieving this goal. This chapter looks at how the transmetallation process, which involves substituting one type of metal atoms for another, can enhance the framework's properties. In our work, we will explore two distinct transmetallation processes: first, the substitution of Zr-Based MOFs with Th-MOFs. and second, the replacement of U-Based MOFs with either Th-MOFs or Pu-MOFs. This presents a novel method for the sequestration of plutonium cations.

5.2 Computational Methods

All of the density functional theory (DFT) calculations used the same functionals and setting as used in Chapter 4. To remain consistent in our comparisons, the 5f state of the uranium, plutonium, and thorium atoms was described by the DFT+U method,[72] with effective Hubbard U parameters of 4.0 eV,[144] 4.5 eV[145] and 6 eV[146] respectively,

‡ This part of work has been published in Park, K. C.; Kittikhunnatham, P.; Lim, J.; Thaggard, G. C.; Liu, Y.; Martin, C. R.; Leith, G. A.; Toler, D. J.; Ta, A. T.; Birkner, N.; Lehman‐Andino, I.; Hernandez‐Jimenez, A.; Morrison, G.; Amoroso, J. W.; zur Loye, H.; DiPrete, D. P.; Smith, M. D.; Brinkman, K. S.; Phillpot, S. R.; Shustova, N. B. F‐Block MOFs: A Pathway to Heterometallic Transuranics. *Angew. Chemie Int. Ed.* 2023, *62* (5).

which are suitable values to guarantee electron localization. The number of valence electrons present in the pseudopotentials used is: 12 for zirconium ($4s^2 5s^2 4p^6 4d^2$), 14 for uranium ($6s^2 6p^6 5f^2 7s^2 6d^2$), 16 for plutonium ($6s^2 6p^6 5f^4 7s^2 6d^2$), 12 for thorium ($6s^2 6p^6 5f^1 7s^2 6d^1$), six for oxygen ($2s^2 2p^4$), and four for carbon ($2s^2 2p^2$). To account for solvent effects, the solvation behavior of U-Me_2BPDC-8 and Th-Me_2BPDC-8 metal nodes was implicitly modeled with VASPsol.[77,78] In VASPsol, the bulk dielectric constant is set to 80, the width of the dielectric cavity is 0.6, the cutoff charge density is 0.0025 $Å^{-3}$, and a surface tension parameter is 0.525 meV/$Å^2$.

Proton dissociation energies were also assessed for U-Me_2BPDC-8 and Th-Me_2BPDC-8 nodes. Specifically, our methods followed those reported by Ho *et al.*[147] and were performed via the Gaussian16[148] software package. Calculations used either the CRENBL or the Stuttgart effective core potentials to model uranium and thorium.[149,150] To ensure consistency between the two potentials, the relativistic large core (RLC) effective pseudopotential, MWB78, was used for uranium and thorium,[150,151] and also in the Stuttgart potential. The MWB means that multi-electron fit quasi-relativistic, and 78 means there are 78 core electrons. Thus, there are 14 and 12 valence electrons in uranium and thorium, respectively. The 6-31G** basis set[149] was used for the C, O, and H atoms, while the B3LYP[152] level of approach was used in all DFT calculations.

5.3 MOF Secondary Unit Buildings (SBUs) Structures

In Figure 5-1, we present a standard MOF-SBU. Depending on the number of organic ligands associated, these can be categorized into MOF-8, MOF-10, and MOF-12. For the current purposes, the default MOF-SBU referred to is MOF-8, with MOF-10 and MOF-12 being explicitly mentioned as required. In MOF-8, the metal atoms at the

top and bottom are coordinated to eight oxygen atoms each, whereas those on the equatorial plane are coordinated to six oxygen atoms. Conversely, for MOF-10 and MOF-12, metal atoms are coordinated to seven and eight oxygen atoms, respectively.

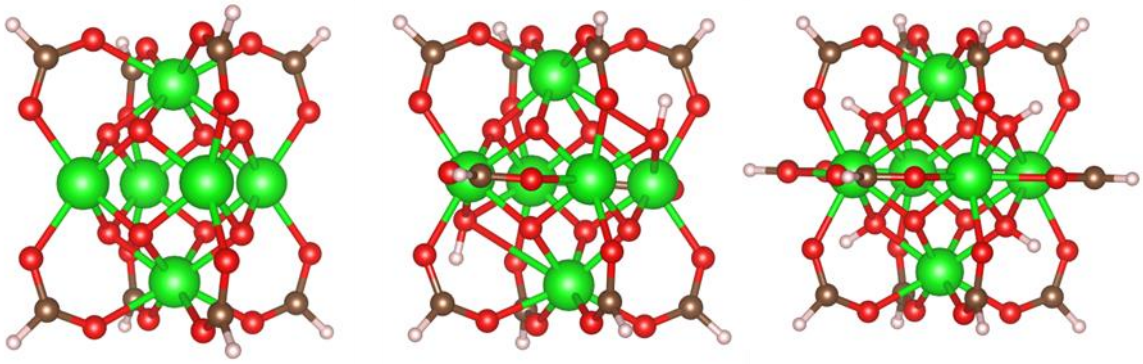

Figure 5-1. Schematic representation of MOF-SBU structures. From left to right: MOF-8, MOF-10, and MOF-12. For clarity, organic ligands are represented by hydrogen atoms. Color coding: metal atoms in green, oxygen in red, carbon in brown, and hydrogen in white.

5.4 Results

5.4.1 Formation Energy of Zr- and Th-Based SBUs

As highlighted in Chapter 3, Zr-based MOFs have been proposed as candidates for radionuclide sequestration. Building on this idea, we explore the potential of MOFs based on elements other than zirconium. Consequently, substituting Zr with Th in MOFs presents an alternative method for sequestering actinide ions. However, the stability of Th-based MOFs remains uncertain. In this section, we aim to compare the stability of Th- and Zr-based MOFs. Given existing literature reports[153,154] attesting to the stability of Zr-MOFs at room temperature, our focus will be on the stability of Th-MOFs. Specifically, we will calculate the formation energy of SBU units. If the formation energy for Th-MOFs is more negative than that of Zr-MOFs, it suggests that synthesizing Th-

MOFs is thermodynamically favorable. The equation used to determine formation energy was defined as:

$$E_f = E_{total} - a * \mu_M - b * \mu_O - c * \mu_C - d * \mu_H \quad (5\text{-}1)$$

Here, E_f is the formation energy, E_{total} is the total energy of Zr-/Th-SBU from DFT results, a is the number of Zr/Th atoms in SBU, μ_M is the Zr/Th chemical potential, b is the number of oxygens, μ_O is the oxygen chemical potential, c is the number of carbons, μ_C is the carbon chemical potential, d is the number of hydrogens and μ_H is the hydrogen chemical potential. All of the chemical potential data came from the work of Kirklin *et al*.[155] The results of formation energies with different coordination SBUs are shown in Table 5-1

Table 5-1. The formation energy of Zr-/Th- SBU with different coordinations, unit in eV.

Coordination	Zr-SBU	Th-SBU
8	-94.86	-97.79
10	-108.32	-111.96
12	-120.80	-125.50

Table 5-1 demonstrates that, irrespective of the SBU coordination, Th-SBU consistently has a lower formation energy compared to Zr-SBU. This finding emphasizes the inherent stability advantage of Th-SBU over its Zr counterpart. Nevertheless, understanding the influence of the organic ligand is crucial. For a more comprehensive insight, we simulated the SBU in tandem with the organic ligand. Figure 5-2 depicts the specific MOF-12 structure, where each metal node is connected to 12 organic ligands, which in turn link to other metal nodes. In the MOF-12 coordination, we introduced the phenyl functional group in two scenarios: one with a single phenyl group and the other with two. The consequent formation energy findings are tabulated in Table 5-2. Reinforcing our initial observations from Table 5-1, the data from Table 5-2 bolsters

our hypothesis about the superior stability of Th-SBU. All of those data demonstrate that the Th-MOF exhibits greater stability compared to the Zr-MOF.

Table 5-2. The formation energy of Zr-/Th- SBU-12 with different numbers of additional phenyl functional groups, unit in eV.

Coordination	One phenyl functional group	Two phenyls functional groups
Zr-SBU-12	-184.83	-189.73
Th-SBU-12	-189.64	-194.69

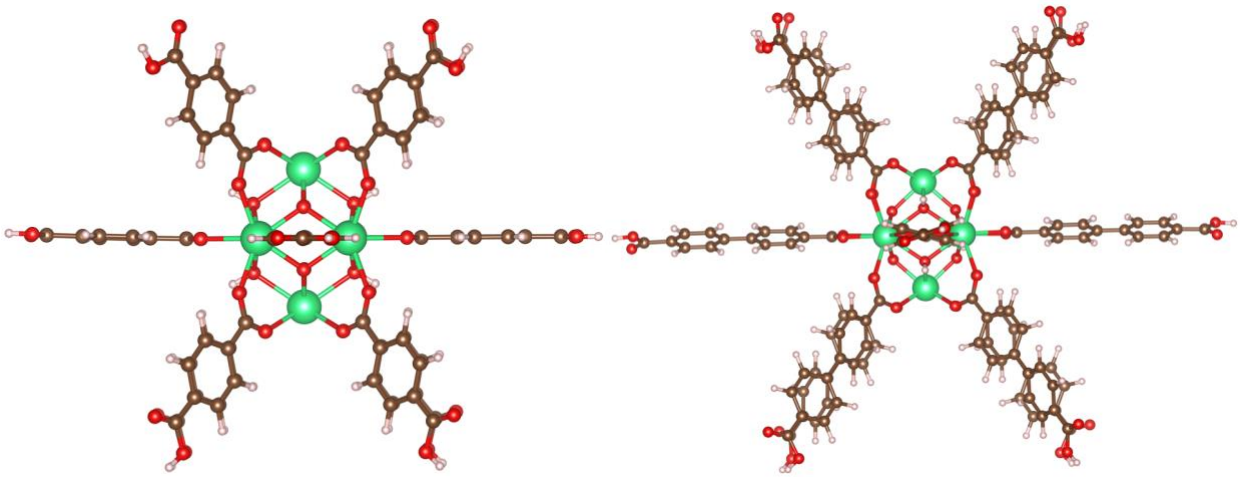

Figure 5-2. The Zr-/Th-SBU-12 with one additional phenyl functional group (left) and two additional phenyls functional groups (right).

5.4.2 Formation Energy of Transmetallation U-SBUs to Th-SBUs

In the last section, we established the stability of Th-SBUs by comparing their formation energies with those of the corresponding Zr-based MOFs. In this section, we present alternative methods for synthesizing Th-MOFs, specifically through the transmetallation process involving U-SBU. Initially, we calculated the formation energy of SBU based on the number of uranium atoms replaced by thorium. The equation used to determine formation energy was defined as:

$$E_f = E_{SBU} - (6-n) * \mu_{Th} - n * \mu_U - 8 * \mu_C - 24 * \mu_O - 8 * \mu_H \quad (5\text{-}2)$$

where E_{SBU} is the total energy of the MOF-SBU cluster, *n* is the number of uranium atoms in the MOF-SBU, the chemical potential source is the same as from the last section 5.4.1.

In Table 5-3, we have detailed the formation energies associated with the heterometallic MOF-SBUs represented by the formula ($An_6O_8(COOH)_8$). A distinct pattern emerges: as we replace uranium atoms with thorium within the structure, the formation energy tends to shift to a more negative value. This shift in energy is significant because not only does it underline the thermodynamic favorability of incorporating thorium into the structure, but it also suggests that initiating the synthesis of Th-MOFs from U-MOFs base could be a viable strategy. This opens up a potential avenue for the effective sequestration of thorium elements, especially considering the growing interest in harnessing thorium for various nuclear applications.

Table 5-3. The formation energy of each MOF-SBU cluster.

Composition	E_{form} (eV)
U_6-8	-70.41
U_5Th_1-8	-73.04
U_4Th_2-8	-75.67
U_3Th_3-8	-77.84
U_2Th_4-8	-80.01
U_1Th_5-8	-82.06
Th_6-8	-84.33

5.4.3 Estimating Enthalpy of the Transmetallation reaction of U-SBUs to Th-SBUs

It is important to compare our computer-based findings with actual experiments. While there are not any experimental data on formation energy of Th-MOFs, there are experimental results on the energy changes when uranium is replaced by thorium. So, we should focus on calculating this energy change and comparing it to these experimental values. In experiments, the reaction takes place in a solvation

environment, the following equation (5-13) shown below is the reaction describe it overall transmetallation process:

$$U_6\text{-}8_{(s)} + nTh(Cl)_{4,(s)} + \frac{1}{2}nO_{2,(g)} + nH_2O_{(l)} \rightarrow U_{6-n}Th_n\text{-}8_{(s)} + nUO_2Cl_{2,(aq)} + 2nHCl_{(aq)} \quad (5\text{-}3)$$

The transmetallation energy equation is then defined as,

$$\Delta E_{trans} = \sum E_{products} - \sum E_{\text{reactants}} \quad (5\text{-}4)$$

where the ΔE_{trans} is the transmetallation energy, the $\sum E_{\text{reactants}}$ is sum up the total energy of reactants and $\sum E_{products}$ is the sum up of the total energy of products. However, VASP cannot explicitly account for solvent effects directly and, in turn, cannot calculate the total energies of aqueous species such as UO_2Cl_2 and HCl. Due to computational constraints, simulating this exact scenario is quite challenging. We first consider the calculation therefore in the easier way. Conventionally, the reaction is calculated under a vacuum environment and the reaction is more specifically,

$$U_6\text{-}8_{(g)} + nTh(Cl)_{4,(g)} + \frac{1}{2}nO_{2,(g)} + nH_2O_{(g)} \rightarrow U_{6-n}Th_n\text{-}8_{(g)} + nUO_2Cl_{2,(g)} + 2nHCl_{(g)} \quad (5\text{-}5)$$

Based on the above reaction, the transmetallation energy, ΔE_1, is then

$$\Delta E_1 = E_{U_{6-n}Th_n\text{-}8_{(g)}} + n\,E_{UO_2Cl_{2,(g)}} + 2n\,E_{HCl_{(g)}} - E_{U_6\text{-}8_{(g)}} - n\,E_{Th(Cl)_{4,(g)}} - \frac{1}{2}n\,E_{O_{2,(g)}} - n\,E_{H_2O_{(g)}} \quad (5\text{-}6)$$

where $E_{U_{6-n}Th_n\text{-}8_{(g)}}$ is the total energy of substituted actinide-MOF SBU, $E_{UO_2Cl_{2,(g)}}$ is the total energy of the gas state of UO_2Cl_2, $E_{HCl_{(g)}}$ is the total energy of the gas state of HCl, $E_{U_6\text{-}8_{(g)}}$ is the total energy of uranium SBU, $E_{Th(Cl)_{4,(g)}}$ is the total

energy of gas state $Th(Cl)_4$, $E_{O_2,(g)}$ is the total energy of oxygen gas, $E_{H_2O_{(g)}}$ is the total energy of water gas, and *n* is the number of the uranium is replaced by the thorium.

To account for the effects of water solvent, an implicit model was implemented using VASPsol. Because UO_2Cl_2 and HCl are present in reaction (5-3) as aqueous species, their gaseous components from reaction (5-5) will be represented by their respective ionic counterparts.

$$UO_2Cl_{2,(g)} \rightarrow UO_{2,(aq)}^{2+} + 2\ Cl_{(aq)}^{-} \tag{5-7}$$

$$HCl_{(g)} \rightarrow\ H_{(aq)}^{+} +\ Cl_{(aq)}^{-} \tag{5-8}$$

Physically these ionic species should also be coordinated with water molecules. Experimentally, UO_2^{2+} have been shown to be solvated with five water molecules,[156] Cl^- have been reported to be solvated with a range of 5-7 water molecules,[157] and H^+ is known to be solvated by four water molecules.[158] Therefore, to improve the calculation accuracy, an explicit number of waters were coordinated to model the first solvation shell of each ion in addition to being optimized with VASPsol. These explicit solvation spheres are illustrated with the following reactions,

$$UO_{2,(aq)}^{2+} +\ 5\ H_2O_{(l)} \rightarrow UO_2^{2+} \cdot (H_2O)_{5,(aq)} \tag{5-9}$$

$$Cl_{(aq)}^{-} +\ z\ H_2O_{(l)} \rightarrow\ Cl^- \cdot (H_2O)_{z,(aq)} \tag{5-10}$$

$$H_{(aq)}^{+} +\ 4\ H_2O_{(l)} \rightarrow H^+ \cdot (H_2O)_{4,(aq)} \tag{5-11}$$

Collectively, the above reactions (5-9), (5-10), and (5-11) models the UO_2Cl_2 solvation reaction and can be rewritten by the following,

$$UO_2Cl_{2,(g)} + 5\ H_2O_{(l)}\ + 2z\ H_2O_{(l)} \rightarrow UO_2^{2+} \cdot (H_2O)_{5,(aq)} + 2\ Cl^- \cdot (H_2O)_{z,(aq)} \tag{5-12}$$

which gives the following solvation energy of $UO_2Cl_{2,(g)}$, ΔE_2,

$$\Delta E_2 = E_{UO_2^{2+}\cdot(H_2O)_{5,(aq)}} + 2\,E_{Cl^-\cdot(H_2O)_{z,(aq)}} - E_{UO_2Cl_{2,(g)}} - E_{(H_2O)_{5,(l)}} - 2\,E_{(H_2O)_z,(l)} \quad (5\text{-}13)$$

where $E_{UO_2^{2+}\cdot(H_2O)_{5,(aq)}}$ is the total energy of $UO_2^{2+}\cdot(H_2O)_{5,(aq)}$, $E_{Cl^-\cdot(H_2O)_{z,(aq)}}$ is the total energy of $Cl^-\cdot(H_2O)_{z,(aq)}$, $E_{UO_2Cl_{2,(g)}}$ is the total energy of gaseous $UO_2Cl_{2,(g)}$, $E_{(H_2O)_{5,(l)}}$ is the total energy of a five water molecule cluster, and $E_{(H_2O)_z,(l)}$ is the total energy of a *z* =5, 6, or 7 water cluster.

Furthermore, the $\mathrm{HCl_{(g)}}$ solvation chemical reaction can be modeled by reactions (5-9), (5-10), and (5-11) to provide the following,

$$HCl_{(g)} + z\,H_2O_{(l)} + 4\,H_2O_{(l)} \rightarrow Cl^-\cdot(H_2O)_{z,(aq)} + H^+\cdot(H_2O)_{4,(aq)} \quad (5\text{-}14)$$

Reaction (5-14) can then be used to represent the solvation energy of $HCl_{(g)}$, ΔE_3,

$$\Delta E_3 = E_{Cl^-\cdot(H_2O)_{z,(aq)}} + E_{H^+\cdot(H_2O)_{4,(aq)}} - E_{HCl_{(g)}} - E_{(H_2O)_{z,(l)}} - E_{(H_2O)_{4,(l)}} \quad (5\text{-}15)$$

where $E_{Cl^-\cdot(H_2O)_{z,(aq)}}$ is the total energy of $Cl^-\cdot(H_2O)_{z,(aq)}$, $E_{H^+\cdot(H_2O)_{4,(aq)}}$ is the total energy of $H^+\cdot(H_2O)_{4,(aq)}$, $E_{HCl_{(g)}}$ is the total energy of gaseous $HCl_{(g)}$, $E_{(H_2O)_{4,(l)}}$ is the total energy of a four water molecule cluster, and $E_{(H_2O)_{z,(l)}}$ is the total energy of a *z* =5, 6, or 7 water cluster, which is same as the definition shown above. From Eq. (5-6), (5-13) and (5-15), the final transmetallation energy can be calculated to be:

$$\Delta E_{trans} = \Delta E_1 + n\,\Delta E_2 + 2n\,\Delta E_3 \quad (5\text{-}16)$$

where the *n* is the number of the uranium atoms substituted by the thorium atoms. Table 5-4 shows the transmetallation energy based on different reference states for chloride ion.

Table 5-4. Comparing the transmetallation energy based on the different reference states and experimental data. Unit in eV.

Composition	Reference $Cl(H_2O)_5^-$	Reference $Cl(H_2O)_6^-$	Reference $Cl(H_2O)_7^-$	Experimental[102]
U6-->U5	-4.667	-4.676	-3.623	/
U6-->U4	-9.333	-9.349	-7.244	/
U6→3.2	/	/	/	-6.061±1.385
U6-->U3	-13.545	-13.570	-10.413	/
U6→U2.3	/	/	/	-11.022±1.732
U6-->U2	-17.755	-17.787	-13.578	/
U6→U1.8	/	/	/	-14.363±2.116
U6-->U1	-21.836	-21.877	-16.614	/
U6→U0.4	/	/	/	-19.631±1.748
U6-->Th6	-26.142	-26.191	-19.876	/

The data from Table 5-4 are also shown graphically in Figure 5-3**.** The theoretical and experimental transmetallation energy results have the same trend and similar values. These results indicate that the transmetallation of uranium atoms by thorium in the MOF-SBU cluster is energetically favored. Computational results for $Cl(H_2O)_5^-$ and $Cl(H_2O)_6^-$ were essentially identical but the smallest difference between theoretical and experimental energies were observed when the chloride ion was treated with a solvation shell of seven water molecules and implicit solvation.

The outcomes from our calculations closely mirror experimental findings, affirming the robustness of our computational model. Expanding upon this foundation, we extended our computations to scenarios entailing the substitution of U-SBUs with Pu

elements, for which there are not yet any experimental counterparts. The resulting data are shown in Figure 5-4. Given the good agreement between the transmetallation energies for U-Th, the observed negative transmetallation energies for U-Pu suggest that is probably possible to formation a Pu-SBU also. This realization of this prediction could offer a new direction in effectively capturing and managing plutonium.

5.4.4 Estimation of DOS and Optical Bandgap of Transmetallation From U-SBUs to Th-SBUs

Another approach to corroborate the accuracy of our computational findings is to juxtapose the predicted bandgap values of the MOFs with their experimentally observed counterparts. This comparison provides a direct metric to gauge the reliability of our computational models. In Pandey *et al.*[71] the bandgap of the uranium MOF-SBU cluster was influenced by the magnetic moment due to the existing spin-polarization of the uranium atom. There are two possibilities for the apical, eight-coordinated uranium atoms: two spins aligned in the same direction or the two spins aligned anti-parallel. For the equatorial atoms, there are three possibilities: (1) all four spins are in the same direction, (2) three spins are in one direction and one in the other, and (3) two up-spins and two down-spins, for which the two parallel spins can be adjacent to each other or diagonally opposite to each other. Figure 5-5 illustrates the configurations of each magnetic moment case. For more details on these structures, see Pandey, *et al.*[71] Their research primarily and solely on the pure U-MOF, our study encompasses the transmetallation of U/Th-MOF. Given that thorium lacks spin-polarization, only one configuration exists for both Th_6-8 and U_1Th_5-8 cases. The bandgap is also influenced by the U/Th ratio. Consequently, we've introduced a new equation to determine the bandgap.

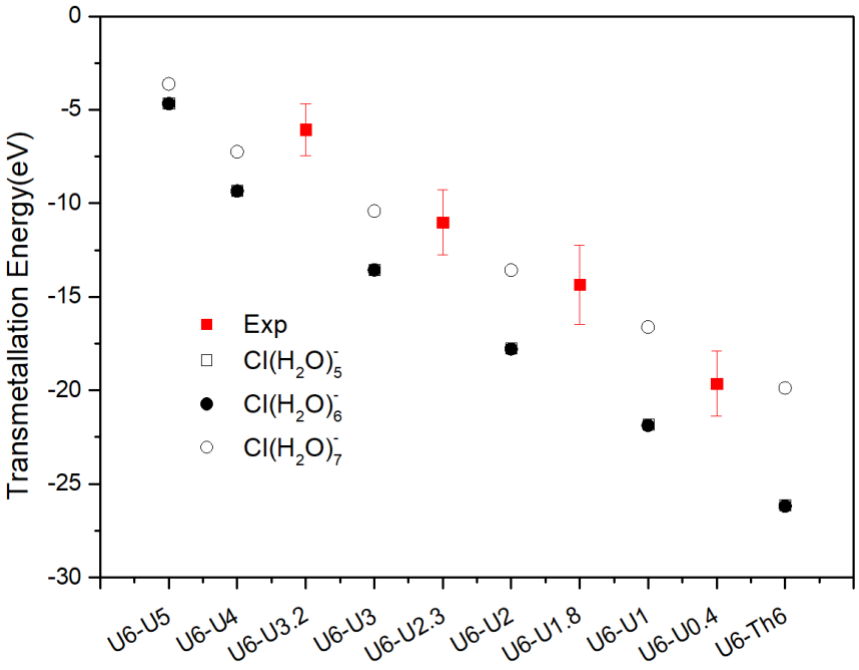

Figure 5-3. A comparison of the transmetallation energy with theoretical and experimental[102] data is reported in Table 5-2.

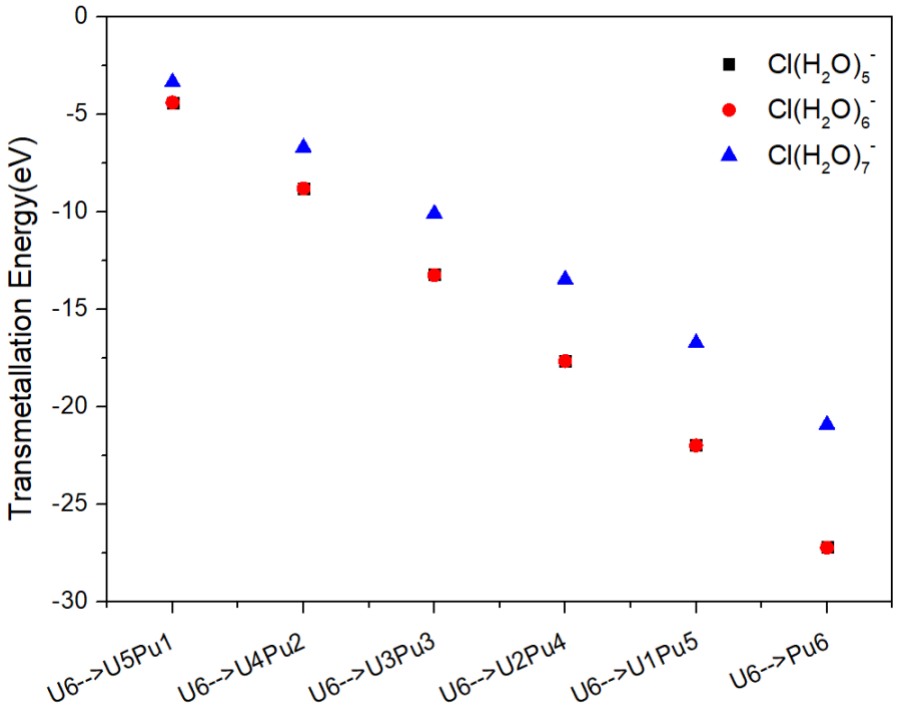

Figure 5-4. Transmetallation energy of substituted U-SBU by Pu-SBU. The results for $Cl(H_2O)_5^-$, black squares, lie essentially below those for $Cl(H_2O)_6^-$, red circles.

To determine the overall effects of the heterometallic MOF cluster versus the bandgap, the weighted bandgap is defined as,

$$Weighted\ Bandgap = \frac{\sum_i \exp\left(-\frac{\Delta E_i}{RT}\right) * Bandgap_i}{\sum_i \exp\left(-\frac{\Delta E_i}{RT}\right)} \quad (5\text{-}17)$$

where the ΔE_i is the energy difference between the i^{th} spin state energy and the ferromagnetic state (reference state). $Bandgap_i$ is the i^{th} spin state bandgap value, R is the gas constant and T is the temperature (which was considered to be 298 K). Calculated weighted bandgaps are also reported in Table 5-5.

From Table 5-5, it's evident that the bandgap decreases as uranium is increasingly substituted by thorium. We've cross-referenced these findings with experimental data, as illustrated in Figure 5-6. Impressively, our computational results for the bandgap align well with the experimental data, reinforcing the reliability of our simulations.

To delve deeper into the nature of the bandgap, we've charted the density of states (DOS) for each heterometallic MOF metal node. Detailed discussions on the electronic DOS for the most energetically favorable configurations will follow in the upcoming sections. For a robust analysis, Figure 5-7 will also present the ferromagnetic alignment of spin-polarized structures: both the ferromagnetic configuration and the configuration exhibiting the lowest overall energy. Together, these analyses provide a thorough understanding of the electronic dynamics within the system we're examining. The difference or gap between the Highest Occupied Molecular Orbital (HOMO) and the Lowest Unoccupied Molecular Orbital (LUMO) edges is predominantly influenced by the

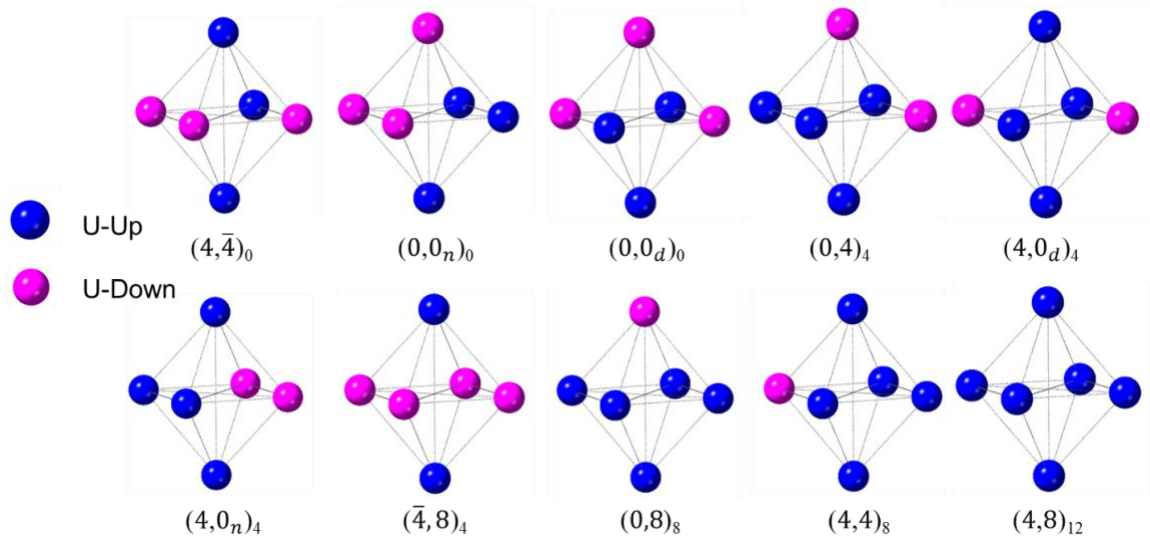

Figure 5-5. Possible magnetic moments of U-8 configurations adapted from Pandey *et al.*.[71] Blue atoms are uranium with an up spin-polarization direction while pink atoms are those with a down spin. The first number in the magnetic order label represents the net magnetic moment of the eight-coordination uranium. The second number denotes the net magnetic moment of equatorial uranium. The bar on the number means the net magnetic moment direction of eight-coordinated uranium is opposite to the six-coordinated uranium. The subscripts outside the parentheses in the nomenclature indicate the net magnetic moment of the SBU; subscripts *n* and *d* state that the similar spins are either adjacent or diagonal from one another, respectively.

Table 5-5. The bandgap of each magnetic moment and weighted bandgap of heterometallic MOF-SBU. Unit in eV. The lowest energy configuration for each composition is denoted by red text.

Composition	The bandgap of each configuration										Weighted bandgap
U_6-8	$(4,\bar{4})_0$	$(0,0_n)_0$	$(0,0_d)_0$	$(0,4)_4$	$(4,0_d)_4$	$(4,0_n)_4$	$(\bar{4},8)_4$	$(0,8)_8$	$(4,4)_8$	$(4,8)_{12}$	2.58
	2.59	2.77	2.61	2.55	2.59	2.69	2.46	2.50	2.57	2.44	
U_5Th_1-8	$(2,4)_2$		$(2,0_n)_2$		$(2,0_d)_2$	$(2,8)_6$		$(2,4)_6$		$(2,8)_{10}$	2.60
	2.60		2.62		2.78	2.50		2.56		2.48	
U_4Th_2-8	$(0,0_n)_0$			$(0,0_d)_0$		$(0,4)_4$			$(0,8)_8$		2.64
	2.63			2.84		2.59			2.47		
U_3Th_3-8	$(0,2_n)_2$			$(0,2_d)_2$			$(0,6)_6$				2.69
	2.86			2.66			2.56				
U_2Th_4-8	$(0,0_d)_0$					$(0,4)_4$					2.90
	2.91					2.89					
U_1Th_5-8	$(0,2)_2$										2.92
	2.92										
Th_6-8	$(0,0)_0$										3.70
	3.70										

presence of the U-f orbital. As the system sees a substitution of uranium with thorium, there is a noticeable expansion in the bandgap. This observed increase in the bandgap is in harmony with empirical data, as demonstrated in Figures 5-7. It's worth emphasizing that the defining characteristic of the edge is in the Th-f orbital in Th-6.

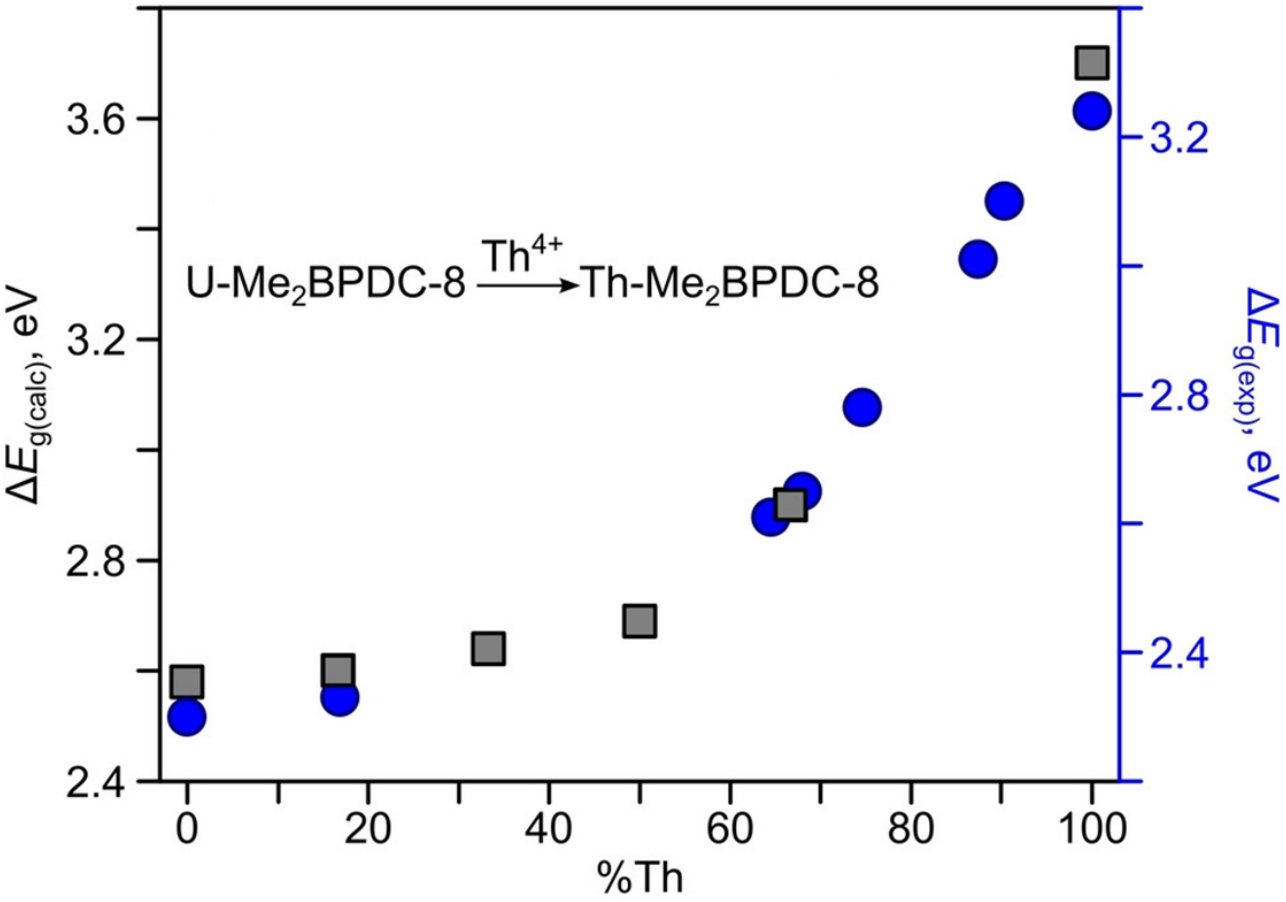

Figure 5-6. The comparison bandgap of heterometallic of metal node between calculated (gray squares) and exprimental[102] (blue circles) as a function of %Th.

5.4.5 O–H bond deprotonation energy in U-8 and Th-8 nodes

Before determining the deprotonation energy of U-SBUs, it is crucial to establish its reference state. Given the variable spin states of U-SBUs detailed in section 5.4.4, our objective was to discern the spin state with the lowest total energy. In our

calculations for U-SBUs, we utilized a multiplicity of 13, which was determined by examining the potential number of paired f-orbital electrons. The results are depicted in Figure 5-8. The absence of a multiplicity of 7 for the CRENBL pseudopotential is due to a difficulty with convergence.

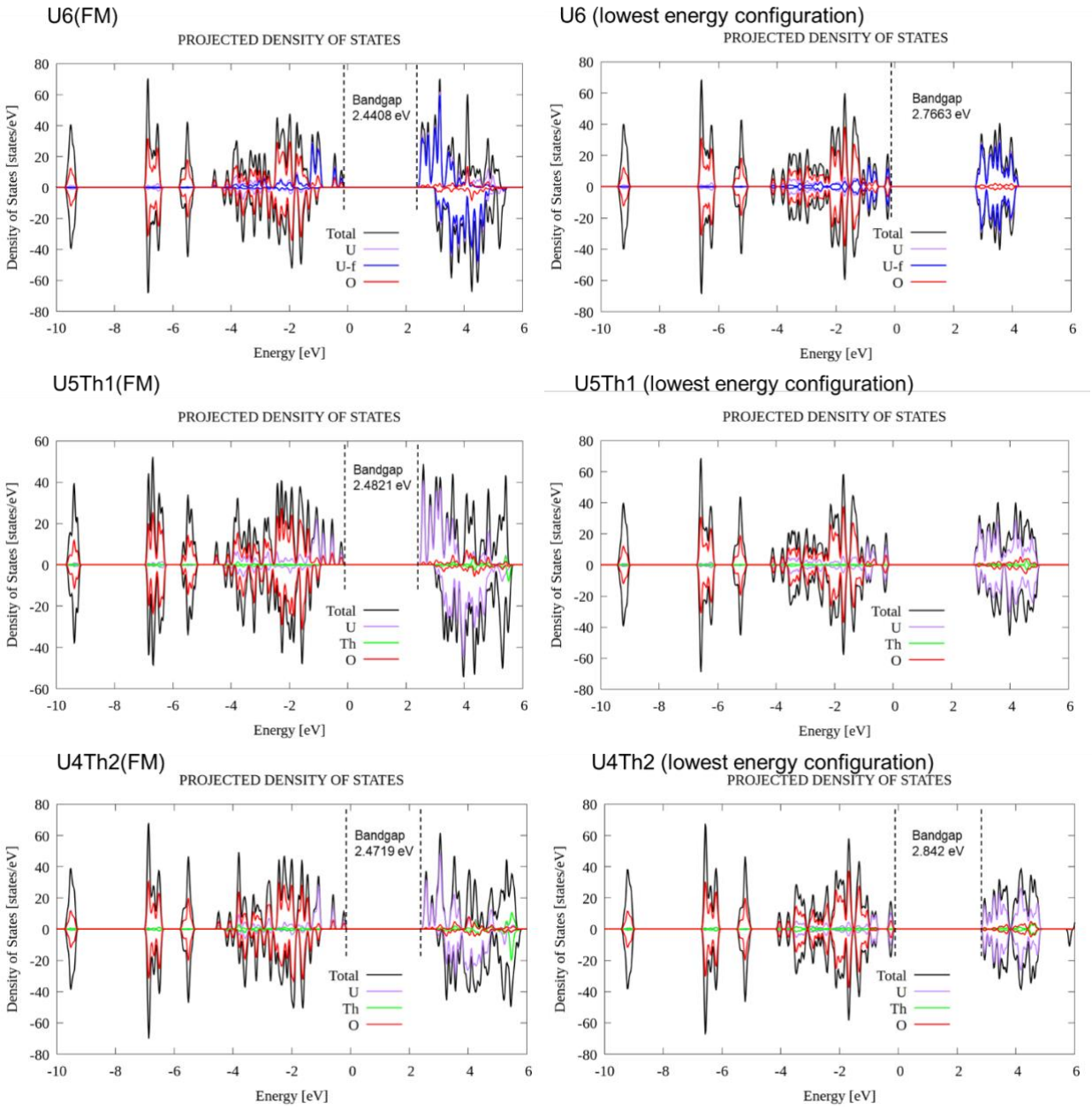

Figure 5-7. The DOS plots of each lowest total energy configuration of each MOF composition.

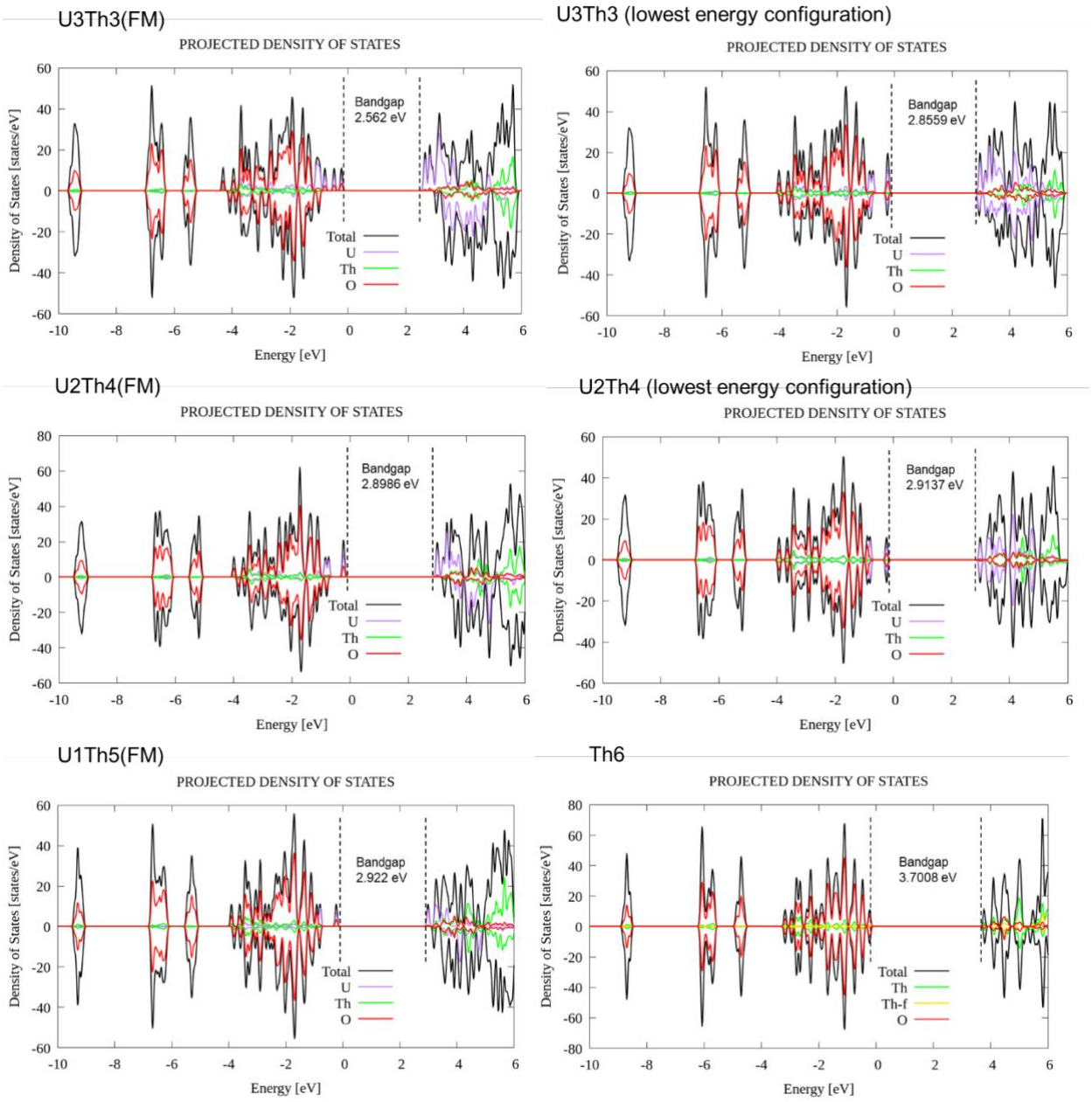

Figure 5-7. Continued.

The relative total energies we report are derived using the singlet configuration as the foundational reference state. In our endeavors to strike a balance between computational accuracy and efficiency, we opted for the CRENBL and Stuttgart pseudopotentials as the basis set for C, H, and O atoms. This choice was made in lieu

of the computationally demanding 6-31G** large basis set, which can significantly increase computational time.

It's noteworthy that the system in which each uranium atom possessed 2 unpaired electrons—resulting in an aggregate of 12 unpaired electrons and thus a multiplicity of 13—proved to be the most stable configuration. This stability was observed consistently in calculations using both the CRENBL and Stuttgart potentials.

We want to evaluate the ionic conductivity of actinide MOF, therefore, there are three unique hydrogen deprotonation sites in actinide SBU and are shown in Figure 5-9. The deprotonation energy of the actinide MOF-SBUs was defined as:[147]

$$E_{diss} = E_{SBU\text{-}O^-} - E_{SBU\text{-}OH} \tag{5-18}$$

where E_{SBU-OH} is the total energy of the relative actinide SBU while $E_{SBU\text{-}O^-}$ is the total energy of the actinide SBU from which a proton is removed, leaving a negatively charged SBU. The deprotonation energies for U-8 and Th-8 are shown in Table 5-6.

Table 5-6. The deprotonation energies (in kcal/mol) of the U-8 and Th-8 clusters.

Composition	CRENBL			Stuttgart RLC		
U-8	Site_1	Site_2	Site_3	Site_1	Site_2	Site_3
	323.99	325.38	327.11	322.78	322.78	325.88
Th-8	Site_1	Site_2	Site_3	Site_1	Site_2	Site_3
	330.04	330.04	329.21	328.29	328.30	327.38

Our calculations of the deprotonation energy using both the CRENBL and Stuttgart RLC potentials indicate consistent findings for sites 1 and 2 across both U-SBU and Th-SBU. However, the site 3 case takes slightly less energy than the first two sites in Th-SBU, while slightly more in U-SBU. Also, regardless of the potential used, the deprotonation energy of Th-SBU is slightly higher than that of U-SBU. As a result, the incorporation of actinide ions would marginally impact the proton affinity of the MOF's metal node.

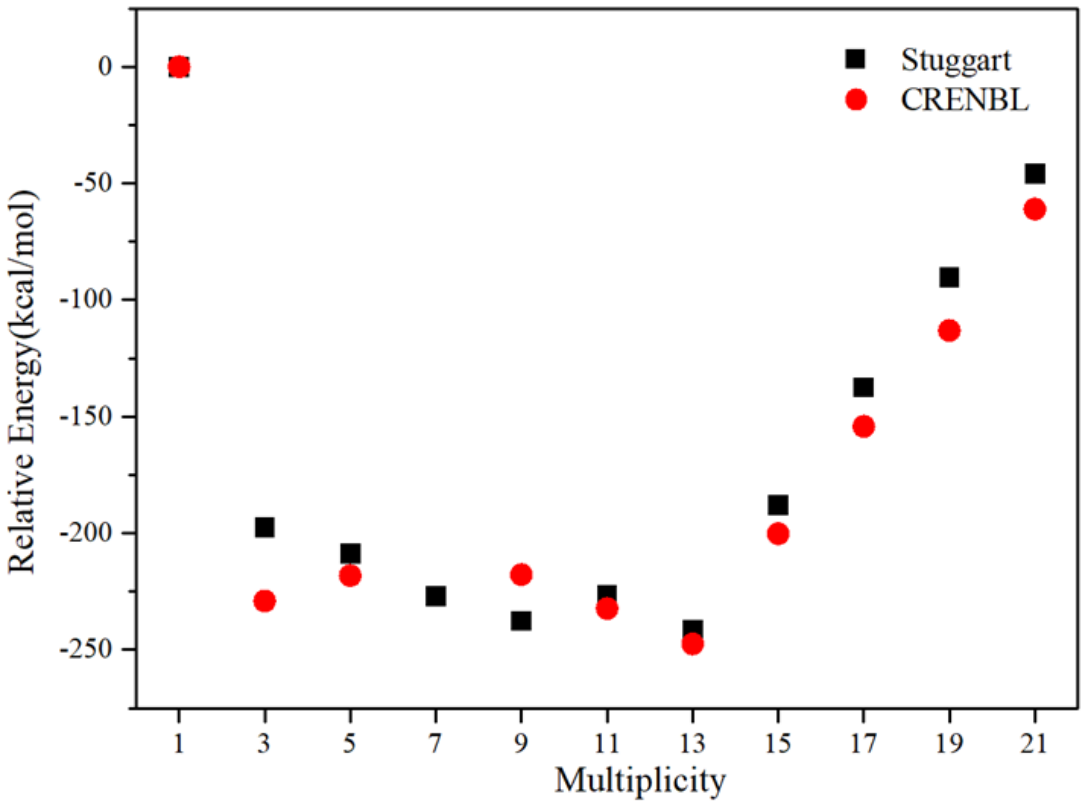

Figure 5-8. The relative total energies of the different multiplicities of U-SBU. The reference is singlet multiplicity.The black is for the Stuggart pseudopotential while the red is for the CRENBL pseudopotential.

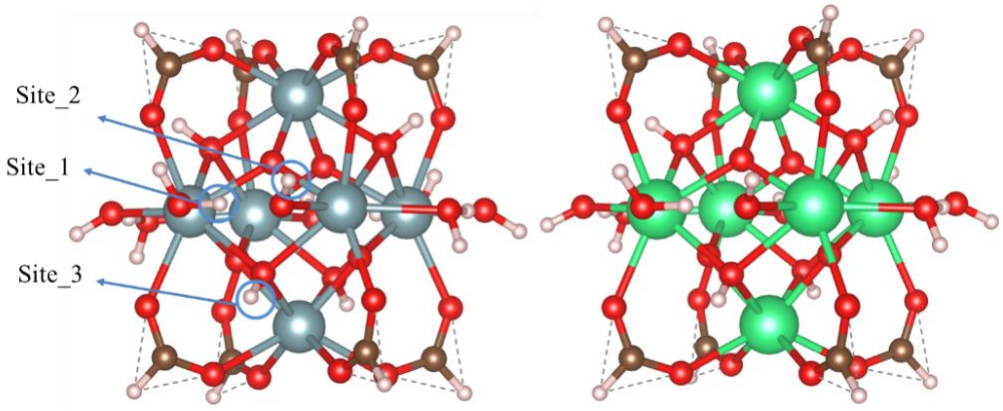

Figure 5-9. Optimized actinide SBU structure and protonation sites. Uranium atoms are shown in grey, thorium in green, oxygen in red, carbon in brown, and hydrogen in white. Each equatorial actinide atom is coordinated with the -OH_2 (site_1) and -OH (site_2) groups. And the three coordinated oxygen will be with terminal hydrogen. (site_3).

5.5 Conclusions

In this chapter, we employed density functional theory (DFT) to simulate the formation energy of Zr- and Th-based SBUs. Our investigations extended to computing the energy within the context of organic ligands. The findings consistently revealed a more negative binding energy for Th-SBU, suggesting superior stability of Th-MOF in comparison to Zr-based MOFs.

Additionally, we explored a comparative analysis between U-SBU and Th-SBU by determining the transmetallation energy when U-SBU is replaced by Th. The transmetallation energy and bandgap results aligned well with experimental observations, in which proven our simulation accuracy, in turns, making the substitution of U-SBU with Th favorable. Leveraging this approach, we further extrapolated to ascertain the transmetallation energy when U-SBU is substituted by Pu. The derived negative binding energy infers that such a substitution is thermodynamically favored, paving a promising pathway for plutonium ion sequestration. Our research spectrum also spanned the dissociation energy landscapes of Th-SBU and U-SBU, examining three different protonation sites. Intriguingly, the energies turned out to be quite analogous.

CHAPTER 6
FERROCENE INTERCALATION IN VANADYL PHOSPHATE: A DENSITY FUNCTIONAL THEORY STUDY OF POLARIZABLE ION DETECTION

6.1 Background

As the global energy crisis intensifies, nuclear energy emerges as a viable solution due to its low carbon footprint. However, the daunting challenge remains: managing the radioactive nuclear waste produced. While previous chapters have explored strategies for effective waste sequestration, this chapter shifts focus to an alternative energy storage - lithium-ion batteries. Herein, we delve into the potential of a novel cathode material for these batteries, namely vanadyl phosphate ($VOPO_4$).

Vanadyl phosphate ($VOPO_4$) has garnered considerable attention as an intriguing inorganic material, owing to its unique properties and potential applications in energy storage,[159,160,161,19] catalysis,[162,163,164,165,166] and ion conduction.[167] Due to the relatively weak interlayer bonds, neighboring layers of $VOPO_4$ are believed to exhibit relative independence, enabling the intercalation of various ions and molecules (both inorganic and organic) into the interlayer spaces. Numerous studies have focused on the intercalation of $VOPO_4$ with lithium,[168,169] sodium,[170] potassium[171], and zinc ions,[172] envisaging this complex material as a potential cathode in batteries. For example, recently, Zhu *et al.*[173] successfully intercalated zinc ions into $VOPO_4$, resulting in zinc-$VOPO_4$ composite cathodes that greatly enhance battery performance.

However, the majority of these studies have centered around the intercalation of small ions. The intercalation of small ions into $VOPO_4$ involves three interactions: the solvent-host ($VOPO_4$) interaction, the solvent-guest (cation) interaction, and the host-guest interaction.[174] Fortunately, intercalation with ferrocene, $Fe(C_5H_5)_2$, is simpler in that the solvent-guest interaction is negligible due to the large size of the ferrocene and

its poor interaction with the solvent.[174] But the interaction between ferrocene and $VOPO_4$ namely host-guest interaction, has not been discussed thoroughly yet. Therefore, in this paper, we will focus solely on host-guest interaction. Additionally, the resulting intercalated material may exhibit enhanced electrochemical performance. This is due to the reversible redox properties of ferrocene, which allows it to undergo oxidation and reduction reactions easily.[175,22] When intercalated into $VOPO_4$, ferrocene can act as a redox mediator, facilitating charge transfer processes during electrochemical reactions. Therefore, understanding how ferrocene interacts with $VOPO_4$, as well as its diffusion within the layers, could provide valuable insights for designing improved energy storage systems.

Density functional theory (DFT) is a powerful method for simulating the atomic-level interactions between ferrocene and the $VOPO_4$ layer, making it a suitable approach to determine the most stable configurations of ferrocene located within the $VOPO_4$ layer by examining the system's total energy using DFT. This paper aims to identify these stable configurations, and then it reveals how $VOPO_4$ layer interacts with ferrocene, namely host-guest interaction, in which provide a theoretical insight on the ferrocene intercalation process.

6.2 Computational Methods

The DFT calculations performed in this study utilized the Vienna Ab-initio Simulation Package (VASP) software,[176,177] employing the Perdew-Burke-Ernzerhof (PBE) exchange-correlation functional within the Generalized Gradient Approximation (GGA)[178] method. Projector-augmented wave (PAW)[179,180] pseudopotentials were utilized. For vanadium five valence electrons ($3d^4 4s^1$) were explicitly included, for phosphorus five valence electrons ($3s^2 3p^3$), for iron eight valence electrons ($3d^7 4s^1$), for

oxygen six valence electrons ($2s^2 2p^4$), and for carbon four valence electrons ($2s^2 2p^2$). To ensure convergence of the calculations, a wave-function plane cut-off energy of 600 eV was employed. The DFT+U[114] method was adopted to account for electron localization in the 3d states of vanadium, with a U parameter for 3.25 eV.[181,182] The DFT+D3[183,184] correction was applied to better incorporate van der Waals interactions.

The atomic structures were optimized using a conjugate gradient method[185,186] until the average force reached a value less than 0.025 eV/Å, with an energy tolerance of 1×10^{-6} eV for each electronic step. Spin-polarization was considered in all calculations. Gaussian smearing with a width of 0.05 eV was employed during optimizations.

For the characterization of pure vanadyl phosphate, we employed a dense 8x8x12 gamma-centered point k-mesh density, an approach meticulously chosen to ensure an accurate representation and subsequent relaxation of its inherent structure. However, the scenario necessitated a different approach when ferrocene was introduced into the system. To preclude any unintended interactions between adjacent ferrocene molecules, a consequence of the periodic boundary conditions, we strategically opted for a 2x2x1 supercell configuration of $VOPO_4$, as depicted in Figure 1a. Notably, the introduction of ferrocene into the vanadyl phosphonate framework resulted in a considerable structural expansion predominantly in the c-axis direction. This morphological alteration provided us with the flexibility to modify a 4x4x5 k-mesh density for our computational analyses. The charge density difference calculations were performed using VASPKIT.[123] The visualization of structure, charge density difference, and electron localization function(ELF)[135] were carried out with VESTA.[124] The Hirshfeld

surface analysis[187] was implemented by the Mutlwfn 3.8,[188] and visualization by VMD.[189]

6.3 Structures

6.3.1 Vanadyl Phosphate

The crystal structure of dehydrated vanadyl phosphate ($VOPO_4$) was sourced from the Material Project database, MP-19000.[190] In Figure 6-1a, the crystal structure unit cell is depicted and the corresponding structure parameters are provided in Table 6-1. The space group is P4/nmm, a tetragonal crystal structure characterized by a two-dimensional $VOPO_4$ sheet in the a-b plane, periodically repeated in the c direction in Figure 6-1b. The phosphorus atoms are tetrahedrally coordinated to four oxygen atoms, with all P-O bond lengths measuring 1.54 Å. Two of the oxygens (colored blue in Figure 6-1) lie on the top surface of each $VOPO_4$ layer while the other two oxygens (colored red in Figure 6-1) lie on the bottom surface. The line between the two red atoms associated with a particular phosphorous is at 90˚ to the line joining the blue atoms; one line lies in the [100] direction while the other lies in the [010] direction. Vanadium atoms form bonds with five oxygen atoms in a square pyramid configuration. Four V-O bonds form the non-flat base of the pyramid with equal length, 1.90 Å. Each of the oxygen in the base are associated with a different PO_4 tetrahedron; thus, two are ‘red’ oxygen and two ‘blue’ oxygens in each base. The V-O-P bond angle is approximately 131.91°. The fifth V-O bond defines the apex of the pyramid and lies in the c direction. The bond between the V and this apical oxygen is shorter, 1.60 Å. This apical oxygen is shown in pink in Figure 6-1 and subsequent figures. Half of these VO_5 pyramids point above the a-b plane and half below. Using the unit cell shown in Figure 6-1a, rows of up-pointing

and down-pointing VO_5 pyramids alternate along the b direction (y-axis); the alternate in a checkerboard pattern in the [110] and [1-10] directions in Figure 6-1c.

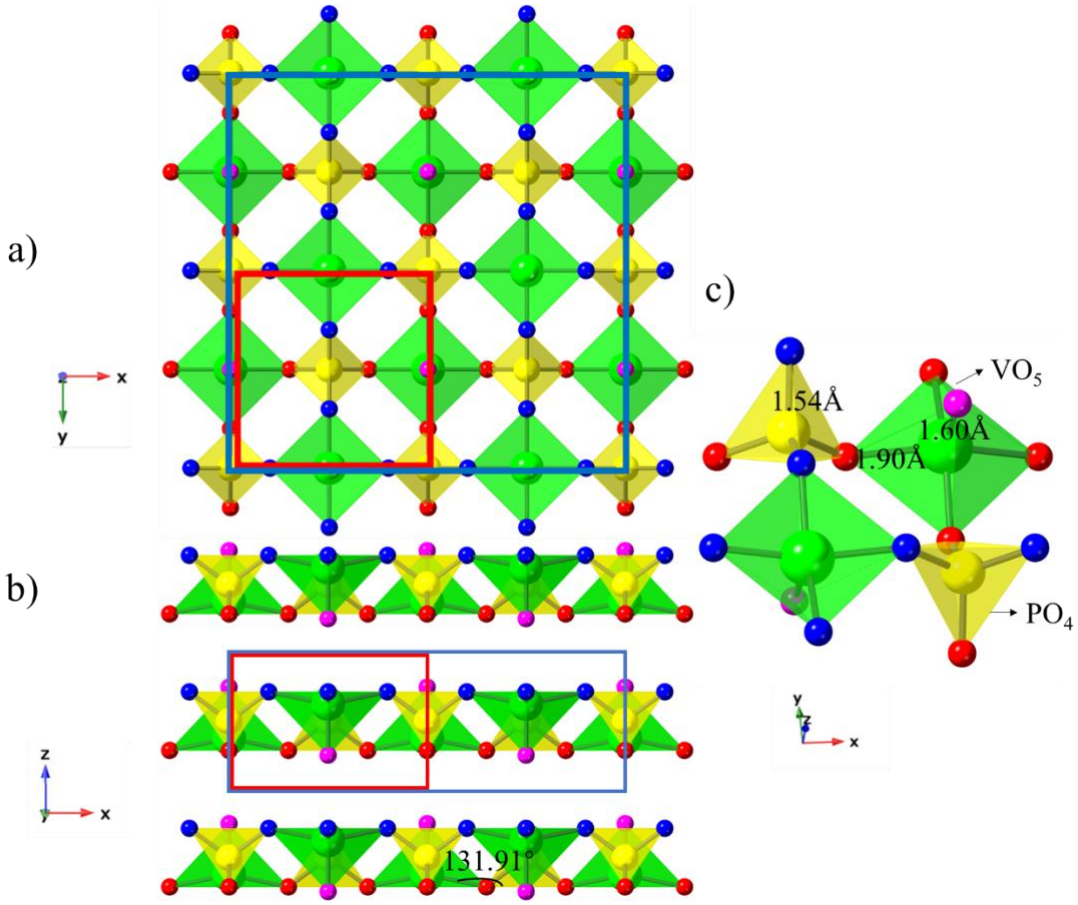

Figure 6-1. The crystal structure of dehydrated $VOPO_4$, a) along the [001] direction. Here and in subsequent figures, the vanadium is in green, phosphorus in yellow, the apical oxygen of the VO_5 pyramid is pink, oxygen on the bottom of the layers (defined as +z) are red, and oxygen on top of the layers in blue. The red box is the unit cell, and the blue box is the 2*2*1 supercell, we intentionally shrink the red box to be slightly smaller than the blue box. b) The $VOPO_4$ sheets are periodically repeated in the c direction. c) The connection pattern between VO_5 and PO_4.

In Table 6-1, we both show the dehydrated and hydrated form $VOPO_4$ from DFT results and compared with experimental structures.[191] The a and b lattice parameters do not strongly change from dehydration to hydration case. And they both agree very well with the experiment. We ascribe the slight difference between the a and b lattice

parameters to the fact that the computational supercell contains two $VOPO_4$ formula units and four waters; the a and b lattice parameters are thus sensitive to their specific arrangements. If we were to calculate a significantly larger unit cell, something which is computationally prohibitive, we would expect this difference to decrease significantly. The calculated c lattice parameter of the dehydrated system is much lower than that of the hydrated system. Upon hydration there is much better agreement between the calculation (7.273 Å) and the experiment (7.410 Å). The remaining ~2% difference arises from the weak secondary bonding between the layers. Indeed, a calculation of the energy of the system at the experimental lattice parameters yielded an energy of only 0.35meV/atom higher than the structure shown in Table 6-1. This shows that the potential energy surface is very flat.

Table 6-1. The lattice parameters of $VOPO_4$ by using GGA+U with D3 correction and compared with experimental data of $VOPO_4 \cdot 2H_2O$.

Lattice	$VOPO_4$ GGA+U_D3	$VOPO_4 \cdot 2H_2O$ GGA+U_D3	$VOPO_4 \cdot 2H_2O$ Experimental[191]
a (Å)	6.212	6.234	6.202
b (Å)	6.212	6.215	6.202
c (Å)	4.285	7.273	7.410
α °	90	90	90
β °	90	90	90
γ °	90	90	90

To confirm that this is the $VOPO_4$ structure's lowest total energy, we varied the in-plane position of one layer relative to the other in a calculation of a system with two layers. Based on the symmetry of vanadyl phosphate, we explored two types of displacement. Defining zero displacements as when the V atoms in one layer lie exactly over the top of the V atoms in the neighboring layer. We then allow two different layer sliding, one involved displacement along the [100] direction, as illustrated in Figure 6-

2a, while the other entailed displacement along the [110] direction, depicted in Figure 6-2b. Figures 6-2c and 6-2d illustrate the total energy of the displaced structures relative to the non-displaced structure. These calculations show that the non-displaced structure has the lowest energy and represents the ground state of the system.

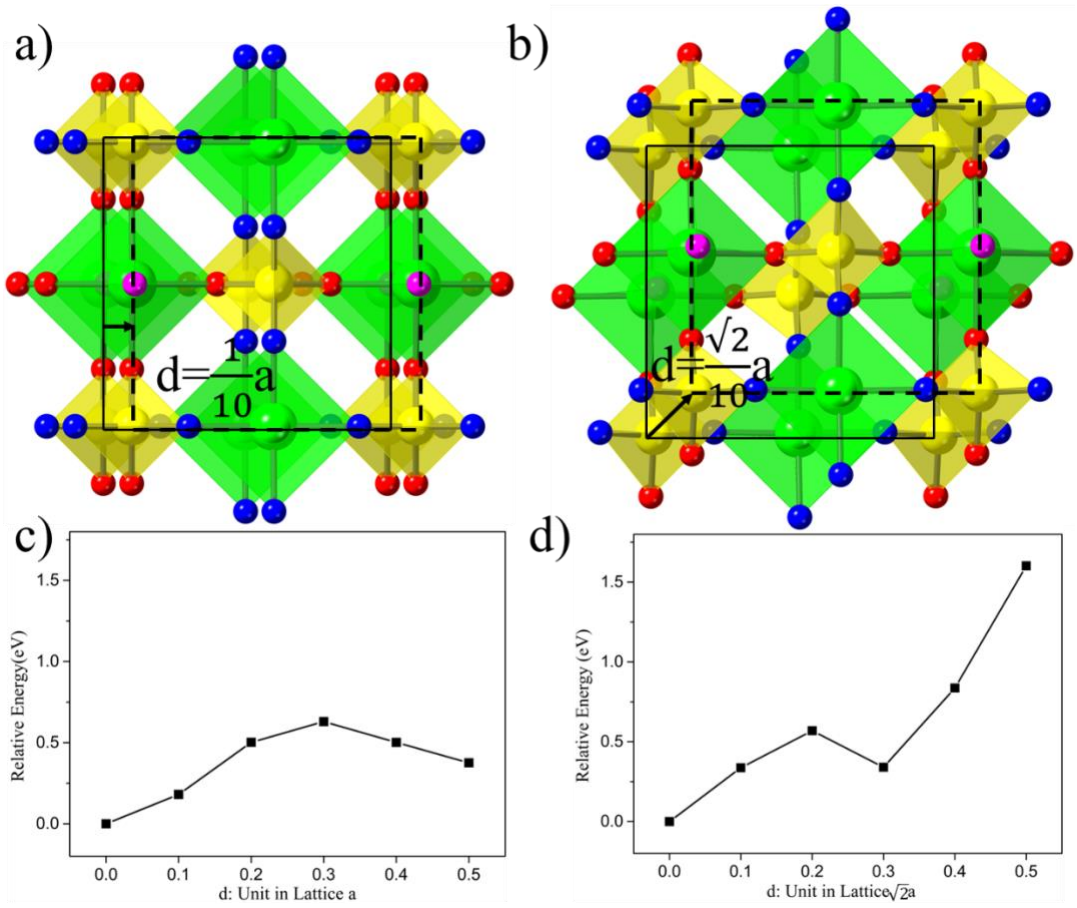

Figure 6-2. Illustration of the $VOPO_4$ layer displacement a) along the [100] direction and b) along the [110] direction. The solid black squares in a) and b) denote the original position of the second layer with respect to the first layer; the dashed black square denotes the displacement of the second layer. The corresponding energies as a function of displacement relative total energy as the reference of the original structure are shown in c) and d).

6.3.2 Ferrocene

Ferrocene consists of two cyclopentadienyls, C_5H_5, rings with an iron atom located in the center between the two rings. Previous experimental studies[192] have

identified two distinct ring configurations: eclipsed and staggered, as depicted in Figure 6-3. Both experimental[192] and theoretical[193] investigations have consistently indicated that the eclipsed configuration is energetically favored, exhibiting lower energy by 0.039 eV[192] and 0.027 eV,[193] respectively. Our calculations also support this trend, as we found that the eclipsed configuration is lower in energy by 0.043 eV compared to the staggered configuration, aligning well with experimental observations. The difference between our results and the prior theoretical [193] work can be attributed to the different DFT methods and basis sets. In our study, we employed the GGA-PBE with D3 functional with plane wave basis set, while the previous work utilized the B3LYP hybrid functional with m6-31G(d). Considering the high computational resource requirements of the hybrid method, the GGA+U_D3 method is suitable for our calculations. Additionally, given the periodic structure ($VOPO_4$) in our study, the plane wave basis set is the better choice.

Table 6-2 presents the bond lengths of the eclipsed configuration obtained from our calculations, along with other theoretical and experimental data. Rappoport et al.[194] showed that the GGA functional is generally more suitable for 3d element complexes, such as iron, whereas the hybrid functional is more advantageous for 4d and 5d element complexes. Overall, these results demonstrate a high degree of consistency among different sources, thus validating the accuracy and reliability of our calculations.

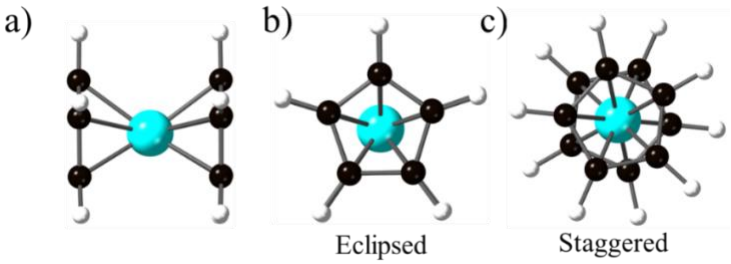

Figure 6-3. Side view (a) depiction eclipsed (b), and staggered (c) configurations of ferrocene. The iron is in cyan, carbon in black, and hydrogen in white.

Table 6-2. Optimized bond distances of eclipsed ferrocene from our calculations and other works. Unit in (Å).

Bond distance	This work	B3LYP[193]	Experimental[192]
Fe-C_5^*	1.634	1.670	1.660
Fe-C	2.039	2.065	2.064±0.003
C-C	1.434	1.428	1.440±0.002
C-H	1.086	1.082	1.104±0.006

*Denotes the distance from the iron atom to the center of the cyclopentadienyl ring.

6.4 Results

6.4.1 Configurations of Ferrocene on Vanadyl Phosphate

In our quest to comprehensively investigate the various configurations of ferrocene positioned above the VOPO4 layer, we meticulously evaluated every conceivable arrangement. In Section 6.3.2, we found that the eclipsed structure (denoted as E) is the lowest energy structure of the ferrocene in a vacuum. Although the staggered structure (S) of the isolated ferrocene molecule was 0.043 eV higher in energy than the eclipsed structure, it remains a plausible arrangement during intercalation and is thus included in our analysis. In Figure 6-1, two distinct positions are identified for intercalation: between vanadium (V) and oxygen-vanadium (O-V), or between phosphorus and phosphorus (P/P). Taking into account the five-carbon rings of ferrocene, we, therefore, consider two distinct orientations for the eclipsed ferrocene on the vanadium site. The left panel of Figure 6-4a, denoted the E-VO configuration, has the apex hydrogen of the ferrocene pointing to the VO. The second to left panel denoted the E-V configuration has the apex hydrogen of the ferrocene pointing to the V. The third possibility is shown in the third panel, in which the ferrocene is in the staggered configuration, for which there is only one structure, the S-V configuration.

For the three distinct structures—E-V, E-VO, and S-V—we took into account two specific orientations concerning the axis of the ferrocene molecule. In the initial configuration, the ferrocene's axis is aligned parallel to the [100] direction, which is congruent to [010]. This orientation is designated as having a rotation angle of 0˚. In the subsequent configuration, the axis is aligned with the [110] direction, a direction synonymous with [-110], [1-10], and [-1-10]. This orientation is represented by a rotation angle of 45˚, as illustrated in Figure 6-4b. Consequently, when considering these orientations in conjunction with the specified structures, a total of six unique configurations are derived at the V-VO site: E-V-0˚, E-V-45˚, E-OV-0˚, E-OV-45˚, S-V-0˚, and S-V-45˚.

We turn now to the ferrocene on the phosphorous. Considering first the eclipsed structure, in which apical H in each C_5H_5 group points similarly towards the VO side as it intercalates on the V/VO side, we'll refer to this as the E-PVO configuration in Figure 6-5. In this structure, when it faces the V side during intercalation on the V/VO side, we'll call it the E-PV configuration. When considering the rotation of ferrocene, we find several identical configurations due to the tetrahedral coordination of phosphorus. For example, the E-PVO-0˚ is equivalent to E-PV-90˚, and E-PVO-90˚ is the same as E-PV-0˚. There is no distinction between E-PVO-45˚ and E-PV-45˚, and then simplified as E-PVO-45˚. For the staggered structure, there is no distinction between 0˚ and 90˚. There are thus only two staggered structures: S-P-0˚, and S-P-45˚.

In summary, there are six unique configurations intercalated on the vanadium site (E-V-0˚, E-V-45˚, E-VO-0˚, E-VO-45˚, S-V-0˚, and S-V-45˚) and five unique configurations on phosphorus site (E-PVO-0˚, E-PV-0˚, E-PVO-45˚, S-P-0˚, and S-P-

45˚). The next step is to determine the total energy of each of these eleven configurations. For more information about all of configurations in Figure 6-6.

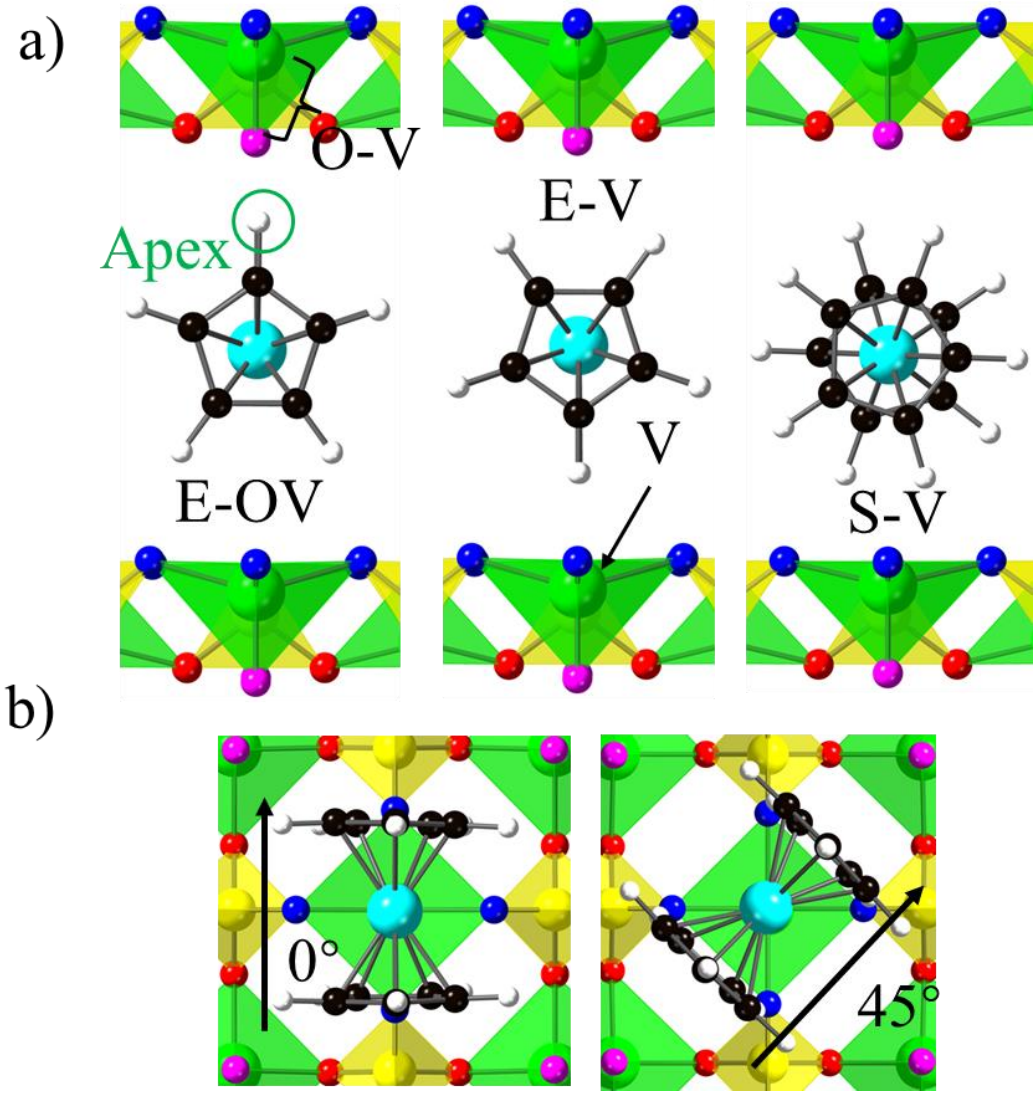

Figure 6-4. The possible orientation of ferrocene intercalted on V side. a) Different orientations of the cyclopentadienyl ring of ferrocene intercalation on the V/OV site, b) the different rotation degrees of ferrocene.

6.4.2 Effect of the magnetic moment

Although in isolation neither the ferrocene nor the VOPO4 layers had a magnetic moment, after optimizing the various configurations, we observed the presence of magnetic moments in both the ferrocene and $VOPO_4$ layers. This magnetic behavior

arises due to the charge transfer between iron and vanadium, detailed later in Section 6.4.4 After intercalation, the magnetic moments of iron and vanadium are found to be 1.06 and 1.10 μB, respectively. Consequently, the total magnetic moment of these configurations can be either 0.04 μB or 2.16 μB. However, we find that the total energies for the same configuration with these respective magnetic moments are nearly identical. For instance, in the E-OV-0° configuration, the difference in total energy between the two magnetic moment states is only 2.6×10^{-3}meV/atom. Based on this finding, we conclude that the magnetic moment has a negligible effect on these configurations. In order to maintain consistency, we will utilize the total energies corresponding to a magnetic moment of 0.04 μB.

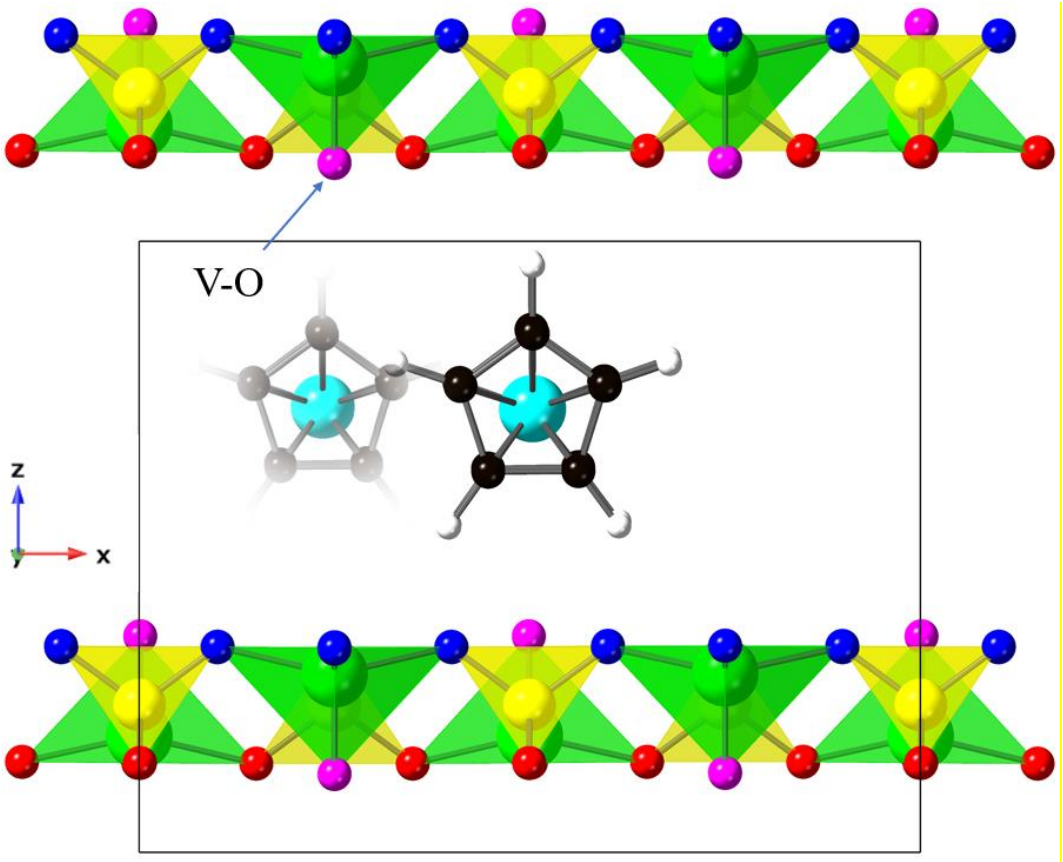

Figure 6-5. Ferrocene intercalation on the P/P site, a) E-P_{VO}-0°, viewed along [010] direction. Black box is the unit cell.

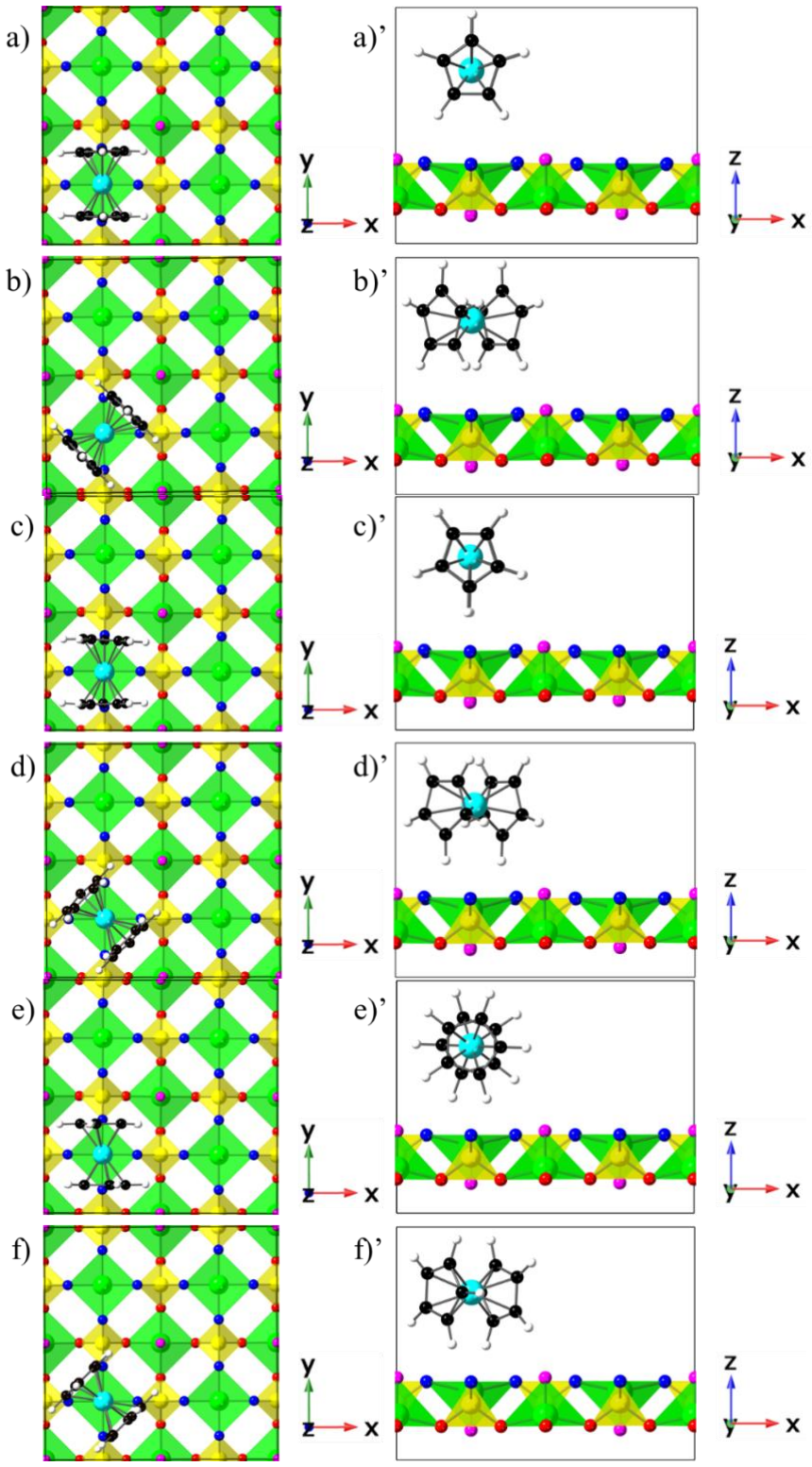

Figure 6-6. The crystal configurations of a) E-OV-0° and b) E-OV-45°, c) E-V-0° and d) E-V-45°, e) S-V-0° and f) S-V-45°, g) E-Pvo-0°, g) E-P-45°, i) E-Pv-0°, j) S-P-0° and k) S-P-45° are viewed along the [001] direction. The corresponding pictures denoted with prime (') are viewed along the [010] direction.

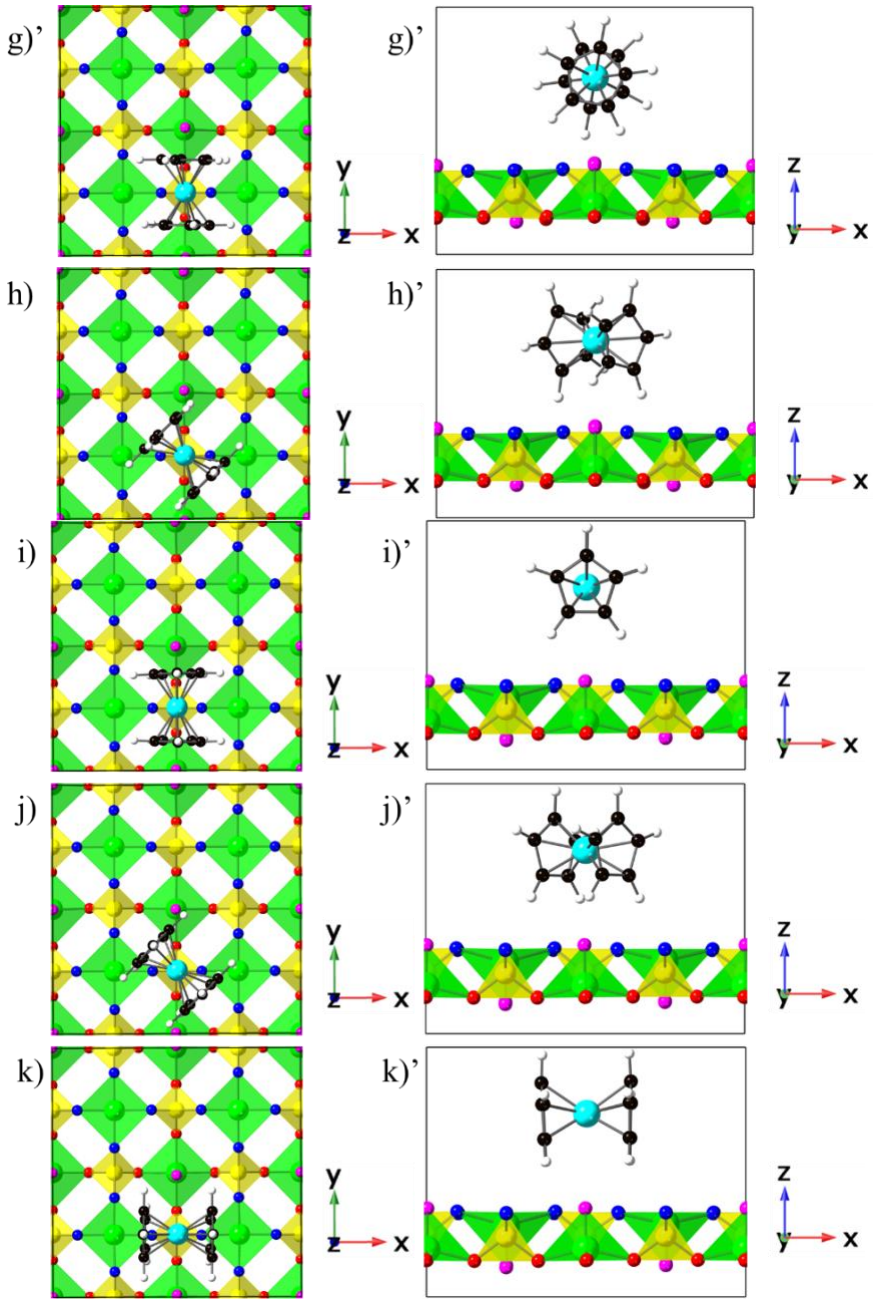

Figure 6-6. Continued.

6.4.3 The Total Energy Comparison

The E-V-45° structure, which has the lowest energy of all. Figure 6-7 shows the energies of all 11 structures, relative to to this lowest energy configuration. The notation is based on the initial configurations. However, the final optimized structures differ from

these initial configurations. Some of them have shown substantial distortion which will be discussed in the below paragraphs. For more details about optimized structures information, please refer to section 6.6.

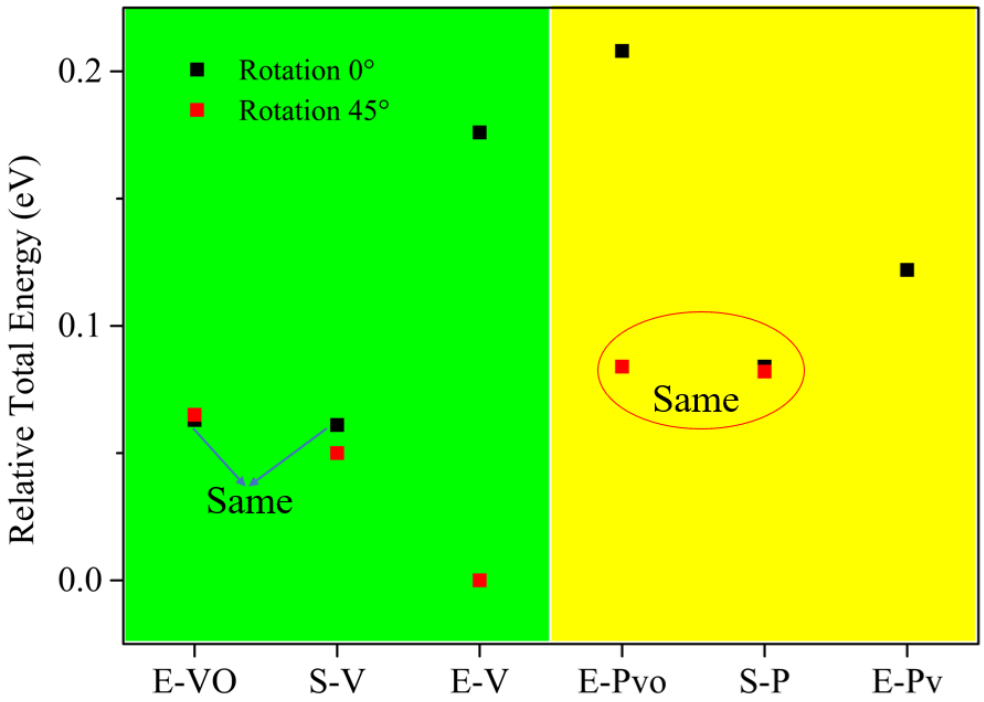

Figure 6-7. The relative total energy of 11 different configurations. The reference is E-V-45°. The green region means the ferrocene located on V/OV site, while yellow region means the ferrocene located on P/P site.

Considering the V-VO structures first, we see that the next lowest energy structure is the S-V-45°, with the E-OV-0°, E-OV-45°, and S-V-0° all having essentially the same energy. The highest energy is that of the E-V-0° structure. From the energy perspective, when the apex faced the O-V, we observe that the rotation degree does not significantly impact the total energy (E-OV-0° vs E-OV-45°), but it has a notable effect on the apex faced the V configurations (E-V-0° vs E-V-45°). This behavior can be attributed to the distortion of the ferrocene structure and the resulting changes in van der Waals interactions, discussed later in Section 6.4.5. Interestingly, we find that the initially staggered configuration with a rotation degree of 0° exhibited the same total

energy as the apex-faced O-V configuration, that is because the final relaxation structure shows that the ferrocene is actually not staggered but eclipsed, and thus the relaxation structure of S-V-0° is the same as E-OV-0°. Moreover, although the ferrocene with a rotation degree of 45° can be staggered, the total energy is higher 0.05 eV than the eclipsed configuration with a 45° rotation degree. Therefore, the ferrocene adopts an eclipsed over the staggered arrangement intercalated between V and O-V sites. Finally, the total number of unique configurations of ferrocene on the V/OV site is reduced from 6 to 5.

The lowest energy for the ferrocene over the P site is for the S-P-0°, S-P-45°, and E-P_{VO}-45°,each of which has the same energy. This could be attributed to the fact that these three configurations have identical final relaxation configurations. Unlike E-P-0° and E-P-90°, which retained the eclipsed ferrocene arrangement, these three configurations show that the orientation of ferrocene is rotated approximately 20° degree relative to the [010] direction in the (001) plane, and simultaneously companies with cyclopentadienyl rings structure deviating from an eclipsed or staggered conformations and settling to a gauche arrangement (Figure 6-8). So we call these three configurations as G-P-20°, where G represents gauche arrangement, P is ferrocene locates on P/P site and 20° repsresnts the ferrocene vector is rotated relative to the [010] direction.Furthermore, it is noteworthy that the G-P-20° configuration exhibits lower energies compared to the E-P_{VO}-0° and E-P_{V}-90° configurations. This implies that the ferrocene tends to adopt the structures depicted in Figure 6-8 rather than the eclipsed configuration when located on the P/P site. And thus the total number

of unique configurations of ferrocene intercalated between phosphorus is reduced from 5 to 3.

When we compare the total energy of ferrocene intercalated on V/OV and P/P, most configurations have lower total energy on V/OV than on P/P, except the E-V-0° configuration. Also, the lowest total energy is the E-OV-45° configuration, which is on the V/OV site. Therefore, we conclude that the ferrocene prefers to reside on the V/OV site rather than on the P/P site. This can be attributed to the charge transfer between vanadium and iron which is discussed in section 6.4.4.

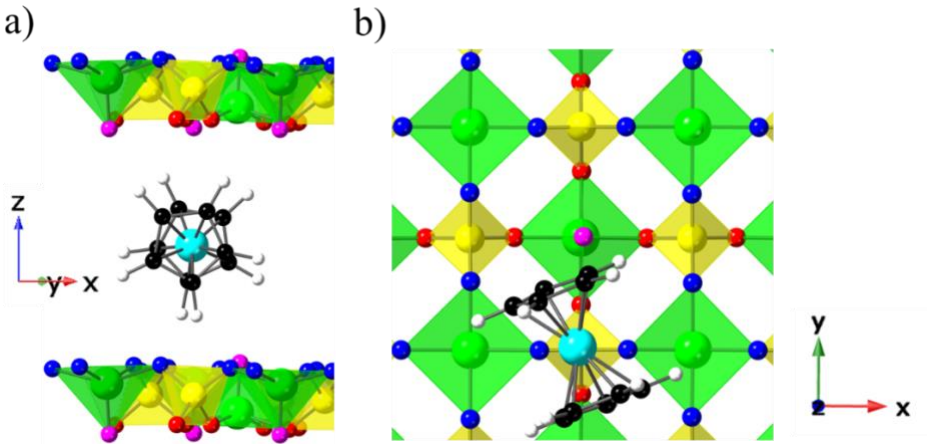

Figure 6-8. The optimization of the most stable (gauche) configuration of ferrocene intercalated between phosphorus and phosphorus, viewed a) along the [-120] direction and b) along the [001] direction.

In summary, our calculations identified three key points. First, the intercalation of ferrocene onto V/OV is energetically more favorable than on P/P, as evidenced by the lower total energy. Second, the configuration with the lowest total energy, indicating the most stable arrangement, is E-V-45°. Third, the ferrocene adopts eclipsed arrangement on the V/OV site, whereas on P/P, a stable configuration involves a gauche arrangement of the cyclopentadienyl rings along with a simultaneous rotation of the ferrocene vector by approximately 20° degree relative to the [010] direction in (001)

plane. These findings provide valuable insights into the preferred configurations and stability trends of ferrocene intercalated within the $VOPO_4$ matrix. The optimized structures in Figure 6-9.

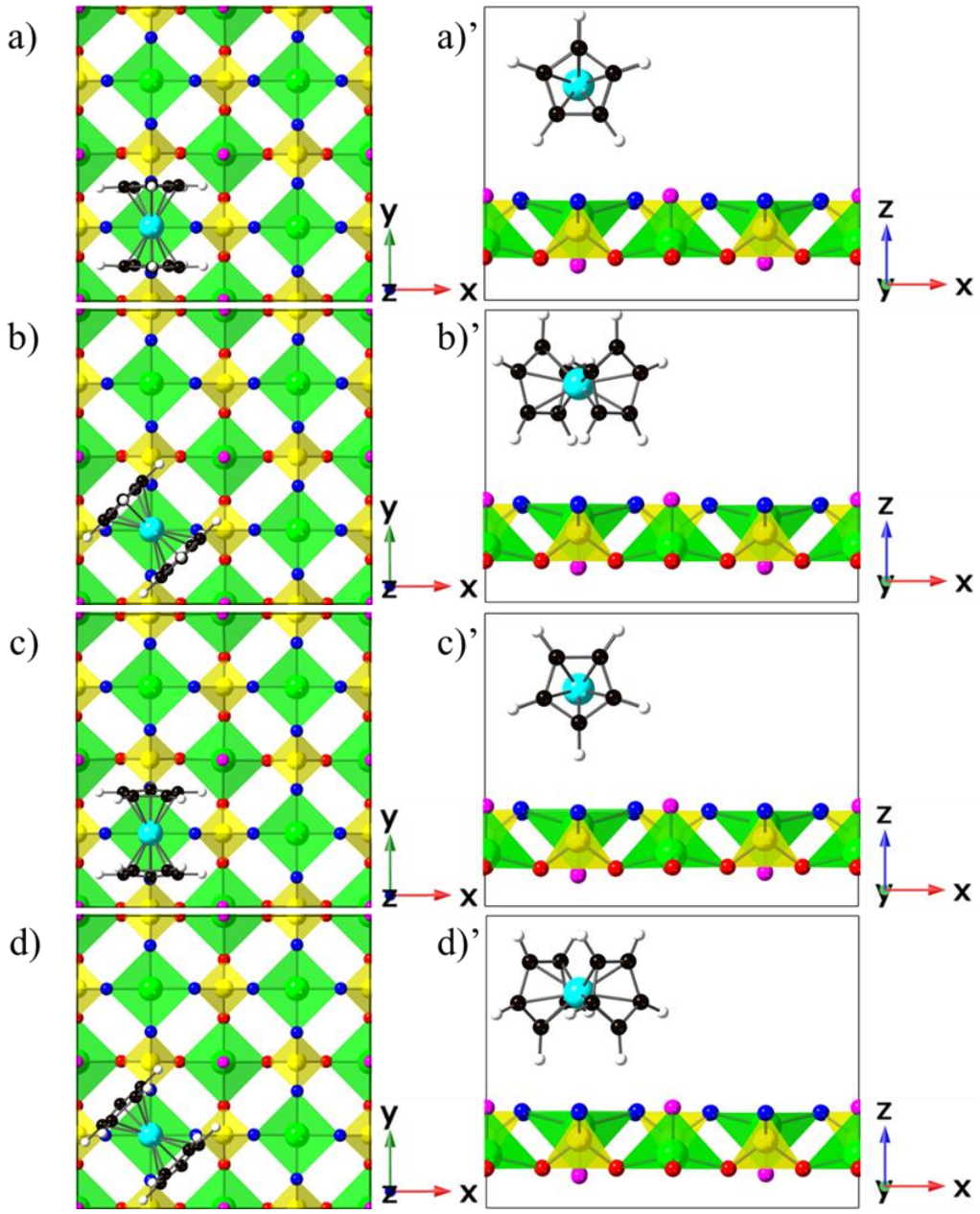

Figure 6-9. The configurations of a) E-OV-0°, b) E-OV-45°, c) E-V-0°, d) E-V-45°, e) S-V-45°, f) E-Pvo-0°, g) E-Pv-0°, and h) G-P-20° are viewed along the [001] direction. The corresponding pictures denoted with prime (') are viewed along the [010] direction.

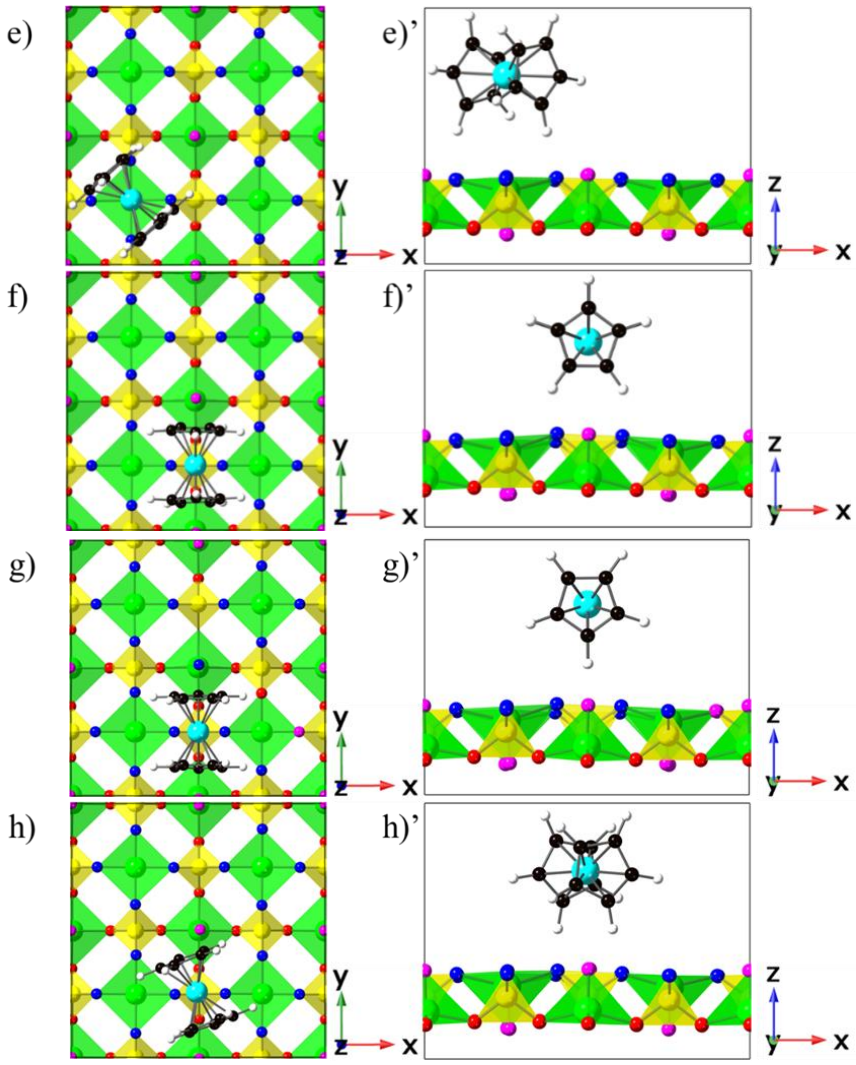

Figure 6-9. Continued.

6.4.4 Charge Density Difference

In Section 6.4.3, we explored the preference of ferrocene to intercalate onto the vanadium/oxygen-vanadium site rather than onto the phosphorus site within the $VOPO_4$ structure. To gain insights into the underlying mechanisms, we investigated the charge distribution after ferrocene intercalation. In a related experimental study on alpha-$VOPO_4$,[22] it was reported that the charge state of iron transitioned from +2 to +3, while

vanadium changed from +5 to +4. This indicates a charge transfer of one electron between iron and vanadium.

To compare, we performed Bader charge analysis[131–134]on the eight energetically distinct configurations identified in the energy and structure analysis. The results demonstrate that the charge on the ferrocene is approximately +0.95, with only slight variations among the different configurations in Figure 6-10. This finding is in good agreement with the experimental data.[22]

To visualize the charge transfer, we generated charge density difference maps for each structure. These maps were obtained by subtracting the charge density of the ferrocene-VOPO4 complex from the isolated ferrocene and the VOPO4 layer at the corresponding positions. In Figure 6-11, charge accumulations were observed on vanadium atoms, while charge deficits were observed on iron atoms, regardless of whether ferrocene is located above vanadium or phosphorus.

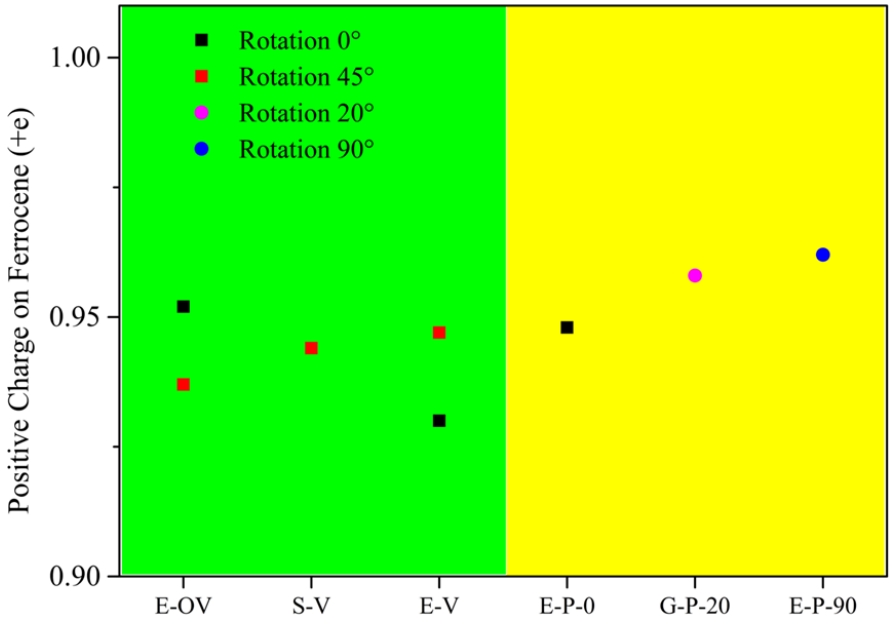

Figure 6-10. Bader charges analysis of eight unique configurations and compared them with experimental data.[175,22] The green region means the ferrocene located on V/OV site, while yellow region means the ferrocene located on P/P site.

However, when ferrocene is intercalated at the P/P site, four possible sites for charge accumulation on the vanadium are observed. These sites are labeled as V_Top, V_Bottom, V_Left, and V_Right, as illustrated in Figure 6-12. Considering the symmetry of $VOPO_4$ is tetrahedral, the V_Left should be equal to V_Right and V_Top should be equal to V_Bottom. Interestingly, upon applying charge accumulation to the right or left vanadium, the total energy difference between the two scenarios was $3.9*10^{-2}$ meV/atom. This negligible difference suggests that charge accumulation on either the right or left vanadium is essentially equivalent, in which proven our thoughts in Table 6-3.

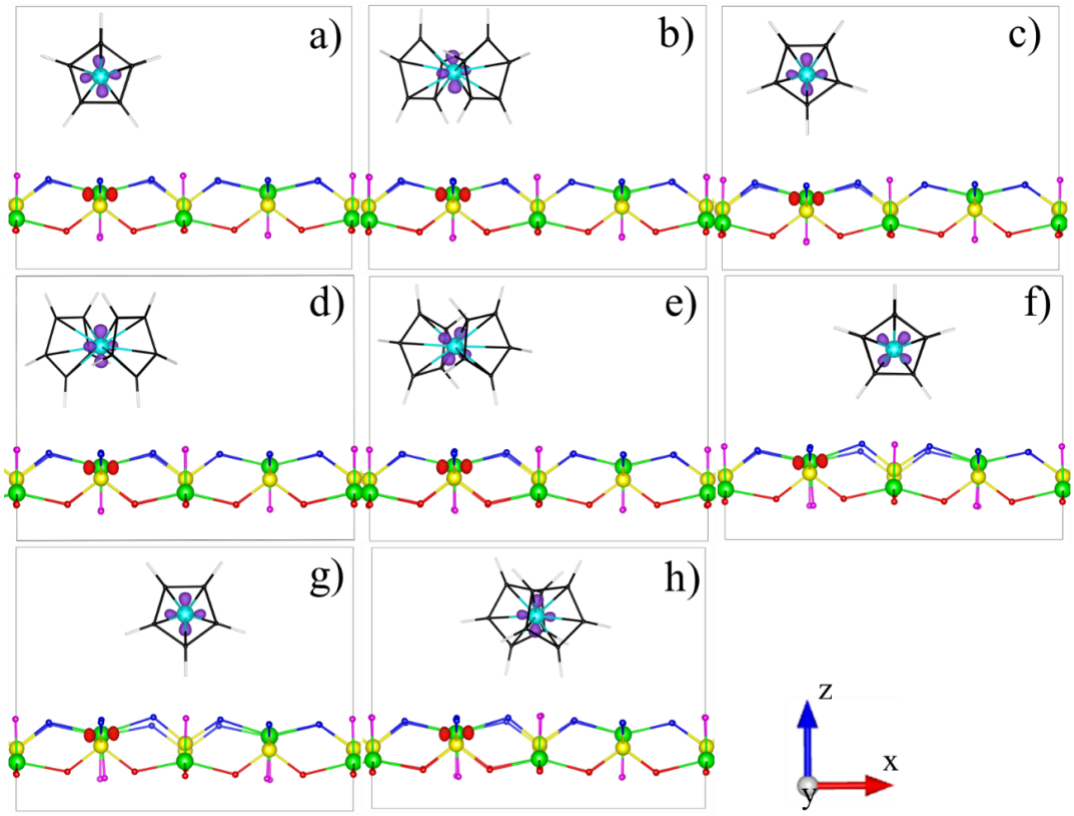

Figure 6-11. The charge density maps of a) E-OV-0°, b) E-OV-45°, c) E-V-0°, d) E-V-45°, e) S-V-45°, f) E-P-0°, g) E-P-90°, and h) G-P-20°. The red region means the charge accmulation, while the violet region means the charge reduction. The issovalue is 0.04 e/Å3. All of pictures viewed along [010] direction. The black box is the unit cell.

Table 6-3. The Relative total energy of four possible charge accumulation of vanadium. The reference is the charge accumulation on the left. Unit in eV.

Charge Accumulation	Relative total energy (eV)
V_Left	0
V_Right	+0.003
V_Top	+0.040
V_Bottom	+0.041

Also, the V_Top and V_Bottom shown the same total energy, but both are higher than the V_Left and V_Right, and thus, when the charge accumulation happen on the V_Top or V_Bottom, it was not as stable as the former two cases. At last, for consistency in our analyses, charge accumulation was applied on the left vanadium.

To gain further insights into charge accumulation, we constructed a plane using four vanadium atoms. This plane allows us to distinguish which vanadium atoms exhibit charge accumulation and which ones do not. In this work, we only shown the two most stable configurations located on vandanium and phosphorus respectively due to the very simliar charge distribution.

Figure 6-13 illustrates this plane and clearly shows that when ferrocene is located on vanadium, charge accumulation occurs. The ferrocene, which sits on top of the V at the bottom left has been omitted due to the clarity. The red region means the charge accumulation. The black box indicated the unit cell. The issovalue is 0.04 e/Å^3. However, none of the remaining three vanadium atoms nor any of the phosphorus, off this plane and at midpoints between the V atoms exhibit any charge transfer. While intercalated on phosphorus, it shows a similar charge difference with Figure 6-13a, as shown in Figure 6-13b.

As mentioned in Section 3.2, both iron and vanadium exhibit magnetic moments, resulting in dipolar coupling between them.[22] The dipolar coupling energy is determined

by the following equation 3-1.[195,196]

$$E = -\frac{\mu_0 \gamma_1 \gamma_2}{4\pi r^3}(3\cos^2\theta - 1) \quad (3\text{-}1)$$

Where, E is the dipolar energy term, γ_1 and γ_2 the magnetic dipole moments of the two atoms, respectively, μ_0 is the permeability and r is the distance between two atoms. θ is the angle between the line connecting two atoms and external magnetic field. And thus, the dipolar coupling energy is proportional to the product of two magnetic dipole moments and inversely proportional to the cube of the distance ($1/r^3$). As ferrocene moves from vanadium to phosphorus, the distance between iron and vanadium increases, leading to weakened dipolar coupling. This change is likely a contributing factor to the higher total energy when ferrocene is intercalated at the phosphorus site.

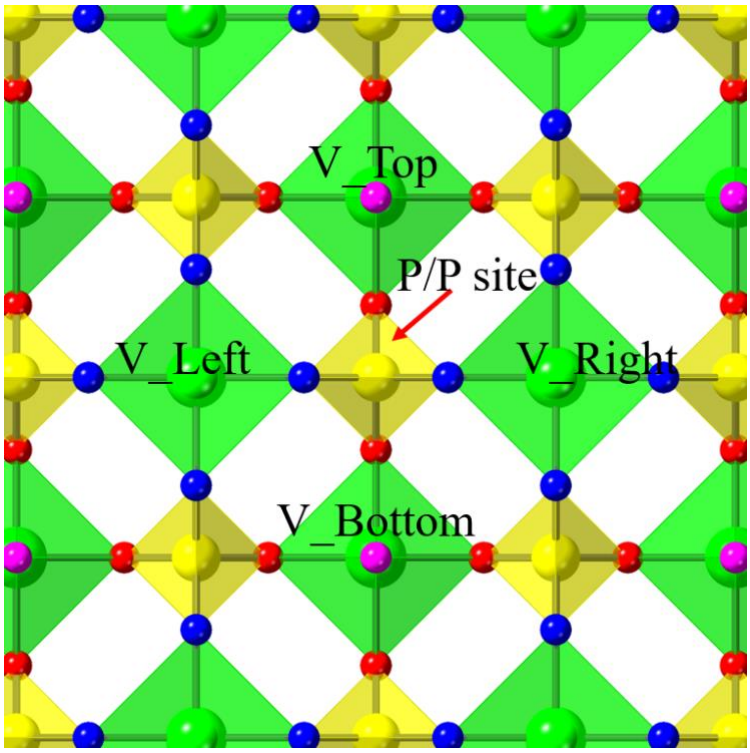

Figure 6-12. The four possible charge accumulations of vanadium.

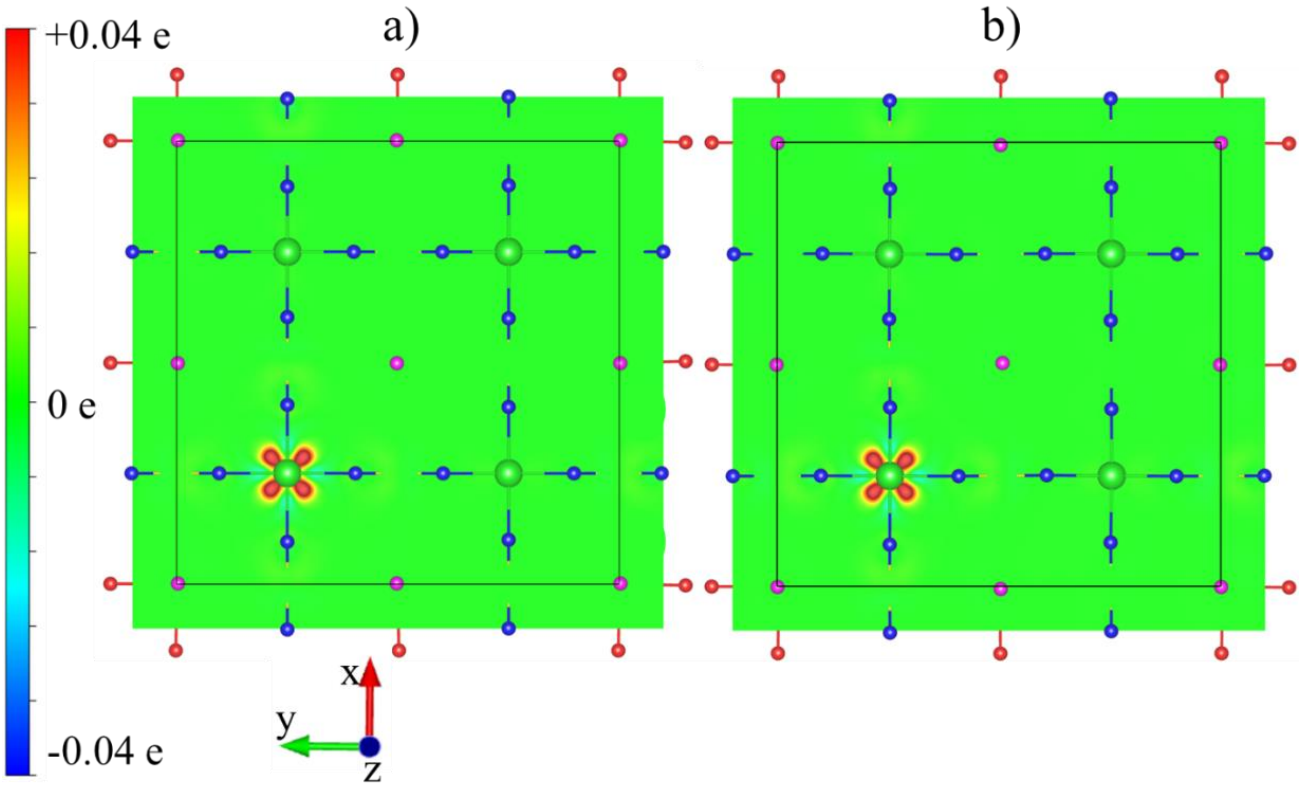

Figure 6-13. The charge density difference map a) E-V-45° and b) G-P-20° built by the four vanadium atoms, viewed along [001] direction.

Based on these findings, we conclude that the reason that ferrocene prefers to stay on vanadium rather than phosphorus is due to the stronger dipolar coupling. The charge accumulation on vanadium indicates a favorable interaction between ferrocene and vanadium, contributing to the stability of the ferrocene intercalated system.

6.4.5 The Electron Localized Function Plots and Hirshfeld Surface Analysis

The analysis presented in Figure 6-7 elucidates the variation of the system's total energy based on the orientation and rotation of the cyclopentadienyl ring in ferrocene intercalated between vanadium and oxygen-vanadium. The primary objective of this section is to gain a comprehensive understanding of the underlying mechanisms driving this variation. When the hydrogen apex from the cyclopentadienyl ring faced oxygen-

vanadium, namely, E-OV configurations, the distortion of the ferrocene remains minimal for in-plane rotations of both 0° and 45°. However, substantial distortion of ferrocene occurs on E-V configurations in Figure 6-14. For rotations of 0° and 45°, the bottom of the cyclopentadienyl ring, where the apical hydrogen faces the V side, expands, while the top shrinks. To determine the cyclopentadienyl ring's distortion, we measured the dihedral angle between the rings (Table 6-4). A higher dihedral angle in the E-V configurations indicates greater distortion in Figures 6-14c and 14d. This distortion of ferrocene can be attributed to two potential reasons. Firstly, it arises from the interactions between the apical hydrogen atoms in the cyclopentadienyl ring and the VO_5 oxygen atoms, leading to van der Waals forces that induce the distortion of the ferrocene cyclopentadienyl ring. Secondly, the distortion might arise from the enhanced electrostatic interactions between the cationic component ($[Cp_2Fe]^+$) and the anionic counterpart ($[VO_5]^-$), a phenomenon which can be described within the framework of the polarizable ion model (PIM).[197]

For the first reason, the distortion of the ferrocene tends to increase the total energy, whereas the van der Waals interactions tend to decrease it. To quantitatively assess the impact of ferrocene distortion, we isolated the ferrocene moiety from the relaxed structure and conducted a single-point calculation, comparing it to the original ferrocene in Table 6-4. Remarkably, the ferrocene extracted from the E-V configurations exhibits the highest relative energy, aligning with our initial assumptions. In other words, E-V-0° possesses a higher total energy than E-VO-0° primarily due to the dominance of ferrocene distortion energy over the reduction in van der Waals energy. However, as

the ferrocene rotates to 45° degrees, the van der Waals interactions strengthen, leading to lower total energy of the system.

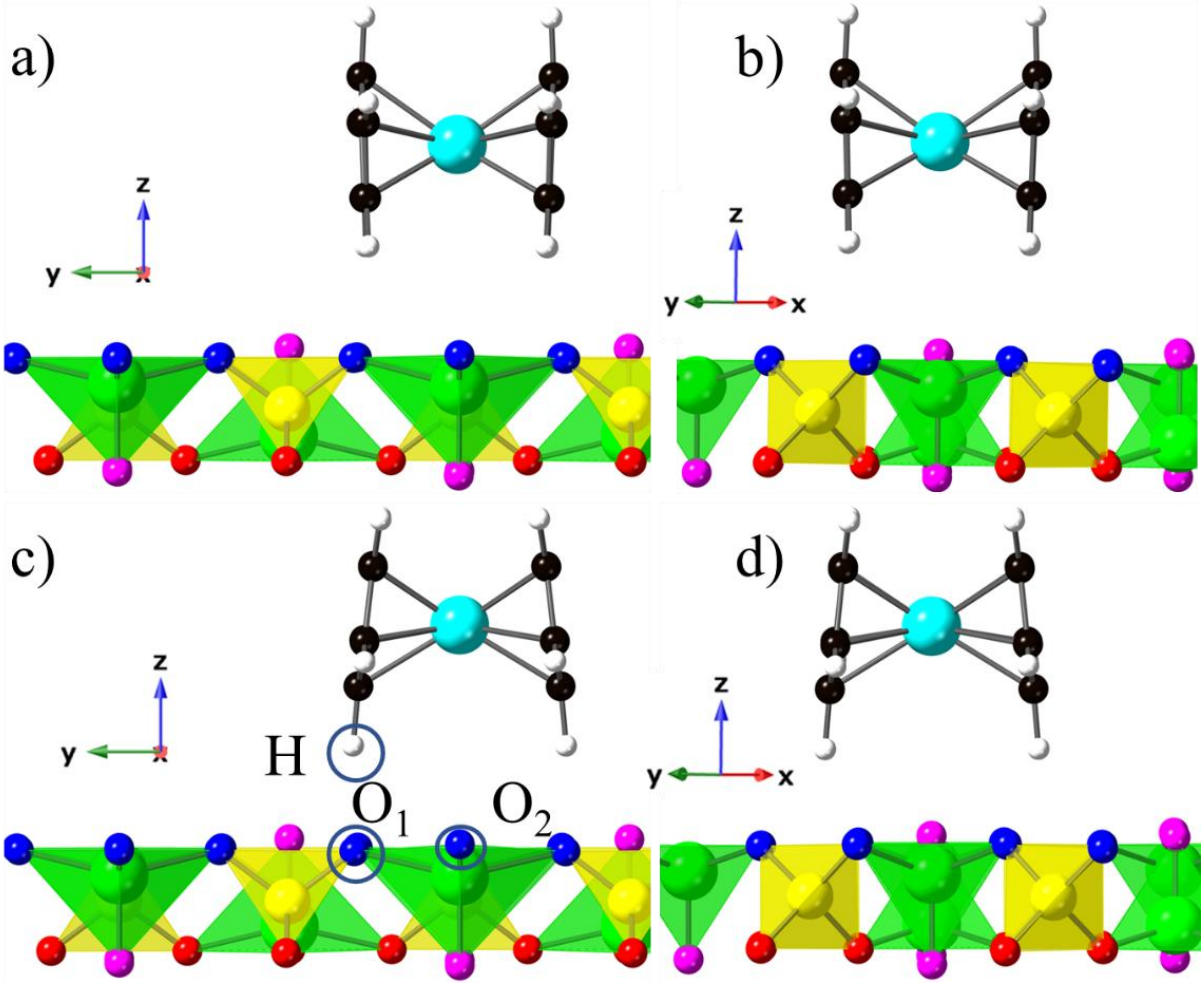

Figure 6-14. The crystal structure of a) E-OV-0° configuration, viewed along [100] direction; b) E-OV-45° configuration, viewed along [110] direction; c) E-V-0° configuration, viewed along [100] direction; and d) E-V-45° configuration, viewed along [110] direction.

Table 6-4. The relative total energy in eV of ferrocene extracted from the $VOPO_4$ layer compared to that of pure ferrocene.

Name	Dihedral Angle (°)	Relative Total Energy
Pure Eclipsed Ferrocene	0	0
E-VO-0° Ferrocene	2.98	+0.15
E-VO-45° Ferrocene	2.34	+0.15
E-V-0° Ferrocene	13.49	+0.21
E-V-45° Ferrocene	12.04	+0.20

To underscore the significance of the van der Waals correction, we perform calculations on the four configurations both with and without the D3 correction. The dihedral angles of ferrocene exhibit minimal deviation irrespective of the presence of the D3 correction, indicating that the optimized geometries are congruent in both scenarios. Nonetheless, upon detailed examination of the total energies present in Table 6-5, discrepancies become evident. The configuration E-V-45° is identified as the most energetically stable in the presence of the D3 correction, whereas the E-VO-0° and E-VO-45° configuration are most stable in without D3 correction. Furthermore, the energy difference between E-V-0° and E-V-45° increases (0.067 eV to 0.176 eV) when the D3 correction is applied, suggesting a stronger van der Waals force in the E-V-45° configuration. In summary, van der Waals forces play a pivotal role in the distortion of ferrocene.

Table 6-5. Relative total energy comparison: with D3 (Reference: E-V-45°) versus without D3 (Reference: E-VO-0°) in eV.

Name	W/ D3 correction	WO/D3 correction
E-VO-0°	+0.063	0
E-VO-45°	+0.065	0
E-V-0°	+0.176	+0.118
E-V-45°	0	+0.051

To reinforce this idea, we plotted the electron localization function (ELF)[135] to examine the interaction between hydrogen atoms and oxygen atoms (specifically O_1 and O_2, these two are the two closest oxygens to the hydrogen) in Figure 6-14c. The ELF is a scalar function ranging from 0 to 1, and it provides insight into the probability density of locating a pair of electrons with the same spin near a reference electron pair. Koumpouras[136] *et al.* reported as follows: values above 0.7 indicate electron localization in the core, covalent bonding, or lone pair regions; values between 0.7 and 0.2 suggest

electron-gas behavior or presence in metallic bonds; values below 0.2 indicate delocalized electrons involved in non-covalent bonds. Furthermore, if ELF is less than 0.2 but not zero and exhibits a V-shaped pattern, it signifies van der Waals interaction. An ELF value approaching zero (less than 0.01) indicates an ionized bond.

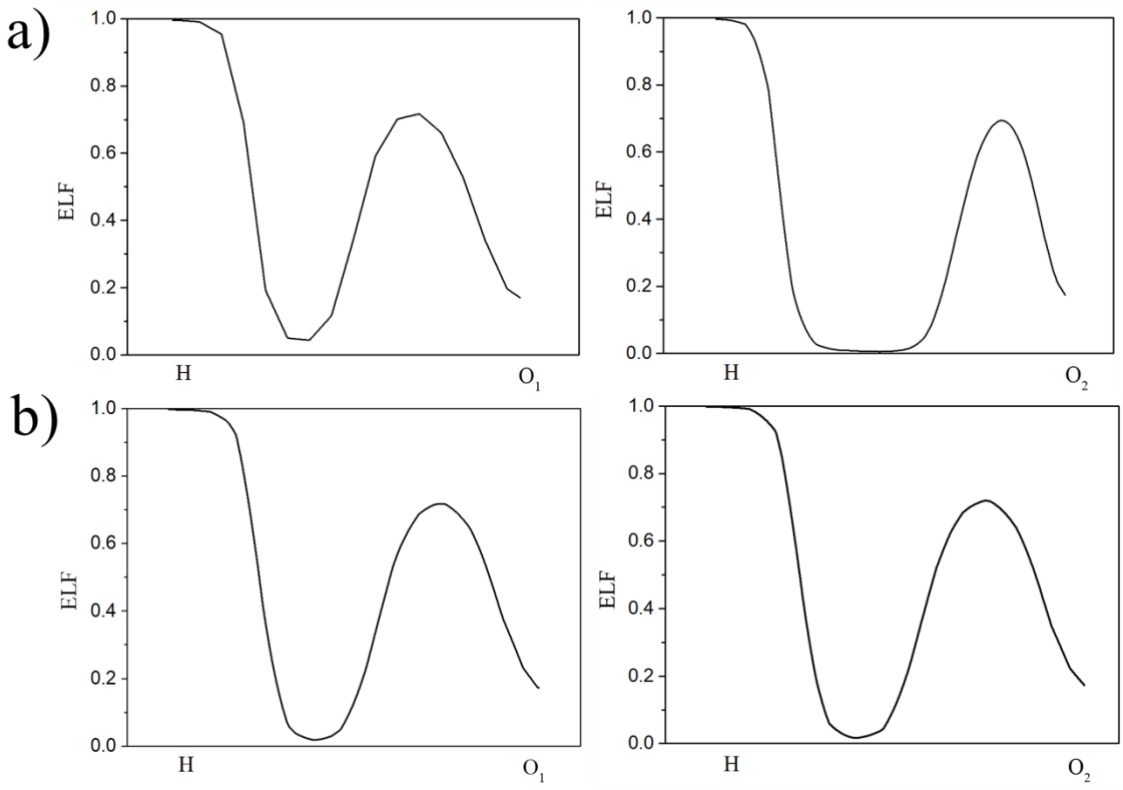

Figure 6-15. The linear profile ELF of H to O_1 and O_2, a) E-V-0° and b) E-V-45°.

In Figure 6-15a, E-V-0° configuration, the ELF analysis clearly shows that the hydrogen and O_1 atoms possess a non-zero, confirming the presence of van der Waals interaction. However, no van der Waals interaction is observed between the hydrogen atom and O_2, as evidenced by the zero value at the minimum point. Nevertheless, when examining the E-V-45° configuration in Figure 6-15b, it becomes apparent that van der Waals interactions exist between the hydrogen atom and both O_1 and O_2. Thus, our

findings support the notion that this configuration exhibits the lowest total energy due to stronger van der Waals interactions.

For the second reason, PIM, we constructed a supercell in the 'c' direction, as illustrated in Figure 6-16a. This supercell comprises two distinct layers: one intercalated with ferrocene and the other without. According to the principles of the polarizable ion model, the observed bending of ferrocene can be traced back to intensified ferrocene anion-cation interactions with the vanadyl layer. Within two distinct layers, iron may engage in charge transfer with either the bottom or the top vanadyl layer. In scenarios where charge transfers with the bottom layer, the ferrocene exhibits a distortion oriented facing the V side, and conversely, when it's with the top layer, the distortion is towards the V-O side. However, it reveals charge transfer exclusively with the bottom layer after relaxation, resulting in ferrocene consistently facing the V side, as clearly shown in Figures 6-16b.

Despite these findings, the definitive functioning of the PIM remains uncertain. To gain further clarity, we employed the Hirshfeld surface analysis[187] as used in Malischewski *et al.*[197] work. In our supercell study, the E-VO-0° configuration reveals a slight electron density between the bottom vanadyl layers, evident in Figure 6-17a. However, E-V-45° (Figure 6-17b) reveals a denser electron presence between iron and the bottom vanadyl layer. This stronger electron density between the iron and the bottom layer of vanadyl in the E-V-45° configuration supports the theory that ferrocenium maintains a stronger electrostatic anion-cation interaction with the bottom vanadyl layer. Consequently, it can be inferred that the PIM also plays a role in causing the observed bending of ferrocene.

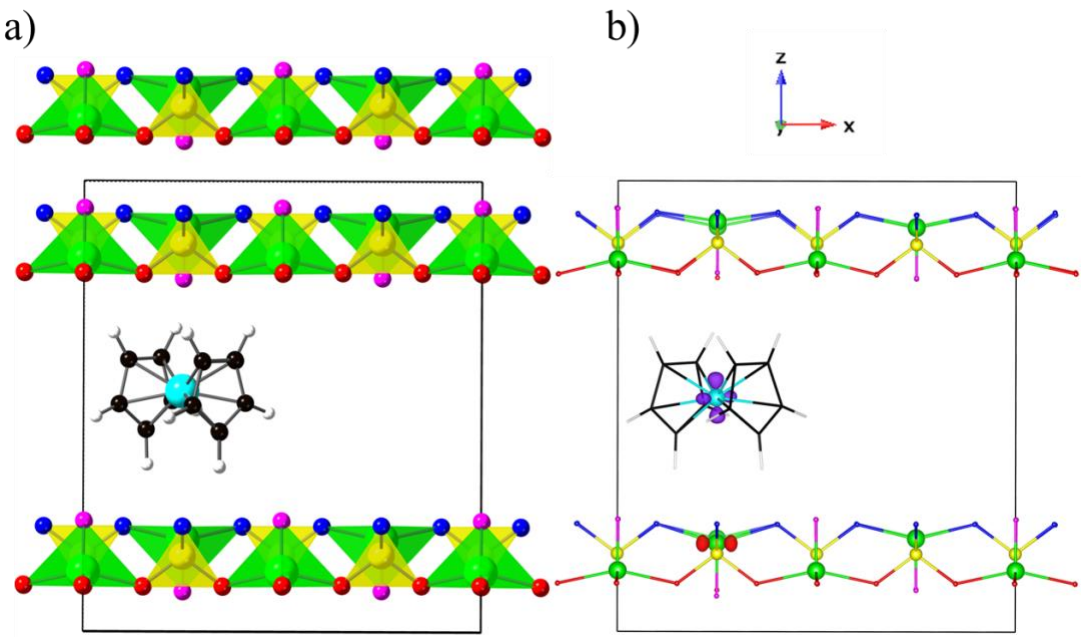

Figure 6-16. The supercell structure of a) E-V-45° configuration, and b) the corresponding charge density difference map, the isovalue is 0.04 e/Å^3, viewed along [010] direction. The black box is the supercell structure.

6.4.6 Ferrocene Immigration Energy Preliminary Results

6.4.6.1 Ferrocene move along [110] direction

In Section 6.4.3, the E-V-45° configuration emerges as the most stable. Beginning with this configuration, we proceed by moving along the [110] direction. It's recognized that from one V position to the next, there exists a symmetrical pattern. Consequently, for efficient computation, we only need to analyze half of this pattern, specifically from V to the VO side. This process is visualized in Figure 6-18 for clarity.

Figure 6-19 displays the energy barrier, for which we utilized the NEB method with 17 images. As observed, the migration energy approximates 0.25 eV. From a structural viewpoint, we noticed a change in the dihedral angle of the cyclopentadienyl ring. We've measured this alteration, as presented in Figure 6-20.

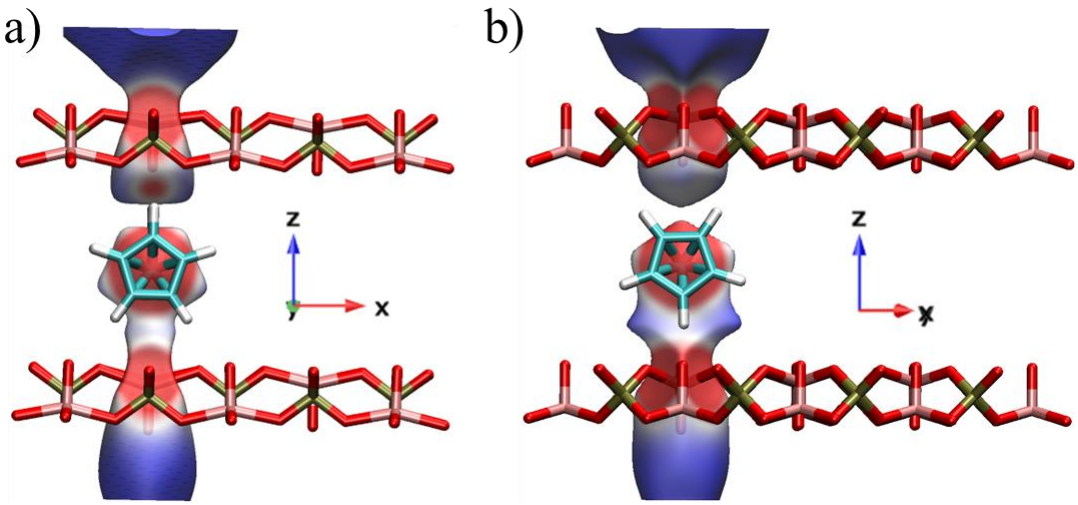

Figure 6-17. The Hirshfeld surface analysis of a) E-VO-0°, viewed along [010] direction, and b) E-V-45°, viewed along [-110] direction. Red means high electron density, white means medium electron density and blue means low electron density.

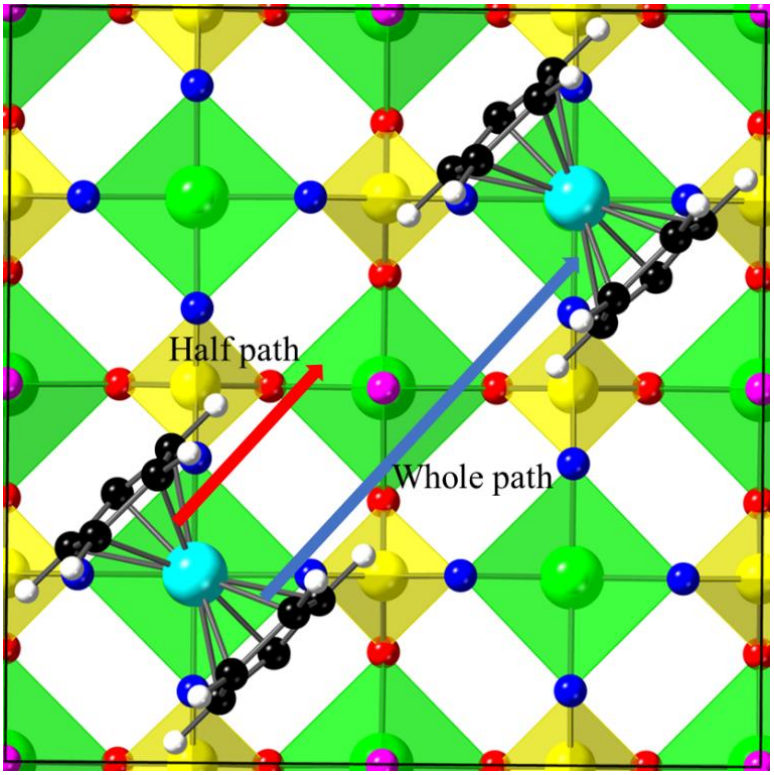

Figure 6-18. The schematic representation showcases ferrocene moving along the [100] direction. The blue arrow depicts the entire path, while the red arrow represents half of that path.

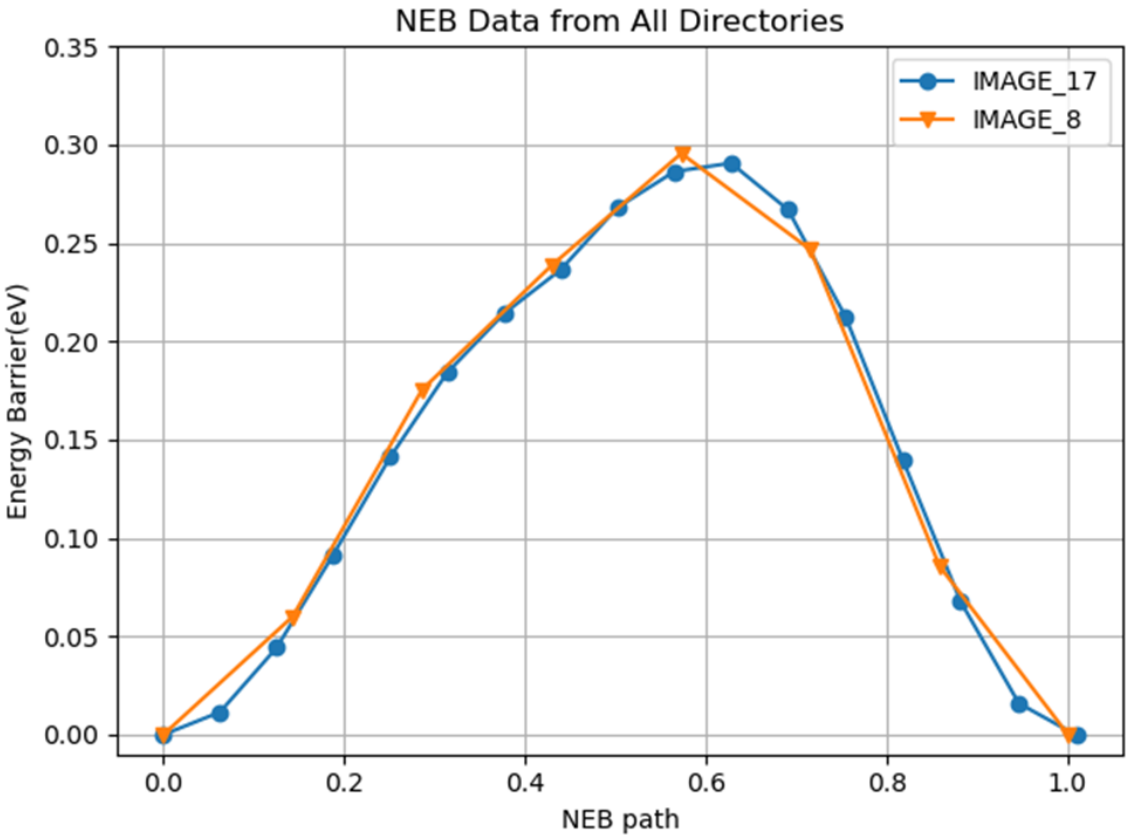

Figure 6-19. The energy barrier of ferrocene moving along [110] direction by using NEB method, blue is eight (coarse) images and orange is seventeen(dense) images.

The precision of migration energy calculations increases with the number of intermediate images we use between the initial and final states. However, it's crucial to find a balance between computational efficiency and result accuracy. As shown in Figure 6-19, we compared results using 17 images with those using 7 images. While the exact location of the peak migration energy differed slightly between the two, the peak values were strikingly similar. Notably, the overall migration path using 7 images closely resembled that from the 17-image approach. Based on these observations, we've decided to utilize less images for our upcoming calculations to achieve both efficiency and accuracy.

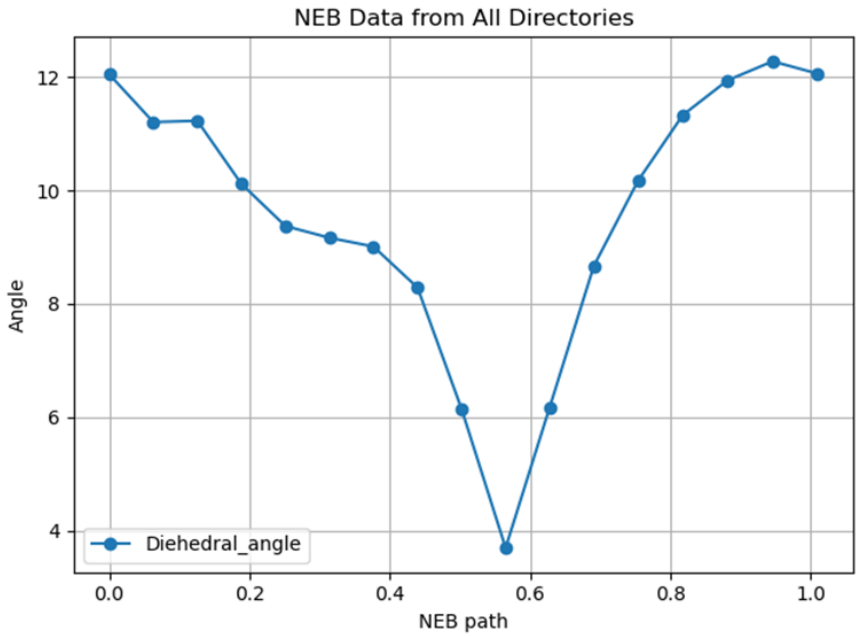

Figure 6-20. The dihedral angle of cyclopentadienyl ring.

6.4.6.2 Ferrocene move along [100] direction

In the section 6.4.3, we identified eight distinct configurations: five for the V/OV intercalation site and three for the P/P site. In this section, we employ the NEB method to compute the migration energy barrier along [100] direction. It's intricate to account for the various configurations of ferrocene during intercalation at both the V/OV and P/P sites. These complexities arise due to the arrangement of the cyclopentadienyl ring and the rotation of the ferrocene molecule. To simplify this, we used the eight configurations identified in the previous calculations as initial guesses and kept the ferrocene fixed during the NEB calculations. Preliminary results of these computations are presented in Figure 6-21.

We observe three distinct steps. Initially, the red square is the most stable around 0.3. This is followed by the blue circle being the most stable between 0.3 and 0.85. Finally, the black circle emerges as the most stable. As a result, the configurations

of ferrocene may transition from E-V-45° to E-P-90°, and finally to G-P-20°. These findings are somewhat ambiguous, and we plan to delve deeper into this area to discern the true optimal path as ferrocene moves through the layers.

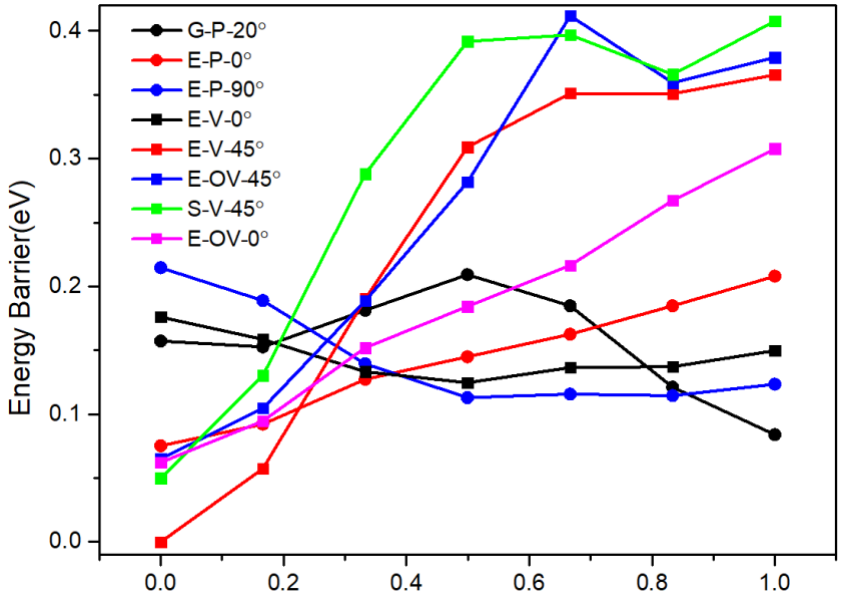

Figure 6-21. The NEB calculations of ferrocene immigrated through VOPO4.

6.7 Conclusions

In this study, DFT calculations (GGA+U_D3) accurately reproduced experimental observations for ferrocene intercalation into $VOPO_4$. The calculated bond lengths and stability of the eclipsed configuration of ferrocene, lattice expansion, Bader charge analysis, and charge density differences all agreed well with experimental data. Thus, the DFT method reliably captures the structural, energetic, and charge-related aspects of the intercalation process.

We investigated the 11 possible configurations of ferrocene intercalation into the $VOPO_4$ layer. By optimizing these configurations, we found that there are only 8 distinct configurations due to some of them having the same final equilibrated structures. From

the perspective of relative total energies, our calculations revealed three key findings. First, ferrocene prefers to reside on V/OV rather than on P, attributed to charge transfer between iron and vanadium. Second, the most stable configuration is E-V-45°, which exhibits stronger van der Waals interactions between hydrogens of the cyclopentadienyl ring and oxygens of the VO_5 group, as supported by the electron localization function (ELF) analysis. Third, ferrocene adopts an eclipsed conformation intercalated between vanadium and oxygen-vanadium, while gauche conformation between phosphorus and phosphorus.

However, when ferrocene diffused from the V/OV site to the P/P site, it needs to overcome the Coulombic attraction forces resulting from charge transfer between vanadium and iron. Additionally, the configuration of ferrocene undergoes changes upon intercalation in both the V/OV and P/P sites, including the arrangement of the cyclopentadienyl ring and rotation of the ferrocene molecule. Consequently, the diffusion behavior of ferrocene is complex. Therefore, this paperwork provides a valuable starting point for future analysis of diffusive behavior. In the future, we will carry out these structures and use nudged elastic band calculations[198,199] to elucidate the energy barriers associated with the diffusion of ferrocene on the $VOPO_4$ layer. And then, these calculations would provide insights into the dynamics and kinetics of ferrocene intercalation, further enhancing our understanding of the intercalation process.

CHAPTER 7
SUMMARY AND FUTURE WORK

In Chapter 3, we examined the dissociation energy of the uranyl cation and its binding with the Zr-MOF metal node. We analyzed 19 unique uranyl cation configurations within Zr-MOFs. To ensure accuracy, we benchmarked our simulations of pristine Zr-MOF, using the GGA+U_D3 and VASPsol methods, both of which aligned well with experimental data. Moreover, the hydration energy for the uranyl cation matched existing literature values. However, as we further examined the uranyl cation's behavior when attached to the metal node, complexities arose. We modeled scenarios for both charged and neutral systems. The binding energies derived from charged systems presented inconsistencies, leading us to utilize a neutral system in which we artificially incorporated two additional hydroxy groups to balance the charge. Notably, while the trends observed using the aforementioned methods were consistent, there were discrepancies in the absolute values.

We then examined the binding preferences of the uranyl ion within the Zr MOFs. Our findings corroborated prior research regarding the bonding of the uranyl ion to surfaces like titanium dioxide and calcite. In these earlier studies, binding energy was predominantly influenced by the protonation state of the surface and the specific binding sites. First, our results showed that the binding affinity of the uranyl ion markedly enhanced in deprotonated of Zr-MOF compared to its protonated counterparts. This was attributed to a greater amount of charge transfer in deprotonated states between Zr-MOF and uranyl cation. Second, among the total 19 configurations explored, the most stable one involved the uranyl ion attaching to both the deprotonated middle oxygen and the edge oxygen of the Zr metal node, as it facilitated not only the U–O

bonds but also formed a Zr-O_u bond between the Zr-MOF and the axial oxygen present on the uranyl ion.

In Chapter 3, our study emphasized the significant capability of Zr-MOFs to form stable bonds with uranyl ions. Despite the influence of protonation levels on binding strength, which varied with the system's pH, some binding sites consistently showed strong affinities over a broad pH range. This suggested that Zr-MOFs held immense promise as key materials for effectively capturing uranyl ions.

In Chapter 4, our primary focus was on the organic ligand binding with radionuclides: understanding the binding of cerium nitrate to the crown ether system using computational methods. We employed both GGA+U and VDW_DF2+U methodologies, and our findings aligned closely with experimental data. Specifically, the VDW_DF2 method revealed a more negative binding energy. This underscored the pivotal role van der Waals interactions played in the cerium nitrate and crown ether relationship. This conclusion was strengthened by the electron localization function (ELF) analysis, illustrating characteristics typical of van der Waals interactions. Therefore, the VDW_DF2 method stood out as ideal for computing the binding energy, particularly due to the limitations of DFT_D3 for americium and curium elements. We also incorporated the solvation effect via the VASPsol method, although the binding energy was less negative in a solvated environment compared to a vacuum, the binding process remained thermodynamically favorable.

In Chapter 4, we also found that the similarity in binding energies for cerium, americium, and curium nitrates with the 18-crown-6 ether. This suggests the potential of using cerium nitrates as surrogates for the more complex americium and curium

nitrates, pointing to cerium's analogous interaction behavior with the crown ether. Further, we probed the effects of substituting oxygen in the crown ether ring with other elements like amine. A pattern emerged, relating the number of amine groups in the ring to binding energy. When compared, amine and imine substitutions exhibited the highest binding energy, largely due to extensive charge transfers with actinide atoms. However, substitutions with sulfur or phosphorus were less effective. Thus, imine/amine-substituted crown ethers seem poised as efficient ligands for radionuclide capture in MOFs.

In our future research, there are still two primary areas of focus that warrant further exploration and investigation. First, our studies operated under the premise of nitrate groups remaining coordinated to metal ions, allowing for comparability with other DFT studies and experimental findings. Even in simulations considering hydration via VASPsol, nitrates persisted in coordination. Addressing the challenge of simulating cerium nitrate in 18-crown-6 ether, where nitrates dissolve in water, is on our future research agenda. Secondly, we're also keen on probing the modification potentials of other crown ethers. By substituting oxygen atoms with nitrogen in these ethers and combining these findings with experimental designs of novel MOFs, we envision enhancing the capacity of MOFs for radionuclide waste management. Through the synthesis of computational and experimental methodologies, we aim to enhance strategies for managing actinide-contaminated environments.

In Chapter 5, our focus was directed towards understanding the formation energy of Secondary Building Units (SBUs) that incorporate both Zr and Th elements. An additional layer to our investigation delved into the energy dynamics in the presence of

organic ligands. Analyzing the data, a clear pattern was observed: the Th-SBU consistently exhibited a more negative binding energy relative to its Zr-based counterpart. This trend offers a compelling argument, indicating that the Th-based MOFs likely possess enhanced stability when compared to the frameworks that rely on Zr-MOFs.

In Chapter 5, we then also conducted a comparative analysis of U-SBU and Th-SBU. Our main aim was to quantify the transmetallation energy required during the transition from U-SBU to Th. Remarkably, our computed values for transmetallation energy and bandgap aligned perfectly with experimental data. This congruence not only reinforced our trust in the accuracy of our computational models but also highlighted the potential benefits of substituting U-SBU with Th. Expanding on this approach, we then examined the transmetallation process involving the replacement of U-SBU by Pu. The results were unequivocal: the observed negative binding energy strongly suggests a thermodynamic favorability for this substitution. This finding presents significant implications, suggesting new strategies for capturing and managing plutonium ions. Expanding our investigative scope, we delved into the dissociation energy landscapes of both Th-SBU and U-SBU. Central to our inquiry were three specific protonation sites. In a surprising turn of events, the energies delineated from both frameworks exhibited marked similarity, presenting an unexpected confluence.

In Chapter 6, we examined the complex intercalation mechanism of ferrocene into $VOPO_4$ using the GGA+U_D3 methods. It is noteworthy that the computational outcomes corresponded closely with the empirical findings, underscoring the robustness of the chosen computational approach. Detailed computational insights into parameters

such as bond length variations, stability trends of the eclipsed configuration of ferrocene, modifications in the lattice structure, Bader charge distribution, and variations in charge density were congruent with the experimentally derived data.

Subsequently, our investigation adopted a rigorous methodology, probing 11 unique configurations associated with ferrocene's intercalation into the $VOPO_4$ layer. However, upon optimization, these configurations culminated into merely 8 distinct structures, a manifestation of certain configurations converging to equivalent equilibrated structures. A threefold insight was derived from our calculations in terms of relative total energies. Foremost, ferrocene exhibited a preference for the V/OV site over the P site. This inclination can be attributed to electron charge transfer between the iron and vanadium atoms. Secondly, the most stable configuration is the E-V-45° configuration, this was predominantly attributed to enhanced van der Waals interactions between the hydrogens of the cyclopentadienyl ring and the oxygens of the VO5 group, a deduction further substantiated by electron localization function (ELF) examinations. Lastly, the intercalated ferrocene presented an eclipsed conformation when positioned between the vanadium and oxygen-vanadium sites, whereas a distinct gauche conformation was observed between the phosphorus sites.

In Chapter 6, we noted a significant observation during ferrocene's shift from the V/OV interstitial site to the P/P position: the molecule underwent distinct dipolar coupling forces. This phenomenon can be attributed directly to the charge transfer interactions occurring between the iron and vanadium centers Along with this transition, there was a noticeable alteration in ferrocene's structural makeup as it intercalated at the V/OV and P/P sites. This was evident in the changed orientation of the cyclopentadienyl ring and

the molecule's rotational dynamics. Taking into account these transformations, the diffusion pathway of ferrocene within the $VOPO_4$ structure can be described as being complex and multifaceted.

In light of these findings, our study serves as a foundational blueprint for subsequent investigations into diffusive behaviors. Our forward-looking strategy encompasses a more granular exploration of these structures, harnessing the prowess of nudged elastic band calculations. Such initiatives are geared towards elucidating the energy barriers inherent to the diffusive pathway of ferrocene across the $VOPO_4$ substrate. We anticipate that these forthcoming calculations will shed light on the dynamism and kinetics of ferrocene intercalation, enriching our grasp on the nuanced intercalation mechanism.

Across all chapters, a recurring theme is the exploration of MOFs as multifunctional materials capable of interacting with various ions and molecules. The chapters collectively demonstrate the adaptability and potential of MOFs in environmental and materials science applications, from ion capture and stabilization to understanding dynamic intercalation processes. The methodologies and findings in each chapter contribute to a holistic understanding of MOFs' capabilities, suggesting new pathways for future research and applications in areas like waste management, environmental remediation, and advanced material design.

LIST OF REFERENCES

(1) Brook, B. W.; Alonso, A.; Meneley, D. A.; Misak, J.; Blees, T.; van Erp, J. B. Why Nuclear Energy Is Sustainable and Has to Be Part of the Energy Mix. *Sustain. Mater. Technol.* **2014**, *1–2*, 8–16. https://doi.org/10.1016/j.susmat.2014.11.001.

(2) Zhan, L.; Bo, Y.; Lin, T.; Fan, Z. Development and Outlook of Advanced Nuclear Energy Technology. *Energy Strateg. Rev.* **2021**, *34*, 100630. https://doi.org/10.1016/j.esr.2021.100630.

(3) Alqadami, A. A.; Naushad, M.; Alothman, Z. A.; Ghfar, A. A. Novel Metal–Organic Framework (MOF) Based Composite Material for the Sequestration of U(VI) and Th(IV) Metal Ions from Aqueous Environment. *ACS Appl. Mater. Interfaces* **2017**, *9* (41), 36026–36037. https://doi.org/10.1021/acsami.7b10768.

(4) Milvy, P.; Cothern, R. Scientific Background for the Development of Regulations for Radionuclides in Drinking Water. *Radon, radium uranium Drink. water* **1990**, 1–15.

(5) Yemisi Olobatoke Manny Mathuthu, R.; Vet Anim Sci, T. J.; Yemisi OLOBATOKE, R.; Mathuthu, M. Radionuclide Exposure in Animals and the Public Health Implications. *Turkish J. Vet. Anim. Sci.* **2015**, *39* (4), 381–388. https://doi.org/10.3906/vet-1502-85.

(6) zur Loye, H.-C.; Besmann, T.; Amoroso, J.; Brinkman, K.; Grandjean, A.; Henager, C. H.; Hu, S.; Misture, S. T.; Phillpot, S. R.; Shustova, N. B.; Wang, H.; Koch, R. J.; Morrison, G.; Dolgopolova, E. Hierarchical Materials as Tailored Nuclear Waste Forms: A Perspective. *Chem. Mater.* **2018**, *30* (14), 4475–4488. https://doi.org/10.1021/acs.chemmater.8b00766.

(7) Zeng, X.; Li, M.; Abd El-Hady, D.; Alshitari, W.; Al-Bogami, A. S.; Lu, J.; Amine, K. Commercialization of Lithium Battery Technologies for Electric Vehicles. *Adv. Energy Mater.* **2019**, *9* (27), 1900161. https://doi.org/10.1002/aenm.201900161.

(8) Manthiram, A. Materials Challenges and Opportunities of Lithium Ion Batteries. *J. Phys. Chem. Lett.* **2011**, *2* (3), 176–184. https://doi.org/10.1021/jz1015422.

(9) Doose, S.; Mayer, J. K.; Michalowski, P.; Kwade, A. Challenges in Ecofriendly Battery Recycling and Closed Material Cycles: A Perspective on Future Lithium Battery Generations. *Metals (Basel).* **2021**, *11* (2), 291. https://doi.org/10.3390/met11020291.

(10) Manthiram, A.; Goodenough, J. B. Layered Lithium Cobalt Oxide Cathodes. *Nat. Energy* **2021**, *6* (3), 323–323. https://doi.org/10.1038/s41560-020-00764-8.

(11) Zhang, H.; Yang, Y.; Ren, D.; Wang, L.; He, X. Graphite as Anode Materials: Fundamental Mechanism, Recent Progress and Advances. *Energy Storage Mater.* **2021**, *36*, 147–170. https://doi.org/10.1016/j.ensm.2020.12.027.

(12) Cui, Y. Silicon Anodes. *Nat. Energy* **2021**, *6* (10), 995–996. https://doi.org/10.1038/s41560-021-00918-2.

(13) Hassoun, J.; Bonaccorso, F.; Agostini, M.; Angelucci, M.; Betti, M. G.; Cingolani, R.; Gemmi, M.; Mariani, C.; Panero, S.; Pellegrini, V.; Scrosati, B. An Advanced Lithium-Ion Battery Based on a Graphene Anode and a Lithium Iron Phosphate Cathode. *Nano Lett.* **2014**, *14* (8), 4901–4906. https://doi.org/10.1021/nl502429m.

(14) Gummow, R. J.; de Kock, A.; Thackeray, M. M. Improved Capacity Retention in Rechargeable 4 V Lithium/Lithium-Manganese Oxide (Spinel) Cells. *Solid State Ionics* **1994**, *69* (1), 59–67. https://doi.org/10.1016/0167-2738(94)90450-2.

(15) Chernova, N. A.; Hidalgo, M. F. V.; Kaplan, C.; Lee, K.; Buyuker, I.; Siu, C.; Wen, B.; Ding, J.; Zuba, M.; Wiaderek, K. M.; Seymour, I. D.; Britto, S.; Piper, L. F. J.; Ong, S. P.; Chapman, K. W.; Grey, C. P.; Whittingham, M. S. Vanadyl Phosphates A x VOPO 4 (A = Li, Na, K) as Multielectron Cathodes for Alkali-Ion Batteries. *Adv. Energy Mater.* **2020**, *10* (47), 2002638. https://doi.org/10.1002/aenm.202002638.

(16) Justinabraham, R.; Durairaj, A.; Ramanathan, S.; Obadiah, A.; John wesley, R.; Lv, X.; Vasanthkumar, S. Synthesis of Porous G-C3N4 Doped Vanadyl Phosphate for Supercapattery Application. *J. Energy Storage* **2021**, *40*, 102786. https://doi.org/10.1016/j.est.2021.102786.

(17) Wu, C.; Lu, X.; Peng, L.; Xu, K.; Peng, X.; Huang, J.; Yu, G.; Xie, Y. Two-Dimensional Vanadyl Phosphate Ultrathin Nanosheets for High Energy Density and Flexible Pseudocapacitors. *Nat. Commun.* **2013**, *4* (1), 2431. https://doi.org/10.1038/ncomms3431.

(18) Liu, X.; Ye, Z. Nitroaromatics as High-Energy Organic Cathode Materials for Rechargeable Alkali-Ion (Li + , Na + , and K +) Batteries. *Adv. Energy Mater.* **2021**, *11* (4), 2003281. https://doi.org/10.1002/aenm.202003281.

(19) Shi, H.; Jia, Z.; Wu, W.; Zhang, X.; Liu, X.; Sun, X. The Development of Vanadyl Phosphate Cathode Materials for Energy Storage Systems: A Review. *Chem. – A Eur. J.* **2020**, *26* (37), 8190–8204. https://doi.org/10.1002/chem.201905706.

(20) Kanno, R. Secondary Batteries - Lithium Rechargeable Systems | Electrolytes: Solid Sulfide. In *Encyclopedia of Electrochemical Power Sources*; Elsevier, 2009; pp 129–137. https://doi.org/10.1016/B978-044452745-5.00212-4.

(21) Zhu, Y.; Peng, L.; Chen, D.; Yu, G. Intercalation Pseudocapacitance in Ultrathin VOPO 4 Nanosheets: Toward High-Rate Alkali-Ion-Based Electrochemical Energy Storage. *Nano Lett.* **2016**, *16* (1), 742–747. https://doi.org/10.1021/acs.nanolett.5b04610.

(22) Davidson, A.; Villeneuve, G.; Fournes, L.; Smith, H. Direct Redox Intercalation of Ferrocene in α-VOPO4. *Mater. Res. Bull.* **1992**, *27* (3), 357–366. https://doi.org/10.1016/0025-5408(92)90065-8.

(23) Martin, R. M.; Martin, R. M. Density Functional Theory: Foundations. In *Electronic Structure*; Cambridge University Press, 2004; pp 119–134. https://doi.org/10.1017/CBO9780511805769.008.

(24) Kohn, W.; Sham, L. J. Self-Consistent Equations Including Exchange and Correlation Effects. *Phys. Rev.* **1965**, *140* (4A), A1133–A1138. https://doi.org/10.1103/PhysRev.140.A1133.

(25) Perdew, J. P.; Burke, K.; Ernzerhof, M. Generalized Gradient Approximation Made Simple. *Phys. Rev. Lett.* **1996**, *77* (18), 3865–3868. https://doi.org/10.1103/PhysRevLett.77.3865.

(26) Perdew, J. P.; Wang, Y. Accurate and Simple Analytic Representation of the Electron-Gas Correlation Energy. *Phys. Rev. B* **1992**, *45* (23), 13244–13249. https://doi.org/10.1103/PhysRevB.45.13244.

(27) Becke, A. D. Density-Functional Thermochemistry. III. The Role of Exact Exchange. *J. Chem. Phys.* **1993**, *98* (7), 5648–5652. https://doi.org/10.1063/1.464913.

(28) Lee, C.; Yang, W.; Parr, R. G. Development of the Colle-Salvetti Correlation-Energy Formula into a Functional of the Electron Density. *Phys. Rev. B* **1988**, *37* (2), 785–789. https://doi.org/10.1103/PhysRevB.37.785.

(29) Goerigk, L.; Grimme, S. Efficient and Accurate Double-Hybrid-Meta-GGA Density Functionals- Evaluation with the Extended GMTKN30 Database for General Main Group Thermochemistry, Kinetics, and Noncovalent Interactions. *J. Chem. Theory Comput.* **2011**, *7* (2), 291–309. https://doi.org/10.1021/CT100466K/SUPPL_FILE/CT100466K_SI_001.PDF.

(30) Anisimov, V. I.; Zaanen, J.; Andersen, O. K. Band Theory and Mott Insulators: Hubbard U Instead of Stoner I. *Phys. Rev. B* **1991**, *44* (3), 943–954. https://doi.org/10.1103/PhysRevB.44.943.

(31) Grimme, S.; Antony, J.; Ehrlich, S.; Krieg, H. A Consistent and Accurate Ab Initio Parametrization of Density Functional Dispersion Correction (DFT-D) for the 94 Elements H-Pu. *J. Chem. Phys.* **2010**, *132* (15), 154104. https://doi.org/10.1063/1.3382344.

(32) Klimeš, J.; Bowler, D. R.; Michaelides, A. Chemical Accuracy for the van Der Waals Density Functional. *J. Phys. Condens. Matter* **2010**, *22* (2), 022201. https://doi.org/10.1088/0953-8984/22/2/022201.

(33) Mathew, K.; Kolluru, V. S. C.; Mula, S.; Steinmann, S. N.; Hennig, R. G. Implicit Self-Consistent Electrolyte Model in Plane-Wave Density-Functional Theory. *J. Chem. Phys.* **2019**, *151* (23), 234101. https://doi.org/10.1063/1.5132354.

(34) Mathew, K.; Sundararaman, R.; Letchworth-Weaver, K.; Arias, T. A.; Hennig, R. G. Implicit Solvation Model for Density-Functional Study of Nanocrystal Surfaces and Reaction Pathways. *J. Chem. Phys.* **2014**, *140* (8), 084106. https://doi.org/10.1063/1.4865107.

(35) Gunceler, D.; Letchworth-Weaver, K.; Sundararaman, R.; Schwarz, K. A.; Arias, T. A. The Importance of Nonlinear Fluid Response in Joint Density-Functional Theory Studies of Battery Systems. *Model. Simul. Mater. Sci. Eng.* **2013**, *21* (7), 074005. https://doi.org/10.1088/0965-0393/21/7/074005.

(36) JÓNSSON, H.; MILLS, G.; JACOBSEN, K. W. Nudged Elastic Band Method for Finding Minimum Energy Paths of Transitions. In *Classical and Quantum Dynamics in Condensed Phase Simulations*; WORLD SCIENTIFIC, 1998; pp 385–404. https://doi.org/10.1142/9789812839664_0016.

(37) Maher, K.; Bargar, J. R.; Brown, G. E. Environmental Speciation of Actinides. *Inorg. Chem.* **2013**, *52* (7), 3510–3532. https://doi.org/10.1021/ic301686d.

(38) Li, D.; Kaplan, D. I. Sorption Coefficients and Molecular Mechanisms of Pu, U, Np, Am and Tc to Fe (Hydr)Oxides: A Review. *J. Hazard. Mater.* **2012**, *243*, 1–18. https://doi.org/10.1016/j.jhazmat.2012.09.011.

(39) Keshtkar, A. R.; Irani, M.; Moosavian, M. A. Removal of Uranium (VI) from Aqueous Solutions by Adsorption Using a Novel Electrospun PVA/TEOS/APTES Hybrid Nanofiber Membrane: Comparison with Casting PVA/TEOS/APTES Hybrid Membrane. *J. Radioanal. Nucl. Chem.* **2013**, *295* (1), 563–571. https://doi.org/10.1007/s10967-012-2110-6.

(40) Ladeira, A. C. Q.; Gonçalves, C. R. Influence of Anionic Species on Uranium Separation from Acid Mine Water Using Strong Base Resins. *J. Hazard. Mater.* **2007**, *148* (3), 499–504. https://doi.org/10.1016/j.jhazmat.2007.03.003.

(41) Chen, Z.; Hanna, S. L.; Redfern, L. R.; Alezi, D.; Islamoglu, T.; Farha, O. K. Reticular Chemistry in the Rational Synthesis of Functional Zirconium Cluster-Based MOFs. *Coord. Chem. Rev.* **2019**, *386*, 32–49. https://doi.org/10.1016/j.ccr.2019.01.017.

(42) Della Rocca, J.; Liu, D.; Lin, W. Nanoscale Metal–Organic Frameworks for Biomedical Imaging and Drug Delivery. *Acc. Chem. Res.* **2011**, *44* (10), 957–968. https://doi.org/10.1021/AR200028A.

(43) Horcajada, P.; Gref, R.; Baati, T.; Allan, P. K.; Maurin, G.; Couvreur, P.; Férey, G.; Morris, R. E.; Serre, C. Metal–Organic Frameworks in Biomedicine. *Chem. Rev.* **2011**, *112* (2), 1232–1268. https://doi.org/10.1021/CR200256V.

(44) Zhang, T.; Lin, W. Metal–Organic Frameworks for Artificial Photosynthesis and Photocatalysis. *Chem. Soc. Rev.* **2014**, *43* (16), 5982–5993. https://doi.org/10.1039/C4CS00103F.

(45) Furukawa, H.; Cordova, K. E.; O'Keeffe, M.; Yaghi, O. M. The Chemistry and Applications of Metal-Organic Frameworks. *Science (80-.).* **2013**, *341* (6149). https://doi.org/10.1126/science.1230444.

(46) Qiu, S.; Xue, M.; Zhu, G. Metal–Organic Framework Membranes: From Synthesis to Separation Application. *Chem. Soc. Rev.* **2014**, *43* (16), 6116–6140. https://doi.org/10.1039/C4CS00159A.

(47) Hou, J.; Wang, H.; Zhang, H. Zirconium Metal–Organic Framework Materials for Efficient Ion Adsorption and Sieving. *Ind. Eng. Chem. Res.* **2020**, *59* (29), 12907–12923. https://doi.org/10.1021/ACS.IECR.0C02683.

(48) Carboni, M.; Abney, C. W.; Liu, S.; Lin, W. Highly Porous and Stable Metal–Organic Frameworks for Uranium Extraction. *Chem. Sci.* **2013**, *4* (6), 2396–2402. https://doi.org/10.1039/C3SC50230A.

(49) Cavka, J. H.; Jakobsen, S.; Olsbye, U.; Guillou, N.; Lamberti, C.; Bordiga, S.; Lillerud, K. P. A New Zirconium Inorganic Building Brick Forming Metal Organic Frameworks with Exceptional Stability. *J. Am. Chem. Soc.* **2008**, *130* (42), 13850–13851. https://doi.org/10.1021/ja8057953.

(50) Howarth, A. J.; Liu, Y.; Li, P.; Li, Z.; Wang, T. C.; Hupp, J. T.; Farha, O. K. Chemical, Thermal and Mechanical Stabilities of Metal–Organic Frameworks. *Nat. Rev. Mater.* **2016**, *1* (3), 15018. https://doi.org/10.1038/natrevmats.2015.18.

(51) Liu, J. M.; Yin, X. H.; Liu, T. Amidoxime-Functionalized Metal-Organic Frameworks UiO-66 for U(VI) Adsorption from Aqueous Solution. *J. Taiwan Inst. Chem. Eng.* **2019**, *95*, 416–423. https://doi.org/10.1016/j.jtice.2018.08.012.

(52) Berseneva, A. A.; Martin, C. R.; Galitskiy, V. A.; Ejegbavwo, O. A.; Leith, G. A.; Ly, R. T.; Rice, A. M.; Dolgopolova, E. A.; Smith, M. D.; zur Loye, H.-C.; DiPrete, D. P.; Amoroso, J. W.; Shustova, N. B. "Boarding-Up": Radiation Damage and Radionuclide Leaching Kinetics in Linker-Capped Metal–Organic Frameworks. *Inorg. Chem.* **2020**, *59* (1), 179–183. https://doi.org/10.1021/acs.inorgchem.9b01310.

(53) Li, Y.; Hu, S.; Hilty, F. W.; Montgomery, R.; Park, K. C.; Martin, C. R.; Shustova, N. B.; Liu, Y.; Phillpot, S. R. Leaching Model of Radionuclides in Metal-Organic Framework Particles. *Comput. Mater. Sci.* **2022**, *201*, 110886. https://doi.org/10.1016/j.commatsci.2021.110886.

(54) Ejegbavwo, O. A.; Martin, C. R.; Olorunfemi, O. A.; Leith, G. A.; Ly, R. T.; Rice, A. M.; Dolgopolova, E. A.; Smith, M. D.; Karakalos, S. G.; Birkner, N.; Powell, B. A.; Pandey, S.; Koch, R. J.; Misture, S. T.; Loye, H.-C. zur; Phillpot, S. R.; Brinkman, K. S.; Shustova, N. B. Thermodynamics and Electronic Properties of Heterometallic Multinuclear Actinide-Containing Metal–Organic Frameworks with "Structural Memory." *J. Am. Chem. Soc.* **2019**, *141* (29), 11628–11640. https://doi.org/10.1021/jacs.9b04737.

(55) Dolgopolova, E. A.; Ejegbavwo, O. A.; Martin, C. R.; Smith, M. D.; Setyawan, W.; Karakalos, S. G.; Henager, C. H.; zur Loye, H.-C.; Shustova, N. B. Multifaceted Modularity: A Key for Stepwise Building of Hierarchical Complexity in Actinide Metal–Organic Frameworks. *J. Am. Chem. Soc.* **2017**, *139* (46), 16852–16861. https://doi.org/10.1021/jacs.7b09496.

(56) Moskaleva, L. V.; Krüger, S.; Spörl, A.; Rösch, N. Role of Solvation in the Reduction of the Uranyl Dication by Water: A Density Functional Study. *Inorg. Chem.* **2004**, *43* (13), 4080–4090. https://doi.org/10.1021/ic035450h.

(57) Hagberg, D.; Karlström, G.; Roos, B. O.; Gagliardi, L. The Coordination of Uranyl in Water: A Combined Quantum Chemical and Molecular Simulation Study. *J. Am. Chem. Soc.* **2005**, *127* (41), 14250–14256. https://doi.org/10.1021/JA0526719.

(58) Perron, H.; Roques, J.; Domain, C.; Drot, R.; Simoni, E.; Catalette, H. Theoretical Investigation of the Uranyl Ion Sorption on the Rutile TiO2(110) Face. *Inorg. Chem.* **2008**, *47* (23), 10991–10997. https://doi.org/10.1021/IC801246K.

(59) Ingram, K. I. M.; Häller, L. J. L.; Kaltsoyannis, N. Density Functional Theory Investigation of the Geometric and Electronic Structures of [UO 2 (H 2 O) m (OH) n] 2−n (n + m = 5). *Dalt. Trans.* **2006**, *0* (20), 2403–2414. https://doi.org/10.1039/B517281K.

(60) Grabias, E.; Majdan, M. A DFT Study of Uranyl Hydroxyl Complexes: Structure and Stability of Trimers and Tetramers. *J. Radioanal. Nucl. Chem.* **2017**, *313* (2), 455–465. https://doi.org/10.1007/s10967-017-5305-z.

(61) Yuan, S.; Lu, W.; Chen, Y.-P.; Zhang, Q.; Liu, T.-F.; Feng, D.; Wang, X.; Qin, J.; Zhou, H.-C. Sequential Linker Installation: Precise Placement of Functional Groups in Multivariate Metal−Organic Frameworks. **2015**. https://doi.org/10.1021/ja512762r.

(62) Vandenborre, J.; Drot, R.; Simoni, E. Interaction Mechanisms between Uranium(VI) and Rutile Titanium Dioxide: From Single Crystal to Powder. *Inorg. Chem.* **2007**, *46* (4), 1291–1296. https://doi.org/10.1021/ic061783d.

(63) Perron, H.; Domain, · C; Roques, · J; Drot, · R; Simoni, · E; Catalette, · H. Optimisation of Accurate Rutile TiO 2 (110), (100), (101) and (001) Surface Models from Periodic DFT Calculations. *Theor Chem Acc* **2007**, *117*, 565–574. https://doi.org/10.1007/s00214-006-0189-y.

(64) Lan, J.-H.; Chai, Z.-F.; Shi, W.-Q. A Combined DFT and Molecular Dynamics Study of U(VI)/Calcite Interaction in Aqueous Solution. *Sci. Bull.* **2017**, *62* (15), 1064–1073. https://doi.org/10.1016/j.scib.2017.07.007.

(65) Kresse, G.; Hafner, J. *Ab Initio* Molecular Dynamics for Liquid Metals. *Phys. Rev. B* **1993**, *47* (1), 558–561. https://doi.org/10.1103/PhysRevB.47.558.

(66) Kresse, G.; Furthmüller, J. Efficient Iterative Schemes for Ab Initio Total-Energy Calculations Using a Plane-Wave Basis Set. *Phys. Rev. B* **1996**, *54* (16), 11169–11186. https://doi.org/10.1103/PhysRevB.54.11169.

(67) Blöchl, P. E. Projector Augmented-Wave Method. *Phys. Rev. B* **1994**, *50* (24), 17953. https://doi.org/10.1103/PhysRevB.50.17953.

(68) Kresse, G.; Joubert, D. From Ultrasoft Pseudopotentials to the Projector Augmented-Wave Method. *Phys. Rev. B* **1999**, *59* (3), 1758. https://doi.org/10.1103/PhysRevB.59.1758.

(69) Choudhary, K.; Tavazza, F. Convergence and Machine Learning Predictions of Monkhorst-Pack k-Points and Plane-Wave Cut-off in High-Throughput DFT Calculations. *Comput. Mater. Sci.* **2019**, *161*, 300–308. https://doi.org/10.1016/J.COMMATSCI.2019.02.006.

(70) Steiner, S.; Khmelevskyi, S.; Marsmann, M.; Kresse, G. Calculation of the Magnetic Anisotropy with Projected-Augmented-Wave Methodology and the Case Study of Disordered Fe1-XCox Alloys. *Phys. Rev. B* **2016**, *93* (22), 224425. https://doi.org/10.1103/PhysRevB.93.224425.

(71) Pandey, S.; Demaske, B.; Ejegbavwo, O. A.; Berseneva, A. A.; Setyawan, W.; Shustova, N.; Phillpot, S. R. Electronic Structures and Magnetism of Zr-, Th-, and U-Based Metal-Organic Frameworks (MOFs) by Density Functional Theory. *Comput. Mater. Sci.* **2020**, *184*, 109903. https://doi.org/10.1016/j.commatsci.2020.109903.

(72) Mosey, N. J.; Carter, E. A. Ab Initio Evaluation of Coulomb and Exchange Parameters for DFT + U Calculations. *Phys. Rev. B* **2007**, *76* (15), 155123. https://doi.org/10.1103/PhysRevB.76.155123.

(73) Dudarev, S. L.; Botton, G. A.; Savrasov, S. Y.; Humphreys, C. J.; Sutton, A. P. Electron-Energy-Loss Spectra and the Structural Stability of Nickel Oxide: An LSDA U Study. *Phys. Rev. B* **1998**, *57* (3), 1505. https://doi.org/10.1103/PhysRevB.57.1505.

(74) Bylander, D. M.; Kleinman, L.; Lee, S. Self-Consistent Calculations of the Energy Bands and Bonding Properties of B12C3. *Phys. Rev. B* **1990**, *42* (2), 1394–1403. https://doi.org/10.1103/PhysRevB.42.1394.

(75) Teter, M. P.; Payne, M. C.; Allan, D. C. Solution of Schrödinger's Equation for Large Systems. *Phys. Rev. B* **1989**, *40* (18), 12255. https://doi.org/10.1103/PhysRevB.40.12255.

(76) Grimme, S.; Ehrlich, S.; Goerigk, L. Effect of the Damping Function in Dispersion Corrected Density Functional Theory. *J. Comput. Chem.* **2011**, *32* (7), 1456–1465. https://doi.org/10.1002/JCC.21759.

(77) Mathew, K.; Kolluru, V. S. C.; Mula, S.; Steinmann, S. N.; Hennig, R. G. Implicit Self-Consistent Electrolyte Model in Plane-Wave Density-Functional Theory. *J. Chem. Phys.* **2019**, *151* (23), 234101. https://doi.org/10.1063/1.5132354.

(78) Mathew, K.; Sundararaman, R.; Letchworth-Weaver, K.; Arias, T. A.; Hennig, R. G. Implicit Solvation Model for Density-Functional Study of Nanocrystal Surfaces and Reaction Pathways. *J. Chem. Phys.* **2014**, *140* (8), 084106. https://doi.org/10.1063/1.4865107.

(79) Pan, Q. J.; Odoh, S. O.; Asaduzzaman, A. M.; Schreckenbach, G. Adsorption of Uranyl Species onto the Rutile (110) Surface: A Periodic DFT Study. *Chem. – A Eur. J.* **2012**, *18* (5), 1458–1466. https://doi.org/10.1002/CHEM.201101320.

(80) Lan, J.-H.; Chai, Z.-F.; Shi, W.-Q. A Combined DFT and Molecular Dynamics Study of U(VI)/Calcite Interaction in Aqueous Solution. *Sci. Bull.* **2017**, *62* (15), 1064–1073. https://doi.org/10.1016/j.scib.2017.07.007.

(81) Becke, A. D.; Edgecombe, K. E. A Simple Measure of Electron Localization in Atomic and Molecular Systems. *J. Chem. Phys.* **1998**, *92* (9), 5397. https://doi.org/10.1063/1.458517.

(82) Silvi, B.; Savin, A. Classification of Chemical Bonds Based on Topological Analysis of Electron Localization Functions. *Nat. 1994 3716499* **1994**, *371* (6499), 683–686. https://doi.org/10.1038/371683a0.

(83) Zhang, Y. J.; Zhou, Z. J.; Lan, J. H.; Ge, C. C.; Chai, Z. F.; Zhang, P.; Shi, W. Q. Theoretical Insights into the Uranyl Adsorption Behavior on Vanadium Carbide MXene. *Appl. Surf. Sci.* **2017**, *426*, 572–578. https://doi.org/10.1016/j.apsusc.2017.07.227.

(84) Oğuz, I. C.; Vassetti, D.; Labat, F. Assessing the Performances of Different Continuum Solvation Models for the Calculation of Hydration Energies of Molecules, Polymers and Surfaces: A Comparison between the SMD, VASPsol and FDPB Models. *Theor. Chem. Acc.* **2021**, *140* (8), 99. https://doi.org/10.1007/s00214-021-02799-w.

(85) Kocevski, V.; Zeidman, B. D.; Henager, C. H.; Besmann, T. M. Communication: First-Principles Evaluation of Alkali Ion Adsorption and Ion Exchange in Pure Silica LTA Zeolite. *J. Chem. Phys.* **2018**, *149* (13), 131102. https://doi.org/10.1063/1.5051347.

(86) Shi, Q.; Meng, X.; Prigiobbe, V. Mechanistic Study of Radium Adsorption onto Goethite. *J. Phys. Chem. C* **2020**, *124* (1), 805–814. https://doi.org/10.1021/acs.jpcc.9b10451.

(87) Bhasker-Ranganath, S.; Xu, Y. Hydrolysis of Acetamide on Low-Index CeO 2 Surfaces: Ceria as a Deamidation and General De-Esterification Catalyst. *ACS Catal.* **2022**, *12* (16), 10222–10234. https://doi.org/10.1021/acscatal.2c02514.

(88) Gao, Z.; Lai, Y.; Gong, L.; Zhang, L.; Xi, S.; Sun, J.; Zhang, L.; Luo, F. Robust Th-MOF-Supported Semirigid Single-Metal-Site Catalyst for an Efficient Acidic Oxygen Evolution Reaction. *ACS Catal.* **2022**, *12* (15), 9101–9113. https://doi.org/10.1021/acscatal.2c02181.

(89) Henkelman, G.; Arnaldsson, A.; Jónsson, H. A Fast and Robust Algorithm for Bader Decomposition of Charge Density. *Comput. Mater. Sci.* **2006**, *36* (3), 354–360. https://doi.org/10.1016/J.COMMATSCI.2005.04.010.

(90) Tang, W.; Sanville, E.; Henkelman, G. A Grid-Based Bader Analysis Algorithm without Lattice Bias. *J. Phys. Condens. Matter* **2009**, *21* (8), 084204. https://doi.org/10.1088/0953-8984/21/8/084204.

(91) Sanville, E.; Kenny, S. D.; Smith, R.; Henkelman, G. Improved Grid-Based Algorithm for Bader Charge Allocation. *J. Comput. Chem.* **2007**, *28* (5), 899–908. https://doi.org/10.1002/JCC.20575.

(92) Yu, M.; Trinkle, D. R. Accurate and Efficient Algorithm for Bader Charge Integration. *J. Chem. Phys.* **2011**, *134* (6), 064111. https://doi.org/10.1063/1.3553716.

(93) Wang, V.; Xu, N.; Liu, J. C.; Tang, G.; Geng, W. T. VASPKIT: A User-Friendly Interface Facilitating High-Throughput Computing and Analysis Using VASP Code. *Comput. Phys. Commun.* **2021**, *267*, 108033. https://doi.org/10.1016/J.CPC.2021.108033.

(94) Runde, W. Americium and Curium: Radionuclides. In *Encyclopedia of Inorganic Chemistry*; Wiley, 2005. https://doi.org/10.1002/0470862106.ia742.

(95) Iryna, P. Toxicity of Radionuclides in Determining Harmful Effects on Humans and Environment. *J. Environ. Sci. Public Heal.* **2017**, *01* (02), 115–119. https://doi.org/10.26502/jesph.96120011.

(96) Olobatoke, R. Y.; Mathuthu, M. Radionuclide Exposure in Animals and the Public Health Implications. *Turkish Journal of Veterinary and Animal Sciences*. TUBITAK January 1, 2015, pp 381–388. https://doi.org/10.3906/vet-1502-85.

(97) Morrison, G.; zur Loye, H.-C. Flux Growth of [NaK 6 F][(UO 2) 3 (Si 2 O 7) 2] and [KK 6 Cl][(UO 2) 3 (Si 2 O 7) 2]: The Effect of Surface Area to Volume Ratios on Reaction Products. *Cryst. Growth Des.* **2016**, *16* (3), 1294–1299. https://doi.org/10.1021/acs.cgd.5b01408.

(98) Su, S.; Che, R.; Liu, Q.; Liu, J.; Zhang, H.; Li, R.; Jing, X.; Wang, J. Zeolitic Imidazolate Framework-67: A Promising Candidate for Recovery of Uranium (VI) from Seawater. *Colloids Surfaces A Physicochem. Eng. Asp.* **2018**, *547*, 73–80. https://doi.org/10.1016/j.colsurfa.2018.03.042.

(99) Liu, Y.; Pang, H.; Wang, X.; Yu, S.; Chen, Z.; Zhang, P.; Chen, L.; Song, G.; Saleh Alharbi, N.; Omar Rabah, S.; Wang, X. Zeolitic Imidazolate Framework-Based Nanomaterials for the Capture of Heavy Metal Ions and Radionuclides: A Review. *Chem. Eng. J.* **2021**, *406*, 127139. https://doi.org/10.1016/j.cej.2020.127139.

(100) Tian, K.; Zhuang, S.; Wu, J.; Wang, J. Metal Organic Framework (La-PDA) as an Effective Adsorbent for the Removal of Uranium(VI) from Aqueous Solution. *Radiochim. Acta* **2020**, *108* (3), 195–206. https://doi.org/10.1515/ract-2019-3145.

(101) Tripathi, S.; Sreenivasulu, B.; Suresh, A.; Rao, C. V. S. B.; Sivaraman, N. Assorted Functionality-Appended UiO-66-NH2 for Highly Efficient Uranium(vi) Sorption at Acidic/Neutral/Basic PH. *RSC Adv.* **2020**, *10* (25), 14650–14661. https://doi.org/10.1039/d0ra00410c.

(102) Park, K. C.; Kittikhunnatham, P.; Lim, J.; Thaggard, G. C.; Liu, Y.; Martin, C. R.; Leith, G. A.; Toler, D. J.; Ta, A. T.; Birkner, N.; Lehman-Andino, I.; Hernandez-Jimenez, A.; Morrison, G.; Amoroso, J. W.; zur Loye, H. C.; DiPrete, D. P.; Smith, M. D.; Brinkman, K. S.; Phillpot, S. R.; Shustova, N. B. F-Block MOFs: A Pathway to Heterometallic Transuranics. *Angew. Chemie - Int. Ed.* **2023**, *62* (5). https://doi.org/10.1002/anie.202216349.

(103) Varathan, E.; Gao, Y.; Schreckenbach, G. Computational Study of Actinyl Ion Complexation with Dipyriamethyrin Macrocyclic Ligands. *J. Phys. Chem. A* **2021**, *125* (4), 920–932. https://doi.org/10.1021/acs.jpca.0c08760.

(104) Ansari, S. A.; Bhattacharyya, A.; Mohapatra, P. K.; Egberink, R. J. M.; Huskens, J.; Verboom, W. Evaluation of Two Aza-Crown Ether-Based Multiple Diglycolamide-Containing Ligands for Complexation with the Tetravalent Actinide Ions Np 4+ and Pu 4+ : Extraction and DFT Studies. *RSC Adv.* **2019**, *9* (55), 31928–31935. https://doi.org/10.1039/C9RA05977F.

(105) Li, K.; Hu, S.; Zou, Q.; Zhang, Y.; Zhang, H.; Zhao, Y.; Zhou, T.; Chai, Z.; Wang, Y. Synthesis and Characterizations of a Plutonium(III) Crown Ether Inclusion Complex. *Inorg. Chem.* **2021**, *60* (12), 8984–8989. https://doi.org/10.1021/acs.inorgchem.1c00886.

(106) Zhang, P.; Wang, Y.-X.; Zhang, P.; Wang, S.-A.; Hu, S.-X. Evaluation of Chemical Bonding in Actinyl(VI/V) Oxo-Crown-Ether Complexes for Actinide Series from Uranium to Curium. *Inorg. Chem.* **2020**, *59* (17), 11953–11961. https://doi.org/10.1021/acs.inorgchem.0c00535.

(107) Shamov, G. A.; Schreckenbach, G.; Martin, R. L.; Hay, P. J. Crown Ether Inclusion Complexes of the Early Actinide Elements, [AnO 2 (18-Crown-6)] n + , An = U, Np, Pu and n = 1, 2: A Relativistic Density Functional Study. *Inorg. Chem.* **2008**, *47* (5), 1465–1475. https://doi.org/10.1021/ic7015403.

(108) Liu, Y.; Wang, C.-Z.; Wu, Q.-Y.; Lan, J.-H.; Chai, Z.-F.; Wu, W.-S.; Shi, W.-Q. Theoretical Probing of Size-Selective Crown Ether Macrocycle Ligands for Transplutonium Element Separation. *Inorg. Chem.* **2022**, *61* (10), 4404–4413. https://doi.org/10.1021/acs.inorgchem.1c03853.

(109) Tamain, C.; Autillo, M.; Guillaumont, D.; Guérin, L.; Wilson, R. E.; Berthon, C. Structural and Bonding Analysis in Monomeric Actinide(IV) Oxalate from Th(IV) to Pu(IV): Comparison with the An(IV) Nitrate Series. *Inorg. Chem.* **2022**, *61* (31), 12337–12348. https://doi.org/10.1021/acs.inorgchem.2c01674.

(110) Bombieri, G.; De Paoli, G.; Immirzi, A. Crown Ether Complexes of Actinide Elements an X-Ray Study of the Conformational Change of the Crown Ether within the UO2(NO3)2(H2O)2(18-Crown-6) Molecule. *J. Inorg. Nucl. Chem.* **1978**, *40* (5), 799–802. https://doi.org/10.1016/0022-1902(78)80154-7.

(111) Jensen, M. P.; Chiarizia, R.; Shkrob, I. A.; Ulicki, J. S.; Spindler, B. D.; Murphy, D. J.; Hossain, M.; Roca-Sabio, A.; Platas-Iglesias, C.; de Blas, A.; Rodríguez-Blas, T. Aqueous Complexes for Efficient Size-Based Separation of Americium from Curium. *Inorg. Chem.* **2014**, *53* (12), 6003–6012. https://doi.org/10.1021/ic500244p.

(112) Takao, K.; Ikeda, Y. Coordination Chemistry of Actinide Nitrates with Cyclic Amide Derivatives for the Development of the Nuclear Fuel Materials Selective Precipitation (NUMAP) Reprocessing Method. *Eur. J. Inorg. Chem.* **2020**, *2020* (36), 3443–3459. https://doi.org/10.1002/ejic.202000504.

(113) Park, K. C.; Martin, C. R.; Leith, G. A.; Thaggard, G. C.; Wilson, G. R.; Yarbrough, B. J.; Maldeni Kankanamalage, B. K. P.; Kittikhunnatham, P.; Mathur, A.; Jatoi, I.; Manzi, M. A.; Lim, J.; Lehman-Andino, I.; Hernandez-Jimenez, A.; Amoroso, J. W.; DiPrete, D. P.; Liu, Y.; Schaeperkoetter, J.; Misture, S. T.; Phillpot, S. R.; Hu, S.; Li, Y.; Leydier, A.; Proust, V.; Grandjean, A.; Smith, M. D.; Shustova, N. B. Capture Instead of Release: Defect-Modulated Radionuclide Leaching Kinetics in Metal–Organic Frameworks. *J. Am. Chem. Soc.* **2022**, *144* (35), 16139–16149. https://doi.org/10.1021/jacs.2c06905.

(114) Dudarev, S. L.; Botton, G. A.; Savrasov, S. Y.; Humphreys, C. J.; Sutton, A. P. Electron-Energy-Loss Spectra and the Structural Stability of Nickel Oxide: An LSDA+U Study. *Phys. Rev. B* **1998**, *57* (3), 1505. https://doi.org/10.1103/PhysRevB.57.1505.

(115) Wu, T.; Deng, Q.; Hansen, H. A.; Vegge, T. Mechanism of Water Splitting on Gadolinium-Doped CeO 2 (111): A DFT + U Study. *J. Phys. Chem. C* **2019**, *123* (9), 5507–5517. https://doi.org/10.1021/acs.jpcc.8b12037.

(116) Da Silva, J. L. F.; Ganduglia-Pirovano, M. V.; Sauer, J.; Bayer, V.; Kresse, G. Hybrid Functionals Applied to Rare-Earth Oxides: The Example of Ceria. *Phys. Rev. B* **2007**, *75* (4), 045121. https://doi.org/10.1103/PhysRevB.75.045121.

(117) Castleton, C. W. M.; Kullgren, J.; Hermansson, K. Tuning LDA+U for Electron Localization and Structure at Oxygen Vacancies in Ceria. *J. Chem. Phys.* **2007**, *127* (24), 244704. https://doi.org/10.1063/1.2800015.

(118) Huang, M.; Fabris, S. CO Adsorption and Oxidation on Ceria Surfaces from DFT+U Calculations. *J. Phys. Chem. C* **2008**, *112* (23), 8643–8648. https://doi.org/10.1021/jp709898r.

(119) Suzuki, C.; Nishi, T.; Nakada, M.; Tsuru, T.; Akabori, M.; Hirata, M.; Kaji, Y. DFT Study on the Electronic Structure and Chemical State of Americium in an (Am,U) Mixed Oxide. *J. Phys. Chem. Solids* **2013**, *74* (12), 1769–1774. https://doi.org/10.1016/j.jpcs.2013.07.006.

(120) Lu, Y.; Yang, Y.; Zheng, F.; Wang, B.-T.; Zhang, P. Electronic, Mechanical, and Thermodynamic Properties of Americium Dioxide. *J. Nucl. Mater.* **2013**, *441* (1–3), 411–420. https://doi.org/10.1016/j.jnucmat.2013.06.043.

(121) Hou, L.; Li, W.-D.; Wang, F.; Eriksson, O.; Wang, B.-T. Structural, Electronic, and Thermodynamic Properties of Curium Dioxide: Density Functional Theory Calculations. *Phys. Rev. B* **2017**, *96* (23), 235137. https://doi.org/10.1103/PhysRevB.96.235137.

(122) Klimeš, J.; Bowler, D. R.; Michaelides, A. Van Der Waals Density Functionals Applied to Solids. *Phys. Rev. B* **2011**, *83* (19), 195131. https://doi.org/10.1103/PhysRevB.83.195131.

(123) Wang, V.; Xu, N.; Liu, J.-C.; Tang, G.; Geng, W.-T. VASPKIT: A User-Friendly Interface Facilitating High-Throughput Computing and Analysis Using VASP Code. *Comput. Phys. Commun.* **2021**, *267*, 108033. https://doi.org/10.1016/j.cpc.2021.108033.

(124) Momma, K.; Izumi, F. VESTA 3 for Three-Dimensional Visualization of Crystal, Volumetric and Morphology Data. *J. Appl. Crystallogr.* **2011**, *44* (6), 1272–1276. https://doi.org/10.1107/S0021889811038970.

(125) FANG;ZHU, T. A. N. M. X. X. N. Synthesis, Characterization, Crystal and Molecular Structure of Complex of Cerium (III) Nitrate with Dibenzo-18-Crown-6. *Acta Chimica Sinica*. pp 167–170.

(126) Callsen, M.; Hamada, I. Assessing the Accuracy of the van Der Waals Density Functionals for Rare-Gas and Small Molecular Systems. *Phys. Rev. B* **2015**, *91* (19), 195103. https://doi.org/10.1103/PhysRevB.91.195103.

(127) Maverick, E.; Seiler, P.; Schweizer, W. B.; Dunitz, J. D. 1,4,7,10,13,16-Hexaoxacyclooctadecane: Crystal Structure at 100 K. *Acta Crystallogr. Sect. B Struct. Crystallogr. Cryst. Chem.* **1980**, *36* (3), 615–620. https://doi.org/10.1107/S0567740880003937.

(128) Lin, Q. Y.; Feng, Y. L. Crystal Structure of Tris(Nitrato-O,O′)Bis(1,10-Phenanthroline-N, N′)-Cerium(III), Ce(NO3)3(C12H 8N2)2. *Zeitschrift fur Krist. - New Cryst. Struct.* **2003**, *218* (4), 531–532. https://doi.org/10.1524/ncrs.2003.218.4.531.

(129) Tan, M.; Wang, X.; Gan, X.; Tang, N.; Guo, F.; Zhu, N. Synthesis, Characterization, Crystal and Molecular Structure of Complex of Cerium (III) Nitrate with Dibenzo-18-Crown-6[J]. *Acta Chim. Sin.* **1989**, *47* (2), 167–170.

(130) Hadisaputra, S.; Purwoko, A. A.; Armunanto, R.; Pranowo, H. D. Theoretical Study of the Substituent and Nitrogen Number Effects on the Uranium Binding Selectivity of Crown Ethers. *Acta Chim. Asiana* **2020**, *3* (1), 147–156. https://doi.org/10.29303/aca.v3i1.30.

(131) Yu, M.; Trinkle, D. R. Accurate and Efficient Algorithm for Bader Charge Integration. *J. Chem. Phys.* **2011**, *134* (6), 064111. https://doi.org/10.1063/1.3553716.

(132) Henkelman, G.; Arnaldsson, A.; Jónsson, H. A Fast and Robust Algorithm for Bader Decomposition of Charge Density. *Comput. Mater. Sci.* **2006**, *36* (3), 354–360. https://doi.org/10.1016/j.commatsci.2005.04.010.

(133) Sanville, E.; Kenny, S. D.; Smith, R.; Henkelman, G. Improved Grid-Based Algorithm for Bader Charge Allocation. *J. Comput. Chem.* **2007**, *28* (5), 899–908. https://doi.org/10.1002/jcc.20575.

(134) Tang, W.; Sanville, E.; Henkelman, G. A Grid-Based Bader Analysis Algorithm without Lattice Bias. *J. Phys. Condens. Matter* **2009**, *21* (8), 084204. https://doi.org/10.1088/0953-8984/21/8/084204.

(135) Savin, A.; Nesper, R.; Wengert, S.; Fässler, T. F. ELF: The Electron Localization Function. *Angew. Chemie Int. Ed. English* **1997**, *36* (17), 1808–1832. https://doi.org/10.1002/anie.199718081.

(136) Koumpouras, K.; Larsson, J. A. Distinguishing between Chemical Bonding and Physical Binding Using Electron Localization Function (ELF). *J. Phys. Condens. Matter* **2020**, *32* (31), 315502. https://doi.org/10.1088/1361-648X/ab7fd8.

(137) Dupouy, G.; Bonhoure, I.; Conradson, S. D.; Dumas, T.; Hennig, C.; Le Naour, C.; Moisy, P.; Petit, S.; Scheinost, A. C.; Simoni, E.; Den Auwer, C. Local Structure in Americium and Californium Hexacyanoferrates – Comparison with Their Lanthanide Analogues. *Eur. J. Inorg. Chem.* **2011**, *2011* (10), 1560–1569. https://doi.org/10.1002/ejic.201001004.

(138) Boubals, N.; Wagner, C.; Dumas, T.; Chanèac, L.; Manie, G.; Kaufholz, P.; Marie, C.; Panak, P. J.; Modolo, G.; Geist, A.; Guilbaud, P. Complexation of Actinide(III) and Lanthanide(III) with H4TPAEN for a Separation of Americium from Curium and Lanthanides. *Inorg. Chem.* **2017**, *56* (14), 7861–7869. https://doi.org/10.1021/acs.inorgchem.7b00603.

(139) Atta-Fynn, R.; Bylaska, E. J.; de Jong, W. A. Importance of Counteranions on the Hydration Structure of the Curium Ion. *J. Phys. Chem. Lett.* **2013**, *4* (13), 2166–2170. https://doi.org/10.1021/jz400887a.

(140) Ugozzoli, F.; Casnati, A.; Pochini, A.; Ungaro, R.; Arnaud, F.; Fanni, S.; Schwing, M. J.; Egberink, R. J. M.; Jong, F. de; Reinhoudt, D. N. Synthesis, Complexation, and Membrane Transport Studies of 1,3-Alternate Calix[4]Arene-Crown-6 Conformers: A New Class of Cesium Selective Ionophores. *J. Am. Chem. Soc.* **1995**, *117* (10), 2767–2777. https://doi.org/10.1021/ja00115a012.

(141) Christy, F. A.; Shrivastav, P. S. Conductometric Studies on Cation-Crown Ether Complexes: A Review. *Crit. Rev. Anal. Chem.* **2011**, *41* (3), 236–269. https://doi.org/10.1080/10408347.2011.589284.

(142) Zhan, C. G.; Dixon, D. A. Absolute Hydration Free Energy of the Proton from First-Principles Electronic Structure Calculations. *J. Phys. Chem. A* **2001**, *105* (51), 11534–11540. https://doi.org/10.1021/jp012536s.

(143) Gokel, G. W.; Leevy, W. M.; Weber, M. E. Crown Ethers: Sensors for Ions and Molecular Scaffolds for Materials and Biological Models. *Chem. Rev.* **2004**, *104* (5), 2723–2750. https://doi.org/10.1021/cr020080k.

(144) Dorado, B.; Jomard, G.; Freyss, M.; Bertolus, M. Stability of Oxygen Point Defects in UO2 by First-Principles DFT+U Calculations: Occupation Matrix Control and Jahn-Teller Distortion. *Phys. Rev. B - Condens. Matter Mater. Phys.* **2010**, *82* (3), 035114. https://doi.org/10.1103/PhysRevB.82.035114.

(145) Chen, J.-L.; Kaltsoyannis, N. DFT + U Study of Uranium Dioxide and Plutonium Dioxide with Occupation Matrix Control. *J. Phys. Chem. C* **2022**, *126* (27), 11426–11435. https://doi.org/10.1021/acs.jpcc.2c03804.

(146) Pegg, J. T.; Aparicio-Anglès, X.; Storr, M.; de Leeuw, N. H. DFT+U Study of the Structures and Properties of the Actinide Dioxides. *J. Nucl. Mater.* **2017**, *492*, 269–278. https://doi.org/10.1016/J.JNUCMAT.2017.05.025.

(147) Ho, W. H.; Li, S.-C.; Wang, Y.-C.; Chang, T.-E.; Chiang, Y.-T.; Li, Y.-P.; Kung, C.-W. Proton-Conductive Cerium-Based Metal–Organic Frameworks. *ACS Appl. Mater. Interfaces* **2021**, *13* (46), 55358–55366. https://doi.org/10.1021/acsami.1c17396.

(148) Frisch, M. J.; Trucks, G. W.; Schlegel, H. B.; Scuseria, G. E.; Robb, M. A.; Cheeseman, J. R.; Scalmani, G.; Barone, V.; Petersson, G. a.; Nakatsuji, H.; Li, X.; Caricato, M.; Marenich, a. V.; Bloino, J.; Janesko, B. G.; Gomperts, R.; Mennucci, B.; Hratchian, H. P.; Ortiz, J. V.; Izmaylov, a. F.; Sonnenberg, J. L.; Williams; Ding, F.; Lipparini, F.; Egidi, F.; Goings, J.; Peng, B.; Petrone, A.; Henderson, T.; Ranasinghe, D.; Zakrzewski, V. G.; Gao, J.; Rega, N.; Zheng, G.; Liang, W.; Hada, M.; Ehara, M.; Toyota, K.; Fukuda, R.; Hasegawa, J.; Ishida, M.; Nakajima, T.; Honda, Y.; Kitao, O.; Nakai, H.; Vreven, T.; Throssell, K.; Montgomery Jr., J. a.; Peralta, J. E.; Ogliaro, F.; Bearpark, M. J.; Heyd, J. J.; Brothers, E. N.; Kudin, K. N.; Staroverov, V. N.; Keith, T. a.; Kobayashi, R.; Normand, J.; Raghavachari, K.; Rendell, a. P.; Burant, J. C.; Iyengar, S. S.; Tomasi, J.; Cossi, M.; Millam, J. M.; Klene, M.; Adamo, C.; Cammi, R.; Ochterski, J. W.; Martin, R. L.; Morokuma, K.; Farkas, O.; Foresman, J. B.; Fox, D. J. G16_a03. *Wallingford CT*. 2016, p Gaussian 16, Revision A.03.

(149) Pritchard, B. P.; Altarawy, D.; Didier, B.; Gibson, T. D.; Windus, T. L. New Basis Set Exchange: An Open, Up-to-Date Resource for the Molecular Sciences Community. *J. Chem. Inf. Model.* **2019**, *59* (11), 4814–4820. https://doi.org/10.1021/acs.jcim.9b00725.

(150) Feller, D. The Role of Databases in Support of Computational Chemistry Calculations. https://doi.org/10.1002/(SICI)1096-987X(199610)17:13.

(151) Schuchardt, K. L.; Didier, B. T.; Elsethagen, T.; Sun, L.; Gurumoorthi, V.; Chase, J.; Li, J.; Windus, T. L. Basis Set Exchange: A Community Database for Computational Sciences. *J. Chem. Inf. Model.* **2007**, *47* (3), 1045–1052. https://doi.org/10.1021/ci600510j.

(152) Kim, K.; Jordan, K. D. Comparison of Density Functional and MP2 Calculations on the Water Monomer and Dimer. *J. Phys. Chem.* **1994**, *98* (40), 10089–10094. https://doi.org/10.1021/j100091a024.

(153) Kandiah, M.; Nilsen, M. H.; Usseglio, S.; Jakobsen, S.; Olsbye, U.; Tilset, M.; Larabi, C.; Quadrelli, E. A.; Bonino, F.; Lillerud, K. P. Synthesis and Stability of Tagged UiO-66 Zr-MOFs. *Chem. Mater.* **2010**, *22* (24), 6632–6640. https://doi.org/10.1021/cm102601v.

(154) Katz, M. J.; Brown, Z. J.; Colón, Y. J.; Siu, P. W.; Scheidt, K. A.; Snurr, R. Q.; Hupp, J. T.; Farha, O. K. A Facile Synthesis of UiO-66, UiO-67 and Their Derivatives. *Chem. Commun.* **2013**, *49* (82), 9449. https://doi.org/10.1039/c3cc46105j.

(155) Kirklin, S.; Saal, J. E.; Meredig, B.; Thompson, A.; Doak, J. W.; Aykol, M.; Rühl, S.; Wolverton, C. ARTICLE The Open Quantum Materials Database (OQMD): Assessing the Accuracy of DFT Formation Energies. *Nat. Publ. Gr.* **2015**. https://doi.org/10.1038/npjcompumats.2015.10.

(156) Hagberg, D.; Karlström, G.; Roos, B. O.; Gagliardi, L. The Coordination of Uranyl in Water: A Combined Quantum Chemical and Molecular Simulation Study. *J. Am. Chem. Soc.* **2005**, *127* (41), 14250–14256. https://doi.org/10.1021/JA0526719.

(157) Bankura, A.; Santra, B.; Distasio, R. A.; Swartz, C. W.; Klein, M. L.; Wu, X.; Distasio, R. A. B. A Systematic Study of Chloride Ion Solvation in Water Using van Der Waals Inclusive Hybrid Density Functional Theory. *Taylor Fr.* **2015**, *113* (17–18), 2842–2854. https://doi.org/10.1080/00268976.2015.1059959.

(158) Stoyanov, E. S.; Stoyanova, I. V.; Reed, C. A. The Structure of the Hydrogen Ion (Haq+) in Water. *J. Am. Chem. Soc.* **2010**, *132* (5), 1484–1485. https://doi.org/10.1021/JA9101826.

(159) Zhu, Y.; Qian, Y.; Ju, Z.; Ji, Y.; Yan, Y.; Liu, Y.; Yu, G. Understanding Charge Storage in Hydrated Layered Solids MOPO 4 (M = V, Nb) with Tunable Interlayer Chemistry. *ACS Nano* **2020**, *14* (10), 13824–13833. https://doi.org/10.1021/acsnano.0c06193.

(160) Zhang, Y.; Huixiang Ang, E.; Yang, Y.; Ye, M.; Du, W.; Chao Li, C.; Zhang, Y. F.; Yang, Y.; Ye, M. H.; Du, W. C.; Li, C. C.; Ang, E. H. Interlayer Chemistry of Layered Electrode Materials in Energy Storage Devices. *Adv. Funct. Mater.* **2021**, *31* (4), 2007358. https://doi.org/10.1002/ADFM.202007358.

(161) Whittingham, M. S.; Siu, C.; Ding, J. Can Multielectron Intercalation Reactions Be the Basis of Next Generation Batteries? *Acc. Chem. Res.* **2018**, *51* (2), 258–264. https://doi.org/10.1021/acs.accounts.7b00527.

(162) Faizan, M.; Li, Y.; Zhang, R.; Wang, X.; Song, P.; Liu, R. Progress of Vanadium Phosphorous Oxide Catalyst for N-Butane Selective Oxidation. *Chinese J. Chem. Eng.* **2022**, *43*, 297–315. https://doi.org/10.1016/J.CJCHE.2021.10.026.

(163) Rüther, F.; Machado, R.; Gioria, E.; Kunz, S. L.; Wittich, K.; Löser, P.; Geske, M.; Schunk, S. A.; Glaum, R.; Rosowski, F. Niobium Insertion into α II -VOPO 4 : Tuning the Catalytic Properties for Selective Oxidation. *ACS Catal.* **2023**, *13* (5), 3295–3307. https://doi.org/10.1021/acscatal.2c06209.

(164) Nakamura, M. The Structure and the Activity of Vanadyl Phosphate Catalysts. *J. Catal.* **1974**, *34* (3), 345–355. https://doi.org/10.1016/0021-9517(74)90047-5.

(165) Di Serio, M.; Cozzolino, M.; Tesser, R.; Patrono, P.; Pinzari, F.; Bonelli, B.; Santacesaria, E. Vanadyl Phosphate Catalysts in Biodiesel Production. *Appl. Catal. A Gen.* **2007**, *320*, 1–7. https://doi.org/10.1016/j.apcata.2006.11.025.

(166) Puzzo, F.; Capece, N.; Setti, L.; Pavarelli, G.; De Maron, J.; Tabanelli, T.; Cavani, F. 1-Butanol Dehydration and Oxidation over Vanadium Phosphate Catalysts. *Appl. Catal. A Gen.* **2023**, *661*, 119243. https://doi.org/10.1016/J.APCATA.2023.119243.

(167) Li, X.; Elshahawy, A. M.; Guan, C.; Wang, J. Metal Phosphides and Phosphates-Based Electrodes for Electrochemical Supercapacitors. *Small* **2017**, *13* (39), 1701530. https://doi.org/10.1002/SMLL.201701530.

(168) Shao, M.; Deng, J.; Zhong, F.; Cao, Y.; Ai, X.; Qian, J.; Yang, H. An All-Vanadium Aqueous Lithium Ion Battery with High Energy Density and Long Lifespan. *Energy Storage Mater.* **2019**, *18*, 92–99. https://doi.org/10.1016/J.ENSM.2018.09.029.

(169) Shi, Y.; Zhou, H.; Britto, S.; Seymour, I. D.; Wiaderek, K. M.; Omenya, F.; Chernova, N. A.; Chapman, K. W.; Grey, C. P.; Whittingham, M. S. A High-Performance Solid-State Synthesized LiVOPO4 for Lithium-Ion Batteries. *Electrochem. commun.* **2019**, *105*, 106491. https://doi.org/10.1016/J.ELECOM.2019.106491.

(170) Wu, H.; Chen, Y.; Wen, T.; Chen, L.; Pu, X.; Chen, Z. Advances in Vanadium-Redoxed Polyanions for High-Voltage Sodium-Ion Batteries. *Batteries* **2023**, *9* (1), 56. https://doi.org/10.3390/batteries9010056.

(171) Liao, J.; Han, Y.; Zhang, Z.; Xu, J.; Li, J.; Zhou, X. Recent Progress and Prospects of Layered Cathode Materials for Potassium-ion Batteries. *ENERGY Environ. Mater.* **2021**, *4* (2), 178–200. https://doi.org/10.1002/eem2.12166.

(172) Li, X.; Chen, Z.; Yang, Y.; Liang, S.; Lu, B.; Zhou, J. The Phosphate Cathodes for Aqueous Zinc-Ion Batteries. *Inorg. Chem. Front.* **2022**, *9* (16), 3986–3998. https://doi.org/10.1039/D2QI01083F.

(173) Zhu, K.; Sun, Z.; Liu, P.; Li, H.; Wang, Y.; Cao, K.; Jiao, L. Intercalation Engineering of Layered Vanadyl Phosphates for High Performance Zinc-Ion Batteries. *J. Energy Chem.* **2021**, *63*, 239–245. https://doi.org/10.1016/J.JECHEM.2021.03.051.

(174) Zhu, Y.; Ji, Y.; Ju, Z.; Yu, K.; Ferreira, P. J.; Liu, Y.; Yu, G. Ultrafast Intercalation Enabled by Strong Solvent–Host Interactions: Understanding Solvent Effect at the Atomic Level. *Angew. Chemie Int. Ed.* **2019**, *58* (48), 17205–17209. https://doi.org/10.1002/anie.201908982.

(175) Zhu, Y.; Qian, Y.; Ju, Z.; Peng, L.; Yu, G. Solvent-Dependent Intercalation and Molecular Configurations in Metallocene-Layered Crystal Superlattices. *Nano Lett.* **2018**, *18* (9), 6071–6075. https://doi.org/10.1021/acs.nanolett.8b03030.

(176) Kresse, G.; Hafner, J. *Ab Initio* Molecular Dynamics for Liquid Metals. *Phys. Rev. B* **1993**, *47* (1), 558. https://doi.org/10.1103/PhysRevB.47.558.

(177) Kresse, G.; Furthmüller, J. Efficient Iterative Schemes for Ab Initio Total-Energy Calculations Using a Plane-Wave Basis Set. *Phys. Rev. B* **1996**, *54* (16), 11169–11186. https://doi.org/10.1103/PhysRevB.54.11169.

(178) Perdew, J. P.; Burke, K.; Ernzerhof, M. Generalized Gradient Approximation Made Simple. *Phys. Rev. Lett.* **1996**, *77* (18), 3865–3868. https://doi.org/10.1103/PhysRevLett.77.3865.

(179) Blöchl, P. E. Projector Augmented-Wave Method. *Phys. Rev. B* **1994**, *50* (24), 17953. https://doi.org/10.1103/PhysRevB.50.17953.

(180) Kresse, G.; Joubert, D. From Ultrasoft Pseudopotentials to the Projector Augmented-Wave Method. *Phys. Rev. B* **1999**, *59* (3), 1758–1775. https://doi.org/10.1103/PhysRevB.59.1758.

(181) Stahl, B.; Bredow, T. Critical Assessment of the DFT + U Approach for the Prediction of Vanadium Dioxide Properties. *J. Comput. Chem.* **2020**, *41* (3), 258–265. https://doi.org/10.1002/jcc.26096.

(182) Sun, D.; Okubo, M.; Yamada, A. Optimal Water Concentration for Aqueous Li + Intercalation in Vanadyl Phosphate. *Chem. Sci.* **2021**, *12* (12), 4450–4454. https://doi.org/10.1039/D0SC04647G.

(183) Grimme, S.; Antony, J.; Ehrlich, S.; Krieg, H. A Consistent and Accurate Ab Initio Parametrization of Density Functional Dispersion Correction (DFT-D) for the 94 Elements H-Pu. *J. Chem. Phys.* **2010**, *132* (15), 154104. https://doi.org/10.1063/1.3382344/926936.

(184) Hujo, W.; Grimme, S. Comparison of the Performance of Dispersion-Corrected Density Functional Theory for Weak Hydrogen Bonds. *Phys. Chem. Chem. Phys.* **2011**, *13* (31), 13942. https://doi.org/10.1039/c1cp20591a.

(185) Bylander, D. M.; Kleinman, L.; Lee, S. Self-Consistent Calculations of the Energy Bands and Bonding Properties of B12C3. *Phys. Rev. B* **1990**, *42* (2), 1394–1403. https://doi.org/10.1103/PhysRevB.42.1394.

(186) Teter, M. P.; Payne, M. C.; Allan, D. C. Solution of Schrödinger's Equation for Large Systems. *Phys. Rev. B* **1989**, *40* (18), 12255–12263. https://doi.org/10.1103/PhysRevB.40.12255.

(187) Spackman, M. A.; Jayatilaka, D. Hirshfeld Surface Analysis. *CrystEngComm* **2009**, *11* (1), 19–32. https://doi.org/10.1039/B818330A.

(188) Lu, T.; Chen, F. Multiwfn: A Multifunctional Wavefunction Analyzer. *J. Comput. Chem.* **2012**, *33* (5), 580–592. https://doi.org/10.1002/jcc.22885.

(189) Humphrey, W.; Dalke, A.; Schulten, K. VMD: Visual Molecular Dynamics. *J. Mol. Graph.* **1996**, *14* (1), 33–38. https://doi.org/10.1016/0263-7855(96)00018-5.

(190) Project, T. M. Materials Data on VPO5 by Materials Project. https://doi.org/10.17188/1193783.

(191) Tietze, H. The Crystal and Molecular Structure of Oxovanadium(V) Orthophosphate Dihydrate, VOPO4,2H2O. *Aust. J. Chem.* **1981**, *34* (10), 2035. https://doi.org/10.1071/CH9812035.

(192) Haaland, A.; Nilsson, J. E.; Olson, T.; Norin, T. The Determination of Barriers to Internal Rotation by Means of Electron Diffraction. Ferrocene and Ruthenocene. *Acta Chem. Scand.* **1968**, *22* (8), 2653–2670. https://doi.org/10.3891/acta.chem.scand.22-2653.

(193) Mohammadi, N.; Ganesan, A.; Chantler, C. T.; Wang, F. Differentiation of Ferrocene D5d and D5h Conformers Using IR Spectroscopy. *J. Organomet. Chem.* **2012**, *713*, 51–59. https://doi.org/10.1016/j.jorganchem.2012.04.009.

(194) Rappoport, D.; Crawford, N. R. M.; Furche, F.; Burke, K. Approximate Density Functionals: Which Should I Choose? In *Encyclopedia of Inorganic Chemistry*; Wiley: Chichester, UK, 2005; Vol. 123, p 104101. https://doi.org/10.1002/0470862106.ia615.

(195) Griffith, K. J.; Griffin, J. M. Solid-State NMR of Energy Storage Materials. In *Comprehensive Inorganic Chemistry III*; Elsevier, 2023; Vol. 1–10, pp 282–329. https://doi.org/10.1016/B978-0-12-823144-9.00147-3.

(196) Chen, K.; Sun, Y.; Hou, G. NMR of Catalytic Sites. In *Comprehensive Inorganic Chemistry III*; Elsevier, 2023; Vol. 1–10, pp 471–513. https://doi.org/10.1016/B978-0-12-823144-9.00151-5.

(197) Malischewski, M.; Adelhardt, M.; Sutter, J.; Meyer, K.; Seppelt, K. Isolation and Structural and Electronic Characterization of Salts of the Decamethylferrocene Dication. *Science (80-.).* **2016**, *353* (6300), 678–682. https://doi.org/10.1126/science.aaf6362.

(198) Henkelman, G.; Jónsson, H. Improved Tangent Estimate in the Nudged Elastic Band Method for Finding Minimum Energy Paths and Saddle Points. *J. Chem. Phys.* **2000**, *113* (22), 9978–9985. https://doi.org/10.1063/1.1323224.

(199) Henkelman, G.; Uberuaga, B. P.; Jónsson, H. A Climbing Image Nudged Elastic Band Method for Finding Saddle Points and Minimum Energy Paths. *J. Chem. Phys.* **2000**, *113* (22), 9901–9904. https://doi.org/10.1063/1.1329672.

BIOGRAPHICAL SKETCH

Born in Hefei, Anhui, China, Yuan Liu started his academic pursuits by earning a bachelor's in materials science and engineering from the Beijing University of Chemical Technology in 2017. In May 2018, Yuan's journey took him to the University of Florida's Department of Materials Science and Engineering. Here, before starting his Ph.D., he collaborated extensively with Prof. Simon R. Phillpot throughout 2019 Fall and 2020 Spring, a rewarding endeavor that led to a Master of Science degree by May 2020. Yuan transitioned to his Ph.D. program in August 2020, diving deep into the EFRC project affiliated with the Center for Hierarchical Waste form Materials at the University of South Carolina. His research primarily revolved around nuclear waste sequestration. By Fall 2023, Yuan's dedication and hard work culminated in a Ph.D. in materials science and engineering from the University of Florida.